THE UNIVERSITY OF HULL

The Growth and Characterisation of Zinc Telluride for Use as a Nuclear Radiation Detector

being a Thesis submitted for the Degree of

DOCTOR of PHILOSOPHY

in the University of Hull

by

Charles Paul Hilton, BSc

January,1988

11 J/

SUMMARY Summary of Thesis submitted for PhD degree

by Charles Paul Hilton

on

The Growth and Characterisation of Zinc Telluride

for Use as a Nuclear Radiation Detector.

As grown ZnTe is a highly conductive p-type semiconductor. In an attempt to produce highly resistive material suitable for fabrication into nuclear radiation detectors various dopants have been added during the Bridgman growth process to try to compenate the shallow acceptor defects that are responsible for the as grown electrical conductivity. Van der Pauw resistivity measurements an samples from each boule have showed that indium and aluminium doping offers a consistant way of producing the high resistivity material. In total 12 devices were fabricated from the indium, aluminium and the one boule of high resistivity lead doped material but it was found that only one device, from an aluminium doped boule, was able to detect nuclear radiation. Further studies on this device showed that it was capable of detecting alpha-particles but not gamma-rays and also that it exhibited the normal polarisation efect. In an attempt to correlate device performance (or lack of it) with the presence of point defects in the material all of the material was subject to studies using electrical, optical and magnetic resonance techniques. The information gathered in these ways has proven, to a great extent, to be inconclusive.

TSC studies on indium doped material revealed the presence of two hole trapping levels. One defect with an activation energy of E_v+0.09eV was found to be present in all samples whereas the activation energy of the deeper defect was found to vary from sample to sample. Only one defect, with an activation energy of E_v+0.13eV, was observed in the aluminium doped material and was suggested as being the $(V_{Zn}Al_{Zn})'$ A centre. The concentrations of

the defects found using this method give an indication why indium doped material did not act as a detector.

The presence of the deep Fe^{+} centre has been observed using EPR. The observation of this signal has been correlated with with near infra-red luminescence common to ZnTe and observed in these samples suggesting the involvement of the Fe^{+} centre in the luminescence process.

The signs of the shallow donor g-factors in CdS in ZnS in ZnSe and in the mixed crystal $ZnS_{0.6}Se_{0.4}$ have, for the first time, been measured directly through ODMR experiments which employ circularly polarised microwaves. In all cases the sign was measured to be positive and provides unequivical experimental conformation of the theoretical calculations carried out by Cardonna. ODMR studies on the 695 nm bound exciton emission in $CdS_{0.98}Te_{0.2}$ indicate that this emission does indeed involve the Te pair bound exciton and is the first reported observation of such ODMR signals. These measurements serve to confirm the Te_2 bound exciton assignment to this emission by Goede et al.

ACKNOWLEDGEMENTS

I would like to thank my supervisors Dr. J.E. Nicholls and Mr. B. Lunn of the University of Hull together with Dr. D.H.J. Totterdell of AERE Harwell for their interest and expert guidance throughout this work. Many thanks go also to Dr. J.J. Davies of the University of Hull for valuable advice and discussions, to Professor F.J.H. Bryant for the use of the laboratory facilities, to Mr. E. Norman and the workshop staff for maintaining the cryostats in working order, to Mr. S. Haughey for advice on computational aspects, to SERC for its financial support and finally to AERE Harwell for awarding the CASE studentship.

CONTENTS

CHAPTER ONE

The Choice of Zinc Telluride (ZnTe) as a Material for a Gamma-Ray Spectrometer

1.1 Historical Introduction to Solid State Detectors

The first practical conduction counter was fabricated by Van Heerden [1] in 1945 and consisted of a crystal onto which two metallic contacts were deposited. This formed a solid state ionisation chamber in which electron -hole pairs were created as nuclear radiation passed through. These charge carriers were then swept to their respective contacts under the influence of a high electric field, created by an applied voltage, producing a current pulse which was detected. However it was noted that poor charge collection and polarisation effects were major problems. Despite this, conduction counters had several potential advantages over gas filled detectors, such as small dimensions, high stopping power and a lower energy of creation of electron-hole pairs. Thus research into their development continued [2,3,4].

Internal polarisation (which reduces the applied electric field with time [5,6]) and carrier traps (which reduce charge collection) still limited the use of such detectors. In order to avoid carrier trapping a strong electric field was required (without any increase in leakage current). Such fields are found in N-P junctions or at metal-semiconductor contacts when the device is reverse biased. Under such conditions a depletion region exists containing no free carriers as the minority carriers are swept away under the influence of the high electric field. Any electron-hole pairs created in this region by the nuclear radiation will be swept towards their respective contacts with small probability of recombining. In 1949 MacKay [7] detected α-particles using a reverse biased germanium diode and in 1958

the first gold-silicon surface barrier detector was fabricated by Davis [8].

In order for such devices to be able to detect higher energy radiation (i.e. the particles have a greater range) larger active volumes were required. The depletion region in a junction detector is proportional to the material resistivity and to the square root of the applied bias. In high purity, high resistivity (20,000 Ω cm) silicon with a reverse bias of a few hundred volts the depletion region thickness is of the order of 2mm [9]. This proved to be insufficient for the detection of radiation above about 100 keV and consequently a new growth technique to increase the resistivity of silicon had to be developed.

This involved the compensation of acceptor impurities in the P-type silicon with donor impurities [10]. Lithium was chosen as the donor since it is easily ionised and, as an ion, it then has a high mobility in the material. The compensation is achieved during growth by applying an electric field which causes the ions to drift into the bulk. A useful thickness of up to 16mm [11] has been achieved in devices fabricated in this way. However because of the low atomic number of silicon (Z=14) the gamma ray detection efficiency of these is low and their use is limited to the detection of gamma rays of energy less than about 100 keV.

In order to achieve greater efficiencies a material with a higher atomic number is required [12] and for this reason lithium compensated germanium (Z=32) detectors were fabricated [13,14,15] . However because of the small band gap of germanium (0.74 eV) and the high mobility of the lithium ions completed devices must be stored and operated at liquid nitrogen temperatures.

Other materials were sought that could be handled and fabricated more easily, that had higher detection efficiencies and that could be operated without cooling. Cadmium telluride (CdTe), with an average atomic number of fifty, relatively high electron and hole mobilities and a band gap of 1.5 eV

at 300K was an attractive candidate. In 1966 Mayer [16] published a paper evaluating its use as a gamma ray detector.

Two types of detector can be fabricated from CdTe; one is made from low resistivity (50-500 Ω cm) n-type crystals with indium and gold evaporated contacts on back and front respectively [17]. This type has a thin sensitive region (100 μm) and because of this its use is limited to detection of gamma energies below about 6 keV. The second type is made from high resistivity (10^8-10^9 Ω cm) p-type crystals with indium or aluminium barrier contacts. The typical sensitive region of this type is in the region of 2 to 5 mm and they can detect energies up to the low MeV range.

A major problem in devices fabricated from this material is that of internal polarisation. Schaub [18] and Triboulet et. al. [19] have shown that by careful control of impurities polarisation free aluminium contacted detectors may be fabricated. Device fabrication methods also affect the polarisation and Serreze et. al. [20] have produced polarisation free detectors by improving these. Thus, by 1980, large sensitive volume polarisation free detectors were available which were able to operate at room temperature without cooling. However the available material still produced devices with greatly varying characteristics even when the methods of Schaub, Triboulet et. al. and Serreze et. al. were employed. Another disadvantage was that because of the band gap of cadmium telluride (1.5 eV at 300 K) any detector would only operate usefully up to a temperature of about 340 K.

In order to be able to fabricate a device capable of elevated temperature operation a new material must be found. The choice of a suitable material can be made only after the consideration of the material requirements for device operation.

These may only be obtained after the principles of the interaction of gamma rays with matter is understood.

1.2 Interaction of Gamma Rays with Matter

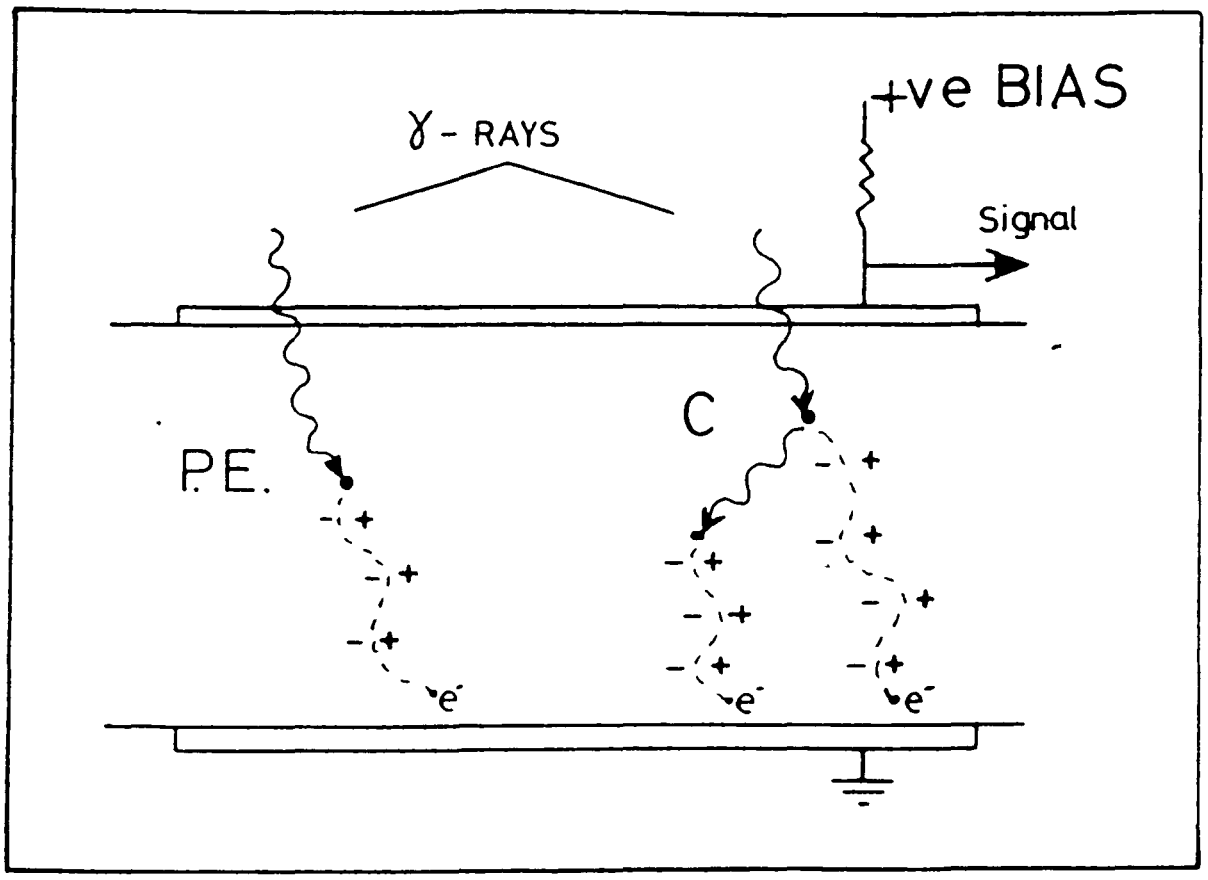

Figure 1.1 Schematic representation of a detector in which Photo-Electric and Compton absorption processes are taking place

Gamma rays interact with semiconductors to produce energetic charged particles (usually electrons) via the Compton (C) and photo-electric (P.E.) effects. These charged particles produce electron-hole pairs within the device (Figure 1.1) which are swept to their respective contacts under the influence of an externally applied electric field producing a current pulse.

The Compton effect can be described as an elastic collision between a photon of energy $E_0 = h\nu_0$ and an orbital electron of the semiconductor. This electron can be considered a free particle since it's binding energy is small compared with E_0. The electron recoils, producing electron-hole pairs in the material. Further electron-hole pairs may be produced by the

scattered photon undergoing multiple Compton scattering processes.

In the photo-electric effect the entire energy of the incident photon is given up to the target atom and one electron is emitted with an energy, E, ($E = E_0$ - binding energy). This electron then produces electron-hole pairs in the material.

1.3 Material Requirements

Several important parameters govern the choice of detector material. These are:

1.3.1 Detector Thickness

Since the detector works by collecting holes or electrons created by ionising radiation the thickness will be determined by the range and energy distribution of the secondary electrons produced by the gamma rays. The highest energy electrons will be the photo-electrons which have a practical range - energy relationship [21] for energies above 0.6 MeV

$$R \ (g/cm^2) = 0.526 \ E(MeV) - 0.094 \qquad (1)$$

Semiconductors usually have densities of about 5 g/cm^3 so that a 1 MeV electron will have a range of about 1 mm. Photo-electrons are created throughout the volume of the device and therefore the minimum detector thickness must be greater than 1 to 2 mm.

Growth techniques that enable single crystals of at least this thickness to be produced must be available.

1.3.2 Atomic Number

The absorption cross-section for the Compton effect is proportional to Z. For the photo-electric effect it is proportional to Z^n $(4<n<5)$ and decreases rapidly with increasing gamma energy ($\sigma_p \propto (h\nu)^{-s}$ where $1<s<3.5$).

Analysis by Sharpe [12] of the energy and atomic number dependence of gamma ray interactions suggests that the atomic number of at least one of the constituents should be greater than 40 to be competitive with germanium whilst keeping the detector thickness below 1 cm.

1.3.3 Band Gap Energy

The energy resolution of the device will depend upon the number of charge carriers created in a gamma ray interaction. This is determined by the average energy, w, required to form an electron-hole pair. Klein [22] derived an expression relating w to the band gap energy, E_g

$$w = 2.67E_g + 0.87 \text{ eV} \qquad (2)$$

indicating that the smaller the band gap the greater the number of electron-hole pairs created and therefore the better the resolution.

However for operation at room temperature and above a large band gap is desirable in order to reduce contributions to the detector current from thermally generated carriers.

It is apparent that elevated temperature operation may only be achieved at the expense of the energy resolution of the device.

1.3.4 Concentration of Trapping Centres

A trapping process is one in which a carrier is captured by a centre and then has a much greater probability of being re-emitted than of

recombining with a carrier of opposite charge. The presence of such centres results in a degradation of resolution due to the current pulse being spread out in time. It is possible to estimate the maximum density, N_T', of effective trapping centres permissible for a given energy resolution. Using the Klein relationship (eqn.(2)) the calculated energy required to create an electron-hole pair in ZnTe (E_g = 2.28 eV at 300K) is 6.9 eV, so that a 1 MeV photo-electron will create approximately 1.5×10^5 electron-hole pairs.

As the carriers move across the detector the number of interactions, n, they will experience is

$$n = N_T' S_T X \qquad (3)$$

Where S_T is the trap capture cross-section and

X is the width of the depletion region (which is the width of the detector when made of high resistivity material).

The energy width may be approximated from equation (3). If this width is to be less than 1% i.e., an energy resolution of 10 keV in 1 MeV, then only 1 carrier in 10^2 pairs created can be trapped.

Assuming $S_T = 10^{-17}$ cm^2 then

$$N_T' = 5 \times 10^{15} \text{ cm}^{-3} \qquad (4)$$

in a 2 mm thick detector and therefore pure material is needed.

1.3.5 $|N_D - N_A|$

The application of a reverse bias produces a high field region within the detector. The width, X, of this region may be calculated directly from Poisson's equation [23]. Assuming that the net concentration of ionised impurities, $|N_D - N_A|$, is independent of X and that the depletion region

extends the throughout the width, L, of the detector then

$$X^2 \approx (\varepsilon_s V)/\frac{(q\,|N_D - N_A|)}{4\pi} \qquad (5)$$

Under a bias of 100 V the net concentration of ionised impurities in a 2 mm detector has thus to be less than about 1.5×10^{12} cm^{-3}
(Note, the total concentration of impurities may be much higher than this if compensation techniques are used to achieve a net $|N_D - N_A|$)

1.3.6 Transit Time and Mobility

The drift velocity, V_D, of free charge carriers under the influence of an applied electric field, E, is proportional to that field (provided that E is low so that V_D < thermal velocity, V_{Th}). The constant of proportionality is known as the mobility, μ thus

$$\mu = V_D/E \ (cm^2V^{-1}s^{-1}) \qquad (6)$$

Free carriers are scattered in semiconductors mainly through interactions with lattice phonons (optical and acoustic) and ionised impurities. These scattering processes influence the mean free time, τ, between interactions. This time is related to the mobility as

$$\mu = q\tau/m^* \qquad (7)$$

where m^* is the electron or hole reduced mass

The carrier mobility is an important property of the semiconductor in terms of detector operation since the mean free path, λ, of the carriers is proportional to the mobility and is given by

$$\lambda = \mu \tau E \qquad (8)$$

and for complete charge collection λ must be greater than the distance between electrodes. This means that in a 2mm thick detector, operating under a bias of 100 V (field strength of 5×10^2 Vcm^{-1}), the $\mu\tau$ product must be greater than 4×10^{-4} cm^2 V^{-1}. With typical lifetimes of the order of 10^{-6} s the mobility, of either carrier, must be greater than 100 cm^2 V^{-1} s^{-1}.

1.4 ZnTe and The Basic Material Requirements

The purpose of the present work is to develop a semiconductor nuclear radiation detector for use at temperatures above that at which CdTe detectors can operate.

From the discussion above it is clear that the material chosen for this use must meet the requirements which are summarised in Table 1.1 below if it is to be an efficient detector with an energy resolution of about 2 %. A consideration of these parameters indicates that ZnTe may be a suitable detector material.

The high average atomic number of ZnTe (Z=41) means that it will allow efficient ionisation by high energy gamma rays within its volume. A band gap of 2.28 eV (at 300 K) should result in a lower dark current than that of CdTe and allow room temperature (and higher) operation without cooling.

PARAMETERS	REQUIREMENTS
Detector Thickness	$L > 2$ mm
Atomic Number	$Z > 40$
Band Gap Energy	$E_g > 2$ eV
Trapping Centres	$N_T < 10^{14}$ cm^{-3}
Donors, Acceptors	$\lvert N_D - N_A \rvert < 10^{12}$ cm^{-3}
Carrier Mobility	$\mu > 100$ cm^2 V^{-1} s^{-1}
$\mu\tau$ Product	$\mu\tau > 4 \times 10^{-4}$ cm^{2}V^{-1}

Table 1.1 Requirements for a gamma detector of 2% resolution

The mobility, at room temperature, of a polar semiconductor such as ZnTe is determined principally by optical phonon and ionised impurity scattering.

The value of the mobility due to optical phonon scattering has been given by Howarth and Sondheimer [24] as

$$\mu_{opt} = \frac{1}{2\alpha\omega_L}\frac{q}{m^*}\frac{8}{3\sqrt{\pi z}}(z)(e^z - 1) \qquad (9)$$

where z is the ratio of Debye temperature ($\hbar\omega_L/k$) to lattice temperature (T) and α is the coupling constant which is a measure of the electron - lattice interaction.

This is determined from

$$\alpha = \frac{q^2}{\hbar}\left[\frac{m^*}{2\hbar\omega_L}\right]^{1/2} \frac{\varepsilon_s - \varepsilon_\infty}{\varepsilon_s\,\varepsilon_\infty} \qquad (10)$$

Here ε_s and ε_∞ are the static and optical dielectric constants.

Inserting the values of the various constants (given in Appendix A) into equations (9) and (10) yields a value of:

$$\mu_{opt} = 187\ cm^2V^{-1}s^{-1} \text{ at } 300\ K$$

In polar semiconductors containing a high concentration of impurites scattering by ionised impurities may also be important at room temperature. The mobility due to this type of scattering was shown by Brooks [25] to be given by (in S.I. units)

$$\mu_I = \frac{64\pi^{1/2}\varepsilon_s^{\,2}(2kT)^{3/2}}{N_I\, q^3\, m^{*1/2}} \left[\ln\left[\frac{24m^*k^2T^2\,\varepsilon_s}{q^2\hbar^2 N_I'}\right]\right]^{-1} \qquad (11)$$

(Assuming that the donors and acceptors are singly ionised)

where N_I is the concentration of ionised impurities = $N_D + N_A$;

and N_I' is the net concentration of free carriers i.e. $|N_D - N_A|$;

Assuming a value for N_I of $10^{18} < N_I < 10^{20}$ cm ^{3} (a maximum likely value in closely compensated material) and a value for N_I' of $N_I' < 10^{12}$ cm ^{3} (limit calculated from equation (5)) equation (11) yields a value of:

$$\mu_I \approx 10^5 - 10^7\ cm^2V^{-1}s^{-1} \text{ at } 300\ K.$$

A comparison between the magnitudes of μ_{opt} and μ_I shows that it is the former type of scattering that will govern the mobility of carriers in ZnTe.

Indeed the experimental values of electron and hole mobilities in ZnTe have been found to be 340 and 110 cm^2 V^{-1} s^{-1} respectively [26,27] which are large enough to allow complete charge collection in a 2 mm thick device.

Although the intrinsic properties of ZnTe suggest that the material may be used as a radiation detector, its extrinsic properties are equally important. In this respect ZnTe has to be grown with a low concentration of trapping centres and be sufficiently compensated to produce high resistivity material. The main problem to overcome is that of production of high resistivity material because as-grown material is normally low resistivity P-type. Compensation by doping during growth has to be carried out in order to produce the uniformly doped, high resistivity material required. This has been done successfully in CdTe by the use of both the Travelling Heater Method (e.g. [28,29]) and the Bridgman method (e.g. [29]). However the problems that this compensation technique produces in CdTe (such as polarisation [30,31,32,33], and the difficulty of producing single crystal of low enough concentration of defects [34] introduced by the high temperature growth method necessary) are likely to occur in ZnTe.

Finally boules of ZnTe must be grown using a method which will allow slices of single crystal of approximately 5 mm diameter and atleast 2 mm thickness to be obtained. The method that has been employed to do this will be discussed in the next Chapter.

CHAPTER ONE REFERENCES

[1] Van Heerden P.J., The Crystal Counter Utrecht Dissertation (1945)

[2] Frerichs R., Phys. Rev. 72 594 (1947)

[3] Stelter G., Verhandl. Deut. Physik. Ges. 22 13 (1941)

[4] Hofstadter R., Phys. Rev. 72 1120 (1947)

[5] Wainters L.F. and Christian R.S., Phys. Rev. 72 1127 (1947)

[6] Chynoweth A.G., Phys. Rev. 83 254 (1951)

[7] MacKay K.G., Phys. Rev. 76 1537 (1949)

[8] Davis W.D., J. Appl. Phys. 29 231 (1958)

[9] Siffert P. and Coche A., Compt. Rend. 259 3277 (1963)

[10] Reiss H. and Fuller C.S., J. Chem. Phys. 25 650 (1956)

[11] Pell E.M., J. Appl. Phys. 31 291 (1960)

[12] Sharpe J., Nuc. Rad. Detect. (Methuen London 1964)

[13] Freck D.V. and Wakefield J., Nature 193 669 (1962)

[14] Webb P.P. and Williams R.L., Nucl. Instr. Meth. 22 361 (1963)

[15] Tavendale A.J., Nuclear Electronics (O.E.C.D. Paris 1963) 235

[16] Mayer J.W., J. Appl. Phys. 38 296 (1967)

[17] Dabrowski A.J., Nuc. Sci. Symp. I.E.E.E. (Nov. 1975)

[18] Scaub B., C.N.R.S. L.E.T.I. Grenoble

[19] Triboulet R., Marfaing Y., Cornet A. and Siffert P., Nature Physical Sci. 245 12 (1973)

[20] Serreze H.B., Nuc. Sci. Symp. I.E.E.E. (Nov. 1973)

[21] Hereford F.L. and Swann C.P., Phys. Rev. 78 727 (1950)

[22] Klein C.A., J. Appl. Phys. 39 2029 (1968)

[23] Mayer J.W., Semicon. Detectors Chap.5 (N. Holland, Amsterdam 1968)

[24] Howarth D. and Sondheimer E.H., Proc. Roy. Soc. A219 53 (1953)

[25] Brooks H., Advances in Electronics and Electron Physics (edited Marton) Vol 7 85 (1955)

[26] Goodman A.M., J. Appl. Phys. 34 329 (1963)

[27] Fischer A.G. and Carides J.N., Sol. State Comm. 2 157 (1964)

[28] Hage-Ali M., Scharager C., Koebel J.M. and Siffert P., Nucl. Instr. and Methods 176 499 (1980)

[29] Zanio K., Krajenbrink F. and Montano H., IEEE Trans. Nucl. Soc. NS21 315 (1974)

[30] Malm H.L. and Martini M., Can. J. Phys. 51 2336 (1973)

[31] MacKay K.G., Phys. Rev. 74 1606 (1948)

[32] Hofstader R., Nucleonics 4 April 2 & May 29 (1949)

[33] Bilbe R.M., Lunn B., Nicholls J.E. and Totterdell D.H.J., Phys. Stat. Sol.(a) 71 239 (1982)

[34] Kyle N.R., J. Electrochem. Soc. 118 1790 (1971)

CHAPTER TWO

Crystal Growth and Materials Assessment

Introduction

The growth process used to transform the polycrystalline charge into single crystal must be able to produce material which will meet the basic requirements for device fabrication as described in the previous Chapter. This means that from the process crystals of the order of a centimeter thick containing a low density of volume defects, such as grain boundaries, dislocations and precipitates, should be available. The growth process should also be flexible enough to allow a dopant to be introduced at this stage in order to produce the high resistivity required of device material.

Inherent in most growth processes is the exposure of the growing crystal to a high temperature environment for considerable times. This creates a potential for impurity in-diffusion, from, for example, the growth capsule or the furnace windings. The high temperatures together with the cooling time and temperature gradient will also affect the nature of the point defect equilibrium. It is these point and volume defects that will ultimately control the device performance and therefore the generation of these should be minimised through optimisation of the growth parameters.

It is clear the crystal growth process is expected to achieve a number of simultaneous goals and that any process can offer only a compromise among the various requirements imposed upon the material when fabricating a nuclear radiation detector.

The Bridgman growth method was chosen as it should allow large volumes of doped single crystal to be produced. However the high growth temperatures used in this process greatly enhances the chance of impurity in-diffusion.

2.1 Compensation in Zinc Telluride

Undoped ZnTe usually exhibits p-type conductivity, with type conversion occurring only when the donor concentration is extremely high (typically 10^{20} atoms cm^{-3} of Al [1]).

The earliest and simplest model developed to describe the defect chemistry mechanisms responsible for the electrical properties was proposed by de Nobel [2]. The basic assumption of this model was that it was the native defects i.e. zinc vacancies mainly in the form of V_{Zn}'' that were responsible for the observed p-type conductivity and it was these defects that shallow donors must compensate to increase the resistivity.

The concentration of neutral zinc vacancies is determined by equilibrium with the vapour phase

$$Zn_{Zn} \rightleftharpoons V_{Zn}^{o} + Zn(g) \qquad (1)$$

$$V_{Zn}^{o} \rightleftharpoons V_{Zn}'' + 2h^{+}$$

The mass action equations are then

$$[V_{Zn}^{o}] = k_1 P_{Zn}^{-1} \qquad (2)$$

$$[V_{Zn}''] = k_2 [V_{Zn}^{o}] p^{-2} = k_2\, p^{-2} P_{Zn}^{-1}$$

where P_{Zn} is the partial pressure of zinc and p is the hole density.

In equilibrium electrical neutrality will also exist which, in the simplified case of p-type ZnTe containing V_{Zn}'', may be given by

$$[D^{\cdot}] - 2[V_{Zn}''] = n - p \qquad (3)$$

(where $[D^{\cdot}]$ is the concentration of ionised donors)

The np product ($np=n_i^2$) together with equation (3) gives

$$p^2 + p[D^+] = 2p[V_{Zn}''] + n_i^2 \qquad (4)$$

(where n_i is the intrinsic carrier density)

Neglecting the electron contribution in equation (4) (valid as ZnTe is p-type) and substituting for $[V_{Zn}'']$ from equations (2) the model of de Nobel predicts a variation in hole density that is proportional to $P_{Zn}^{-1/3}$. Support for this model comes from experimental work on the variation of the hole concentration with P_{Zn} by Thomas et al [3] who found that it did indeed follow a $P_{Zn}^{-1/3}$ law.

However optical measurements on undoped ZnTe has shown that the dominant acceptors involved in the bound exciton recombination processes are not zinc vacancies but involve the impurities copper and lithium [4,5]. Furthermore scanning electron microscopy experiments, carried out in the cathodoluminescence mode, have shown that there are spatial intensity variations in the intensities of these excitonic lines which can be related to the distribution of tellurium precipitates and inclusions found in ZnTe [6,7,8].

A new model was proposed by Pfister [9] to explain these findings. In this model the electrical conductivity is now controlled by an extrinsic impurity defect namely the Cu_{Zn} single acceptor. The copper tends to be stored in the tellurium precipitates (in the form of Cu_2Te) and released during annealing as the tellurium is dissolved. This interchange of the copper between the precipitate and the matrix is described by the chemical equation

$$V_{Zn} + Cu_2Te \rightleftharpoons 2Cu_{Zn} + Te_{Te} \qquad (5)$$

and is seen to conserve the number of acceptors so that zinc vacancies may be thought of as being stored in the form of Cu_{Zn}'. This means that $[V_{Zn}'']$ in equations (2) should be replaced by $[Cu_{Zn}']^2$ which leads to a hole density that varies as $P_{Zn}^{-1/4}$. This power dependence is difficult to distinguish experimentally from the power dependence of the first model and may explain why the simple model worked so well.

Using either model it is apparent that if a dopant species, capable of producing shallow donor states, is introduced into the material compensation of the acceptor levels is likely to occur. This will then produce the high resistivity material that is required for device operation. This simple compensation mechanism is complicated by several factors such as complex formation and self compensation:-

It has been shown experimentally [8] that when donor species (e.g. $Al_{Zn}^{\bullet}$) are present in the material then the $(V_{Zn}D)'$ single acceptor may be formed when an ionised donor, $D^{\bullet}$ is electrostatically attracted to a nearest neighbour V_{Zn}'' so that

$$V_{Zn}'' + D^{\bullet} \rightleftharpoons (V_{Zn}D)' \qquad (6)$$

As the donor level increases then the hole concentration decreases and therefore, from equation (2), the concentration of V_{Zn}'' acceptors increases and self compensation occurs.

If the model of Pfister is correct and the observed p-type conductivity in undoped material is due to the presence of impurity related acceptor states then it should be possible to produce high resistivity material without donor compensation by using chemicals of very high purity or alternatively by purifying the grown crystal. Both of these alternatives are expensive and so costs may be prohibitive in commercial device manufacturing. Although the growth of high resistivity material by purifying the

grown crystal has been reported in CdTe [9] chemical analysis of the material produced in this way showed a high concentration of aluminium (a donor species in both CdTe and ZnTe) to be present which may have produced the compensation in the crystal. For the reasons of high cost and uncertaintity in the cause of the compensation in purified crystal the method of acceptor compensation using a donor dopant was explored as a means of producing high resistivity material.

2.2 Design of the Growth Furnace

When considering the design of the growth furnace one must be aware of the physical requirements imposed by the consideration of the kinetics of the growth process. The most important of these considerations being diffusion and constitutional supercooling. These govern the temperature profile (change of temperature with vertical distance) of the furnace and the lowering rate of the charge.

The kinetic aspects will be outlined below. More detailed studies may be found in most text books concerned with crystal growth [e.g. 12,13]

2.2.1 Diffusion and Constitutional Supercooling

The Phase Rule states :

$$P+F = C+2 \qquad (1)$$

where P = N^{O} of phases = 2 (solid and liquid phases of ZnTe)

C = N^{O} of components = 2 (Zn and Te)

F = N^{O} of degrees of freedom

If the temperature and the pressure are fixed then, from eqn (1), there are no other degrees of freedom and therefore, using these thermodynamic arguments, the equilibrium concentrations of tellurium in the solid (C_s) and

liquid (C_l) are fixed.

Initially $C_l > C_s$ thus as an amount of solid of unit cross- section and width Δz is grown an amount :

$$\Delta z(C_l - C_s)$$

of tellurium must be removed from the growth interface by diffusion.

Consider the case of the solid-liquid interface moving with a velocity, v, in the +z direction and the tellurium having a diffusivity, D, in the liquid. In order to conserve the amount of tellurium present as it is rejected from the growth interface it is required that

$$-D[\partial C/\partial z]_{z=0} \Delta z = (C_l - C_s)v \Delta z \qquad (2)$$

$\partial C/\partial z$ is negative and will be called G_{lc}

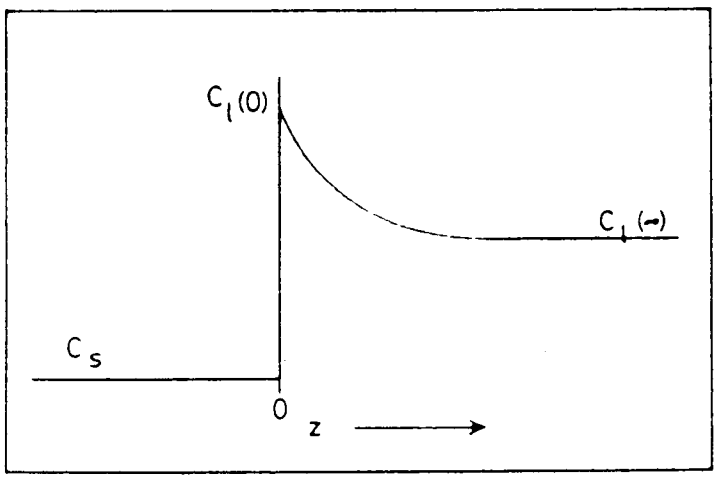

Figure 2.1 Concentration gradient of Te within the liquid caused by too rapid a growth velocity

If v is slow enough to maintain equilibrium conditions then constitutional supercooling will not take place. However, if this is not the case, the concentration of tellurium will increase close to the solid-liquid interface (fig 2.1). As can be seen from the T-x diagram (fig 2.2) this increase in concentration results in a lowering of the melting point of the solid.

Consider now two different experimental arrangements of temperature gradient within a liquid in which a concentration gradient exists (cases I and II in fig 2.3a). As the temperature, T, increases linearly with z and

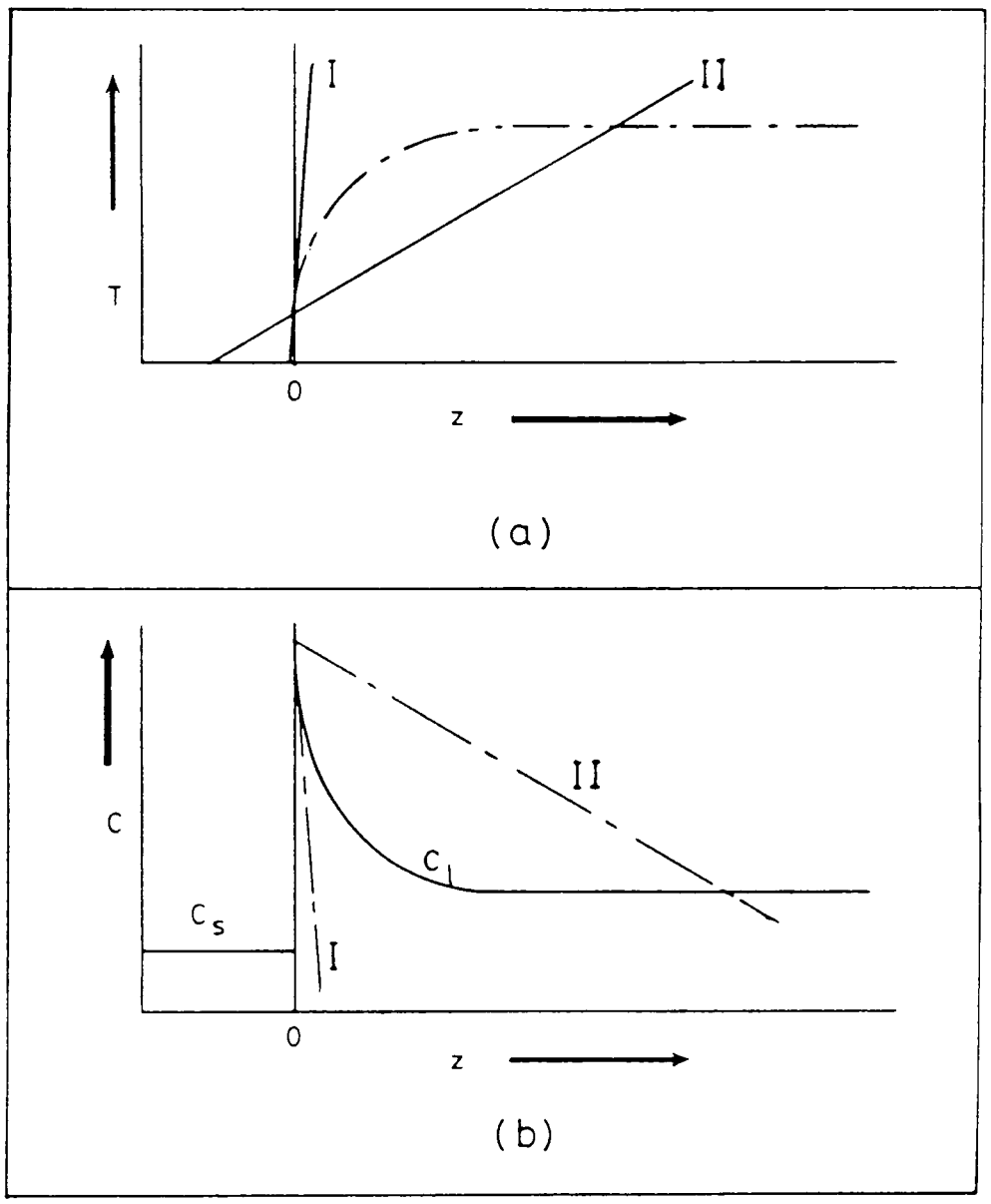

Figures 2.3

The effects of the temperature gradients I and II on Constitutional Supercooling.

2.3(a) shows the comparison between the experimental temperature gradients I and I and the temperature gradient caused by the concentration gradient (broken curve) within the liquid.

2.3(b) shows the relationship between the actual concentration (C_l) and the permitted concentration in cases I and II.

Constitutional Supercooling occurs in case II.

the permitted concentration (that concentration which just keeps the liquid from entering the two phase region at a particular temperature) of tellurium in the liquid decreases approximately linearly with increasing temperature (fig 2.2) then figure 2.3b shows the relationship between the permitted concentration and the actual concentration in the two cases, I and II.

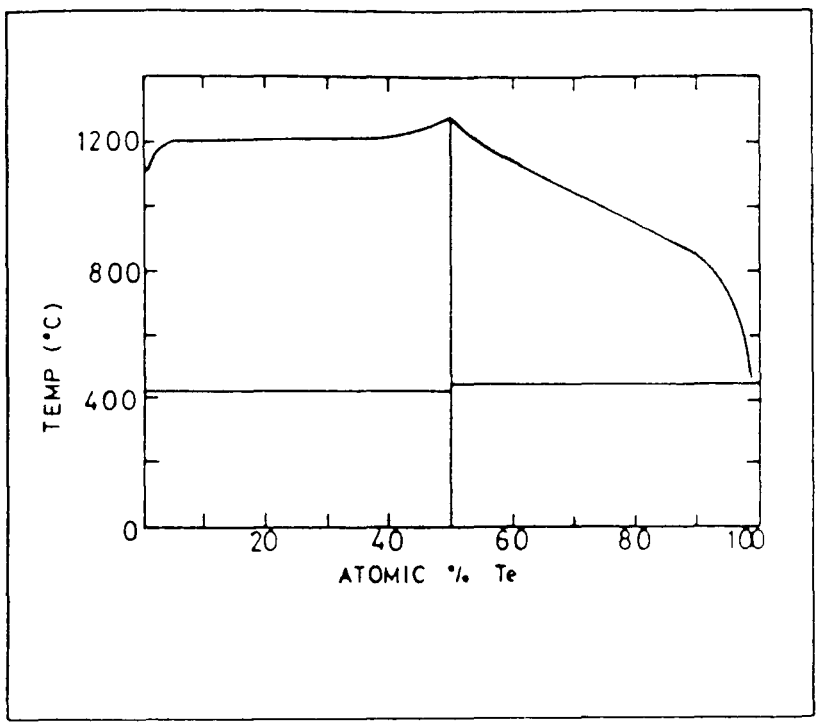

Figure 2.2

T-x diagram for ZnTe

(x is the Atomic % of Te)

In experiment I the temperature gradient is large enough for the permitted concentration to be below the actual concentration for all z. However, in experiment II the permitted concentration close to the growth interface (z=0) is above the actual concentration and the liquid there is said to be Constitutionally Supercooled.

The permitted concentration is given by

$$C_{per} = C_l + z \frac{\partial C}{\partial z}l \qquad (3)$$

This may be rewritten as

$$C_{per} = C_l + zG_l/m \qquad (4)$$

where m = the slope of the liquidus (including the - sign) = $\frac{\partial T_l}{\partial C_l}$

G_l = temp. gradient in liquid = $\frac{\partial T}{\partial Z}$

The condition for constitutional supercooling becomes

$$G_{lc} = -(C_l - C_s)v/D < G_l/m \qquad (5)$$

thus if $m\, G_{lc}/G_l > 1$ constitutional supercooling occurs.

2.2.2 Construction of the Furnace

The growth rate and temperature gradient are the only variables of equation (5) that may be physically altered so as to avoid constitutional supercooling. Furthermore, it can be seen that a large temperature gradient and a slow growth rate is required. However, it is difficult to maintain too high a temperature gradient without making the growth interface concave towards the liquid and very slow growth rates introduce the problem of controlling the temperature accurately over long periods of time. A balance between the two that can be achieved experimentally must be found if supercooling is to be avoided.

The growth furnace is represented schematically in fig 2.4. The resistive heating is provided by two Kanthal wire wound elements, each of approximately 45 Ω resistance, the individual turns of which are separated by Alfrax fire clay to prevent electrical shorting. To help prevent diffusion of impurities, such as copper, from the Kanthal wire into the molten charge a 5 mm thick walled satin silica liner is positioned inside the elements.

Each element is individually controlled to within 0.5 ^{o}C using Barman TC43P temperature controllers (similar in operation to the commercially available Eurotherm 093). The reference temperature for each of these is provided by a platinum / platinum : 13% rhodium thermocouple inserted

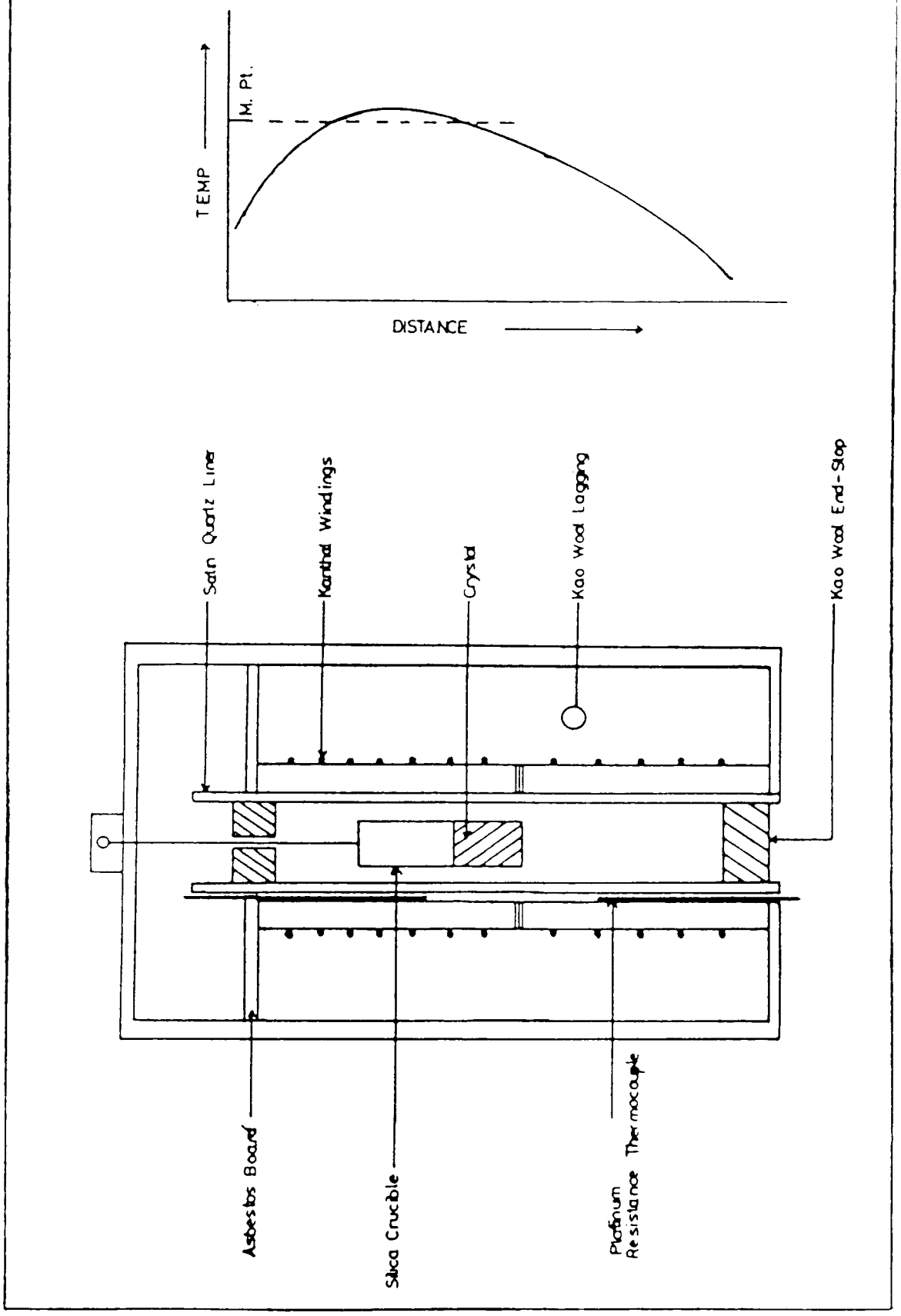

Figure 2.4

Schematic representation of the construction of the furnace. The typical temperature profile of such a furnace is also shown.

between each element and the liner. It must be noted that the temperatures read by these may differ considerably from the temperature experienced by the charge, however these are used only to monitor temperature fluctuations. The absolute temperature within the furnace is found using the method described in the next section.

The furnace is thermally insulated using Kao-wool lagging. By altering the control temperature of the lower element and the positioning of the lagging a maximum temperature gradient of 12 ^{o}C / cm has been achieved.

The charge may be lowered through this temperature gradient at rates of between 1mm and 10cm per day by means of a precision bearing lowering system incorporating a charge rotation facility.

2.3 Experimental Techniques

2.3.1 Temperature Profiling the Furnace

In order to determine the vertical temperature profile of the furnace a probe was constructed which comprised of a vitreous silica capsule embedded in CdTe into which a platinum / platinum : 13% rhodium thermocouple was inserted. The CdTe was chosen as it has approximately the same thermal conductivity as ZnTe [14] but can be melted and cast at a lower temperature (the melting point of CdTe is 1092 ^{o}C). The temperature as registered by this probe was recorded at distances down the furnace. The lagging and set temperatures of the furnace elements were altered so as to produce the typical profile shown in figure 2.4. The main characteristics of such a profile should be a hot zone large enough to ensure that initially the entire charge was molten (typically 7-10 cm) and a decreasing temperature gradient that helps prevent constitutional supercooling.

The probe was constructed using pyrolised, carbon coated, silica tubing and comprised an outer tube, with the same internal diameter as a growth

tube (15 mm), into which a smaller diameter tube (3 mm) was placed. The smaller tube protruded approximately 4 cm into the larger (fig. 2.5a) and acted as the thermocouple housing. Sufficient CdTe was placed into the larger tube so that when the probe was cast the protruding tip of the smaller tube was completely covered. This tube and CdTe arrangement was then evacuated to 10^{-6} torr. and mechanically sealed by heating the silica at a point between the CdTe surface and the vacuum pump and allowing it to collapse under the influence of the atmospheric pressure. The sealed tube was then heated in a furnace to 1092 ^{o}C (the melting point of CdTe). This leaves a vapour space, between the surface of the CdTe and the seal, into which material may distil to leave the tip of the small tube exposed. In order to prevent the exposure of the tip the probe was carefully opened and re-sealed close to the surface, under vacuum, forming the completed probe (fig 2.5b).

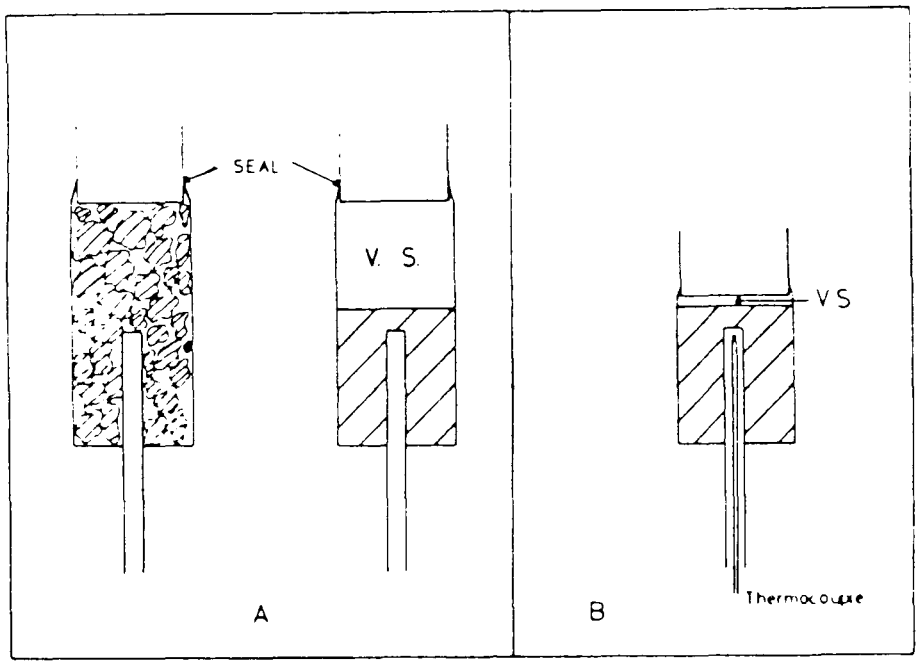

Figures 2.5 Stages in the production of temperature probe.
(A) shows the problems of the vapour space (V.S.) forming as the CdTe is cast. (B) shows the completed probe after re-sealing to reduce V.S.

ELEMENT	Zn	Te	ZnTe Synthesis
Ag	< 0.4	in each	sample
Al	< 2	in each	sample
As	< 10	in each	sample
Au	< 2	in each	sample
B	< 2	in each	sample
Ba	< 0.2	in each	sample
Be	< 0.03	in each	sample
Bi	< 5	in each	sample
Ca	< 2	in each	sample
Cd	< 1	in each	sample
Co	< 1.5	in each	sample
Cr	< 1	in each	sample
Cu	< 4	< 0.3	3
* Fe	4	1	3
Ga	< 2	in each	sample
Ge	< 2	in each	sample
In	< 5	in each	sample
K	< 10	in each	sample
Li	< 0.3	in each	sample
Mg	< 5	in each	sample
Mn	< 0.1	in each	sample
Na	< 2	in each	sample
P	< 10	in each	sample
Pb	< 5	in each	sample
S	< 5	8	< 5
Se	< 20	in each	sample

* concentrations between 9 and 13 p.p.m. were found to be present in boules grown from the synthesised material

Table 2.1 Mass Spectrograph Analysis (MSA) of Zn and Te starting materials together with the MSA of the ZnTe synthesised from these. All figures quoted are parts per million (p.p.m.) of the elements found in the materials.

2.3.2 Synthesis of ZnTe

The tellurium and zinc starting materials are both 99.9999 % pure and are supplied by Cominco Ltd. and Vielle-Montagne respectively. In order to minimise oxidation of the surface the materials are shipped and stored in an Argon atmosphere and the synthesised ZnTe is likewise stored in Argon.

A 60:40 tellurium rich mixture was placed in a large diameter quartz tube and heated to 700 ^{o}C for one week, during which time the 60:40 ZnTe was vapour synthesised.

Table 2.1 shows the results of a Mass Spectrographical Analysis (MSA) carried out on both the starting materials and the synthesised material. The concentrations are quoted in parts per million (ppm) by weight. It is interesting to note that the concentration of iron was found to have increased after the growth of a boule from the synthesised ZnTe. The source of this extra iron contamination remains unknown.

2.3.3 Crystal Growth

A charge comprising finely crushed synthesised material and the dopant is placed in a pyrolised, carbon coated, silica tube. This tube is then evacuated to 10^{-6} torr., mechanically sealed and placed in the hot zone of the furnace. The charge is then lowered at a rate of 3 mm / day through the temperature gradient. When the entire charge has passed through the hot zone and solidified the furnace is switched off and the charge allowed to cool slowly to room temperature. In this way it is hoped to avoid any strain that may be introduced into the crystal by a rapid cooling process.

(a)

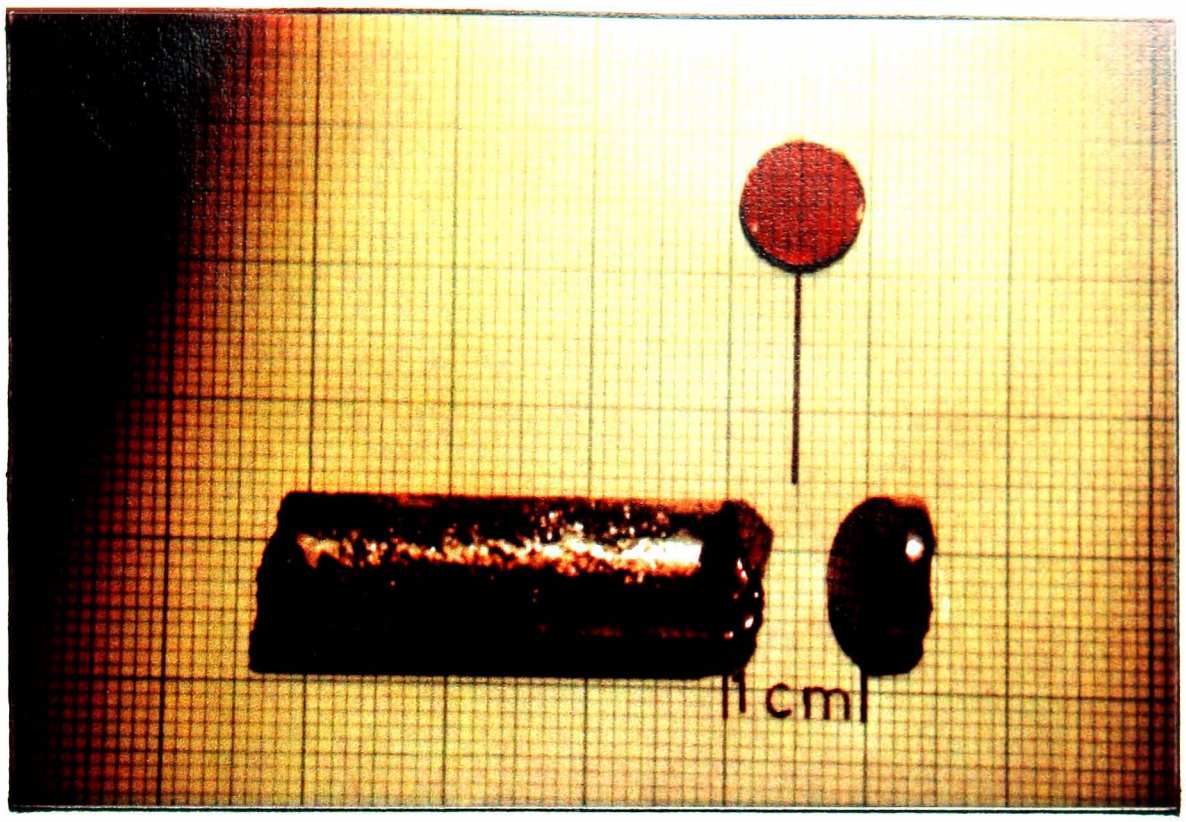

(b)

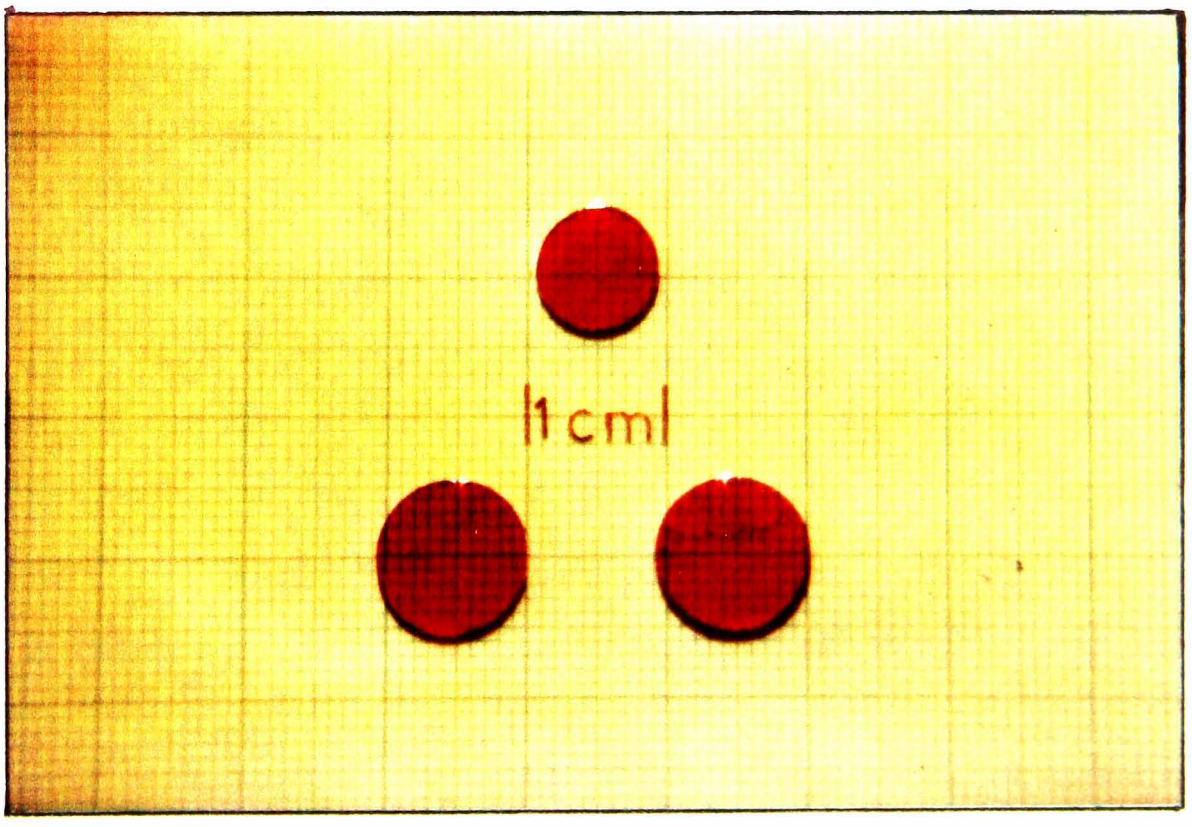

Figures 2.6

Examples of Bridgman grown material.

The approximate position of the single crystal region is indicated in 2.6(a).

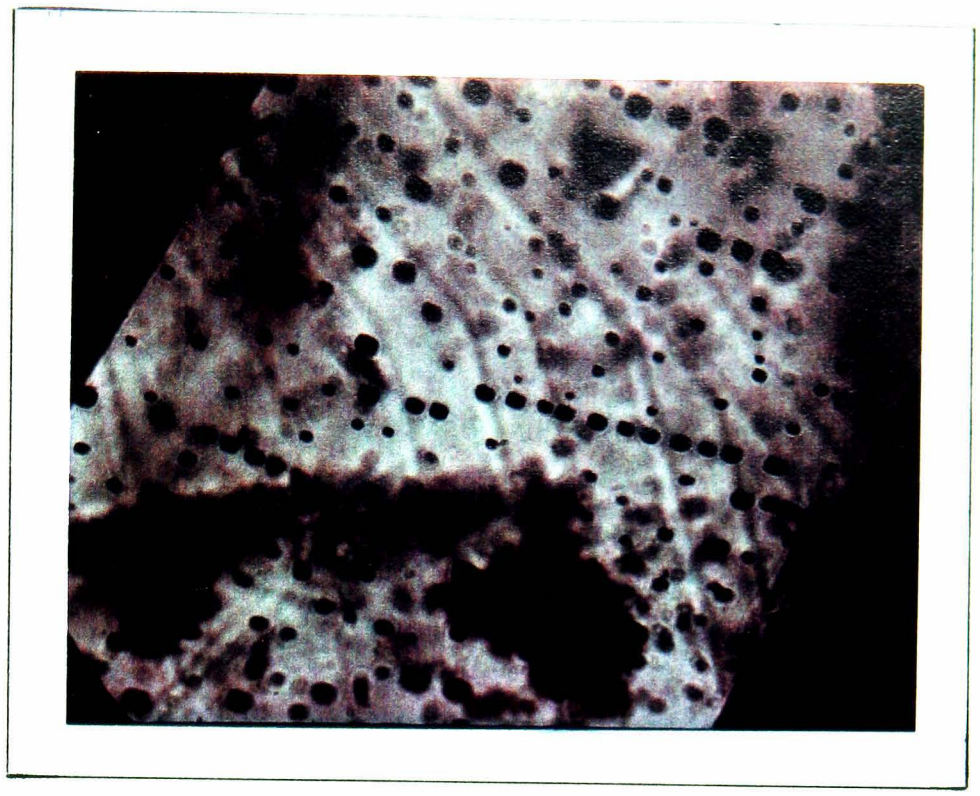

Figure 2.7

A view of the single crystal region through an optical microscope showing many small (~10 μm) tellurium inclusions.

2.4 Crystal Quality

The boules grown by the method described above are typically 7 - 10 cm long and 15 mm in diameter and in all cases the best quality material is found to commence 2 - 3 cm from the first to freeze end of the boule (fig 2.6). This region is typically 2 cm long and consists of both single crystal regions and regions containing 2 or 3 grains. The single crystal region usually exists for between .5 and 1 cm.

Optical microscopic examination on material from this region shows that small ($\sim$ 10 μm long) inclusions are present (fig 2.7) which are thought to be tellurium precipitates. This assignment comes from observations by Pautrat et al. [6] made on similar structures that were present in all of their THM and Bridgman grown ZnTe. Occasionally larger ($\sim$ .1 mm) tellurium inclusions are observed towards the outer edges of the crystal.

The results of Van de Pauw resistivity measurements [15] carried out on single crystal from each boule are shown in table 2.2 and represent an average value from 2 or 3 samples. It was found that the resistivity throughout the single crystal region varied by less than a factor of 10. These results indicate that both aluminium and indium compensated material may be suitable for fabrication into detectors.

BATCH N°	DOPANT	CONC		RESISTIVITY
		calc.	MSA	Ω cm
CPB1	In	125	---	8 10^7
CPB2	In	125	---	-------
CPB3	In	20	14	6 10^3
CPB4	In	30	27	6 10^6
CPB5	In	40	45	3 10^5
CPB6	In	70	---	8 10^3
CPB7	Al	40	09	1 10^6
CPB8	Al	100	07	4 10^5
CPB9	Al	100	31	2 10^7
CPB10	Pb	1000	100	10
CPB11	Pb	100	50	2 10^5
CPB12	Pb	100	50	29
CPB13	Pb	200	30	10
CPB14	F	40	60	30
CPB15	Ni	1000	---	2
CPB16	Sn	100	09	20
CPB17	Fe	100	---	2
CPB18	Un	---	---	5

TABLE 2.2 Resistivity values of doped and undoped (Un) single crystal ZnTe. The concentrations quoted are calculated from the amount of dopant added to the boule (calc.) and, where applicable, those measured from Mass Spectrograph Analysis (MSA)

CHAPTER TWO REFERENCES

[1] Smith F.T.J., Sol. Stat. Com. 9 957 (1971)

[2] de Nobel D., Philips Res. Repts. 14 361 (1959)

[3] Thomas D.G., Sadowski E.A., J. Phys. chem. Sol. 25 395 (1964)

[4] Dean P.J., Venghaus H., Pfister J.C., Schaub B., Marine J., J. Lumin. 16 363 (1978)

[5] Magnea N., Bensahel D., Pautrat J.L., Saminadayar K., Pfister J.C., Sol. Stat. Com. 30 259 (1979)

[6] Pautrat J.L., Magnea N., Faurie J.P., J. Appl. Phys. 53 8668 (1982)

[7] Magnea N., Bensahel D., Pfister J.C., Sol. Stat. Com. 19 35 (1979)

[8] Bensahel D., Magnea N., Dupuy M., Sol. Stat. Com. 30 467 (1979)

[9] Pfister J.C., Rev. de Phys. Appl. 15 707 (1980)

[10] Cox R.T., Bittebierre J., Phys. Rev. B 34 (1986)

[11] Triboulet R., Marfaing Y., Cornet A., Siffert P., J. Appl. Phys. 45 2759 (1974)

[12] Laudise R.A., The Growth of Single Crystals (Prentice Hall Inc. 1970)

[13] Pamplin B.R., Crystal Growth (Permagon Press 1975)

[14] Landolt and Bornstein, vol.bIII pgs.160,459 (1982)

[15] Van der Pauw L.J., Philips Res. Repts. 13 R334 (1958)

CHAPTER THREE

Photoluminescence Studies

Introduction

If a semiconductor emits electromagnetic radiation in excess of that of a black body at that temperature after having absorbed a photon then the semiconductor is said to have undergone photoluminescent emission. The energy of the emitted radiation will depend upon the energy separation of the states taking part in the process. Photoluminescence therefore provides a non-destructive technique for analysing intrinsic and extrinsic defect energy levels within a semiconductor. It is now generally thought that it is the extrinsic defects, rather than the intrinsic ones, that are largely responsible for the photoluminescence and conductivity observed in the II-VI compound semiconductors. Thus by using photoluminescence to both identify the impurities present in ZnTe and also their roles within the material it was hoped that the conductivity may be controlled so as to produce the highly resistive material required for detector operation.

Results presented in this Chapter indicate that the impurities copper and lithium are the dominant acceptors in the undoped material and by introducing either indium or aluminium into the material shallow donors are introduced. Since undoped ZnTe is a low resistivity p-type material it was hoped that these donors would compensate the acceptors and so produce the high resistivity material necessary for radiation detectors. It was found that, in the case of aluminium (and probably indium), the major disadvantage of this compensation technique was that the dopant produced an additional acceptor species in ZnTe with a greater activation energy than those acceptors it was introduced to compensate. Thus although aluminium or indium

doping produced high resistivity material (see Chapter Two) a deep hole trap was introduced which was to prove detrimental to device performance.

3.1 Principles of Radiative Recombination

Radiative recombination in II-VI compounds may be classified by four types of emission band that it produces at low temperatures. These are:

i) Emission due to recombination of electrostatically bound electron-hole pairs (free excitons). This produces bands with an energy just below that of the band gap energy and with line widths of the order of 10 meV.

ii) Emission due to recombination of excitons trapped at defect centres (bound excitons). This usually produces bands, at slightly lower energies than free excitons, with line widths of the order of 0.1 meV. Excitons bound to isoelectronic traps are exceptions to this and produce wide bands (several tenths of an eV) with much lower emission energies.

iii) Emission due to recombination between centres removed in energy from the band edges (e.g. Donor-Acceptor pair recombination) producing relatively broad bands.

iv) Emission due to internal transitions of electrons within a given charge state of an ion. This type of emission is useful in identifying the presence of transition metal ions in ZnTe. These are of interest as they often act as deep centers in the material.

The basic principles of the types i-iii recombinations will be described in the following three sections.

3.1.1 Free Exciton Recombination

When a photon of energy greater than that of the semiconductor's band gap is absorbed an electron is excited from the Valence Band (V.B.) into the Conduction Band (C.B.), leaving behind a hole.

The electron and hole, being equally but oppositely charged, experience a Coulombic force of attraction, which results in a potential, P_e, which is given by

$$P_e = e^2/4\pi\varepsilon_s r \qquad (1)$$

where e is the electronic charge;

ε_s is the static dielectric constant of the material and

r is the spatial separation of the electron and hole.

Mott [1] and Wannier [2] showed that for spatial separations of electrons and holes much larger than the lattice constant the exciton has hydrogen-like energy states. These may be described using the effective mass approximation in the modified Rydberg equation so that

$$E_n = E_g - (\mu^* e^4/4\pi 2\hbar^2 \varepsilon_s^2 n^2) + (\hbar^2 k^2/2(m_e^* + m_h^*) \qquad (2)$$

where μ^* is the reduced electron-hole effective mass;

k is the exciton wave vector and

n is the principle quantum number describing the hydrogenic energy levels.

Thus the ground state binding energy, E_x, (k=0,n=1) of a Mott-Wannier exciton is:

$$E_x = \mu^* e^4/4\pi(2\hbar^2 \varepsilon_s^2)$$

Dean [3] pointed out that, since the free exciton is required to have identical momentum to the photon emitted when it recombines, no-phonon

luminescence from free excitons is unlikely. Thus the free exciton spectrum, even in direct band gap semiconductors, should be dominated by phonon assisted transitions. This was confirmed by Radford et al. [4] who were unable to detect the no-phonon free exciton emission in the cathodoluminescence of cadmium sulphide at helium temperatures, whereas emissions due to the first and second L.O. phonon assisted transitions were observed.

3.1.2. Bound Exciton Recombination

The concept of an exciton becoming localised at (or bound to) defects was first developed by Lampert [5] in 1958. The existence of the bound exciton was first confirmed in the luminescence spectrum of silicon [6] and later in the II-VI compound, cadmium sulphide [7]. In his development of the theory Lampert drew the analogy between the different charge states of the hydrogen atom or molecule and the possible bound exciton configurations in order to calculate their binding energies. This was later extended to the II-VI compounds by Halsted [8].

In the following discussion the notation of Lampert will be used to symbolise the various excitonic configurations. The Lampert representation of each configuration is given in table 3.1.

Electrons, holes, singly ionised donors and singly ionised acceptors are denoted as $-$, $+$, $\ominus$, $\oplus$, respectively and are employed as subscripts to the letter E to denote the binding energies of various aggregates. Exceptions to this are the binding energy of a free exciton, E_X, and the ionisation energies of donors and acceptors, E_D, E_A.

Table 3.1

Localised Charge Notation

Symbol	Description
$\oplus$ ($\ominus$)	Ionised single donor (acceptor)
$\oplus$ - ($\ominus$ +)	Neutral donor (acceptor)
+-	Exciton
$\oplus$ +- ($\ominus$ +-)	Exciton bound to ionised donor (acceptor)
$\oplus$ =+ ($\ominus \overset{+}{+}-$)	Exciton bound to neutral donor (acceptor)

(i) Neutral Donor(Acceptor) $\oplus$ -($\ominus$ +)

The neutral donor (acceptor) is analogous to the hydrogen atom. Thus the ground state binding energy of the neutral donor (acceptor) is given by

$$E_D = (13.6\ m_e^*/m\varepsilon_s^2)eV$$

$$E_A = (13.6\ m_h^*/m\varepsilon_s^2)eV \qquad (3)$$

where m is the free electron mass

Using this analogy the free exciton binding energy given in equation (2) may be written as

$$E_x = (13.6\ \mu^*/m\varepsilon_s^2)eV \qquad (4)$$

By combining equations (3,4) it is possible to estimate the binding energies of hydrogenic donors (acceptors) providing m_e^* and m_h^* are known.

$$\frac{E_x}{E_D} = \frac{\mu^*}{m_e^*} = \left[1 + \frac{m_e^*}{m_h^*}\right]^{-1} \; ; \; \frac{E_x}{E_A} = \frac{\mu^*}{m_h^*} = \left[1 + \frac{m_h^*}{m_e^*}\right]^{-1} \qquad (5)$$

(ii) Exciton Bound to Neutral Donor(Acceptor) $\oplus =+$ ($\ominus \overset{+}{+-}$)

The neutral donor (acceptor) bound exciton is analogous to the hydrogen molecule in the limit $m_h^* >> m_e^*$ [9].

The dissociation energy of the hydrogen molecule is 4.5 eV and therefore the binding energy of an exciton to a neutral donor is given by

$$E \oplus =+ = (4.5/13.6)\, E_D = 0.33\, E_D \qquad (6)$$

limit $m_h^*/m_e^* \longrightarrow \infty$

If $m_h^* << m_e^*$ then the hole has a large orbit and the bound exciton complex is analogous to the H^- ion. The binding of the second electron to the hydrogen atom is 0.75 eV and in this case the binding energy of the exciton is given by

$$E \oplus =+ = (0.75/13.6)\, E_D = 0.055\, E_D \qquad (7)$$

limit $m_h^*/m_e^* \longrightarrow 0$

Similar expressions are obtained when considering the exciton-neutral acceptor complex.

(iii) Exciton Bound to Ionised Donor(Acceptor) $\oplus -+$ ($\ominus +-$)

The ionised donor (acceptor) bound exciton may be regarded as a hole (electron) bound to a neutral donor (acceptor). The exciton binding energy is then equal to the sum of the energies required to firstly remove the hole, then the electron, less the free exciton binding energy i.e.

$$E \oplus (-+) = (E \oplus -) + E_D - E_x \qquad (8)$$

In II-VI compounds m_e^*/m_h^* is $\sim$ 0.25. Substituting this value into equation (5) yields the values for E_x/E_D of $\sim$ 0.8 and for E_x/E_A of $\sim$ 0.2. Thus $E_D < E_A$ which, from equation (8), implies that the energy required to remove an exciton from an ionised donor (acceptor) is largely that of hole (electron) removal.

Using the analogy of the H_2^+ molecular ion Hopfield [10] calculated that a neutral donor (acceptor) would not bind a hole (electron) if $m_h^*/m_e^* < 1.4$ ($m_e^*/m_h^* < 1.4$) and that the binding of excitons to both ionised donors and acceptors should not be possible in any given material. In the II-VI compounds where $m_h^*/m_e^* > 1.4$ ionised acceptors should be incapable of binding an exciton. The binding energy of an ionised donor should be 2-4 meV so that even at low temperatures the binding of an exciton to an ionised impurity is unlikely.

The energy emitted when an exciton bound to a shallow defect recombines is characteristic of the defect and, by using the equations given above, yields the energy position of that defect within the forbidden gap. The nature of the impurity involved in a particular excitonic emission may be identified from Zeeman and back doping experiments. Therefore excitonic luminescence may be used to identify the shallow donors and acceptors present in ZnTe. This identification is important as it is shallow acceptors, involving impurity atoms, that are thought to govern the electrical characteristics of undoped ZnTe [19,20,21] i.e. the electrical conduction observed at room temperature is controlled by the charge carriers that have been released from these defects. With knowledge of the impurities present in the material it was hoped that the method of crystal growth could be optimised to produce the good quality high resistivity material needed

for the fabrication of devices.

3.1.3 Donor - Acceptor Pair (DAP) Recombination

Emission due to DAP recombination occurs when an electron localised at a donor impurity recombines with a hole localised at an acceptor impurity. There exists between an ionised donor-acceptor pair, separated by a distance r, a Coulombic potential of the form $e^2/4\pi\varepsilon_s r$. Consideration of the energy required to bring an electron and hole from infinity to the ionised pair yields the binding energy of the resultant state, E_p,

$$E_p(r) = E_D + E_A - e^2/4\pi\varepsilon_s r \qquad (9)$$

This type of recombination has been investigated both experimentally and theoretically in a number of semiconductors [11,12]. The energy, $h\nu$, of the photon emitted in the zero-phonon recombination of the bound electrons with the bound holes is usually interpreted using the relationship

$$E = h\nu = E_g - E_p + E(r) \qquad (10)$$

where E(r) is the small correction in the simple Coulombic term at small r due to correlation of the electron and hole [13].

From equation (9) it can be seen that the energy of the emitted photon is dependent upon the spatial separation of the pair. If the donors and acceptors occupy discrete lattice sites then the DAP spectrum should consist of discrete lines. In zinc telluride this discrete line spectrum is not observed. This is because the large transition rates in the direct band gap material [11] makes it difficult to saturate the emission from distant pairs by increasing the excitation intensity and therefore the relative emission intensity of the close pairs remains very small. In order to identify DAP

transitions in the absence of discrete line spectra time resolved spectroscopy usually has to be employed.

Thomas et al. [14] have shown that the recombination rate, W(r), for DAP transitions is given by

$$W(r) = \text{Const.}\ r^{2m} \exp(-2r/a_D) \qquad (11)$$

where a_D is the donor bohr radius and

$m = (E_H/E_D)^{1/2} - 1$ (E_H is the ideal binding energy of a hydrogenic donor)

Thus as r increases W(r) decreases so that when the excitation is removed the close pairs will decay first. From equation (10) it can be seen that the smaller the pair separation the higher the energy of the emitted photon so that by monitoring the peak of the emission at different times after removal of the excitation a shift towards lower energies should be noted if the emission process involves DAP recombination [14].

3.2 Literature Review of Luminescence in ZnTe

3.2.1 Free Exciton Luminescence

An intense line, peaking at 2.382 eV, observed in the 4.2 K reflection spectrum of undoped material, has been attributed to the n=1 free exciton by Aten et al. [15]. A second, weaker line was also observed at 7.8 meV higher energy and attributed to the n=2 free exciton. Using the hydrogenic model (equations (2,4)) the theoretical ground state binding energy of the free exciton is $\sim$ 10 meV.

Venghaus et al. [16] studied the free exciton using magnetoreflectance spectroscopy at fields up to 11.5 Tesla and determined the free electron and free hole g values to be -0.57 and -0.13 respectively. The energy

separation of the n=1 and n=2 free exciton states was observed to be 8 meV which is in good agreement with Aten et al [15].

Structure interpreted as being due to the n=1, n=2, n=3 free exciton states was observed in the 4.2 K excitation spectrum of the A_1^{Ag} bound exciton by Venghaus et al [17]. The exciton Rydberg constant, R_o, and the free exciton binding energy were calculated to be 12.8 meV and 13.2 meV respectively from these studies, which also agrees with the work of Aten et al.

3.2.2 Bound Exciton Luminescence

High resolution photoluminescence studies on both undoped and acceptor doped material [18,19,20,21,22] have revealed bound exciton emission lines all with energies close to 2.375 eV. From detailed measurements on these lines neutral acceptors with exciton binding energies of 61 meV, 63.5 meV, 77 meV, 62.8 meV, 124 meV, 272 meV, have been identified as being due to lithium, phosphorus, arsenic, sodium, silver, and gold respectively. Measurements on copper doped material [21] lead to the tentative assignment of an acceptor with a binding energy of 149 meV as being due to copper. This acceptor was directly associated with copper by the observed enhancement of the relevant bound exciton line in high purity material when back doped with copper [22].

Zeeman measurements on a bound exciton emission line at 2.315 eV [23] lead to the assignment of this as involving the exciton recombination at an ionised acceptor (lithium). However this line was correlated with Ag-doping [21] and so it was suggested to be due to an Ag-complex centre. The Zeeman work [23] suggested that a centre of symmetry lower than T_d was involved in the 2.315 eV emission (inconsistent with the assignment involving a point defect) and therefore the latter assignment is more probable.

Zinc firing experiments carried out on high purity material [24] have

lead to the observation of emission from a previously unobserved acceptor bound exciton (A_1^X) at 2.361 eV . This could only be observed after firing above 700 ^oC. At temperatures below this the observed effect was the reduction in intensity of the residual acceptor bound exciton lines (due to Li, Cu, Ag). Zeeman and stress measurements showed that the X centre had T_d symmetry and further that the defect was probably a <u>double acceptor</u>. Since the formation of the centre was favoured under conditions of excess zinc the acceptor is most likely to be substituting for tellurium and was thought to be Si_{Te}.

Le Si Dang et al. [25] observed a bound exciton luminescence line at 2.369 eV, involving a centre labelled A^C. This centre was shown to be a single acceptor with C_S symmetry. Optically detected magnetic resonance (ODMR) studies [26] on Al doped material have identified a single acceptor centre in ZnTe with C_S symmetry suggesting that the centre is the A-centre, $(V_{Zn}Al_{Zn})'$. The g-values were similar to the A^C centre and therefore these two are probably the same centre.

A bound exciton emission at 2.378 eV is generally observed in Zinc Telluride [e.g. 21, 22, 24] and has been attributed to a neutral donor bound exciton. Dean indicated that the donor involved was likely to be $Al_{Zn}^{\bullet}$; however he gave no direct evidence for this but did note that the emission tended to increase in materials doped with acceptors and that the donor species was identical regardless of the nature of the acceptor dopant [27]. Lines of energy 2.3779 eV, 2.3785 eV and 2.3798 eV were observed in the absorption and emission spectra of undoped material and attributed to the neutral donor bound exciton recombination which leaves the donor in the ground and first two excited states respectively (the transition to the excited state is generally known as a two electron transition) [37]. Excitation studies on this donor by Pautrat et al [41] and Venghaus and Dean [17] yielded a donor binding energy of 18.3 meV and separations of the D^2

and D^3 excited states (with respect to the ground state, D^1) of 13.63 meV and 16.18 meV respectively.

3.2.3. DAP and Deep Centre Luminescence in ZnTe

Detailed photoluminescence studies on several zinc substitutional acceptors have been carried out by Magnea et al [21]. Using back doping and two hole satellite spectroscopy they were able to deduce the binding energies of the following neutral acceptors in the material:

Li 61 meV; Na 63 meV; Cu 149 meV; Ag 123 meV; Au 243 meV

It was also shown from these studies that the common DAP band with the zero phonon emission near 2.33 eV involved the recombination between a residual shallow donor with E_D 18.5 meV and the Li_{Zn}' acceptor.

Copper was shown, using back doping [21,38] and Zeeman [39] studies, to be the acceptor involved in the DAP transition series with the zero phonon line near 2.24 eV.

A broad featureless emission band in the yellow region of the luminescence spectrum has been observed in ZnTe:Al by several authors [28, 29,30]. Rodot [28] observed this band in material doped with aluminium in excess of 10^{18} cm^{-3}. The position of the peak of this band was found to vary between 2.080 ev and 2.145 eV depending upon the dopant concentration. A second type of transition, involving the recombination of the $Al_{Zn}^{\bullet}$ donor electron with a hole in the valence band, was also observed in samples doped with 10^{18} cm^{-3} atoms of Al by Rodot [28] from which she deduced the binding energy of the Al donor to be 0.068 eV. This binding energy disagrees with that of the persistent shallow donor (0.0183 eV) in ZnTe which was said to be the $Al_{Zn}^{\bullet}$ donor by Dean [22].

Paramagnetic resonance studies by Title et al. [33] showed that the band at 2.14 eV was due to DAP recombination and involved the $(V_{Zn}Al_{Zn})'$ acceptor. More recently ODMR investigations on the yellow ($\sim$ 2.16 eV)

emission band by Cox [26] have shown it to involve the $(V_{Zn}Al_{Zn})'$ acceptor.Moreover, from the partially resolved phonon structure that was observed during these experiments, Cox was able to deduce a binding energy of 0.19 eV for that centre.

In addition to this band Larsen et al. [29] observed two emission bands; one at 2.11 eV which they assigned to the recombination of an electron in a free exciton state with a hole bound to the $(V_{Zn}Al_{Zn})'$ acceptor and one at 1.63 eV which they assigned to the recombination of an electron bound to the $Al_{Zn}^{\bullet}$ donor with a hole bound to an unidentified native acceptor with a binding energy of 0.60-0.65 eV.

Blashkiv et al [30] and Blashkiv [31,32] observed infra-red emission bands in material doped with Al, In, and Ga all with peaks near 850 nm (1.46 eV) and from the temperature behaviour of these emission bands and thermoluminescence peaks concluded that both the emission and thermoluminescence could be explained by a deep donor to VB transition. In indium doped material Iida [34] observed two emission bands depending upon concentration. In samples containing little indium a band at 750 nm (1.65 eV) was observed. A band at longer wavelength was observed when the dopant concentration increased. This band, unlike the former, showed a shift towards lower energies as the excitation intensity was lowered and was attributed to DAP recombination. Iida noted the similarity in behaviour between this band and the self activated (SA) emission in ZnS [35] and consequently attributed the donor to $In_{Zn}^{\bullet}$ and the acceptor to the $(V_{Zn}In_{Zn})'$ complex. The emission in the material of low indium concentration was not identified.

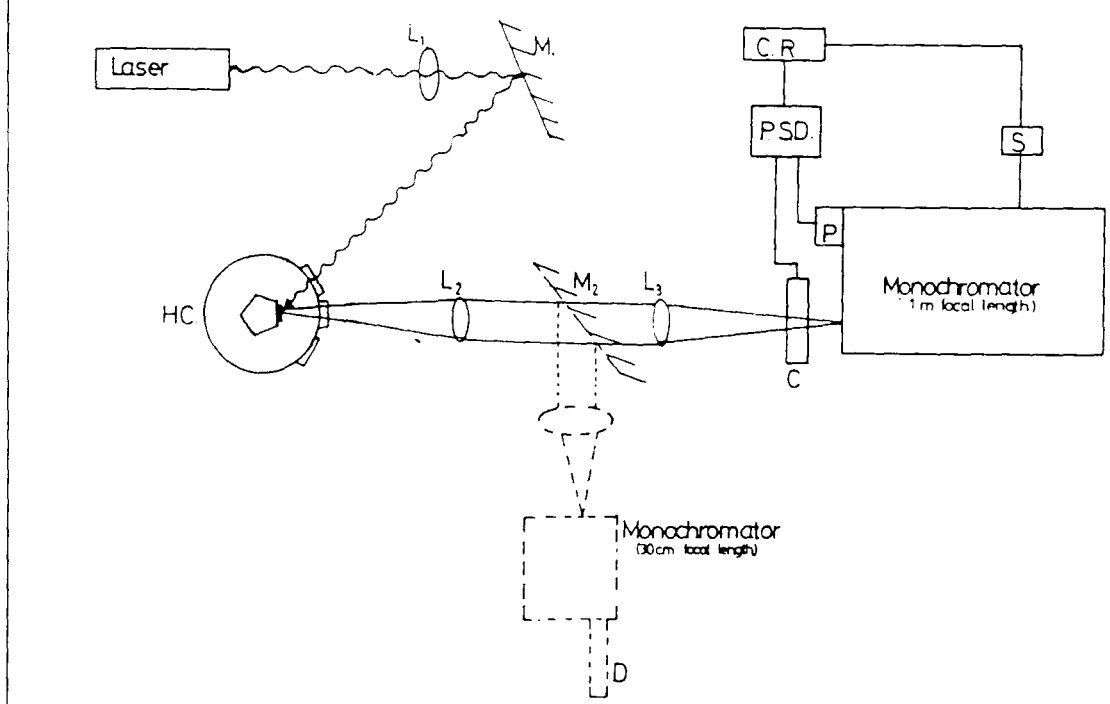

Figure 3.1

Schematic representation of the photoluminescence system. The broken lines represent the arrangement used for the detection of the near infra-red emission.

3.3 Experimental Details

3.3.1 Photoluminescence Measurements

The experimental arrangement used in the excitation and detection of the luminescence is represented in figure 3.1.

Samples were mounted onto a five sided copper cold finger with silver paste and placed in a liquid helium immersion cryostat. The sample holder was able to rotate in the over pumped liquid helium which allowed each of the five stations to be brought, in turn, into alignment with the excitation and detection arrangement.

Luminescence was excited using the 488 nm line of a Spectra Physics 164 argon ion laser. The excitation was incident at 33^{o} to the sample surface and the luminescence emitted perpendicular to the surface was detected. The emission was passed through a mechanical chopper (C) and focussed on to the entrance slit of a Spex, 1 m focal length, monochromator fitted with a 5000 Å blazed grating with 1200 lines/mm. This monochromator could be scanned at rates ranging from 0.002 Å s^{-1} to 100 Å s^{-1} using a Spex Compudrive system which was controlled by a Commodore Pet computer (S). The light passing through the monochromator was detected using a Hamamatsu multialkali photomultiplier. The output was fed through a Brookdeal amplifier and phase sensitive detector (PSD), the reference signal supplied by the chopper, and into the Y input of an XY chart recorder (CR). The X input was taken from the Spex Compudrive and computer system which provided a linear voltage ramp along the X scale in either 1 or 0.1 Å steps. Facilities were available on the computer for the storage of the spectra on floppy disc.

When detecting the emission at wavelengths longer than 700 nm a mirror (M) was inserted into the beam allowing the light to be focussed onto the entrance slit of a low resolution 30 cm focal length Mini-Spex monochromator fitted with interchangeable diffraction gratings which were blazed at 0.5

μm, 1 μm and 2 μm. The emergent light was detected using a liquid nitrogen cooled Northcoast Scientific Corporation (EO-8175) germanium detector (D). The output of this was processed as above.

The relative response of the system was determined by dividing the recorded spectrum of a tungsten filament lamp by the theoretical spectrum of a black body at the temperature of the filament (determined using an optical pyrometer). The recorded luminescence spectra were then corrected, with the aid of a computer, by dividing by the relative response of the system.

Only broad band emissions were corrected in this manner since over the excitonic region the response of the system changed little.

The wavelength accuracy of the Spex system was determined to be better than 0.1 nm by comparing the recorded and true emission wavelengths of a mercury lamp. In order to prevent any discrepancy between recorded spectra due to any backlash effects the monochromators were always scanned in the direction of increasing wavelength.

3.3.2 Time Resolved and Decay Time Measurements

Time resolved spectroscopy is useful in determining whether or not a particular emission is due to DAP recombination if the discrete line spectrum, due to discrete donor and acceptor separations, is absent (see Section 3.1.3).

In both time resolved and decay time measurements the exciting laser beam was pulsed using a light modulating Pockel Cell (Electro-Optic Developments type PC18). The pulse frequency reference was taken from the Pockel cell supply to a Brookdeal scan delay generator. The output from this was used to trigger a linear gate (the scan delay generator and linear gate forming a standard boxcar system).

The pulsed emission was focussed onto the entrance slits of the low resolution monochromator. Light leaving this was detected using a S-20

photomultiplier (Hamamatsu R995). Decay times of 1 μs were able to be measured after connecting a 100 KΩ resistor across the output of the photomultiplier in order to reduce the effects of stray capacitances in the co-axial leads.

Time resolved studies were then carried out by fixing the gate pulse at a desired position in the emission decay and scanning the monochromator using the Spex Compudrive system, as described in Section 3.3.1.The X input of the chart recorder was again connected to the voltage ramp provided by the computer and incremented in 1Å steps. The output from the photomultiplier was fed through the boxcar system into the Y inputs of an oscilloscope and an XY chart recorder.

The shape of the total luminescence decay was recorded using the same system but with the monochromator removed. The output of the photomultiplier was connected to the Y input of the chart recorder and the gate swept across the decay of the emission. A continuous linear voltage ramp output from the linear gate was input into the X channel of the chart recorder.

3.4 Results and Discussion

The energies quoted in this and subsequent sections are calculated using the values of the wavelengths in vacuum, λ_v. The vacuum wavelengths are related to the measured wavelengths, λ_a, that are quoted in the text as

$$\lambda_v = n\lambda_a \qquad (11)$$

where n is the refractive index of air. The value of n used in the calculations is that for dry air at 300 K and 760 mm Hg and is taken as 1.00026.

Figures 3.2

Representative luminescence spectra obtained from:

(a) undoped material

(b) 20 p.p.m. indium doped material

(c) 30 p.p.m. indium doped material

(d) 40 p.p.m. indium doped material

Figure 3.2a

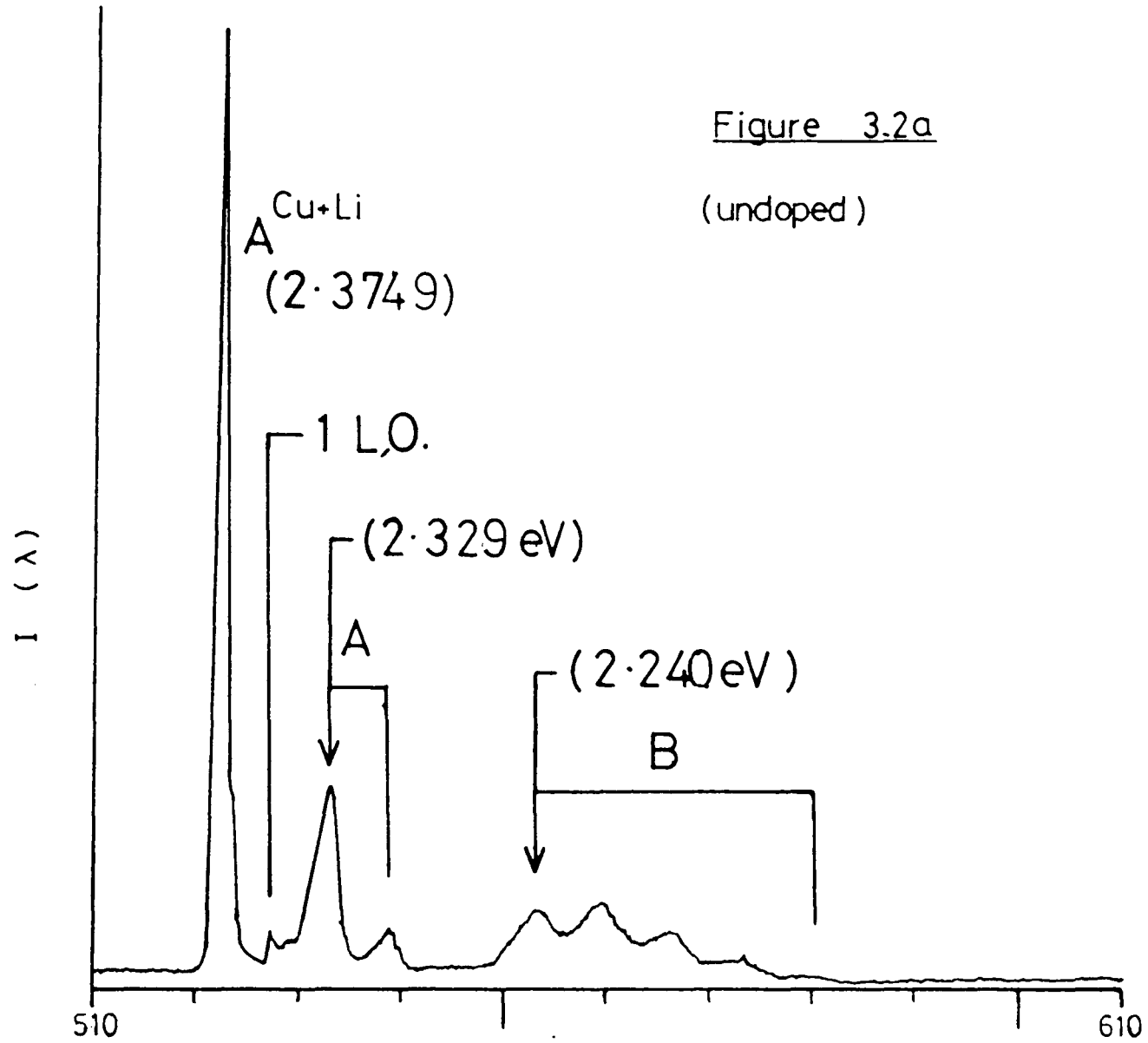

(undoped)

Figure 3.2b

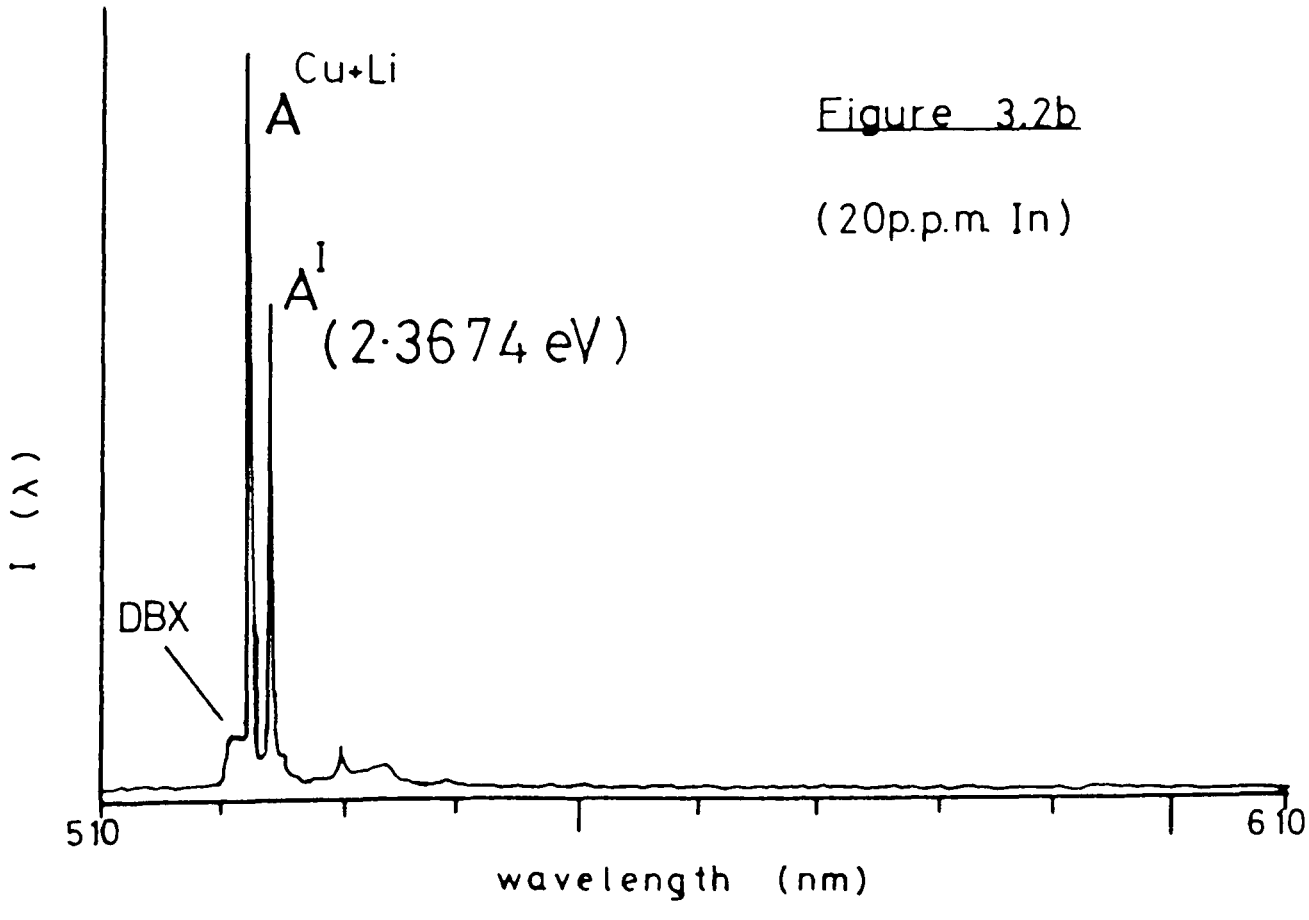

(20p.p.m. In)

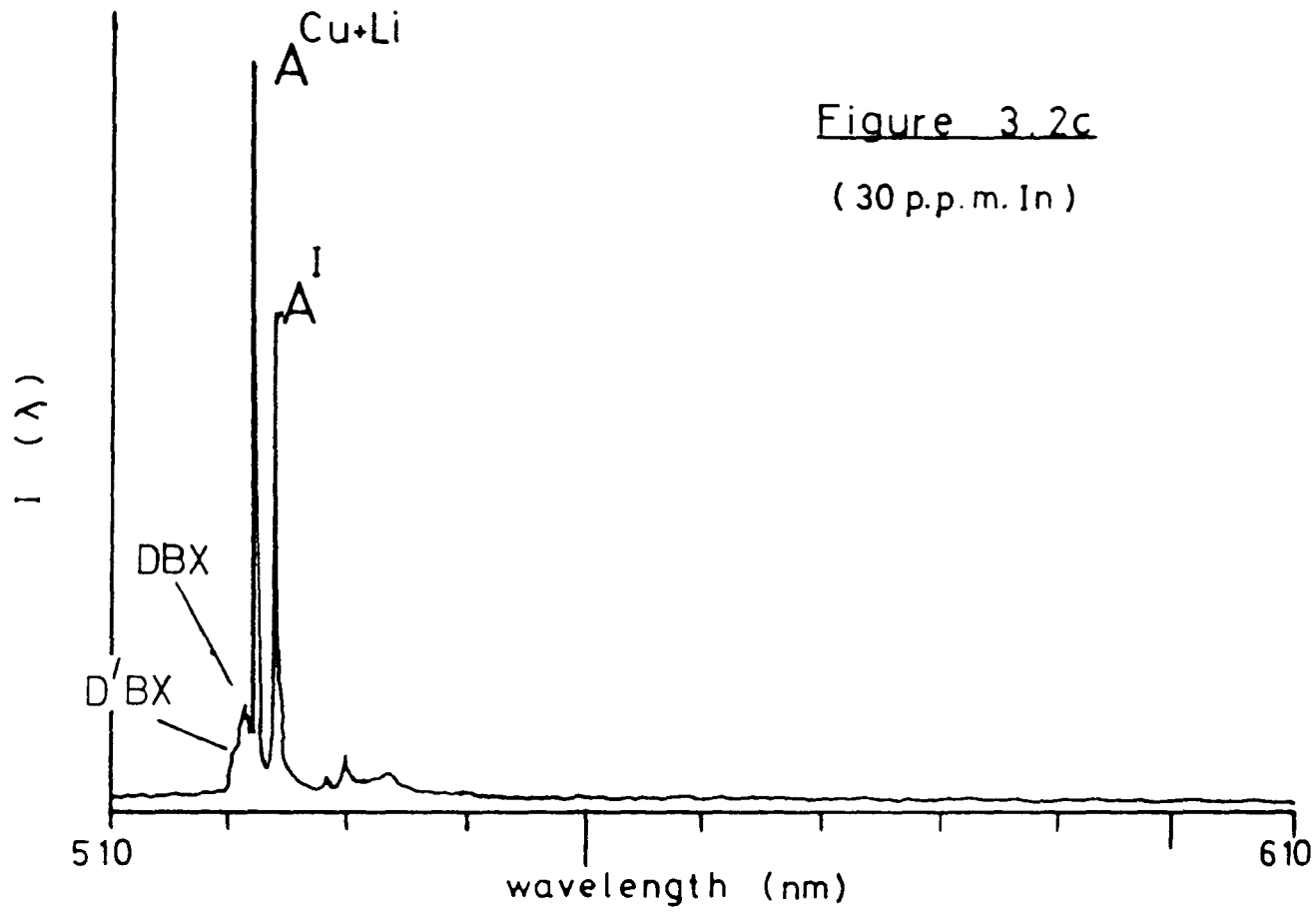

Figure 3.2c

(30 p.p.m. In)

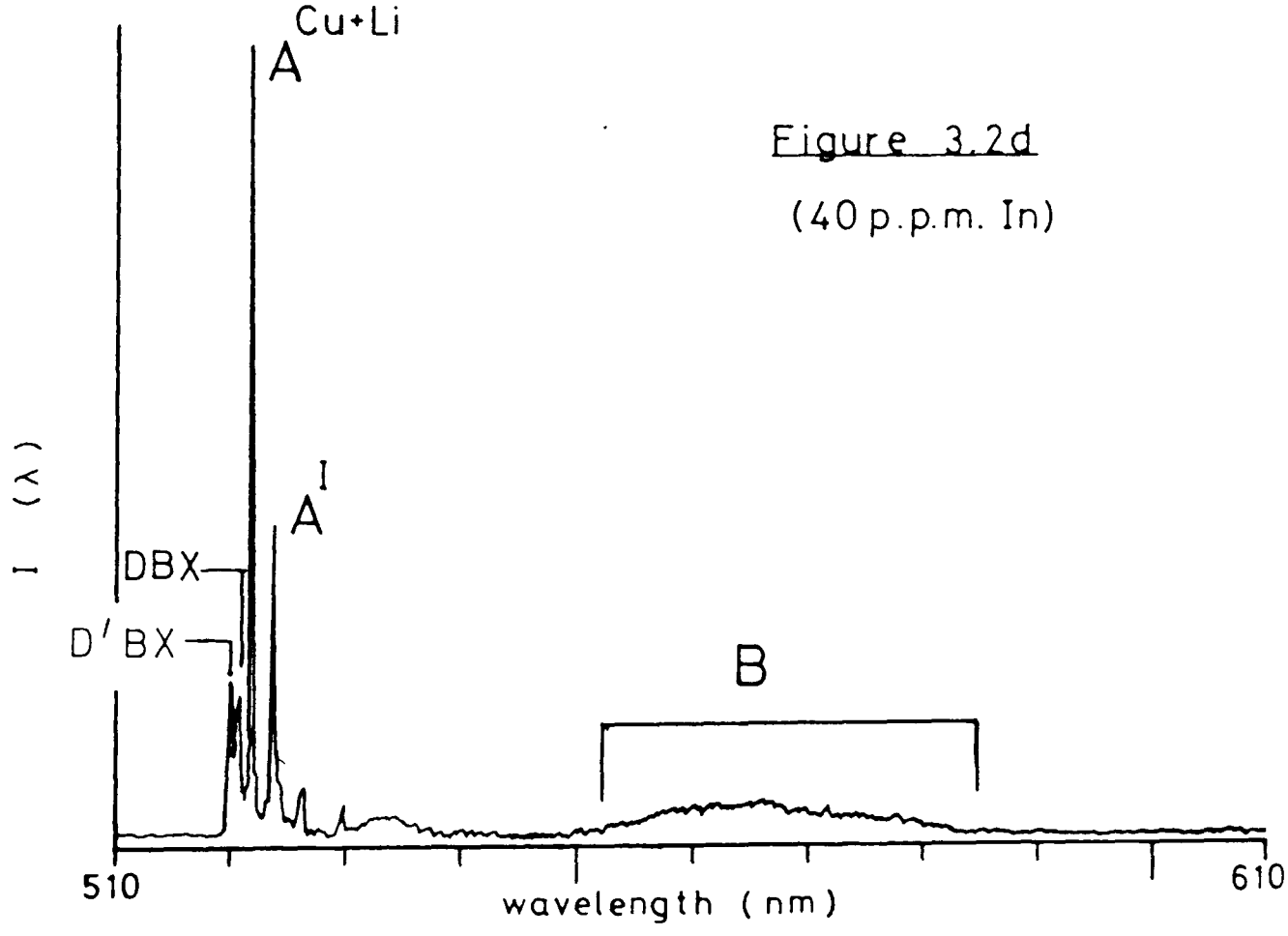

Figure 3.2d

(40 p.p.m. In)

3.4.1 ZnTe : In

Figures 3.2 a,b,c,d show representative luminescence spectra of the nominally pure and of the 20, 30 and 40 p.p.m. indium doped material respectively.

The spectra of both the pure and doped material is dominated by an emission line, labelled A^{Cu+Li} in the above figures, which peaks at 522.04 nm (2.3749 eV). Group Ia, Ib and Va elements have all been observed to produce neutral acceptor bound exciton emission close to 2.375 eV in ZnTe with the emission involving copper (Cu_{Zn}) and that involving lithium (Li_{Zn}) substitutional acceptors occurring at an almost identical energy of 2.3746 eV [18-22]. Since both copper and lithium were found to be present in the material studied here (analysis report in Chapter 2) the emission observed at 2.3749 eV in this study will be ascribed to the bound exciton recombination at the Cu_{Zn} and Li_{zn} neutral acceptors. A shoulder on the low energy tail of this emission line is also seen in the spectra in figures 3.2, the origins of which is unknown but is likely to be another acceptor bound exciton emission. An emission line at 528.0 nm (2.348 eV) is clearly seen in figure 3.2a (labelled 1LO) and is probably the first phonon replica of the A^{Cu+Li} line.(The energy of the LO phonon in ZnTe is 0.026 eV and the energy difference between these two emission lines is 0.027 eV)

The two bands labelled A (fig. 3.2a) and B (figs. 3.2a,d) have zero phonon emission lines near 532.3 nm (2.329 eV) and 553.3 nm (2.240 eV) respectively. Bands with a zero phonon emissions near 2.33 eV and 2.24 eV have been shown by Magnea et al [21,38] and Tews [39] to be shallow DAP recombination involving Li_{Zn} and Cu_{Zn} acceptors respectively. The donor involved was the same in both bands and had a binding energy of 0.018 eV. As the positions of the two zero phonon lines observed here are very similar to those previously observed and since both copper and lithium are impurities in this material then band A is probably due to the DAP emission involving

lithium whilst band B is likely to be due to the DAP emission involving copper.

An emission line at 523.59 nm (2.3674 eV), labelled A^I, is observed only in the indium doped material and therefore probably involves the dopant. This is close to the 2.369 eV emission identified only as the A^C bound exciton line in the Zeeman studies on undoped material by Le Si Dang [25]. Similarities between the g-values observed in that work and for the acceptor in the ODMR studies [26] on the yellow DAP emission in ZnTe:Al has led Cox to tentatively assign the $(V_{Zn}Al_{Zn})'$ acceptor to the C defect. Indium, being in the same group as aluminium, is expected to form an analogous acceptor centre [34], but with a different binding energy, and therefore the A^I emission probably involves an exciton bound to the $(V_{Zn}In_{Zn})'$ complex.

The luminescence spectra of all of the samples taken from the indium doped material show a weak emission at 521.4 nm (2.377 eV) which is labelled DBX in figures 3.2b,c,d. Emissions due to the annihilation of an exciton bound to a neutral donors have been reported to occur at 2.378 eV [21,22,24]; 2.3779 eV [27,37,41]; and 2.3775 eV [18]. In no case has the neutral donor involved in the above emissions been positively identified but Dean did suggest that it was possibly the $Al_{Zn}^{\bullet}$ donor [27]. The DBX emission is only observed in this study in material that has been deliberately doped with a donor species and it is therefore suggested that the emission at 2.377 eV is due to the recombination of a donor bound exciton.

The highest energy emission that has been observed in any of the material studied here occurrs at 520.29 nm (2.3824 eV) in samples containing 30 and 40 p.p.m indium (labelled D'BX in figs. 3.2c,d). The free exciton emission in ZnTe has been observed at 2.382 eV [15-19] but the assignment of the D'BX emission, observed in this study, to one involving the free exciton recombination is unlikely. This is because the emission is only observed in

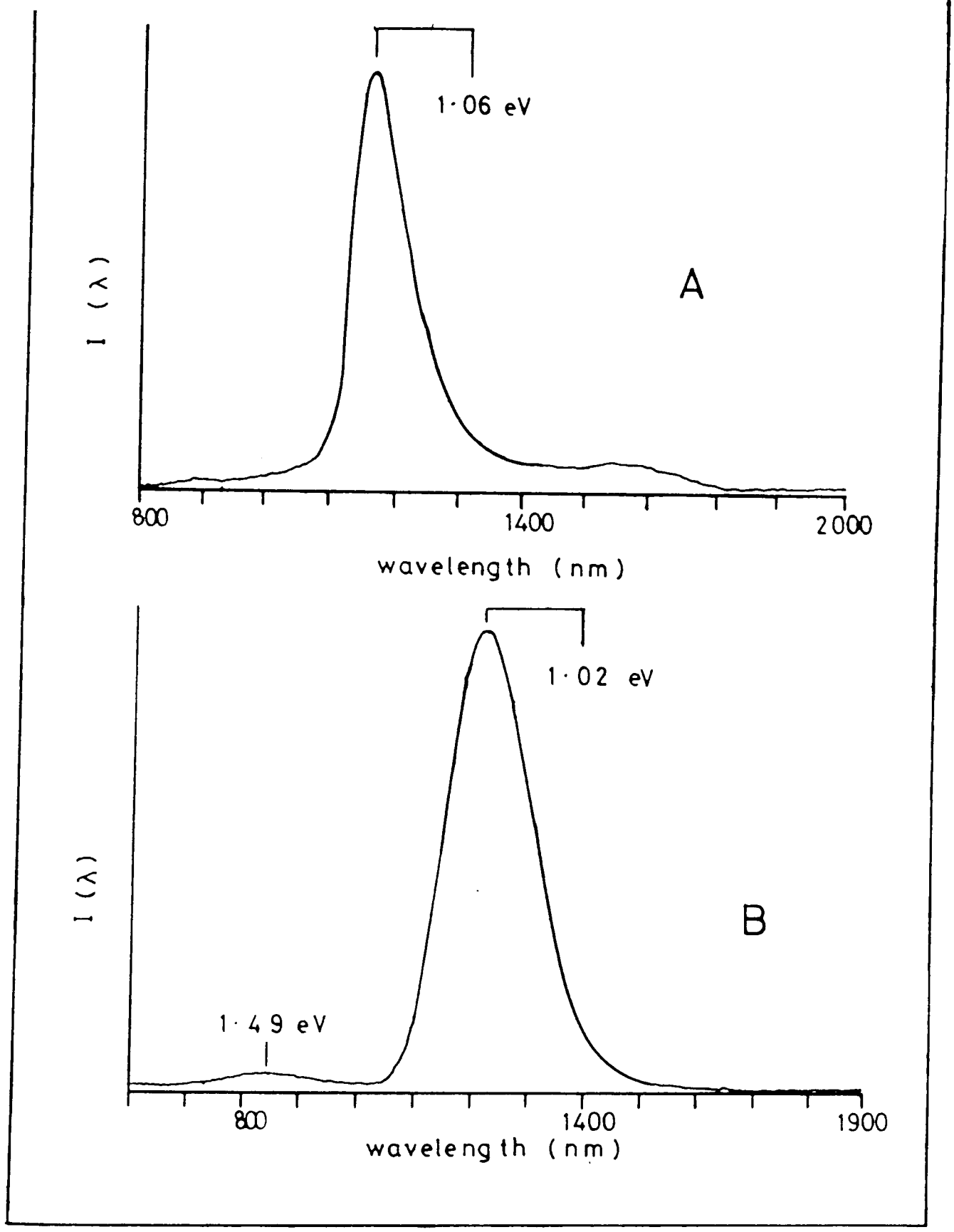

Figures 3.3

Representative near infra-red luminescence spectra obtained from:

(A) Undoped material.

(B) Indium doped material.

the two most heavily doped indium samples and it is therefore thought to be more likely that this emission is again due to a donor bound exciton recombination with the donor involved probably being the In_{Zn} impurity.

The near infra-red luminescence spectra observed in undoped and indium 20,30,40 ppm doped material are shown in figures 3.3a,b respectively. The spectra of all the indium doped material were identical in that they comprised two broad bands the relative intensities of which varied with dopant concentration. The weaker band peaks around 830 nm (1.49 eV) and has a full width at half maximum (FWHM) value of 0.25 eV. The more intense band, peaking at 1215 nm (1.02 eV) and having a FWHM of 0.14 eV, is similar to but not identical with the band observed in the undoped material which peaks at the slightly shorter wavelength of 1170 nm (1.06 eV) and is narrower (FWHM of 0.11 eV). The possible origin of these bands will be discussed in Section 3.5.

3.4.2 ZnTe : Al

The visible luminescesence spectra of material doped with 40 and 100 p.p.m. Al are shown in figures 3.4. Only one broad, featureless, asymmetric band is present with a peak wavelength of between 568 nm and 580 nm (2.14 eV and 2.18 eV) depending upon the boule from which the sample was taken. Boules CPB8 (fig. 3.4b) and CPB9 (fig. 3.4c) were both grown with 100 p.p.m. Al added but as can be seen, the peak energies differ, with the emission from CPB9 peaking at the same energy as that from CPB7 (fig. 3.4a) which is doped with 40 p.p.m. Al. However using Mass Spectrograph analysis (see Chap. 2) the Al content of CPB9 is comparable to that of the 40 p.p.m. doped boule. Although the peak energies of the emissions differ the FWHM of each band is similar, this being approximately 0.1 eV.

Similar bands to these have been observed by several authors [26,27,28] who have attributed the emission to the aluminium self activated (S.A.)

Figures 3.4

Representative luminescence spectra obtained from aluminium doped material.

(a) material grown with 40 p.p.m. aluminium dopant.

(b&c) material grown with 100 p.p.m. aluminium dopant. However M.S.A. showed (a) and (c) contained the same concentration when grown.

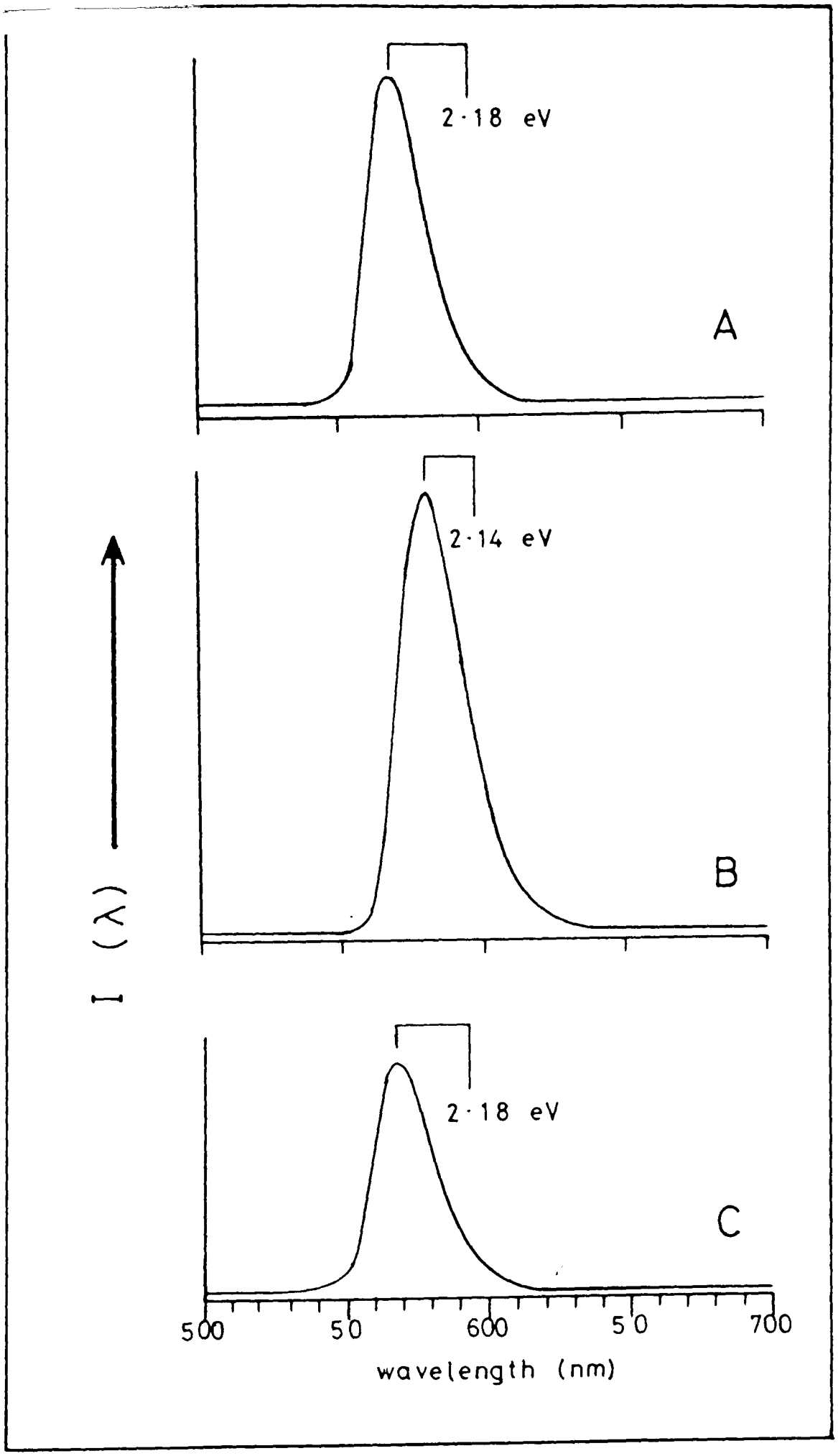
2·18 eV
A
2·14 eV
B
I (λ)
2·18 eV
C
500
50
600
50
700
wavelength (nm)

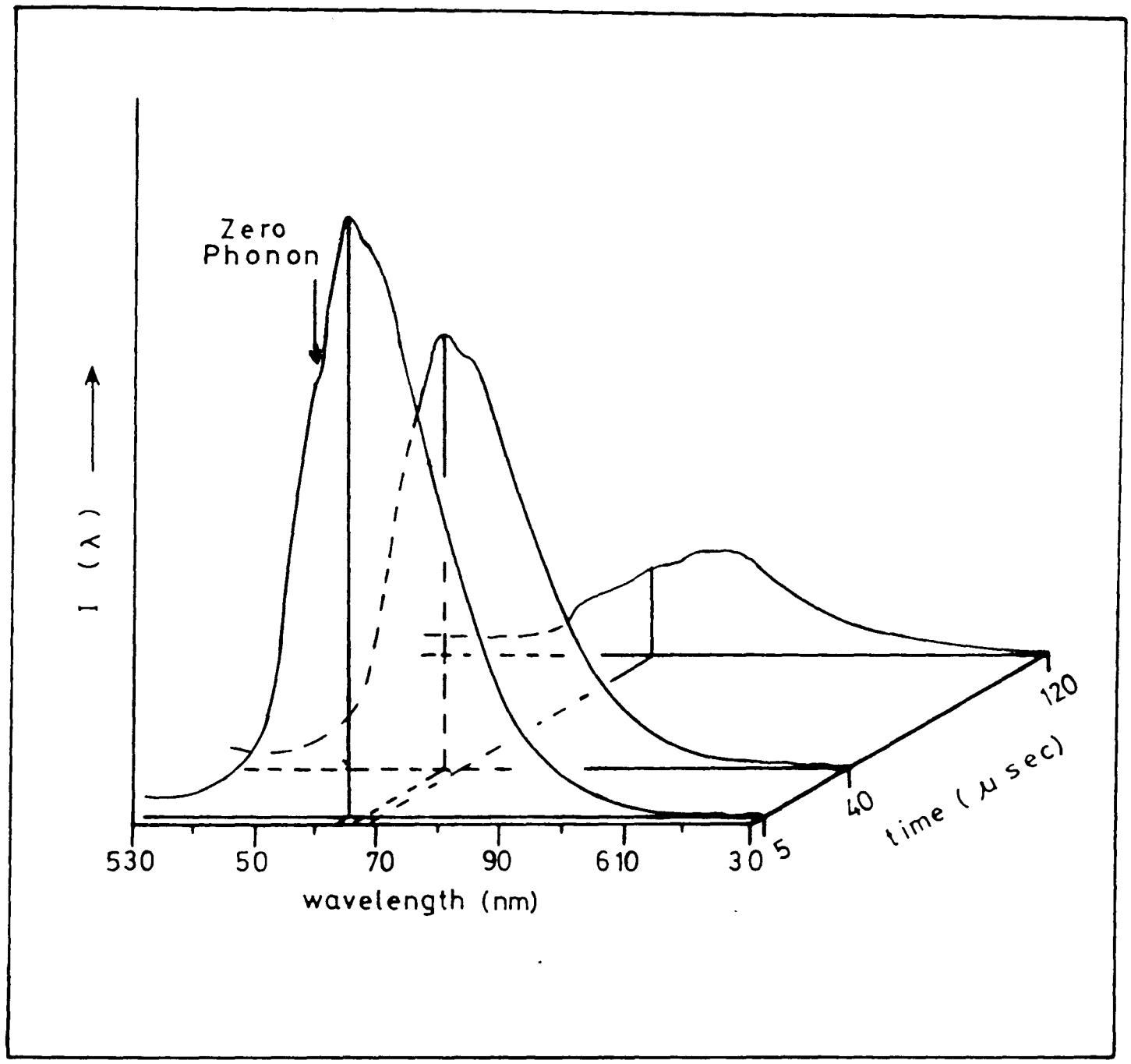

Figure 3.5

Time resolved luminescence spectra obtained from CPB9.

recombination. From ODMR studies on the yellow emission band at 2.16 eV in Al doped material Cox [26] was able to show that the acceptor involved in the recombination process was not of the simple substitutional type but was probably the $(V_{Zn}Al_{Zn})'$ complex. He also estimated the activation energy of the complex to be approximately 0.18 $\pm$ 0.02 eV. This value was similar to that given by Larsen et al. [29], who measured the activation energy of the $(V_{Zn}Al_{Zn})'$ acceptor to be between 0.22 - 0.25 eV.

The time resolved spectrum of CPB9, presented in figure 3.5, shows the movement of the band towards a lower energy with time after cessation of the exciting radiation. This was observed for all three boules and is indicative of a DAP process (eq$^{ns.}$ 10,11). This band is the result of DAP recombination. Figure 3.5 also shows partially resolved phonon structure in which the zero phonon line (the shoulder on the high energy side of the emission) occurs at approximately 558 nm (2.22 eV). The first phonon replica (at the emission peak shown in figure 3.5) is observed near 566 nm (2.19 eV). According to theory of Huang-Rhys [40] the ratio of the intensities of the first to zero phonon emission depends upon the degree of phonon coupling of the centre to the crystal lattice. This ratio is known as the Huang-Rhys factor, S, and obviously the greater the coupling of the centre to the lattice the higher the value of S. As the donor involved in the Al DAP transition is shallow its wavefunction is highly delocalised and therefore any energy change of the donor system will be effectively distributed to the entire crystal lattice. Conversely the acceptor wavefunction is more localised with any energy change being likely to be dissipated only over nearest neighbours and therefore produces a local lattice distortion. The S factor is then a measure of only the acceptor state - lattice phonon coupling. The S factor of the acceptor $(V_{Zn}Al_{Zn})'$ can only be estimated from figure 3.5 since the zero phonon band is not well resolved from the first phonon replica. Nevertheless S can be estimated to be between to 1.5 and 4 which indicates

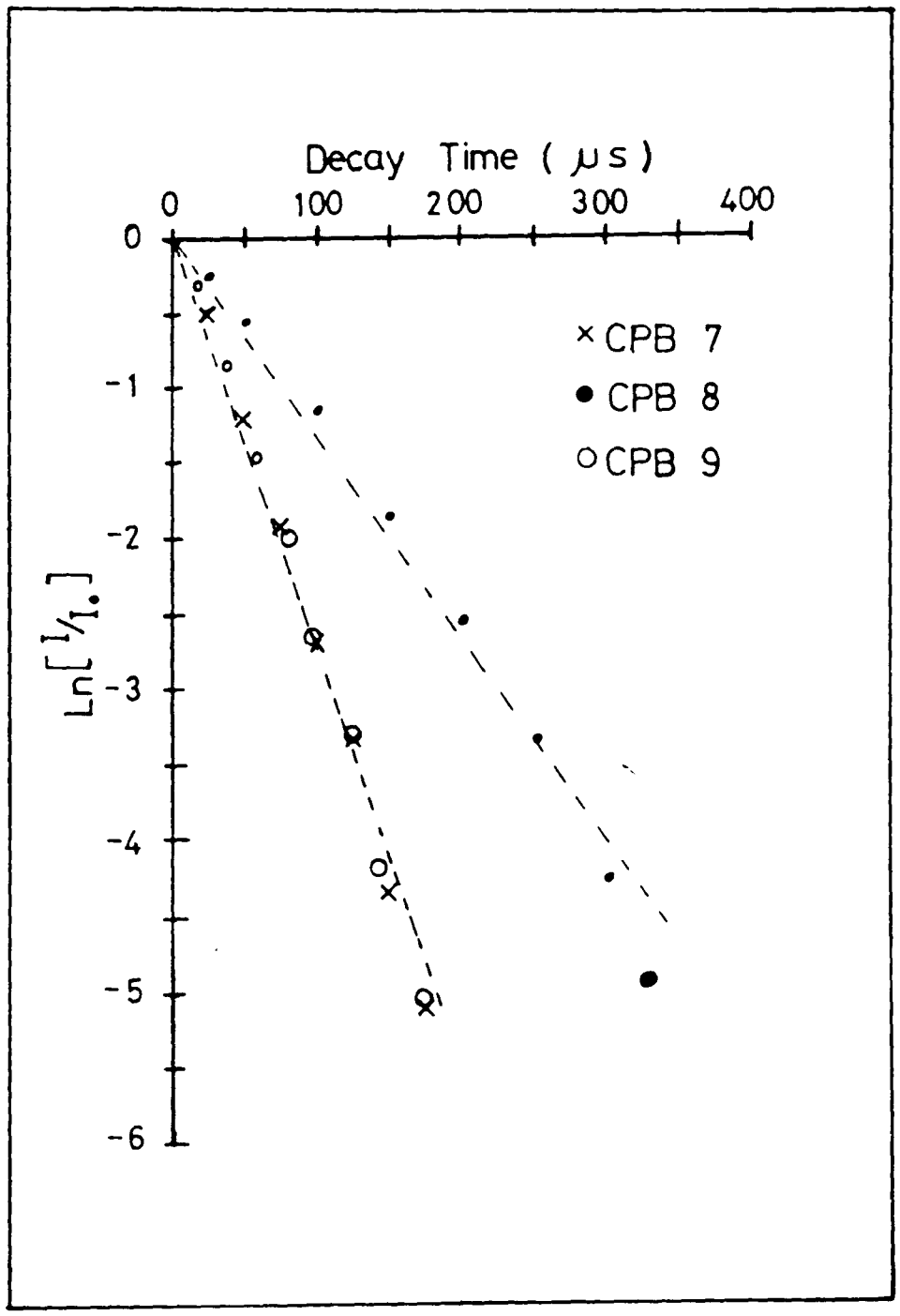

Figure 3.6

Luminescence decay characteristics of the 2.18 eV emission observed in CPB7 and CPB9 together with those of the 2.14 eV emission observed in CPB8.

only a weak coupling of the acceptor to the lattice. This estimation of the phonon coupling is consistent with the ODMR studies on the $V_{Zn}Al_{Zn}'$ acceptor by Cox [26] who found that the centre had a g-factor characteristic of a delocalised orbit. Such a centre would be expected to have only a weak lattice phonon coupling.

The correlation of the peak of the emission band with the concentration of the Al dopant is reflected in the luminescence decay characteristics shown in figure 3.6. The decay of the 2.18 eV band in CPB7 and CPB9 is non exponential, with a decay time of ~25 μsec whereas the decay of the 2.14 eV emission band in CPB8 is non exponential with a longer decay time of ~50 μsec.

The faster non exponential decay of the higher energy DAP band could be interpreted from eqn.(11) as meaning that the range of spatial separations of the pairs is small with the pairs being closely spaced leading to a high recombination probability and a fast decay time. Conversely the lower energy band may involve a greater range of separations of the pairs. The more widely separated pairs recombining more slowly causing the decay time of the band to increase.

The energy shift of the emission, observed in figure 3.4, towards lower energy as the doping concentration increases is opposite to the effect one would expect [36]. That is to say that as the doping concentration is increased the DAP separation may be expected to decrease, increasing the Coulombic potential existing between the ionised donors and acceptors and therefore increasing the energy of the emission band. The observed decrease in emission energy with increasing dopant concentration may possibly be explained by considering that in the case of the S.A. recombination both the donors ($Al_{Zn}^{\bullet}$) and the acceptors (($Al_{Zn}V_{Zn}$)') involve the dopant and that as the dopant concentration is increased there may be a greater tendency for the Al to complex and form the $(V_{Zn}Al_{Zn})'$ centre at the expense of the

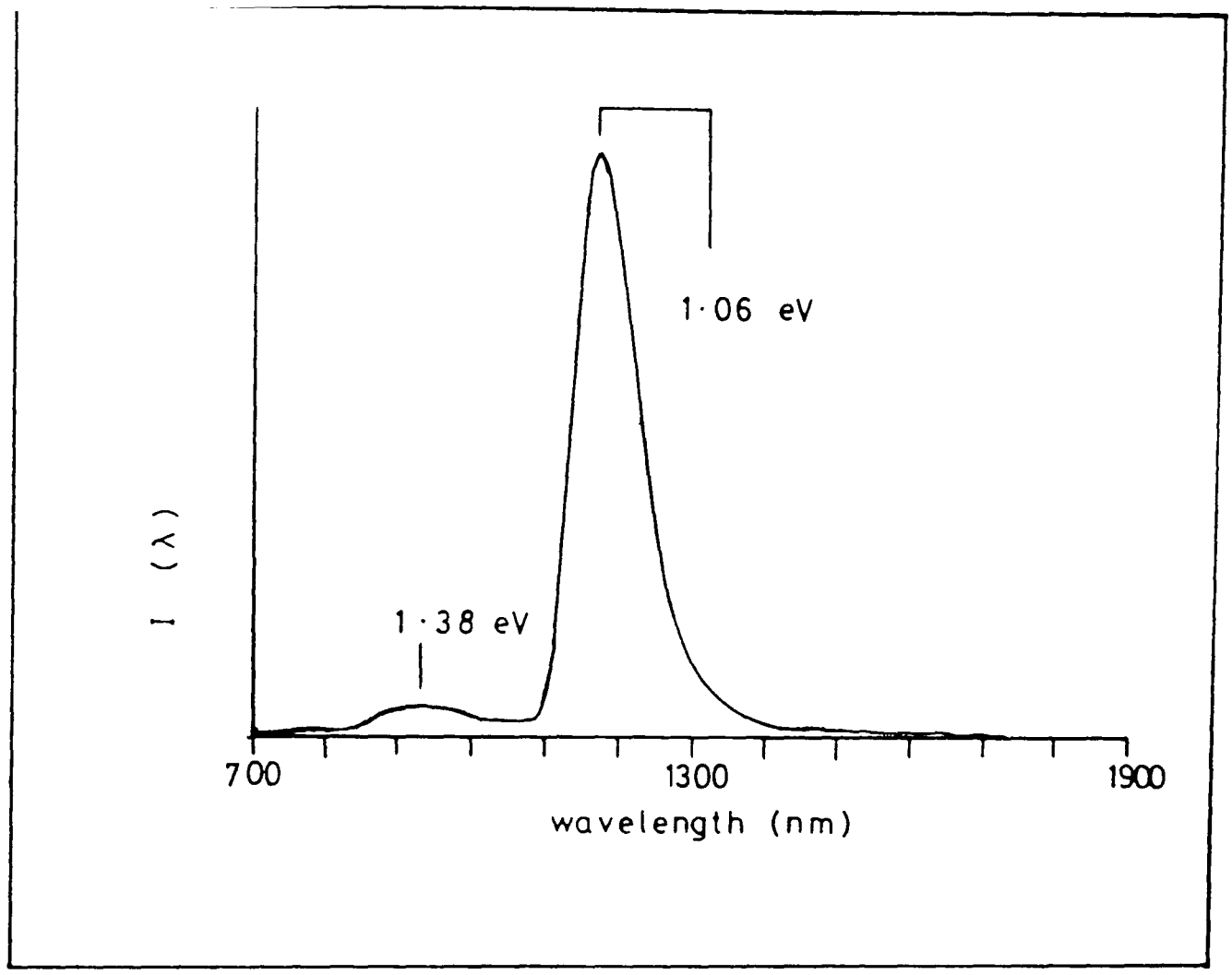

Figure 3.7

Representative near infra-red luminescence spectrum observed in all aluminium doped material.

isolated $Al^{\bullet}_{Zn}$. As a consequence of this the distance between the donors and acceptors would increase with the result that the emission would shift to lower energies as the amount of dopant increased. Furthermore, as the concentration of the complexed Al increased with respect to that of the isolated Al the range of the spatial separation of the pairs may be expected to increase. Thus there would be a greater contribution to the luminescence from more distant pairs and the decay time of the emission would increase and become non exponential.

Figure 3.7 shows a representative infra-red spectrum obtained from the boules CPB 7,8,9. In all cases the spectrum comprises two bands. One with a peak near 1170 nm (1.06 eV) and a FWHM of 0.09 eV and another with a peak near 898 nm (1.38 eV) and a FWHM of 0.25 eV. The possible origins of these peaks will be discussed in Section 3.5.

3.4.3 ZnTe : Pb

Lead, being a group IV element, is amphoteric in nature and has also been used as a dopant in an attempt to increase the resistivity of ZnTe. In Chapter two Van der Pauw resistivity measurements showed that in one case high resistivity material was grown but could not be reproduced. Photoluminescence has been carried out in an attempt to understand this anomaly.

Figure 3.8a,b,c,d shows the photoluminescence spectra obtained from boules CPB- 10,11,12,13. the first two boules are doped with 1000 and 200 ppm lead respectively; the last two boules each with 100 ppm lead.

The spectra of the two samples containing the higher concentrations of lead are in essence identical. They show the intense A^{Cu+Li} PBE transition at 522.04 nm (2.3749 eV) with its associated LO-phonon transition 0.026 eV lower in energy together with the lithium (A) and copper (B) associated DAP series. These spectra are similar to that of the undoped material (fig.3.2a)

Figures 3.8

Representative luminescence spectrum observed in material doped with :

(a) 1000 p.p.m. lead

(b) 200 p.p.m. lead

(c&d) 100 p.p.m. lead

The material producing the luminescence shown in figure (d) also produced high resistivity material.

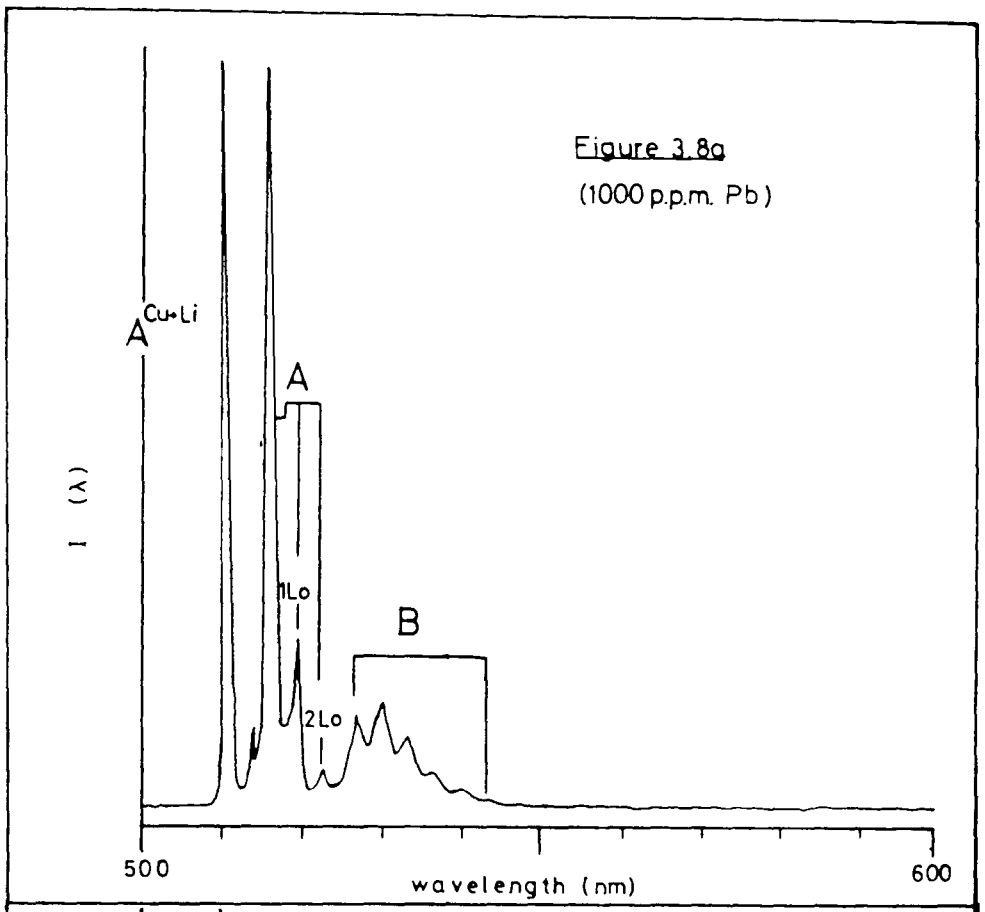

Figure 3.8a

(1000 p.p.m. Pb)

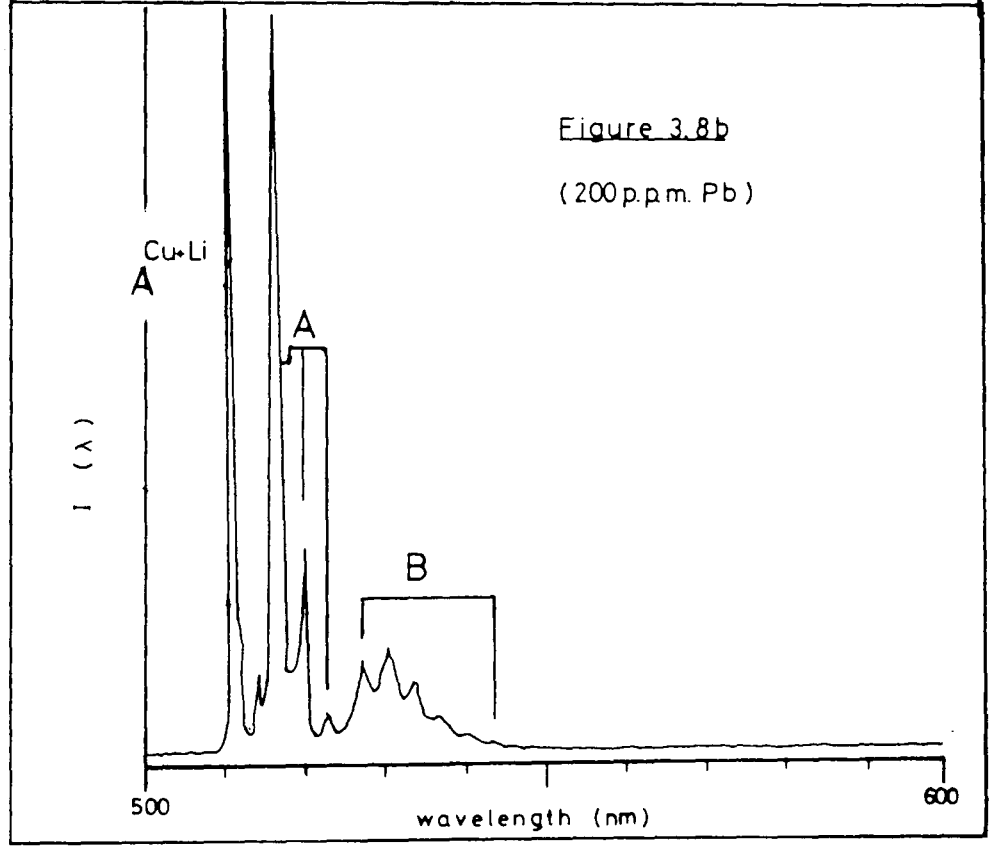

Figure 3.8b

(200 p.p.m. Pb)

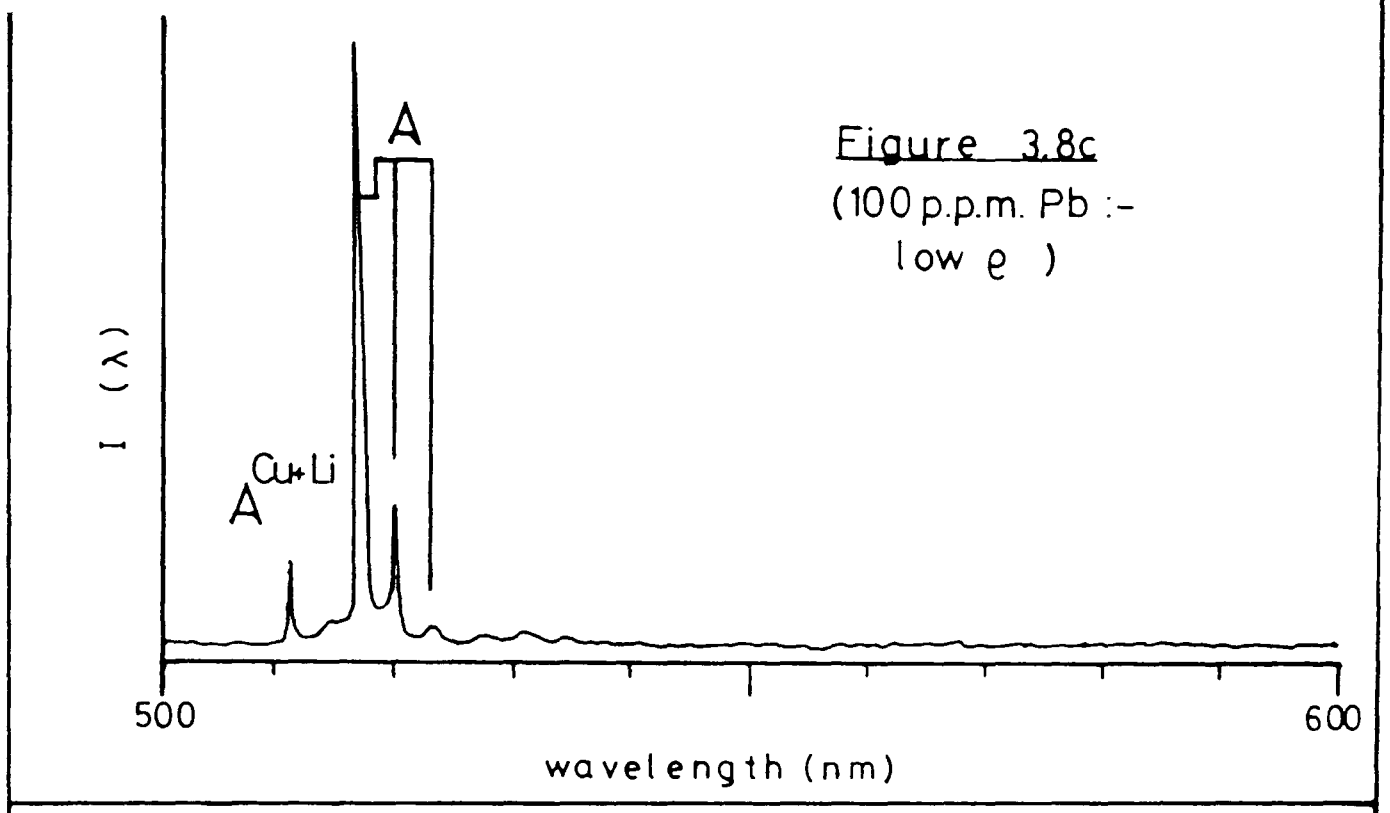

Figure 3.8c
(100 p.p.m. Pb :-
low ℓ)

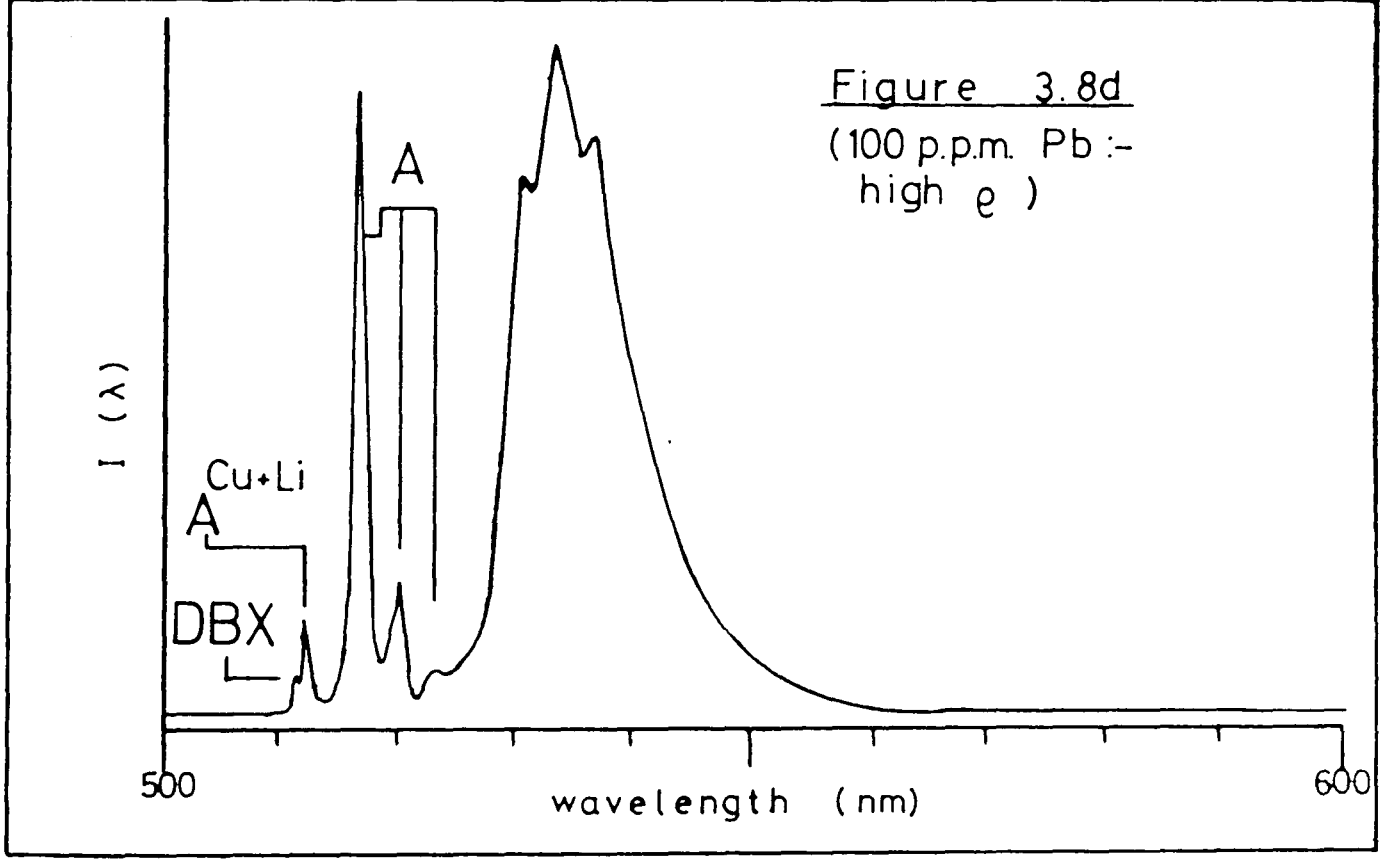

Figure 3.8d
(100 p.p.m. Pb :-
high ℓ)

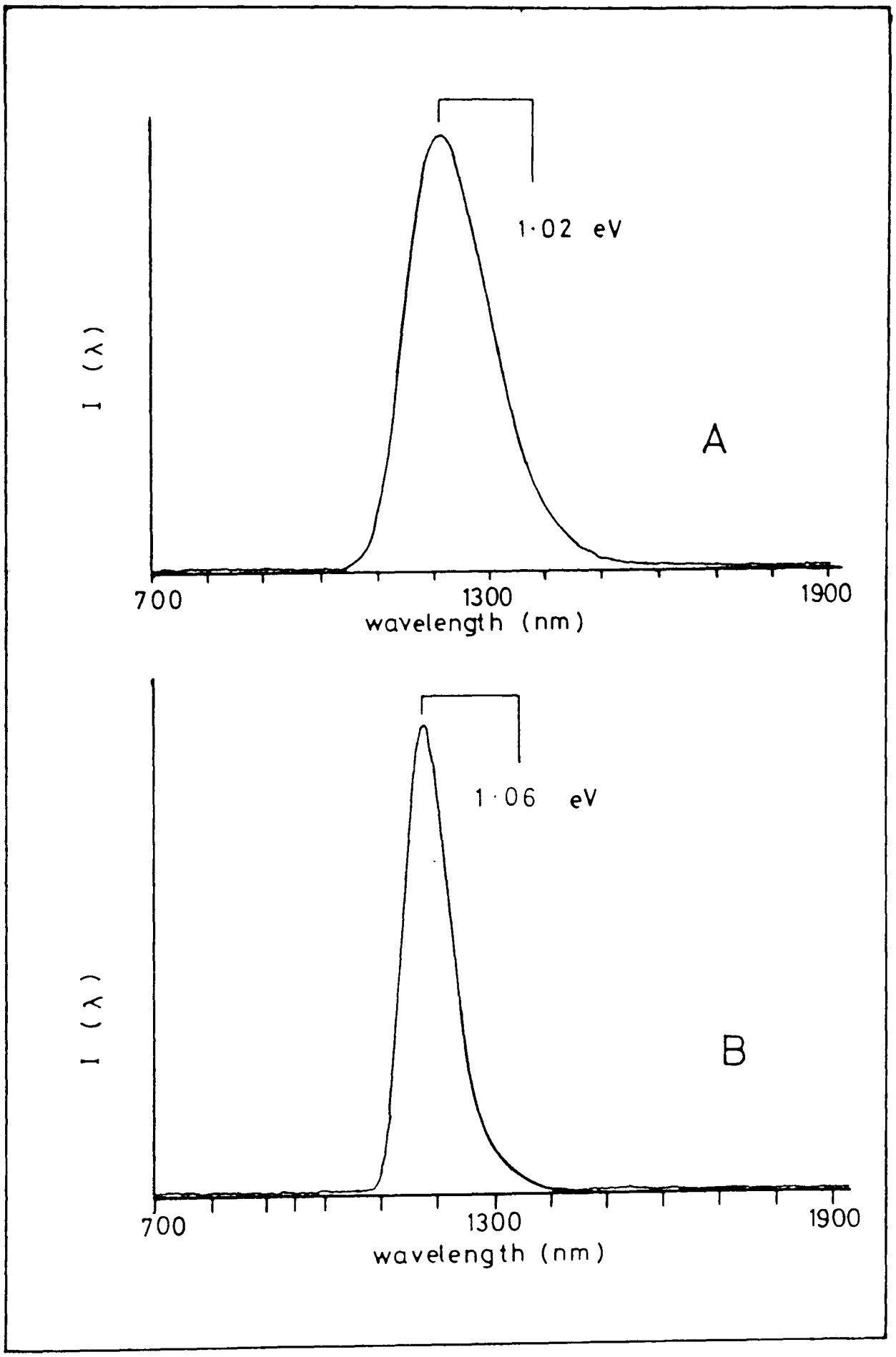

Figure 3.9

Representative near infra-red luminescence spectra observed in lead doped material.

(A) low resistivity material.

(B) high resistivity material.

which seems to indicate that lead has little effect on the band edge spectrum of ZnTe.

The spectra of samples taken from the two boules doped with 100 ppm Pb are shown in figures 3.8c and d. They are both dominated by the Li DAP zero phonon transition near 533.3 nm (2.325 eV) labelled A, and show only a weak A^{Cu+Li} BE transition at 2.3749 eV. Spectra taken from CPB12 show the weak DAP band B , involving copper,whereas that taken from CPB13 shows an intense DAP band in that region. This together with the observation of the DBX transition at 521.4 nm (2.378 eV) indicates an increased donor concentration in CPB13. This would imply a greater compensation of the shallow acceptors Cu and Li with the result that a higher room temperature resistivity is likely to occur. This is infact observed (Chap.2).

It is unlikely that these compensating donors are due to the incorporation of lead since no evidence of these is found in the more highly doped material, or even in the boule doped with the same concentration of lead, and are therefore probably due to the unintentional introduction of an impurity during the growth of CPB13. The identity of these donors remains unknown.

Figure 3.9 a,b shows the infra-red spectra obtained from the low resistivity and the one high resistivity (CPB13) samples respectively. Both types of spectrum contain only one band. The low resistivity samples show a band with a peak position near 1215 nm (1.02 eV) and a FWHM of 0.15 eV whereas CPB13 shows a band peaking near 1170 nm (1.06 eV) with a FWHM of 0.09 eV.

DOPANT	PEAK ENERGY (eV)	FWHM (eV)	ASSIGNMENT	Fe^+ EPR SIGNAL
NONE	1.06	0.11	TYPE I	—
Fe	1.05	0.09	TYPE I	—
Al	1.06	0.09	TYPE I	YES
	1.38	0.25		
In	1.02	0.15	TYPE II	NO
	1.49	0.26		
Pb (CPB13)	1.06	0.11	TYPE I	YES
(OTHERS)	1.02	0.09	TYPE II	—

Table 3.1 Summary of the infra-red bands observed in ZnTe. The assignment of the bands as either type I or type II depend upon peak positions and FWHM values. Where no comment is made for the EPR signal the low resistivity of the samples prevented a standing wave being set up in the resonance cavity.

3.5 Further Discussion of the Infra-Red Luminescence in Pure and Doped Material

Table 3.1 gives a comparison of peak positions and FWHM values of the near infra-red bands found in the samples of ZnTe studied here. It is observed that the band peaking near 1 eV, observed in all samples, may be classified as type I or as type II using the peak position value as the delimitor. Thus the type I bands are those with the peak energy of 1.06 eV and were found to be, in general, narrower than the type II bands where the peak energies are close to 1.02 eV. A further difference between the material possessing the type I band and that possessing the type II band was that EPR experiments showed iron to be present in type I material. In some samples the low resistivity of the material damped the Q-value of the cavity to such an extent that EPR experiments were not possible. These samples are indicated with a line in the Fe^{+} column of Table 3.1

In an attempt to ascertain the origins of all the bands time resolved measurements were undertaken. The intensities of the higher energy bands, present in the ZnTe:In (1.49 eV) and ZnTe:Al (1.38 eV) samples, proved to be too small for such studies and in all cases it was found that the luminescence from both the type I (1.06 eV) and type II (1.02 eV) lower energy bands decayed in times faster than the response time of the cooled germanium detector ($\sim$5 μsec). Consequently time resolved experiments proved unsuccessful in identifying the nature of the processes involved in the type I, type II and higher energy emission bands. In a further attempt to identify the emission processes involved in the infra-red emission the effects of the excitation intensity on the peak positions of the three types band was studied. If the luminescence had involved DAP transitions then as the excitation intensity increased the more distant pair transitions would have saturated resulting in a shift of the peak position towards higher

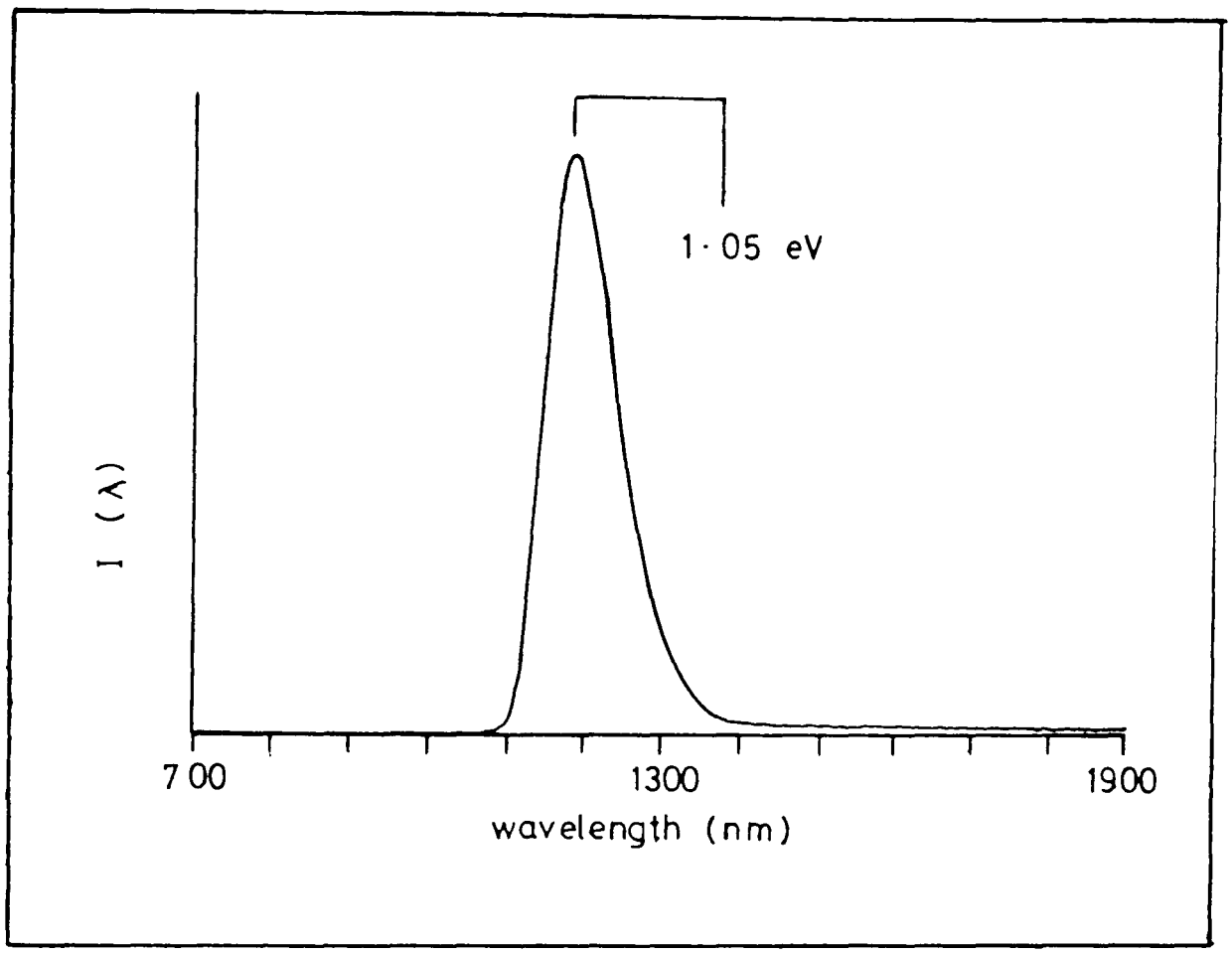

Figure 3.10

Representative near infra-red luminescence spectra observed in iron doped material.

This is the only luminescence band observed in this material.

energy. In experiments carried out on types I, II and the higher energy (1.38 eV and 1.49 eV) bands, in which the incident laser power was varied between 5 mW and 1 W, no such shift was observed from which it is inferred that DAP transitions are unlikely to be responsible for the luminescence bands that have been observed in the near infra-red. However it must be noted that because of the width of the emission any small shifts in the peak position with varying laser power may remain unobserved and DAP transitions may still be involved.

The higher energy bands observed in ZnTe:In (1.49 eV peak) and ZnTe:Al(1.38 eV peak) are thought by Blashkiv et al [30] and Blashkiv [31,32] to involve a recombination between a donor electron and a free hole, with the unknown donor level being 0.64 eV below the CB but could equally as well be due to a free CB electron and deep acceptor situated approximately 0.9 eV above the VB. Either transition would produce no shift in the peak position with laser intensity as is observed in experiments.

The presence of the type I band in the undoped material would seem to indicate that the transition involved an impurity unrelated to the added dopant. One such impurity is iron. Experimental evidence for the possible involvement of iron in the 1.06 eV luminescence was obtained from doping and EPR. Figure 3.10 shows the luminescence band observed in ZnTe grown doped with 500 ppm iron. This band has a peak energy of 1.05 eV and a FWHM of 0.09 eV and represents the only luminescence observed in this material. Furthermore the EPR signal due to Fe^{+}, which is to be described in Chapter Five, was observed only in the material that showed the type I luminescence and only after illumination with above band gap energy radiation and has been interpreted as indicating that iron enters the lattice as Fe^{2+} which can then capture an electron to become Fe^{+}.

The evidence presented above indicates that the luminescence process responsible for the type I emission may not involve DAP recombination but does involve the transition metal impurity iron. Furthermore, when the material showing type I emission was illuminated with above band gap radiation the only EPR signal that was found to involve iron was due to the Fe^{+} centre. Similarities between the type I and the type II emission such as similar positions of the zero phonon emission ($\sim$1.13eV) fast decay times and similar F.W.H.M. values do suggest that the centre involved in the type I emission is also involved in the type II emission. Both the type I and type II emission bands could, then, result from the capture of an electron by the Fe^{2+} centre either directly or indirectly (via internal relaxation of the Fe^{+} ion).

From the above discussion any model that is proposed to explain the type I emission process must be able to describe the following:

1) No peak shift of emission with varying laser power
2) The role of the iron impurity in the process
3) A transition which leaves the iron in the Fe^{+} state after irradiation with above band gap energy light
4) Two emission processes involving the same centre

One possible model to explain the observed luminescent properties of the type I band (i.e. fast decay and not DAP) is shown in figure 3.11. It is proposed that the iron enters the lattice as Fe^{2+}. After irradiation with above band gap light the Fe^{2+} centre captures an electron from either a shallow donor or the conduction band (CB) in a radiationless transition. The luminescence could then be due to the relaxation of the Fe^{+} ion from the ^{4}P excited state to the ^{4}F ground state of the Fe^{+} centre (see Appendix B) thus:

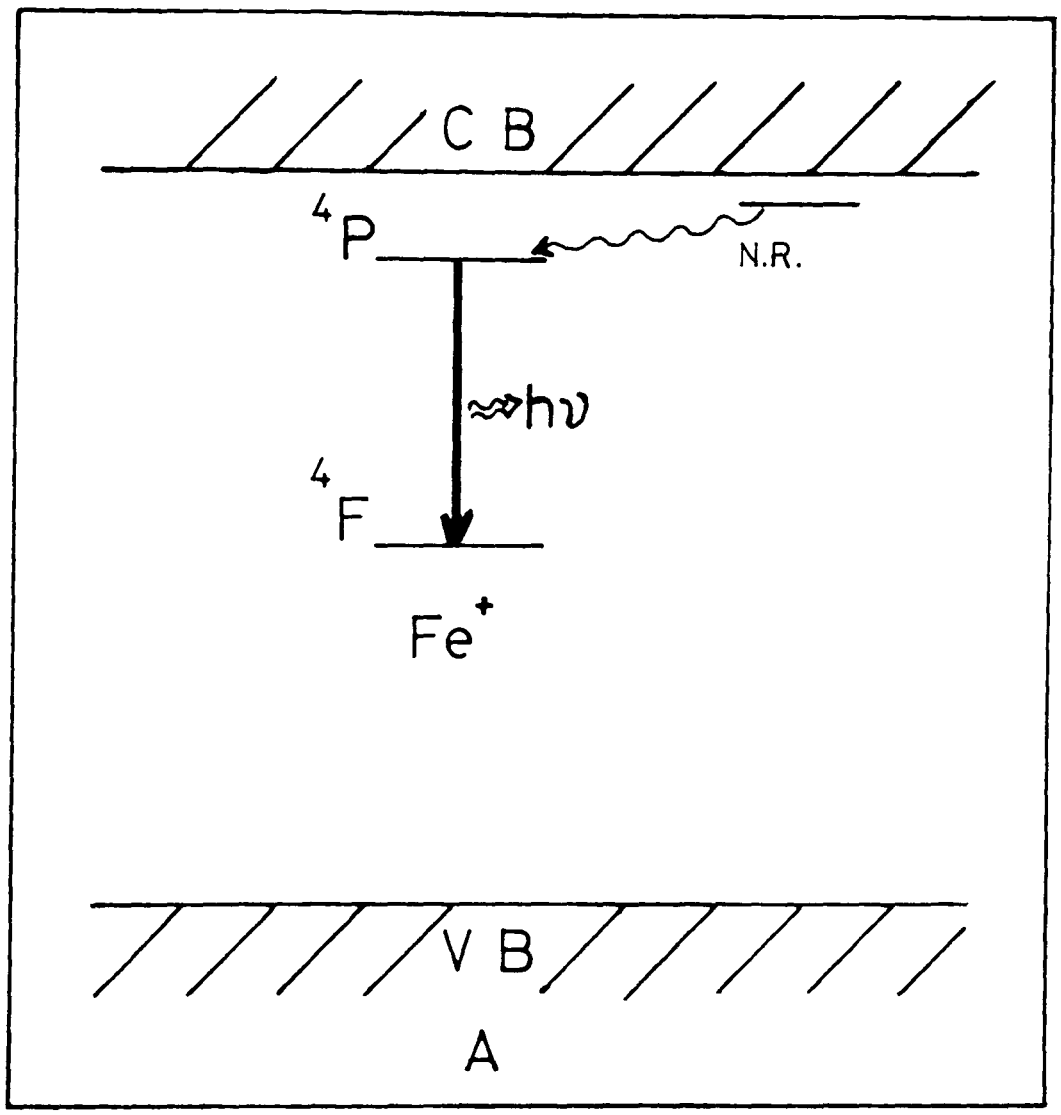

Figure 3.11

Energy band diagram showing internal transition model. An electron is captured by the Fe^{2+} ion in a non radiative (N.R.) process, leaving the Fe^+ in an excited state. The type I emission results from the internal transition between the ^4P excited state and the ^4F ground state.

$$Fe^{2+} + e^{-} \longrightarrow (^{4}P)Fe^{+} \longrightarrow (^{4}F)Fe^{+} + h\upsilon\,(1.13\ eV) \qquad (12)$$

(where 1.13 eV is the position of the zero phonon transition as estimated from the high energy tail of the type I and type II emission bands shown in figures 3.3, 3.7 and 3.9)

In Appendix B it is shown that the most likely transition is from the excited state into the $^{4}A_{2}$ ground state which would require the Racah parameter B to be 323 cm^{-1} compared to that of 810 cm^{-1} for the free ion. Although large shifts in B have been observed for a similar d^{7} ion, Co^{2+}, in ZnTe no data concerning Fe^{+} is available and therefore the type I luminescence cannot conclusively be ascribed to an internal transition.

In fact using the internal transition model the differences in peak position and FWHM between the type I and II emissions cannot be explained since the energy of emission in an internal transition process of a deep centre, such as Fe^{+}, is unaffected by the dopant impurities that are deliberately introduced during growth (i.e. Al,In,Pb) and depends only on the host material. It is therefore thought unlikely that both the type I and the type II luminescence could be due to the same internal transition within the Fe^{+} centre.

Two further models, which explain the emission as arising from the Fe^{2+}/Fe^{+} transition, are represented in figures 3.12 a,b. These models are essentially the same, with the iron again entering the lattice as Fe^{2+} which then captures an electron from either the CB or a shallow donor after an electron-hole pair has been created by illumination with above band gap radiation. This converts the Fe^{2+} ion into the Fe^{+} ion. The Fe^{+} then loses an electron which recombines with a hole in the valence band (VB) thus:

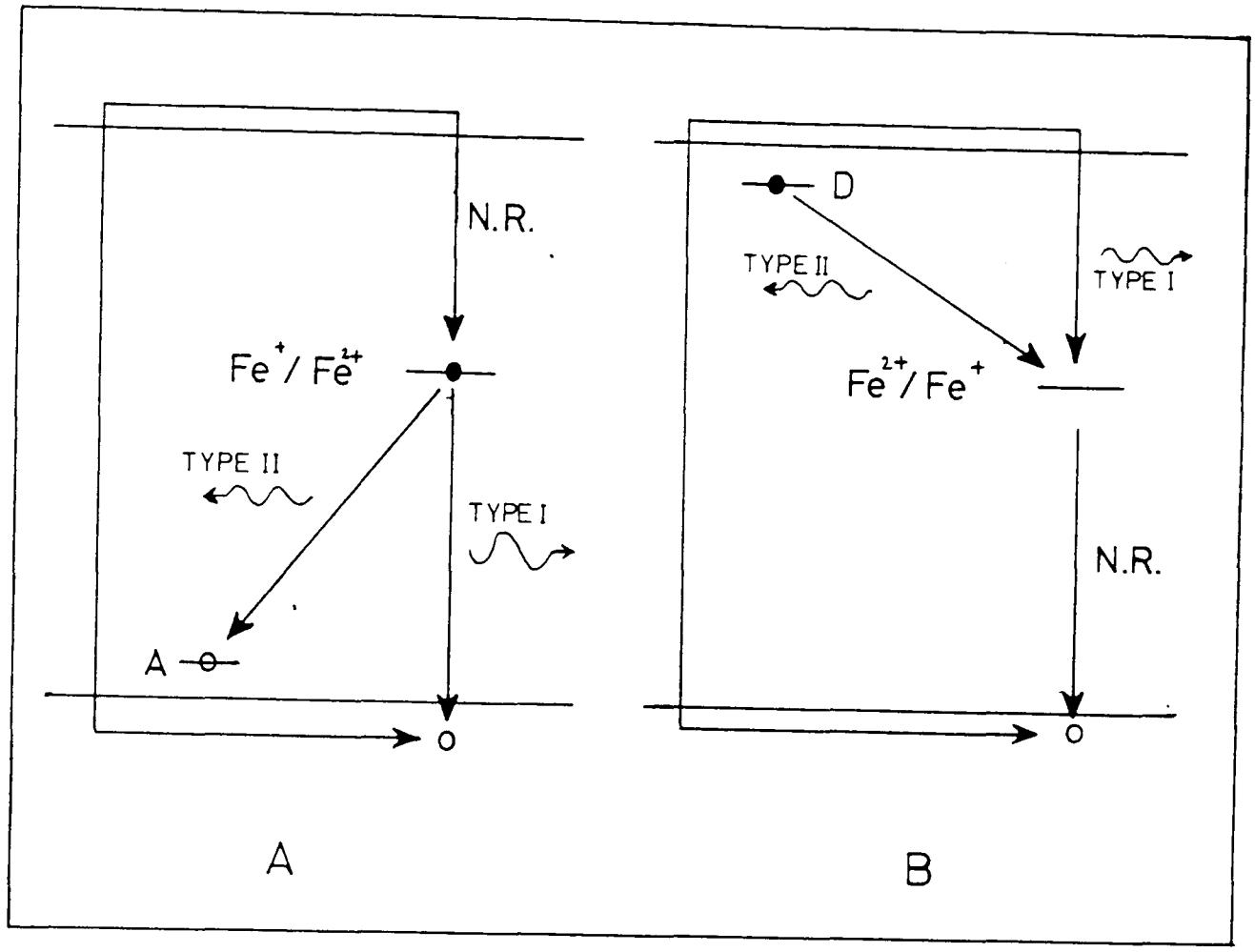

Figure 3.12

Energy band diagram showing possible models for type I (1.06 eV) and type II (1.02 eV) luminescence observed in ZnTe.

A) An electron is excited across the band gap and captured by a Fe^{2+} ion in a non radiative (N.R.) process. The type I emission arises from the recombination of that electron (now on a Fe^{+} ion) and a hole in the valence band. Type II emission arises from the recombination of the Fe^{+} electron with a hole on the acceptor.

B) An electron is excited across the band gap and type I emission arises from the capture of that electron by the Fe^{2+} ion. Type II emission results from the capture of a shallow donor (D) electron by the Fe^{2+} centre. The captured electron falls to the valence band via N.R. processes.

$$Fe^{2+} + e^- \longrightarrow Fe^+$$

$$Fe^+ + h^+ \longrightarrow Fe^{2+} \qquad (13)$$

The difference in the two models is the step in the process which is radiative (giving the 1.13 eV zero phonon emission). The model described in figure 3.12a shows the initial capture of the electron to be the non radiative step with its subsequent release as being radiative. The reverse is true for the model shown in figure 3.12b and no firm distinction between the two models can be made on the basis of the available experimental results.

With the model shown in figure 3.12a the types I and II emissions may be explained if it is assumed that the type I emission arises from the capture of an Fe^+ electron by a valence band hole and the type II emission arises from the capture of an Fe^+ electron by an acceptor, A. As an electron at a deep centre, such as Fe^+, is expected to be highly localised at that centre recombination between the Fe^+ electron and a hole on an acceptor could only arise if the spatial separation of the iron centre and the acceptor centre was small, possibly only 1 or 2 lattice spacings. (In this case the Fe^+ centre behaves as a deep donor state).

If the concentration of acceptor levels was small then the number of available unionised acceptors that were available to accept the Fe^+ electron would be small; the spatial separation between the acceptor and Fe^+ centres large; and recombination with the holes in the valence band more likely. This gives rise to the type I emission that has been observed in the boules doped with aluminium and lead (CPB13). If, in the case of indium doped material, the number of available unionised acceptor states was larger owing to the dopant introducing more shallow acceptors (through perhaps complex formation) than either lead or aluminium then the rate of recombination of

the Fe^{+} electrons holes trapped at the acceptors might increase, resulting in transitions at a lower energy which would then broaden and shift the emission band to produce the observed type II emission in indium doped material. This model can also be used to explain why no shift in the emission peak occurred when the incident laser power was varied. In the case of the type I emission the recombination is free to bound and therefore no shift would be expected. In the case of the type II emission no peak shift is observed because no coulomb shift of the emission is expected. The lack of coulomb interactions between the iron and acceptor (A) centres can be understood by considering the charge states of the two types of centre before and after emission. The type II emission process may be described by:

$$[Fe^{+}]^{-} + [A]^{o} \longrightarrow [Fe^{2+}]^{o} + [A]^{-} + h\nu \qquad (14)$$

negative neutral neutral negative type II

As can be seen from equation (14) both before and after the emission one of the centres is neutral whilst the other is negatively charged with respect to the lattice. Hence no coulomb interaction between the centres occurs.

If the emission processes are described using the model shown in figure 3.12b then the type I emission would be due to the radiative capture of a conduction band electron by the Fe^{2+} centre and the type II emission would be due to the capture of a shallow donor state electron (D) by the Fe^{2+} centre (This is an example of a donor to deep donor transition). No peak shift with varying laser power in the observed emission would be expected for the type I emission process as this is a free to bound recombination process. However in the case of the type II emission process a shift in the peak position with varying laser power should occur because a coulomb shift of the emission is expected. Again the origin of the coulomb interaction may

be understood by considering the charge states of the iron and donor centres before and after recombination. In this case the type II emission process can be described by:

$$[Fe^{2+}]^{o} + [D]^{o} \longrightarrow [Fe^{+}]^{-} + [D]^{+} + h\nu \qquad (15)$$

neutral neutral negative positive type II

Equation (15) shows that the two types of centre are neutral before emission. After emission the iron centre is negatively charged and the donor is positively charged and therefore experience a coulombic force of attraction.

As no shift in the peak of the type II emission was observed when the laser power was varied it is suggested that the recombination mechanisms described in figure 3.12a are probably more likely than those described in figure 3.12b to result in the types I and II luminescence that has been observed in this study.

3.6 Conclusions

The as-grown ZnTe grown in our laboratory has been found to be always low resistivity p-type. The photoluminescence spectra of such material has been found to be dominated by emissions involving the shallow acceptors Cu_{Zn} and Li_{Zn} and therefore it is these centres that are thought to be responsible for the low resistivity. In an attempt to compensate these acceptors with shallow donors various dopants were introduced during growth. Indium and aluminium were found to be most effective at producing high resistivity material. This compensation by donor doping was reflected in the luminescence spectra observed in the high resistivity ZnTe:Al, ZnTe:In and the anomalous ZnTe:Pb material. The DBX donor bound exciton line was evident

in all In doped material with a second, D'BX, bound exciton line becoming stronger as the In doping level was increased. The DBX emission was also observed in the high resistivity ZnTe:Pb material but the emission in this material was dominated by shallow DAP luminescence. Evidence of an increased donor concentration in ZnTe:Al was also found in the luminescence spectra of the material which in all cases comprised of a single broad Al self activated luminescence.

Although some correlation between the resistivity and the luminescence spectra of samples was found it is difficult to see any correlation between the characteristics of the photoluminescence spectra and device performance. The lack of any correlation in this respect was demonstrated by the fact that spectra of samples taken from the same boule of ZnTe:Al were found to be essentially identical but only one device out of three fabricated from that material was able to function as a radiation detector.

There is also some evidence, presented here, of the involvement of iron in the luminescence bands that were observed in all material close to 1 eV. Although the precise model for this luminescence cannot be deduced from the data presented in this Chapter it is suggested, from the evidence given here and from EPR data presented in Chapter Five, that the most probable model to explain the type I emission involves the bound to free recombination of an electron bound to a Fe^{+} centre with a free hole. The type II emission may then be due to recombination of the same Fe^{+} electron with a hole bound to a shallow acceptor. Support for these models comes from a recent report on Fe^{+} implantation in CdTe [42] where recombination involving the deep centre, Fe^{+}, has been shown to produce a broad band emission near 1.03 eV with a decay time of 0.1 μsec. The fast decay time and lack of any shift in the peak wavelength of the band as the laser power was varied led to the conclusion that the emission involved a free to bound transition process.

The work presented in this Chapter indicates that iron acts as a deep

trap in ZnTe. It is this type of deep defect that is thought to be a cause of polarisation in radiation detectors, and as a consequence, poor device performance and it is certainly likely that iron is a cause of poor device performance in the material investigated in the present work. Therefore any procedure likely to introduce iron into the material should be avoided.

CHAPTER THREE REFERENCES

[1] Mott N.F., Trans. Faraday Soc. 34 500 (1938)

[2] Wannier G.H., Phys. Rev. 52 191 (1937)

[3] Dean P.J., Appl. Sol. State Sci. 1 1 (1969)

[4] Radford C.J., Hagston W.E. and Bryant F.J., J. Lumin. 5 47 (1972)

[5] Lampert M.A., Phys. Rev. Let. 1 450 (1958)

[6] Haynes J.R., Phys. Rev. Let. 4 361 (1960)

[7] Thomas D.G. and Hopfield J.J., Phys. Rev. 128 2135 (1962)

[8] Halsted R.E., Phys. Chem. II-VI Comp. Chap.8 (N. Holland, Amsterdam 1967)

[9] Khon W., Footnote in Haynes [6]

[10] Hopfield J.J., Proc. Int. Conf. Phys. Semicon. (Dunod Paris 1964) pg. 725

[11] Dean P.J., Prog. Sol. Stat. Chem. 8 1 (1973)

[12] Hagston W.E., J. Lumin. 5 285 (1972)

[13] Williams F.E., J. Lumin. 7 35 (1973)

[14] Thomas D.G., Hopfield J.J. and Augustiniak W.M., Phys. Rev. 140 A202 (1965)

[15] Aten A.C., van Doorn C.L. and Vink A.T., Proc. Int. Conf. Phys. Semicon. (Exeter England 1962) pg. 696

[16] Venghaus H., Simmonds P.E. and Pfister J.C., J. Phys. C 11 3641 (1978)

[17] Venghaus H. and Dean P.J., Phys. Rev. B 21 1596 (1980)

[18] Dean P.J., Venghaus H., Pfister J.C., Scaub B. and Marine J., J. Lumin. 16 363 (1978)

[19] Dean P.J., J. Lumin. 18/19 755 (1979)

[20] Dean P.J. and Venghaus H., Sol. Stat. Comm. 31 897 (1979)

[21] Magnea N., Bensahel D., Pautrat J.L. and Pfister J.C., Phys. Stat. Sol.(B) 94 627 (1979)

[22] Dean P.J., J. Lumin. 21 75 (1979)

[23] Hollis R. and Scott J.F., Sol. Stat. Comm. 21 145 (1977)

[24] Magnea N., Pautrat J.L., Le Si Dang, Romestain R. and Dean P.J., Sol. Stat. Comm. 47 9 (1983)

[25] Le Si Dang, Nahmani A. and Romestain R., Sol. Stat. Comm. 46 743 (1983)

[26] Bittebierre J. and Cox R.T., Phys. Rev. B 34 N$^{O.}$4 (1986)

[27] Dean P.J., Herbert D.C. and Lahee A.M., J. Phys.(C) 13 5071 (1980)

[28] Rodot H., Cryst. Latt. Def. 1 351 (1970)

[29] Larsen T.L., Varotto C.F. and Stevenson D.A., J. Appl. Phys. 43 172 (1972)

[30] Blashkiv V.S. and Gomenyuk A.F., Sov. Phys. Semi. 10 166 (1976)

[31] Blashkiv V.S., Sov. Phys. Semi. 8 662 (1974)

[32] Blashkiv V.S., Sov. Phys. Semi. 8 1467 (1974)

[33] Title R.S., Mandel G. and Morehead F.F., Phys. Rev. 136 A300 (1964)

[34] Iida S., J. Phys. Soc. Jpn. 32 149 (1972)

[35] Era K., Shionoya S. and Washizawa Y., J. Phys. Chem. Sol. 29 1872 (1968)

[36] Nakashima S. and Nakamura A., Sol. Stat. Comm. 38 1289 (1981)

[37] Romestain R. and Magnea N., Sol. Stat. Comm. 32 1201 (1979)

[38] Magnea N., Molva E., Bensahel D. and Romestain R., Phys. Rev. B 22 2983 (1980)

[39] Tews H., Phys. Rev. B 23 587 (1981)

[40] Huang K. and Rhys A., Proc. Roy. Soc. (London) A204 406 (1951)

[41] Pautrat J.L., Francou J.M., Magnea N. and Molva E., J. Crys. Growth 72 194 (1985)

[42] Kernocker R., Lischka K. and Palmetshofer L., Proceedings II-VI Compounds Conference 1987 to be published in J. Crys. Growth.

CHAPTER FOUR

Electrical Characterisation of Defects

Introduction

The presence of imperfections in the crystal lattice in the form of either physical defects or chemical impurities may give rise to defect levels within the forbidden band of a semiconductor. These defect levels may act as carrier (electron or hole) traps. This charge trapping and detrapping is a major influence upon the energy resolution of a semiconductor radiation detector [1].

When trapping is severe only part of the electron-hole cloud will reach the electrodes resulting in a reduction in the pulse height produced by the detector. This deterioration in the response of a device will occur when the mean free drift length, λ, of either charge carrier is reduced to the same order of magnitude as the detector thickness. In ZnTe the device resolution is particularly affected by hole trapping since these carriers possess the smaller mobility and hence the longer transit time when compared with electrons.

The trap depth is an important property of the defect level to determine when considering its potential effect upon device performance. Shallow levels (within about 0.1 eV of any band edge) tend not to hinder charge collection since, at room temperature, carriers trapped at these levels are thermally re-emitted in times shorter than the transit time. However very deep traps (situated approximately mid-gap) are presumed to be responsible for the polarisation effect [2] in semiconductor detectors which is described in Chapter 6.

Thermally stimulated current (TSC) measurements are able to provide information on the activation energy, concentration and capture cross section of traps present in high resistivity material. By carrying out TSC studies on ZnTe it is hoped that traps present in the material may be identified and their possible effects on device performance estimated.

An important property of the charge carriers in ZnTe is their mobility. This is because the mobility governs the drift length of the carriers and if this becomes less than the device dimensions then a degradation in signal occurs. In an attempt to determine the mobilities of electrons and holes in the device material time of flight measurements [3,4] were undertaken. This technique has been widely applied to the measurement of carrier mobilities in high resistivity CdTe radiation detector material [5,6,7,8,9] but less so to high resistivity ZnTe [10]. In all of these cases nuclear radiation (usually α-particles [5,6,7,8,10] or low energy γ-rays [9]) has been employed to generate carriers close to the surface of the specimen which drift through the material under the influence of an externally applied field and are detected at the opposite face.

4.1 Literature Review

Thermally stimulated luminescence (TSL) investigations undertaken on Al, I and In doped ZnTe by Blashkiv et al [11] revealed hole trapping levels at 0.17, 0.19, 0.22 and > 0.4 eV above the Valence Band. These were found to be present irrespective of the dopant and it was therefore suggested that these traps were due to unidentified native defects.

Similar experiments were carried out on ZnTe:In by Iida [12]. He observed the presence of two trapping levels at 0.15 eV - 0.17 eV and 0.18 eV - 0.2 eV which, since the intensities of both TSL peaks increased as the concentration of In increased, he associated with the dopant.

In ZnTe doped with either Al or In Kase [13] observed identical peaks in the electroabsorption spectra of the material. In both lightly doped and undoped material a trap with an activation energy of 0.065 eV was observed. The associated peak was replaced by one due to a trap with an activation energy of 0.139 eV when the doping level was increased. These levels were ascribed to the first and second ionisation levels of the zinc vacancy respectively.

Hall measurements carried out on heavily In doped material by Hoschl et al [10] indicated the presence of an acceptor level at E_V + 0.48 eV. The origin of this level was proposed to be the $(V_{Zn}In_{Zn})'$ complex, however no supporting evidence for this assignment was given. In these studies it was observed that the ZnTe:In crystals were highly electrically resistive and further it was concluded that the mobility of the holes ($\mu_h < 10^{-7}$ $cm^2V^{-1}sec^{-1}$) was too low for device performance.

Larsen et al [14] carried out Hall, photoconductivity and TSC studies on ZnTe:Al. A hole trapping level at E_V + 0.25 eV was observed which was assigned to the $(V_{Zn}Al_{Zn})'$ complex. In addition an electron trap with an activation energy of E_c - 0.1 eV was observed which they suggested as being due to the substitutional Al donor $Al_{Zn}^{\bullet}$. A defect with an activation energy of E_c - 0.2 eV was assigned to the $In_{Zn}^{\bullet}$ donor by Nahory and Fan [15].

DLTS studies on zinc annealed ZnTe by Verity et al [16] yielded values of 0.28 eV, 0.51 eV and 0.59 eV above the Valence Band for hole traps present in the material. The shallowest level was considered as being due to the Au_{Zn} acceptor after comparisons with previously published data [17,18].

In the previous Chapter it was shown that the p-type conductivity observed in undoped material was probably due to the shallow acceptor defects which were introduced by the impurities copper and lithium. In order to compensate these defects and so produce the high resistivity material required for detector operation shallow donors were introduced by doping with the group III elements aluminium and indium. However, from this

literature review it is clear that the use of these dopants will probably introduce acceptor defects of greater ionisation energies than those they are intended to compensate. Thus the expected degree of compensation may not be achieved. Furthermore, polarisation and an increase in the charge carrier trapping time of the defects, either of which will adversely affect device performance, may result if deeper defect levels are introduced into ZnTe.

4.2 Thermally Stimulated Current (TSC) Studies

4.2.1 Principles of the Technique

Consider an excess of carriers injected into a semiconductor (either optically or electrically) at low temperatures so that any carriers trapped at trapping centres will remain there. If the semiconductor is now heated to a sufficiently high temperature in the dark the trapped carriers will be released. In TSC studies these carriers are detected as a transient current, above that of the dark current,when a bias is supplied across the semiconductor. The shape of the TSC curve is related to the position of the trap in the band gap.

4.2.2 Theoretical aspects

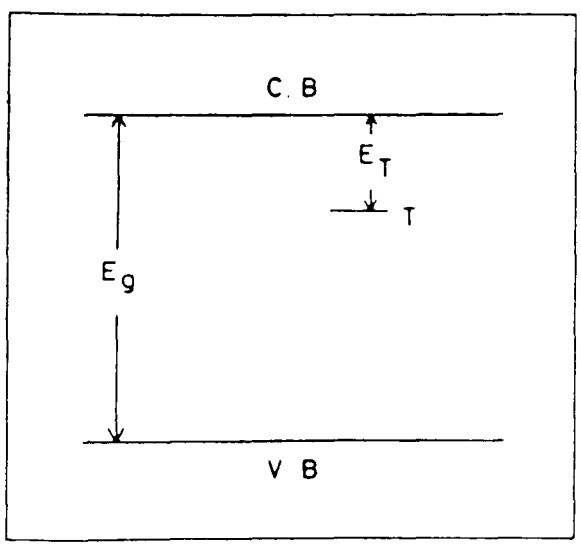

Figure 4.1 Schematic representation of a semiconductor of band gap E_g containing one type of trap, T, at a depth E_T below the conduction band, C.B.

Consider the simple case (figure 4.1) of a homogeneous electrically neutral direct band gap semiconductor containing an electron trapping level, T, of depth E_T.

If the sample is now cooled, minimising intrinsic conduction, and illuminated with radiation of energy greater than the band gap, Eg, carriers will be excited from the valence band to the conduction band and become trapped at T.

After removing the illumination let there be a density, n_o, trapped electrons, and furthermore let the density of electrons in the conduction band be much less than n_o.

4.2.2.1 The Case of No Retrapping

The probability, P, of an electron escaping from the trap to the conduction band is strongly temperature dependent and is given by

$$P = f \exp[-E_T/kT] \qquad (1)$$

where f is the escape frequency factor.

The emission intensity, I, is the rate at which electrons escape

$$I = dn/dt = -n\,P = -n\,f \exp[-E_T/kT] \qquad (2)$$

where n is the density of trapped electrons at time t.

Assuming a constant heating rate, β, then (2) may be re-written as

$$I = \beta\, dn/dT = -n\,P = -n\,f \exp[-E_T/kT] \qquad (3)$$

Thus

$$dn/n = (-f/\beta) \exp[-E_T/kT]\, dT \qquad (4)$$

The variation of n with temperature is found by integrating (4) over the temperature region of interest and is given by

$$n = n_0 \exp[-X] \tag{5}$$

where n_0 is the initial density of trapped electrons and

$$X = (f/\beta) \int_{T_0}^{T} \exp[-E_T/kT]\, dT$$

Combining (3) and (5) the variation of intensity with temperature is given by

$$I = n_0 f \exp[-E_T/kT] \exp[-X] \tag{6}$$

The escape frequency factor is related to the trapping constant, α, as

$$f = \alpha N_C/g \tag{7}$$

where g is the degeneracy factor of the trap and is taken to equal 1 and

N_C is the effective density of states in the conduction band

$$N_C = 2\,(2\pi m_e^* k\, T/h^2)^{3/2} \tag{8}$$

where m_e^* is the effective mass of the electron in the conduction band which is equal to $0.128\ m_e$ for ZnTe (appendix A)

and α is given by

$$\alpha = S_T V_e \tag{9}$$

where S_T is the capture cross-section of the trap and

V_e is the mean thermal velocity of the electron in the conduction band

$$V_e = (3\ k\ T/m_e^*)^{1/2} \tag{10}$$

equation (6) may be re-written as

$$I = C\ n_0\ S_T\ T^2\ \exp[-E_T/kT]\ \exp[-Y] \tag{11}$$

where $C = (3k/m_e^*)^{1/2} \times 2(2\pi km_e^*/h^2)^{3/2} = 1.128 \times 10^{25}\ m^{-2}s^{-1}K^{-2}$ for ZnTe and

$$Y = (C\ S_T/\beta)\int_{T_0}^{T} T^2\ \exp[-E_T/kT]\ dT$$

The current, i, produced by thermally released carriers when a bias V is applied to the semiconductor is given by

$$i = q\frac{A}{t}\mu\ V\ n_c \tag{12}$$

where q is the electronic charge

A is the cross sectional area of the sample

t is the sample thickness

μ the carrier mobility (assumed independent of temperature)

n_c the density of free carriers and is equal to $\tau\, dn/dt$

τ is the free carrier lifetime (assumed to be a constant)

Then, from equation (2), the current is related to I as

$$i = q\frac{A}{t}V\mu\tau\ I \tag{13}$$

This may be written as

$$i = q \frac{A}{t} V \mu\tau C n_O S_T T^2 \exp[-E_T/kT] \exp[-Y] \qquad (14)$$

4.2.2.2 The Case of Retrapping

Consider now the case of the semiconductor containing a density of N electron traps of which a density n are filled at any instant. There will be (N-n) empty traps. The probability that an escaping electron will not be retrapped is

$$n/((N - n) + n) = n/N \qquad (15)$$

The intensity becomes

$$I = (n^2/N) f \exp[-E_T/kT] \qquad (16)$$

warming at a constant rate, β, then

$$n = n_0/(1 + (\frac{-n_0 f}{\beta N} \int \exp[-E_T/kT] dT)) \qquad (17)$$

combining (15) and (16) the variation of intensity with temperature is

$$I = \frac{n_0^2 f \exp[-E_T/kT]}{N(1+([n_0 f/\beta N] \int \exp[-E_T/kT]dT))^2} \qquad (18)$$

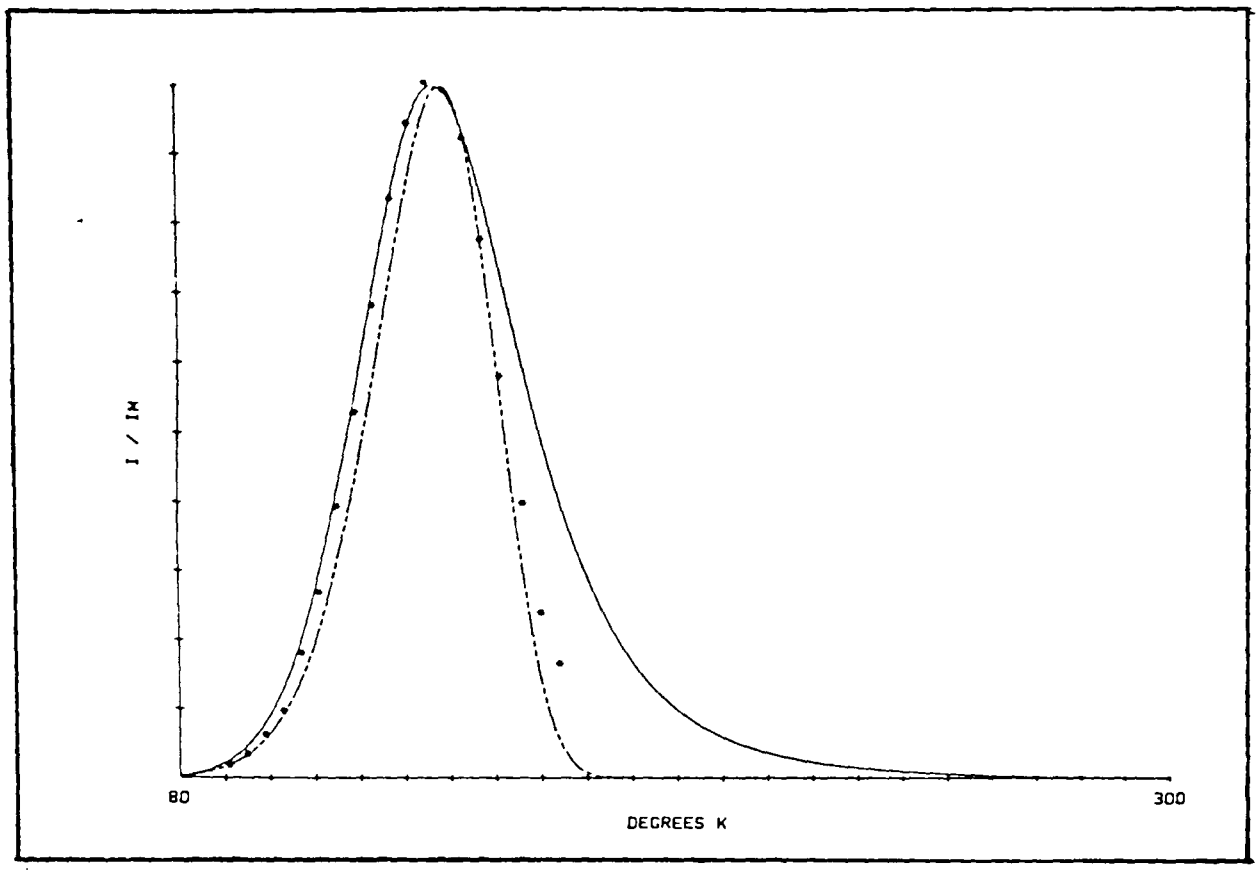

Figure 4.2

A comparison between the theoretical curves, generated from considering the retrapping (————) and the no retrapping (— -·- —) cases, and the experimental points (•) obtained from the sample CPB9 TSC curve.

Using arguments analogous to those presented in the previous section, the current generated by the free carriers is

$$i \approx \frac{q\mu\tau\, Cn_0^2 S_T T^2 \exp[-E_T/kT]\, AV}{t\,(N+[n_0/\beta] \int \exp[-E_T/kT]dT)^2} \qquad (19)$$

For hole traps N_C, m_e^*, V_e is replaced by with N_V, m_h^*, V_h in the equations of the previous two sections. With m_h^* equal to 0.6 x m_e C becomes equal to $1.954 \times 10^{25}\ m^{-2}s^{-1}K^{-2}$.

In order to ascertain which case best describes the experimental form of current variation with temperature the theoretical variations for both the no retrapping and retrapping cases are computed using equations (14) and (19) respectively, and are shown, together with experimental points obtained from the TSC spectrum of CPB9, in figure 4.2.

As can be seen from this the current variation of the experimental curve is best approximated by the case of no retrapping, which shows the more rapid reduction in the high temperature tail of the curve, and therefore further discussions shall be based upon this model.

4.2.3 Methods of Analysis of TSC Data

Using equations similar to those presented in section 4.2.2.1 various authors have, after making simplifying assumptions, presented different methods for the analysis of TSC curves. These methods will be categorised as follows

A) Geometric approximation methods

B) Variation of heating rate methods

C) Other methods

In each category the basic principles will be outlined and a selection of methods presented.

These methods will then be applied to the theoretical curves obtained from the computer solutions of equation (14). The values of trap depths obtained using each method can then be compared with those used in the theoretical computations. In this way the validity of the assumptions made is tested and the most reliable method of determining trap depths obtained.

A Geometric Approximations

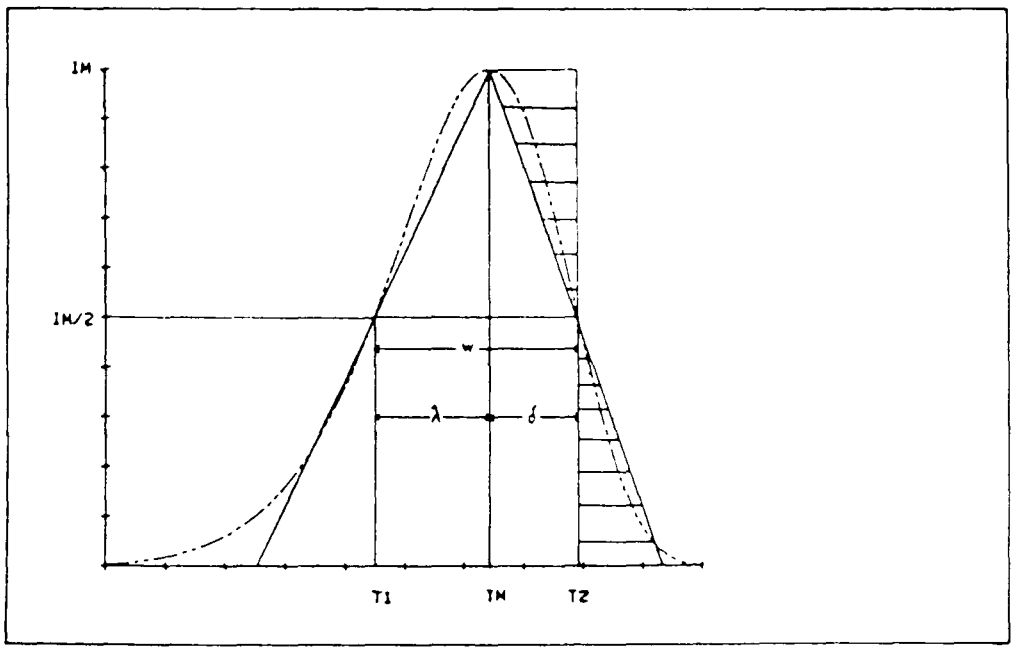

Figure 4.3 General shape of an isolated TSC curve illustrating illustrating some constants defined in the text. The shaded triangles have the same area; a property used in obtaining the approximations.

Figure 4.3 shows the general shape of an isolated TSC curve. From this several parameters used in the derivation of expressions for the trap depth

may be defined

$$W = T_2 - T_1 \; ; \qquad \lambda = T_M - T_1 \; ; \qquad \delta = T_2 - T_M \; ;$$

$$u_g = \delta / W \; ; \qquad \chi = \delta / \lambda \; ; \qquad \Delta = E_T / kT_M$$

As is shown in figure 4.3 the TSC curve may be approximated roughly by a triangle. Using this approximation, an expression for the trap depth may be derived as follows

From equation (2) it can be seen that

$$\frac{\left[\frac{dn}{dT}\right]_{Tm}}{\left[\frac{dn}{dT}\right]_{T_1}} = \frac{n_{Tm} f \exp[-E_T/kT_m]}{n_{T1} f \exp[-E_T/kT_1]} = \frac{n_{Tm}}{n_{T1}} \exp\left[\frac{E_T}{kT_1} - \frac{E_T}{kT_m}\right] \qquad (20)$$

where

$$n_{TM} = \int_{Tm}^{\infty} I \, dT \qquad ; \; n_{T1} = \int_{T_1}^{\infty} I dT \qquad (21)$$

Using the triangle approximation expressions for n_{TM} and n_{T1}, containing only experimentally determined quantities, may be derived as follows:

Since the areas of the two shaded triangles, shown in figure 4.3, are equal then n_{Tm} is given by the area of the rectangle thus:

$$n_{TM} = \delta \, I_M \qquad (22a)$$

also

$$n_{T1} = \frac{I_M \lambda}{4} + \frac{I_M \lambda}{2} + n_{TM} = I_M \left(\delta + \frac{3\lambda}{4} \right) \qquad (22b)$$

By definition the left hand side of equation (20) is equal to 2. Thus

$$E_T = \frac{kT_1T_m}{\lambda} \; Ln(2 + 3\lambda/2\delta) \qquad (23)$$

Similar expressions to that of equation (23) have been deduced by other authors. Some of these are presented below.

Method 1 Luschik [19]

$$E_T = kT_M^2/\delta$$

Method 2 Halperin and Branner 1 [20]

$$E_T = (1.72\ kT_M^2/\lambda)(1 - 5.16/\delta)$$

when $u_g < \exp[-1]x(1 + 2/\delta)$

Method 3 Halperin and Branner 2 [20]

$$E_T = kT_M^2/\lambda$$

when $u_g > \exp[-1]x(1 + 2/\delta)$

Method 4 Chen [21]

$$E_T = 2.8\ \delta\ kT_M^2/W\lambda$$

B Heating Rate Variations

The methods presented in this section are based upon the principle that the shape of a TSC curve due to a particular trapping level varies as the heating rate varies (eqns. 14 and 19). Several authors have deduced methods of calculating trapping parameters based on this principle, all of which involve the measurement of the variations in either the temperature position

of the current maximum or the temperature width at half maximum of each TSC curve produced at each heating rate.

In the subsequent descriptions the following symbols will be used: i_{Mn}:the maximum current ; T_{Mn}:the temperature at which i_{Mn} occurs ; T_{1n}:the lower temperature where $i = 0.5\ i_{Mn}$; β_n:the heating rate of the n^{th} experiment.

Method 5 Hoogstraten, Bube [22,23]

A plot of

$$\mathrm{Ln}(T_{Mn}{}^2/\beta_n) \text{ vs } 1/T_{Mn}$$

will yield a straight line of gradient E_T/k.

Method 6 Haering and Adams [24]

A plot of

$$\mathrm{Ln}(i_{Mn}) \text{ vs } 1/T_{Mn}$$

will yield a straight line of gradient $-E_T/k$.

Method 7 Unger [25]

A plot of

$$\mathrm{Ln}(i_{Mn}) \text{ vs } 1/T_{1n}$$

will yield a straight line of gradient $-E_T/k$.

Method 8 Boiko, Rashba and Trofimenko [26]

A plot of

$$\mathrm{Ln}(\beta_n/T_{Mi}{}^{3.5}) \text{ vs } 1/T_{Mn}$$

will yield a straight line of gradient $-E_T/k$.

This is an extension of the method of Schon [9].

C Other Methods

Method 9 Grossweiner [27]

This expression is similar to those using the triangle approximation however this is derived by integrating equation (21).

$$E_T = 1.51\ kT_M T_1/\lambda$$

Method 10 Sandomirskii and Zhdan [28]

This is the Grossweiner formula corrected with the aid of computer calculations.

$$E_T = (1.455\ kT_M T_1/\lambda) - 0.79\ kT_1$$

Method 11 Garlick and Gibson [29]

This method uses the approximation that in the initial rise of the TSC current the exponential integral factor in equation (14) may be ignored. Then a plot of

$$\mathrm{Ln}(i/T^2) \text{ vs } 1/T$$

will yield a straight line of slope $-E_T/k$.

In practice, however, the region of the initial rise is rather arbitrary. In the next section the calculations were made in the regions between:

0.75% and 20% ; 0.75% and 40% ; 0.75% and 60%; of i_M.

4.2.3.1. Reliability of Methods

In order to test the reliability of the methods presented above equation (14) is solved numerically to generate a TSC curve assuming a certain trap depth, E_T. Each of the above methods is then applied to the generated TSC curves and the value of the trap depth obtained compared with the value, E_T, used to generate that particular curve.

The values of the relevant parameters used to generate the theoretical curves are:

$$\mu\tau = 1 \times 10^{-8}\ m^2\ V^{-1}$$

$$V = 10\ V$$

$$E_T = 0.1,\ 0.2\ eV$$

$$n_0 = 5 \times 10^{22}\ m^{-3}$$

$$S_T = 5 \times 10^{-24}\ m^2$$

$$\beta = 0.5,\ 0.75,\ 1,\ 1.5,\ 2\ Ks^{-1}$$

$$v = 2 \times 10^{-8}\ m^3$$

$$t = 2 \times 10^{-3}\ m$$

METHOD	TRAP DEPTH	
	0.1 eV	0.2 eV
1	0.126	0.249
2	--	--
3	0.126	0.229
4	0.118	0.230
5	0.120	0.229
6	0.122	0.234
7	0.115	0.260
8	0.104	0.202
9	0.127	0.259
10	0.118	0.236
11/20	0.098	0.196
11/40	0.097	0.193
11/60	0.096	0.190

Table 4.1 Values of trap depths calculated from the various methods when applied to theoretical curves. Energies quoted from methods 1,3,4,9,10 are the average values of those obtained using each heating rate. Method 2 is not applicable.

Table 4.1 shows the values of the trap depth (in eV) that were obtained from calculations using the various methods previously described. The most obvious result shown here is the unreliability of any geometrical approximation technique (methods 1-4, 9, 10). Of the types of analyses that use heating rate variations of peak position and TSC peak shape the method of Boiko et al [26] (method 8) leads to a value of the trap depth that is within 5% of the theoretical value.

The initial rise method of Garlick and Gibson [29] (method 11) is also seen to be accurate to within 5%, even when the 'initial' rise is 60% of the maximum. This technique has been chosen over that of Boiko et al as the method of analysis of the TSC data presented in this Chapter for a number of reasons. The main reason being that only one temperature scan is required to provide all the information required compared with at least four scans at different heating rates for the Boiko method. Even in the case when retrapping is present the Garlick and Gibson plot of $\ln(i/T^2)$ / $1/T$ may be used to obtain the trap depth since the denominator in the equation developed (eqn.19) to describe this case reduces to N for the initial rise.

As was previously shown, in Section 4.2.2, the better theoretical approximation to the experimental data is obtained by using the no retrapping description (eqn.14).

Fig. 4.4

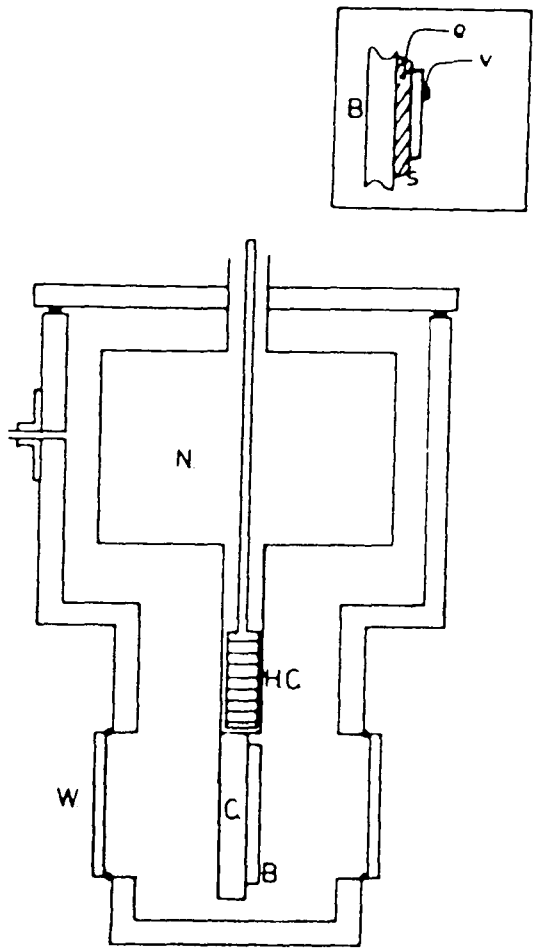

Figure 4.4

The TSC cryostat.

The insert shows the sample mounting arrangement

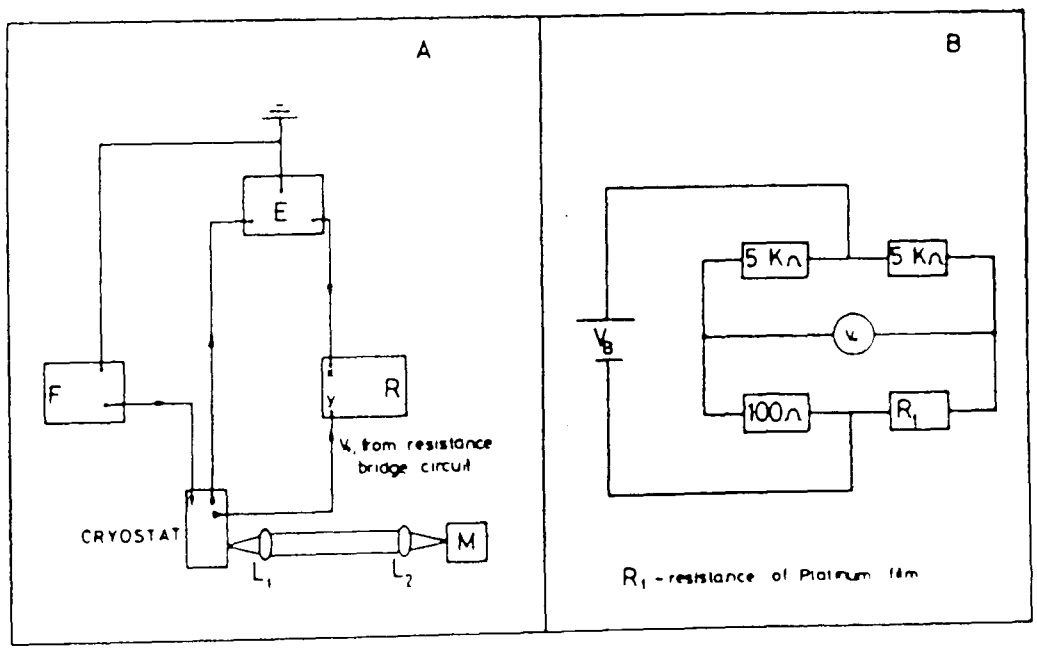

Figures 4.5

(A) The experimental arrangement for the detection of TSC.

(B) The bridge circuit used in temperature measurement.

4.2.4 Experimental Technique

4.2.4.1 Equipment

The cryostat used for this purpose is shown in fig 4.4 and comprises a machined aluminium body into which a stainless steel nitrogen can (N) and cold finger is placed. A heater coil (HC) can be inserted into the cold finger. The sample is mounted, together with a platinum film resistance thermometer (type RS 158-238), on a beryllia plate (B) with silver paste. The plate itself is attached to the copper block (C), again by silver paste. This arrangement ensures good thermal conduction and electrical insulation between the sample and the cryostat. Contacts were formed on the sample with silver paste. The windows (W) are made of infrasil, allowing radiation of up to 2 um to be incident upon the sample without strong absorption.

The experimental arrangement for the detection of the TSC is shown in fig 4.5(a). Illumination, provided by a Wotan 200W high pressure mercury lamp (M) and a W18b Wratten filter, is focused through the lenses (L_1 and L_2) onto the sample. A sample bias (V_s) of up to 30 V is provided by a Farnell constant power supply (F). The current passing through the sample is monitored by a Keithley 610C electrometer (E), the output of which is taken into the X-input of a Gould Advance HR 2000 XY recorder (R). The Y input is provided by the potential difference developed across the platinum film resistor bridge circuit (B). Figure 4.5(b) gives a schematic representation of this circuit. The two bridge resistors are high precision, wire wound, resistons the values of which were chosen so that when the voltage (V_B) was applied a change in the potential difference V_o of 1 mV was produced when a temperature change of 1 K occurred in the platinum film resistor. Both this potential difference (V_o) and the bias voltage (V_s) are monitored using a Thurlby digital multimeter (DVM). The constant heating rate is provided by passing a current of 1 amp through a Kanthal wire-wound

heater coil.

4.2.4.2 Method

The sample is cooled to 77 K and illuminated, under bias, for a period of 30 minutes to ensure saturation filling of the traps. It is then heated at a constant rate, in the dark, and the resulting TSC spectrum recorded. In order to deduce whether the carriers that are released from a trap are electrons or holes the bias is then reversed and the procedure repeated.

This identification is based on the principle that electron-hole pairs are created very close to the surface when the sample is illuminated with radiation which is greater in energy than the band gap. Thus if the sample is illuminated through the positive electrode holes will be repelled and swept through the bulk and hole traps will be filled. Conversely if the negative electrode was irradiated then electron traps become filled. By monitoring the TSC peak intensities as the top electrode is irradiated under a positive then a negative bias the type of carrier trap can be identified.

The trap parameters are determined using the initial rise method (Section 4.2.3:-method 11). However in the cases where the initial rise is masked by a nearby peak the procedure of thermal cleaning is followed [30]. This involves the trap filling previously described but the sample is only warmed until the lower temperature peak maximum is reached and is then immediately recooled to 77 K. This leaves the initial rise of the higher temperature curve free for analysis.

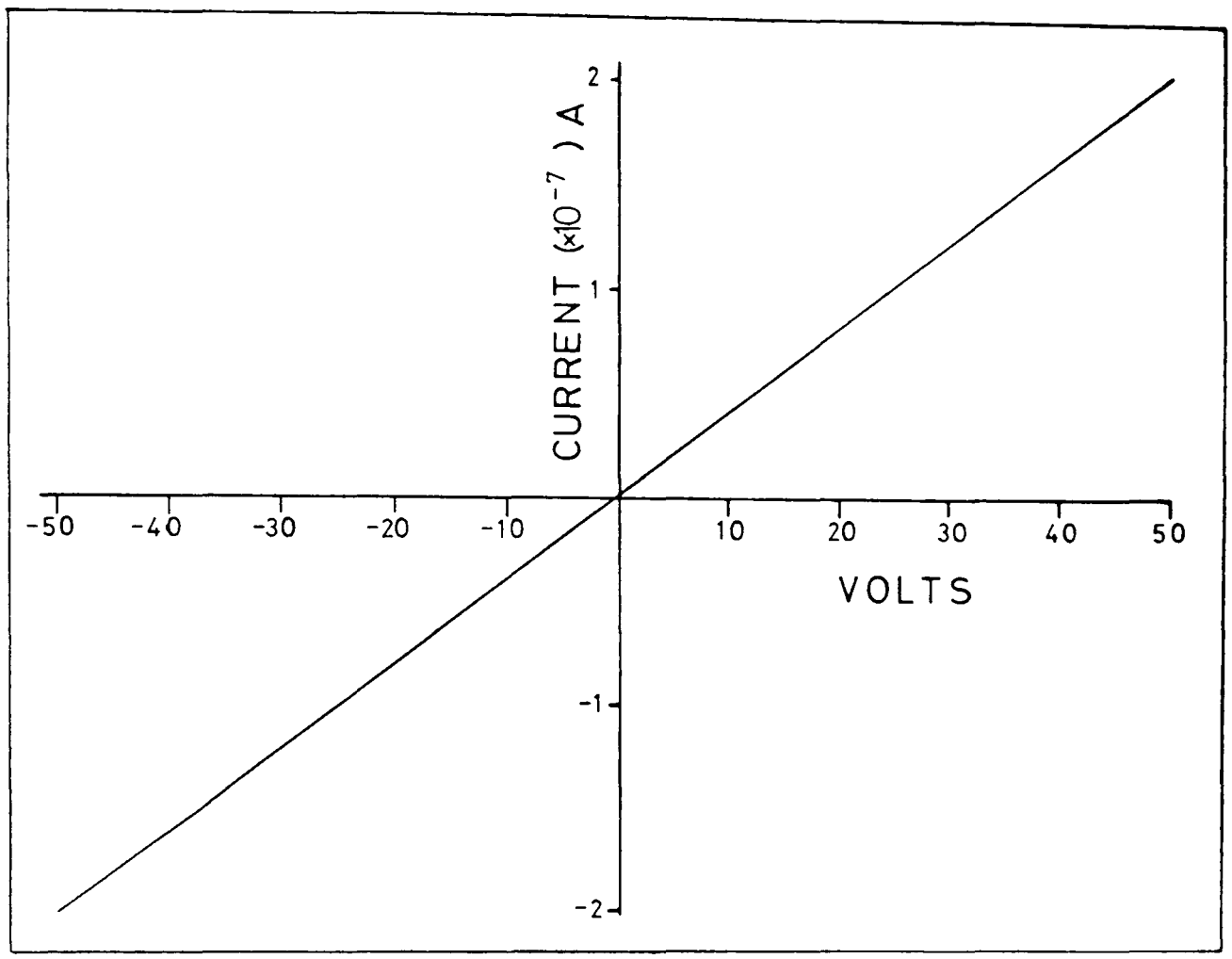

Figure 4.6

I - V characteristics of Ag paste contacts on a sample taken from the indium doped boule CPB4.

Figures 4.7

These show TSC spectra obtained from boules doped with 20,30 and 40 p.p.m indium. The solid curve in each figure represent the TSC spectrum obtained when the positive contact was illuminated and the broken curve represent the TSC spectrum obtained when the negative electrode was illuminated. The inserts show a plot of $Ln(i/t^2)$ against 1/T for the 'initial rise' of each TSC peak after the dark current was subtracted.

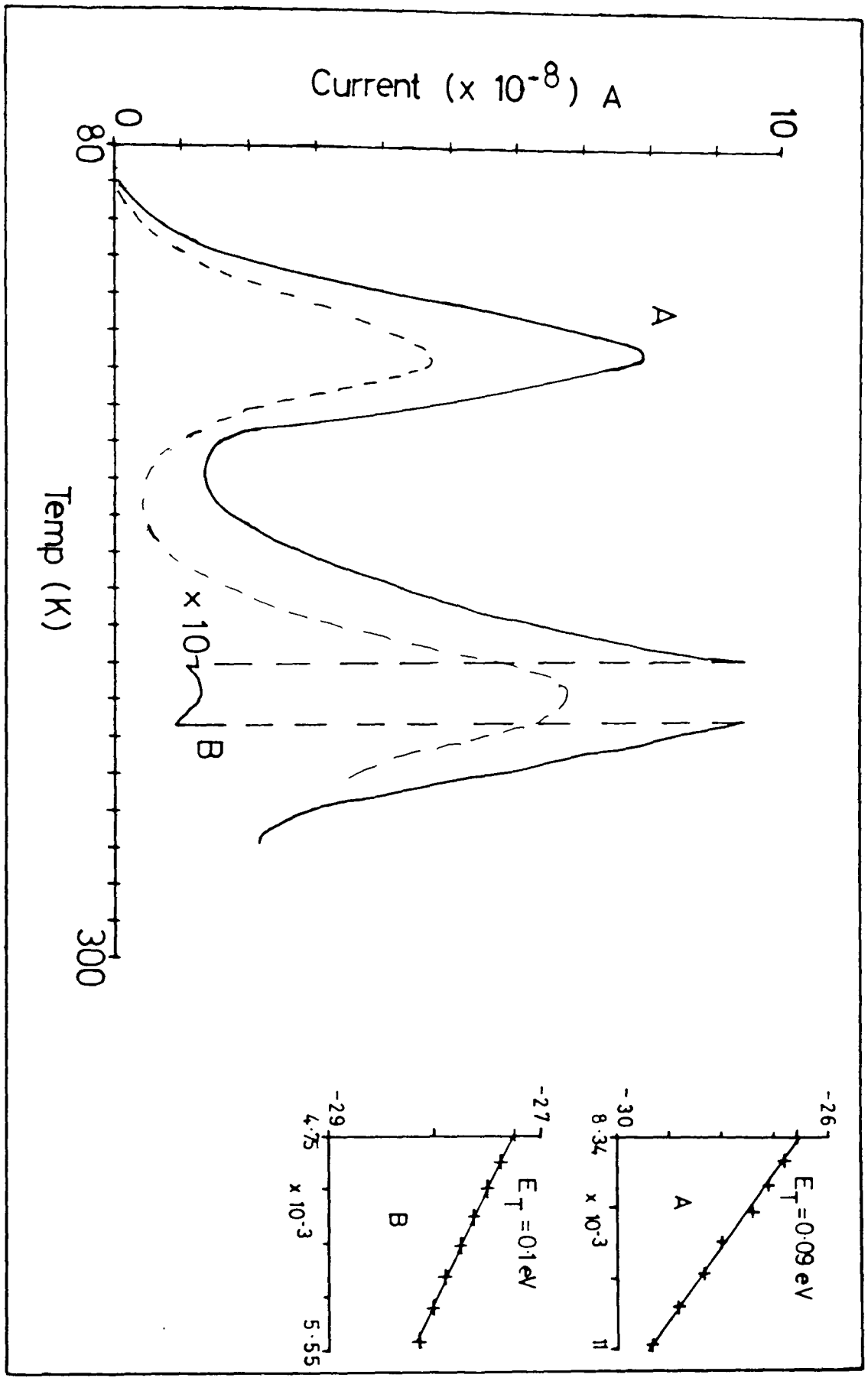

Figure 4.7(a)

TSC spectrum obtained from boule CPB3

doped with 20 p.p.m indium.

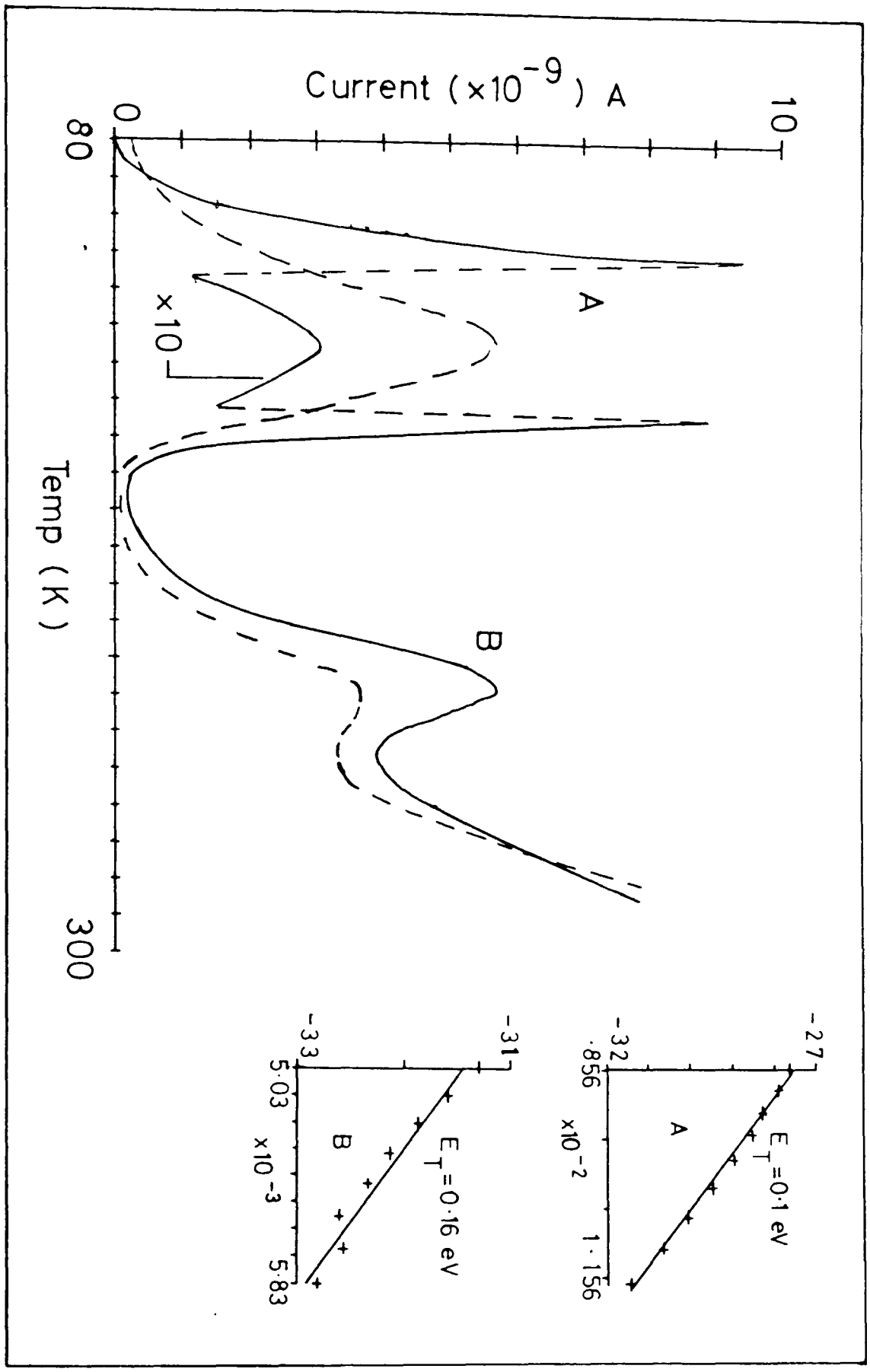

Figure 4.7(b)

TSC spectrum obtained from boule CPB4

doped with 30 p.p.m indium.

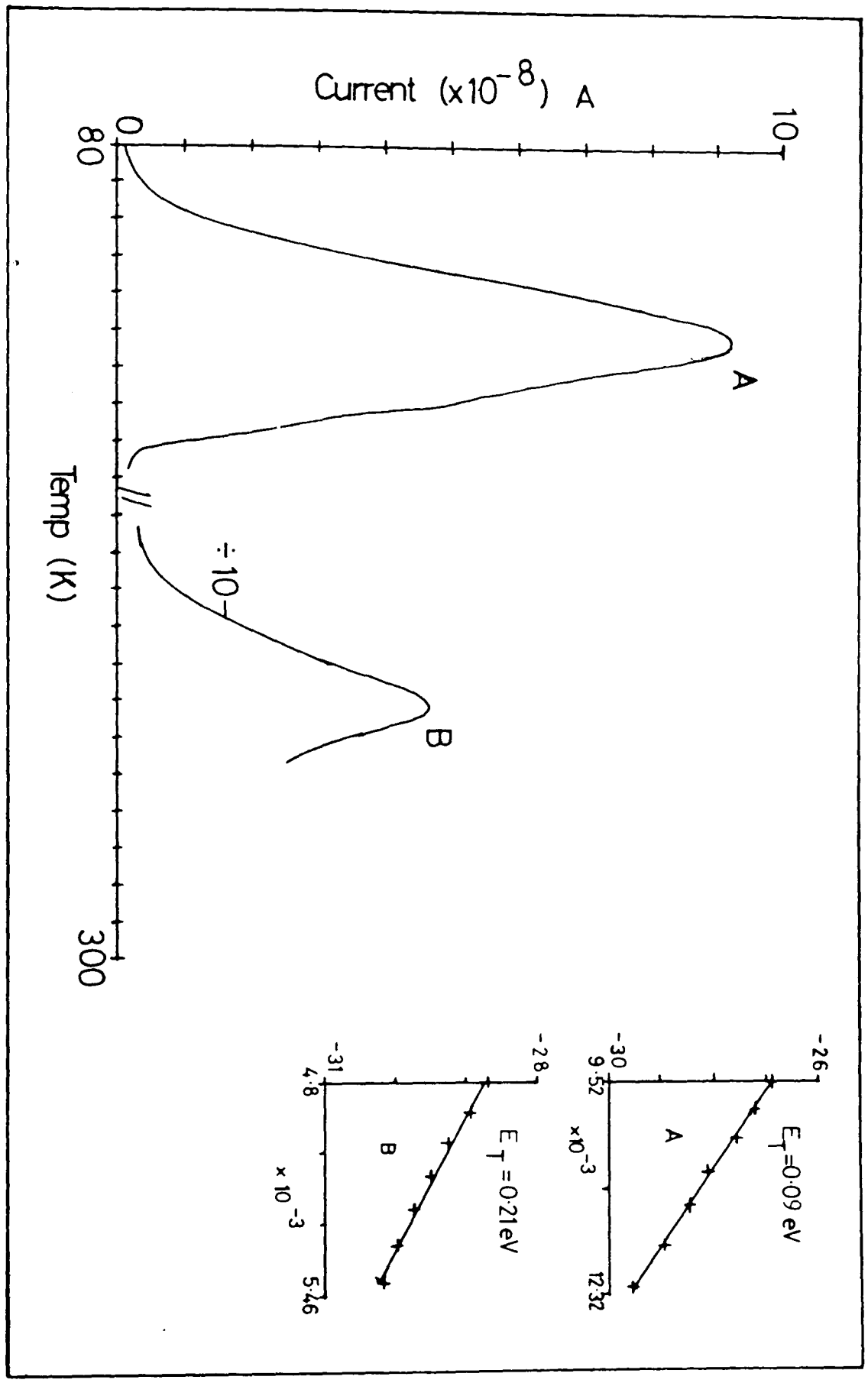

Figure 4.7(c)

TSC spectrum obtained from boule CPB5

doped with 40 p.p.m indium.

4.2.5 Results and Discussion

The I-V characteristics of ZnTe samples which have been contacted with silver paste are shown in figure 4.6 and indicate that such contacts are ohmic when formed on ZnTe. In the following experiments silver paste was therefore always used for ohmic contacts onto the material.

4.2.5.1 ZnTe : In

Figures 4.7 show representative TSC spectra obtained from samples cleaved from boules grown with 20,30,40 ppm In (CPB3,CPB4,CPB5) as dopant. In all samples studied the spectra comprised only two peaks.

The trap parameters for the peaks observed in In doped material, together with the concentration of dopant atoms, are presented in Table 4.2. As can be seen from table 4.2 a trap with an activation energy of around E_V + 0.09 eV was observed in all indium doped material showing TSC. In addition to this trap only one other trap, in each of the samples, has been detected, although the activation energy of this trap has been found to vary even between samples taken from the same boule. Five different activation energies have been measured for the second trap and therefore it is concluded that six different traps have been detected in ZnTe:In. These possess activation energies of 0.09 eV, 0.1 eV, 0.16 eV, 0.21 eV, 0.30 eV and 0.38 eV. The effects on the intensities of the TSC from traps present in CPB3 and CPB4 when the positive and negative electrodes (broken curves) were illuminated in turn with above band gap radiation are shown in figures 4.7a and b. Similar results were also obtained from samples taken from CPB5 and from these observations it is apparent that all trapping centres found in the TSC experiments act as hole traps.

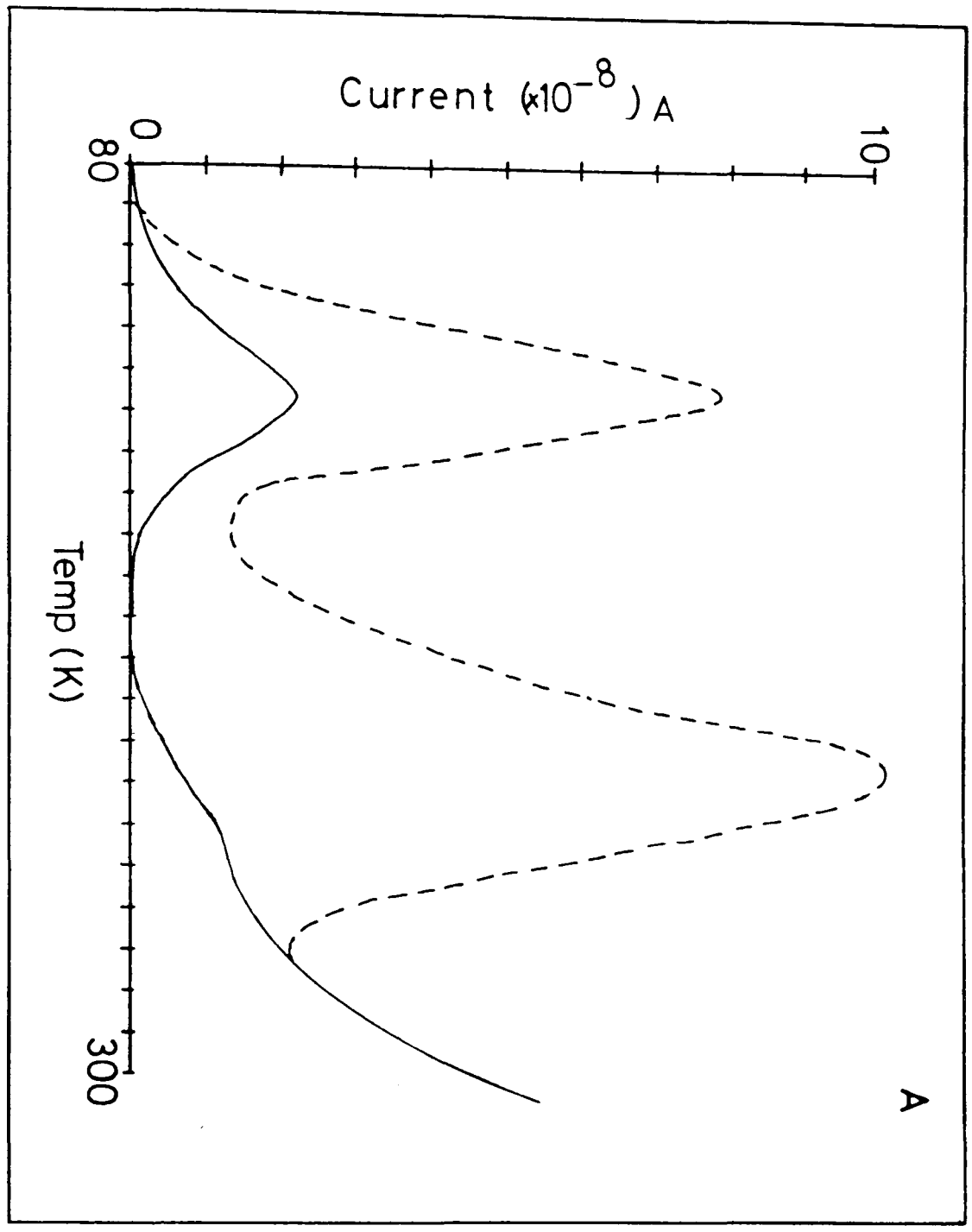

Figure 4.8(A)

The effects of additional indium diffusion on a sample taken from CPB3. The broken curve represents the TSC spectrum after the diffusion.

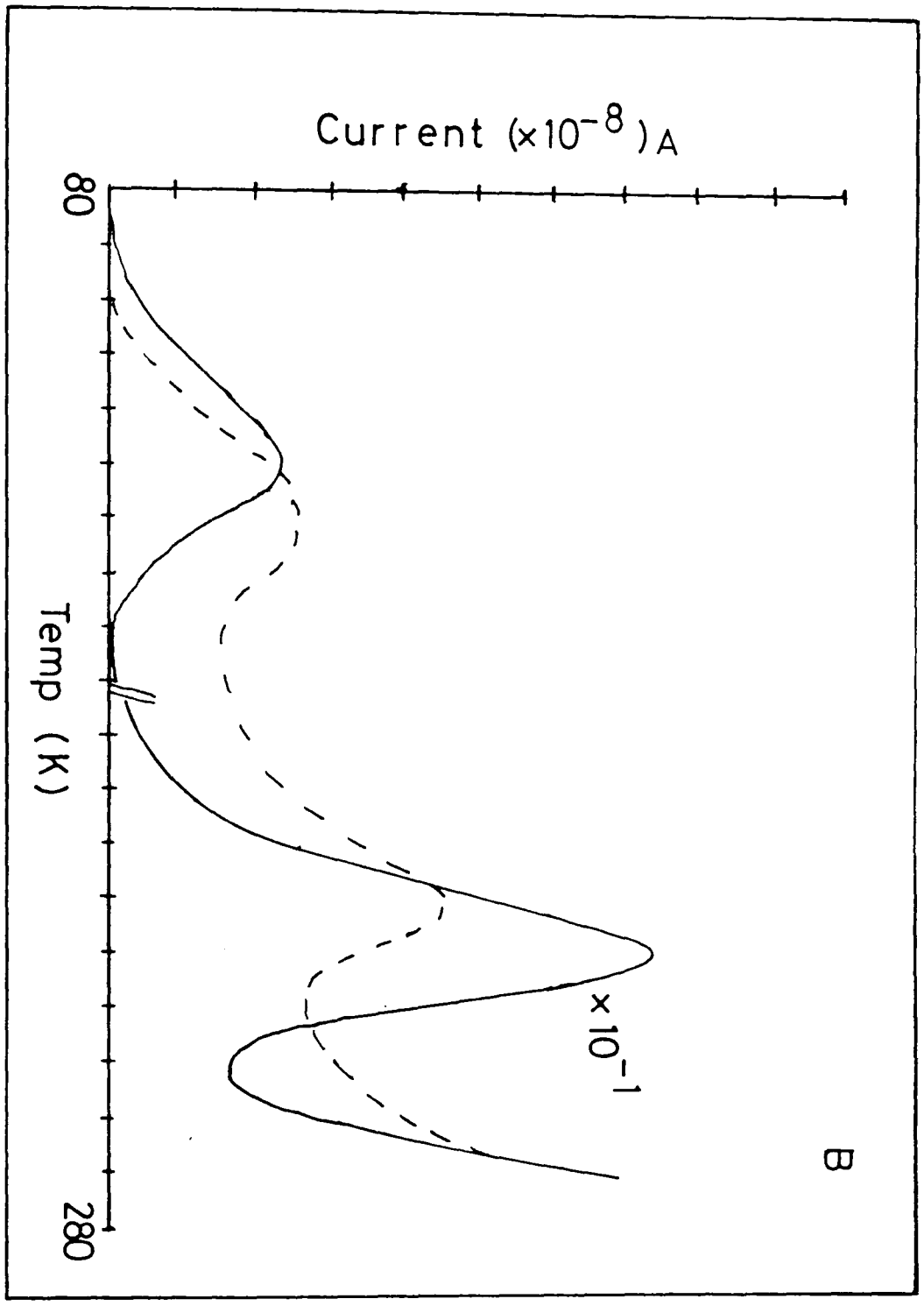

Figure 4.8(B)

The efects of additional indium duffusion on a sample taken from CPB4. the broken curve represents the TSC spectrum after the diffusion.

Diffusion of additional In into samples from CPB3 and CPB4 was achieved by evaporating a layer of indium onto the surface of the samples and then annealing the samples in vacuum at a temperature of 250 ^{o}C for two hours. The effects of the diffusion of additional indium into samples from CPB3 and CPB4 on the TSC spectra are shown in figures 4.8 (a),(b) respectively. The additional indium caused an increase in intensity of the TSC curves associated with the traps in the material.

4.2.5.2 ZnTe : Al

Of the three boules (CPB7,CPB8,CPB9) grown with Al as the dopant only samples cleaved from CPB9 showed current peaks in their TSC spectra. The resistivity of material from the other aluminium doped boules was less than that of CPB9. This results in a higher dark current in samples from CPB7 and CPB8. The lack of any TSC peaks in spectra from these samples does not indicate an absence of trapping levels but shows only that the number of carriers released from traps at any temperature is much less than the number of intrinsic carriers and therefore contribute little to the total current. Material taken from CPB7 and CPB8 may infact have a lower concentration of deep traps (an advantage for devices) but they do have a lower resistivity (a disadvantage for devices) and therefore a lack of TSC peaks does not indicate that devices fabricated from this material will perform better than those fabricated from CPB9.

Figure 4.9 shows the TSC spectrum obtained from CPB9 which shows only one peak. The trap producing this has a depth of 0.13 $\pm$ 0.03 eV.

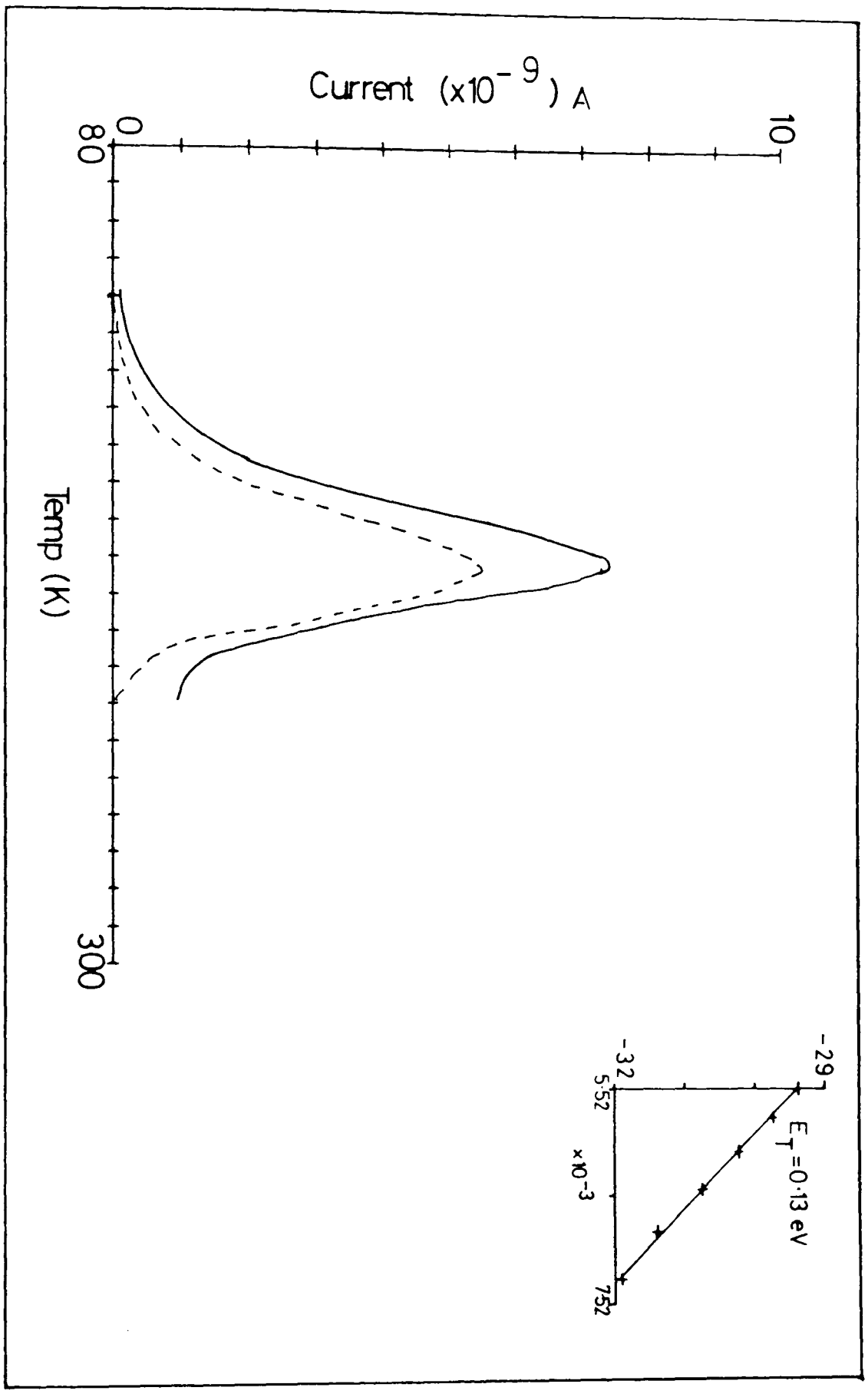

Figure 4.9

TSC spectrum obtained from boule CPB9

doped with 100 p.p.m aluminium.

BOULE N^{O}.	E_T (eV)
	0.09 ± 0.03
CPB3	0.1 ± 0.01
(20 ppm In)	0.16 ± 0.07
	0.1 ± 0.02
CPB4	0.16 ± 0.08
(30 ppm In)	0.38 ± 0.05
	0.09 ± 0.03
CPB5	0.21 ± 0.04
(40 ppm In)	0.30 ± 0.06
CPB9	0.13 ± 0.03
(100 ppm Al)	

Table 4.2 Summary of trapping parameters of those defects observed in TSC studies.

Selective filling of the trap, by illumination of either the positive or negative electrode, indicates that this trap, present in CPB9, also acts as a hole trap (broken curve fig. 4.9). TSC investigations on samples into which additional Al had been diffused proved unsuccessful as the resistivity of the samples then dropped to too low a value. However aluminium was found to be present in this material in concentrations of around 30 ppm by weight (Mass Spectrograph analysis presented in Chapter 2), resulting in a concentration of about 4×10^{18} atoms cm^{-3}.

The defect that produces a trapping level at $E_V + 0.09$ eV in the indium doped material and the defect that produces the trapping level at $E_V + 0.13$ eV in the aluminium doped material may be of a similar origin as they have similar activation energies and capture cross sections. In both cases the defect has been shown to act as a hole trap and, in the cases of indium doped samples, the concentration of the defect responsible for the level has been shown to depend on the doping concentration. This correlation in aluminium doped material could not be verified as the resistance of the samples dropped to too low a value for TSC measurements to be employed. In all cases the concentrations of these traps have been sufficiently small so as to be accountable for by the concentrations of the dopant atoms found in the materials.

Alternatively as this level has been observed in all samples showing TSC spectra then the defect responsible may not be the dopant atom but may be a native defect. However it is then difficult to explain why the addition

of a donor species, such as indium or aluminium, would increase the acceptor concentration. It is more likely then that the defects are dopant related and that the level, in both the Al and In doping cases, is due to a similar acceptor complex. In the Al doped material the most obvious acceptor complex involving the dopant is the A-centre $(Al_{Zn}V_{Zn})'$. Indeed evidence for it's existence has been presented in the previous chapter where, from measurements on the zero-phonon luminescent emission, the depth of the centre is calculated to be $E_v + 0.22 \pm 0.02$ eV. Indium, also a group III element, may be expected to form an isomorphic defect. However no photoluminescence band associated with this centre has been observed in these studies although the $In_{Zn}V_{Zn}'$ centre has been reported by several authors [12,31,32] as being involved in the 1.6 eV luminescence band observed in ZnTe heavily doped with indium.

If the A-centre model is correct then there is an apparent discrepancy in the depth of the trap deduced from optical and thermal data. Such a discrepancy may be due the effects of electron - lattice coupling, the effects of which may be more easily visualised with the aid of a configurational coordinate diagram (CCD) [33].

Such a diagram is shown in figure 4.10 for an A-centre. Here A^o represent the A-centre which is neutrally charged with respect to the lattice and A^- the A-centre when it has captured an electron. The configurational coordinate, Q, represents a distortion in the local crystal lattice due to the change in energy of the centre.

The lowest curve represents the energy of the A^- centre in its ground state whilst the uppermost curve is the A^- excited state after photoexcitation of a free electron-hole pair. This curve is centred about Q=0 since the creation of a free hole and electron changes the energy of the entire lattice. The vertical distance between the minima of these curves is the band gap energy, E_g. The A^o centre is formed by the capture of a hole

from the valence band and following this capture the centre relaxes to a new equilibrium configuration, the energy of which is represented by the curve centred at Q > 0. The hole is localised at the A-centre and thus the energy of this new system is unable to be dissipated in the entire crystal, leading to a local (probably nearest neighbour) lattice distortion and a change in Q coordinate. The two dashed curves represent the energies of the system after electron capture by a shallow donor (the donor electron is highly delocalised and therefore the energy change of the donor system is given to the entire lattice).

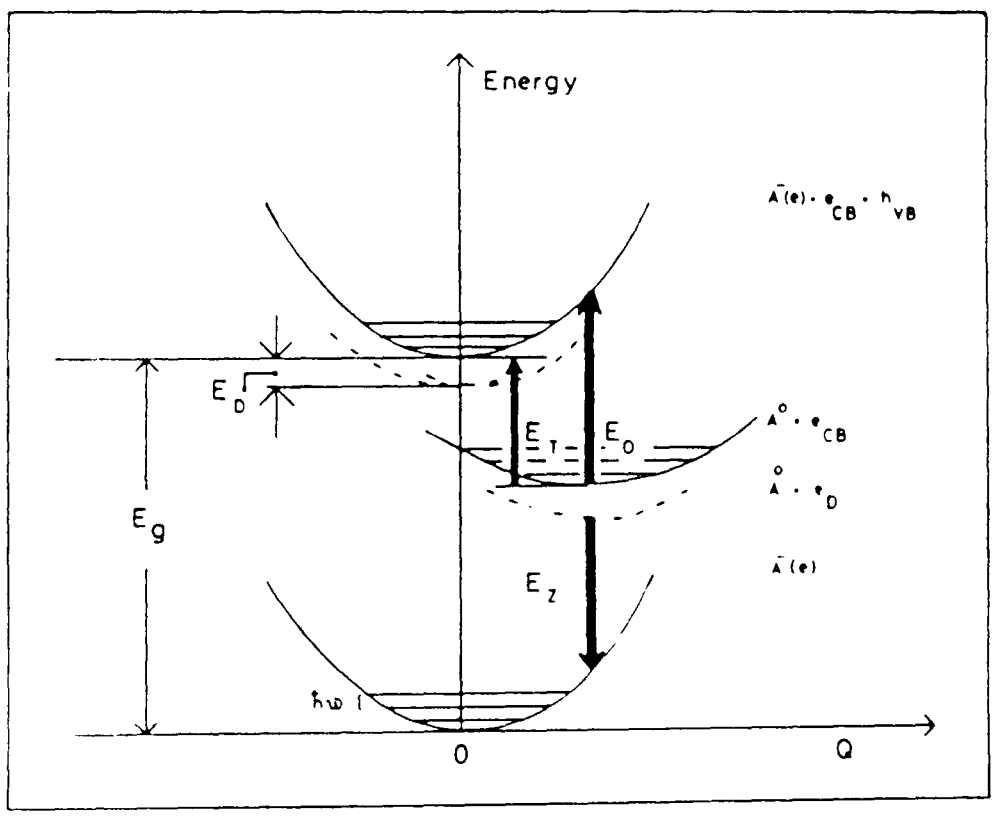

Figure 4.10 The Configurational Coordinate Diagram (CCD) representing a DAP system. The horizontal lines represent the quantised vibrational levels. E_O, E_T, E_D represent the optical and thermal depths of the acceptor and the depth of the donor respectively.

As optical transitions occur in times shorter than that required to allow the system to relax to it's new equilibrium position they are represented on the CCD by vertical transitions. Thus E_z in figure 4.10 represents the energy given up in the zero phonon DAP self activated emission observed in the photoluminescence studies on ZnTe:Al presented in Chapter Three. If E_D is the energy of the donor then the value of E_o, the optical depth of the A-centre, is:

$$E_g - E_D - E_z \qquad (24)$$

This value represents E_A calculated neglecting any Coulomb interactions between the neutral donor and acceptor after recombination.

Thermal transitions occur in times that allow lattice relaxation and therefore the thermal depth, E_T, of the A-centre is the energy difference of the minima of the $A^o + e_{CB}$ and the $A^- + e_{CB} + h_{VB}$ bands. If lattice relaxation occurs when an electron is trapped then, as indicated in figure 4.10, there will always exist an energy difference between the optically and thermally deduced trap depths with $E_o > E_T$.

The vibrational levels of each state are not continuous but are quantised into discrete vibrational levels (represented as horizontal lines in the CCD) of energies, E_n, such that

$$E_n = (n + 1/2)\, \hbar\omega \qquad (25)$$

where $\hbar\omega$ is the energy of a lattice phonon.

The energy difference between E_o and E_T may be described in terms of this lattice phonon as

$$E_o - E_T = S\, \hbar\omega \qquad (26)$$

S is the Huang-Rhys factor [34], a dimensionless quantity that indicates the

degree of phonon coupling of the centre to the lattice. Substituting the values of

$$E_o = 0.22 \pm 0.02 \text{ eV (Al zero phonon measurement Chapter 3)}$$

$$E_T = 0.13 \pm 0.03 \text{ eV (this Chapter)}$$

$$\hbar\omega = 0.026 \text{ eV (LO phonon energy)}$$

into equation (26) then $2 < S < 5$.

This should be compared with a value of 1.5 obtained from the optical data on the aluminium A-centre presented in Section 3.4.2 of Chapter 3. Both values of S indicate a weak coupling of the centre to the lattice and therefore the photoluminescence and TSC could involve the same centre.

Blashkiv [11] observed the presence of two hole trapping levels in ZnTe doped with group III and VII elements which were present irrespective of the dopant and as a consequence were assigned to unidentified native defects. The activation energies of these defects were observed to vary from sample to sample and were 0. 17, 0.19, 0.22 and 0.4 eV. The second hole trapping level that is observed in each indium doped sample in this study also has an activation energy that is seen to vary from sample to sample. Activation energies of 0.1, 0.16, 0.21, 0.3 and 0.38 eV have been recorded, three of which (0.16, 0.21, 0.38 eV) are in agreement with those observed by Blashkiv. As the results of this study show these defects have also been found to vary from sample to sample and therefore probably involve native impurities. However it has also been observed in these studies that the concentrations of these defects increase after diffusion of additional indium into the samples. In order to reconcile the involvement of both indium and a native impurity in the formation of these traps it is suggested that indium forms a complex with the native impurity to produce the observed defects.

4.3 Mobility Measurements in Doped ZnTe Using The Time of Flight Technique

Carrier mobility is an important property of the material in terms of its suitability for device fabrication. Although the Hall Effect is generally used to determine carrier mobility it cannot be used in this case as the current produced in the high resistivity samples is too low and so time of flight measurements were attempted.

Time of flight measurements involve the determination of the time taken for charge carriers generated close to one surface of the sample to traverse that sample under the influence of an electric field. The carriers can be generated in one of a number of ways: by nuclear radiation [5-10]; by a pulsed electron beam [3] or by a pulsed light source [3]. The last method is employed in the studies presented here primarily because of the availability of a source of narrow pulse excitation from a N_2 laser.

The sample to be studied is fitted with electrodes on two opposite faces and charge carriers generated near the top electrode by a fast excitation pulse. Carriers of one type (depending on the polarity of the top electrode) are drawn across the specimen under the influence of a steady external electric field . The transit time, T_t, of these carriers is able to be determined from the shape of the observed current transient (unless severe trapping occurs) and from this the drift mobility, μ, can be deduced. The mobility serves as an indication as to the suitability of the material for detector fabrication.

Since this technique has been widely discussed elsewhere and as it has not proved possible to deduce transit times from the present data the experimental method and data analysis will be outlined only briefly. For more detailed descriptions of these the reader is referred to the paper by Spear [3] and that by Canali et al [4] and the references therein.

4.3.1 Experimental Method

The experimental arrangement for the production of the sheet of charge and the detection of the transient current it produces is shown in figure 4.11.

The excitation source is a Lambda Physics pulsed N_2 laser which is capable of delivering a pulse of 337 nm radiation of 6 ns duration. The average power in the beam is 200 mW but the peak intensity is of the order of 700 kW. The change in voltage, Δ V, developed across the resistor, R, as the transient current flows is detected using a Tektronics 466 storage scope, S. The rise time of this electronic system is 3.5 ns and therefore it should be possible to measure transit times of the order of tens of nano seconds using this experimental arrangement.

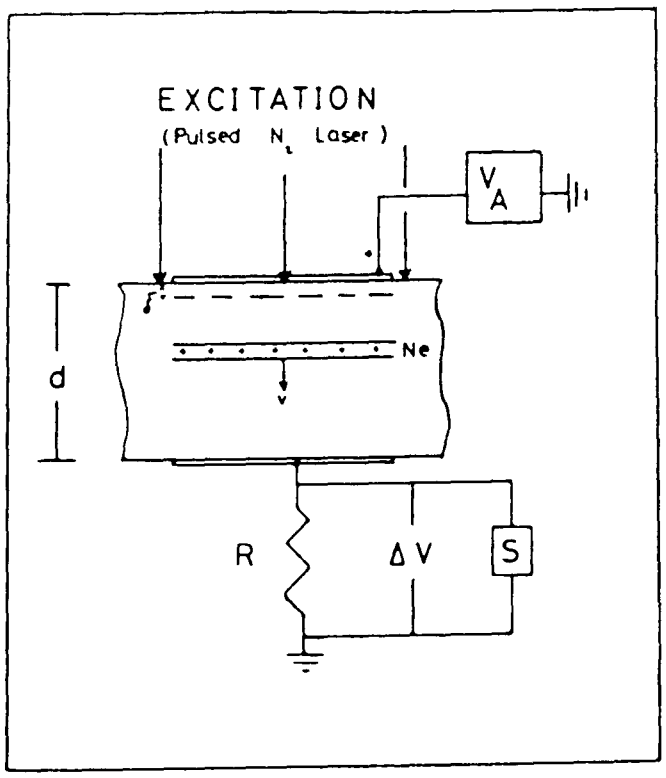

Figure 4.11 Experimental arrangement for transit time measurements.

4.3.2 The Current Waveform

Assuming that the electric field is uniform and constant and that the any trapping centres are distributed uniformly throughout the specimen volume then the current produced by the movement of the photo-generated carriers can be described by

$$i(t) = Nqv / d = N q / T_t \qquad (27)$$

where N is the number of carriers which escape recombination inside the penetration depth, δ (determined from optical absorption experiments to be between 50 and 150 μm), and v is the drift velocity of the carriers.

The change in voltage developed across the resistor will then be

$$\Delta V = RNq / T_t \qquad (28)$$

In this case the shape of the waveform viewed on the scope will be similar to that depicted by the broken line in figure 4.12a.
If the generated carriers are trapped (without detrapping) and the mean free time, τ^+, of the carriers is comparable to the transit time T_t then the modified current pulse may be described by

$$i(t) = (Nq \exp(-t/\tau^+)) / T_t \qquad (29)$$

where τ^+ is given by

$$\tau^+ = 1 / N_T S_T V_e \qquad (30)$$

N_T, S_T and V_e have their usual meanings

The shape of this transient is represented by the solid curve of figure 4.12a.

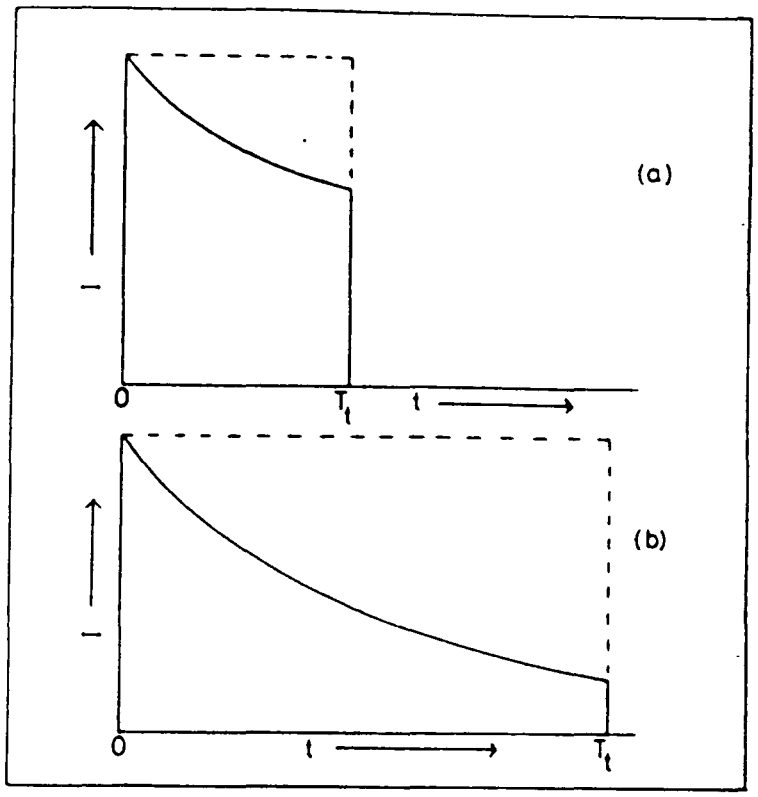

Figure 4.12 Theoretical current waveforms.
(a)--- no trapping;
—— trapping but no detrapping.
(b) —— trapping but with detrapping.

If the carriers are trapped and detrapped in times shorter than the transit time the current waveform will have the shape represented by the solid curve in figure 4.12b. If this process is severe then the tail of the exponential decay may be lost in the noise and in such cases no transit times can be measured.

When T_t has been found the carrier mobility is simply calculated using

$$\mu = d / (\mathcal{E} T_t) \qquad (31)$$

where $\mathcal{E}$ is the applied field and is V_A/d

Although it was not possible to deduce charge carrier transit times in the material in the present experiments the shape of the waveform can still

Figures 4.13

The shape of the current transients obtained from a sample of indium doped material (CPB4) when the top contact was:

(A) Positive

(B) Negative

In both cases the horizontal scale is 50 μ sec /division and the vertical scale is 10 mV/division.

(A)

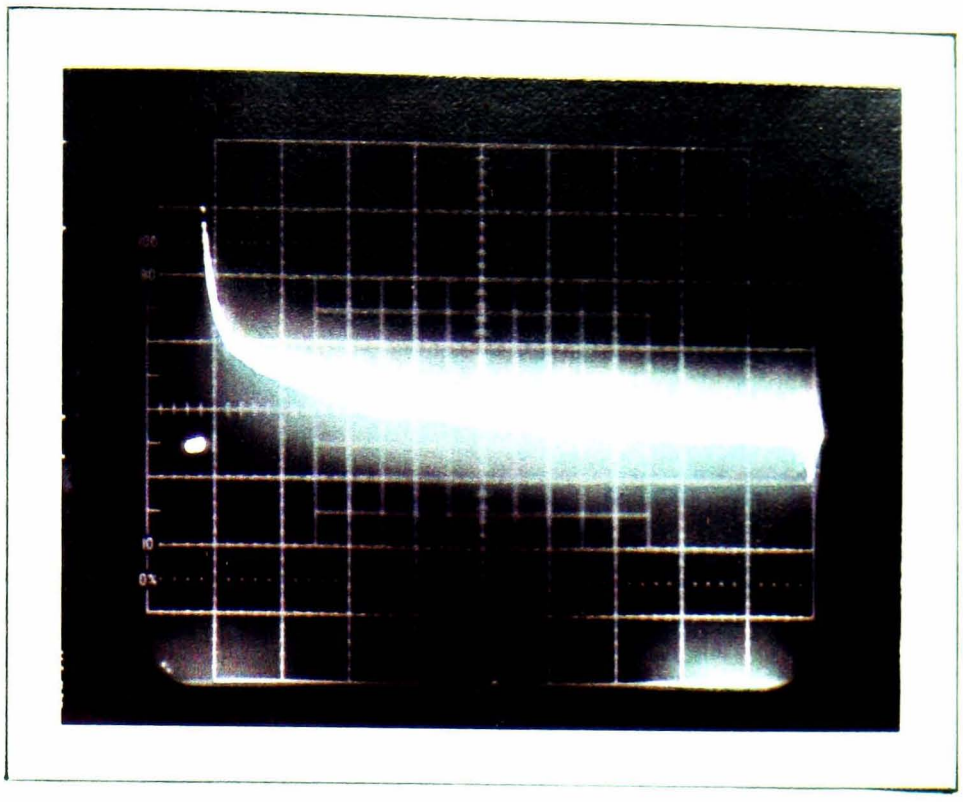

(B)

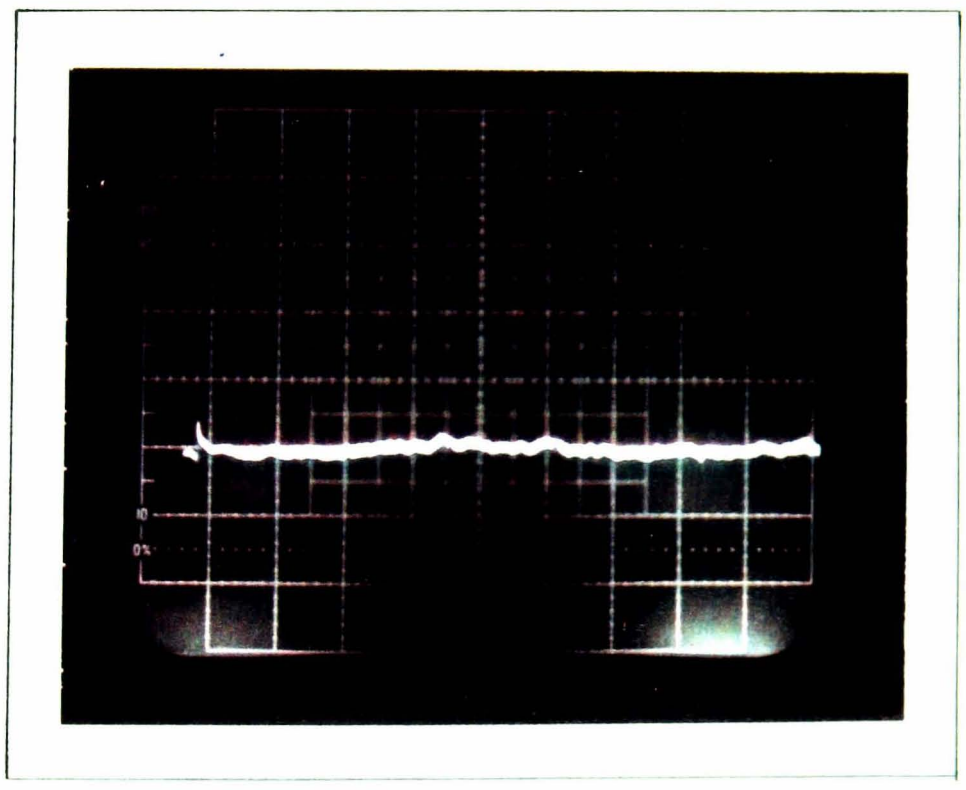

Figures 4.14

The shape of the current transients obtained from a sample of aluminium doped material (CPB9) when the top contact was:

(A) Positive

(B) Negative

In both cases the horizontal scale is 50 μ sec /division and the vertical scale is 50 mV/division.

(A)

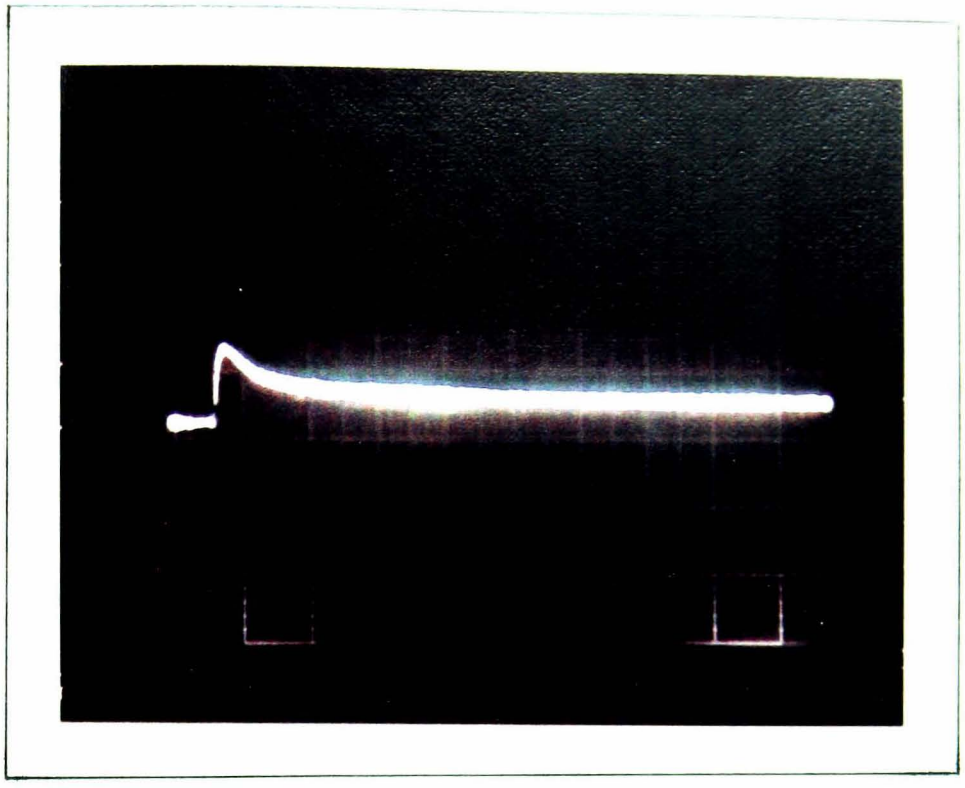

(B)

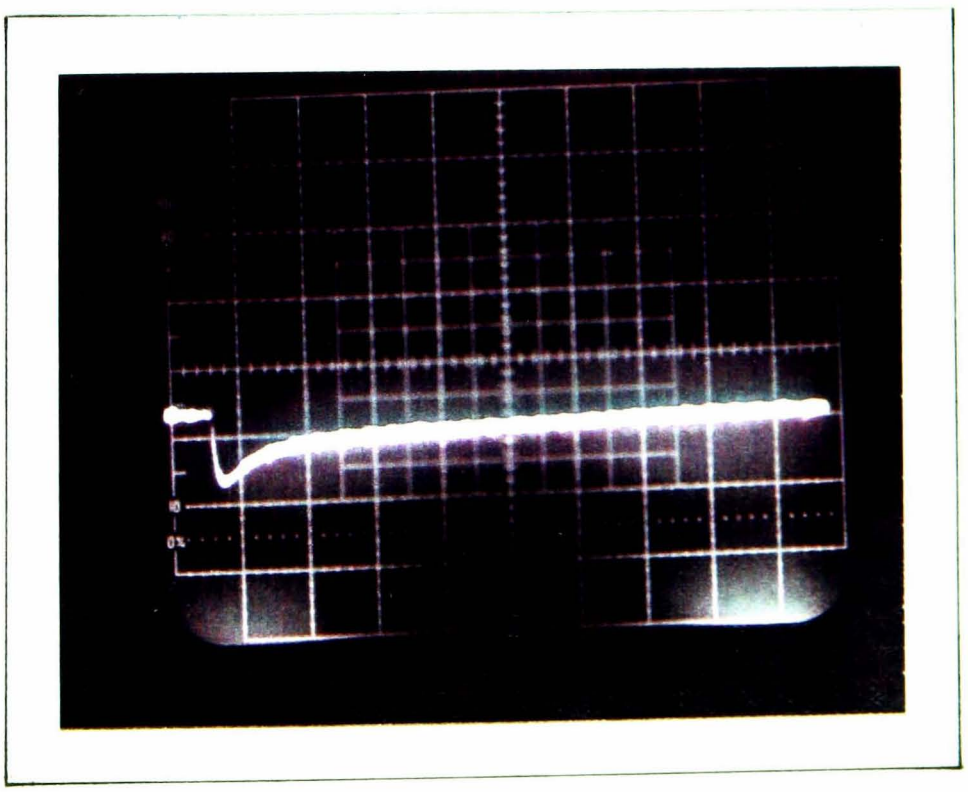

provide information on the extent and nature of any trapping processes occurring in the material as. It is these processes that govern how charge carriers move through the material and hence the shape of the current waveform: as was illustrated in this Section.

4.3.3 Results and Discussion

The shapes of the current transient for the indium doped samples from the boule CPB4 are shown in figures 4.13 and those of aluminium doped samples from boule CPB9 are shown in figures 4.14 and 4.15. In each case the suffix a or b indicates that the current transient was measured when the top contact was respectively positively or negatively biased.

For all samples, when the bias was positive, the decay of the current waveform was characterised by a long tail of the order of milli-seconds. The shape of the waveform made determinations of the transit time impossible. However, using the arguments presented in Section 4.3.2, the shape of the transient does serve to indicate that as the charge carriers pass through the bulk of the material they undergo many trapping and detrapping processes, sufficient to degrade any signal due to such carrier movement and therefore adversely affecting any radiation detector fabricated from the material. When the bias applied to the top contact was negative no signal was observed from any sample except the one aluminium doped sample (CPB9) that was able to detect nuclear radiation. This absence of signal was probably due to the low concentration and mobility of electrons in p-type ZnTe. Both of these effects lead to an increase in the probability of recombination of the electrons and a consequent reduction in charge collection. This observation indicates that any detector is likely to operate with a greater efficiency under a positive bias. This will be seen to be the case from results of device performance presented in Chapter Six.

In some cases there also appears a very rapid decay, in the opposite

Figures 4.15

The rapid initial pulse observed in aluminium doped samples when the top contact was:

(A) Unbiased

(B) Positive

(C) Negative

In all cases the horizontal scale is 0.05 μ sec /division and the vertical scale is 5 mV/division.

(A)

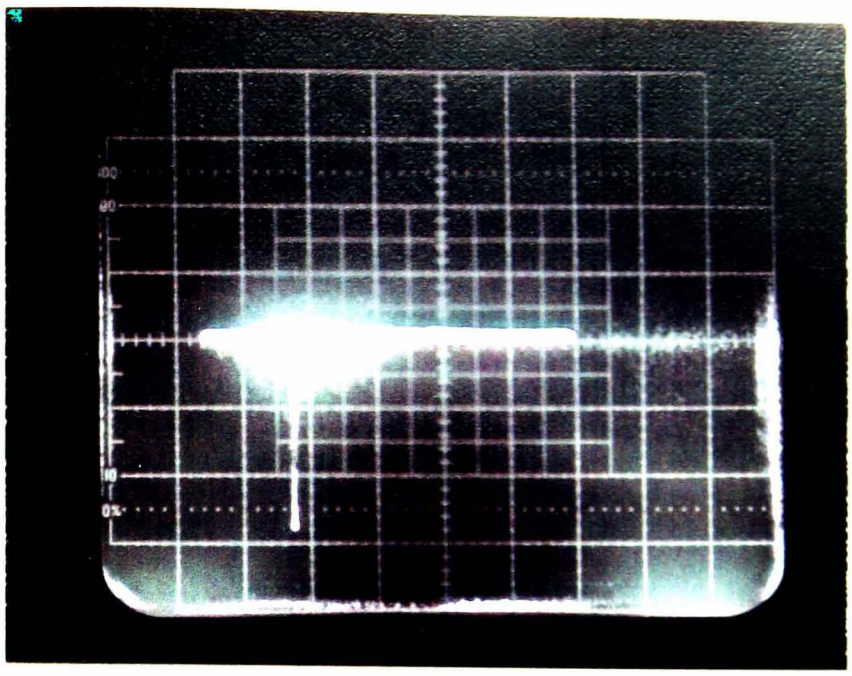

(B)

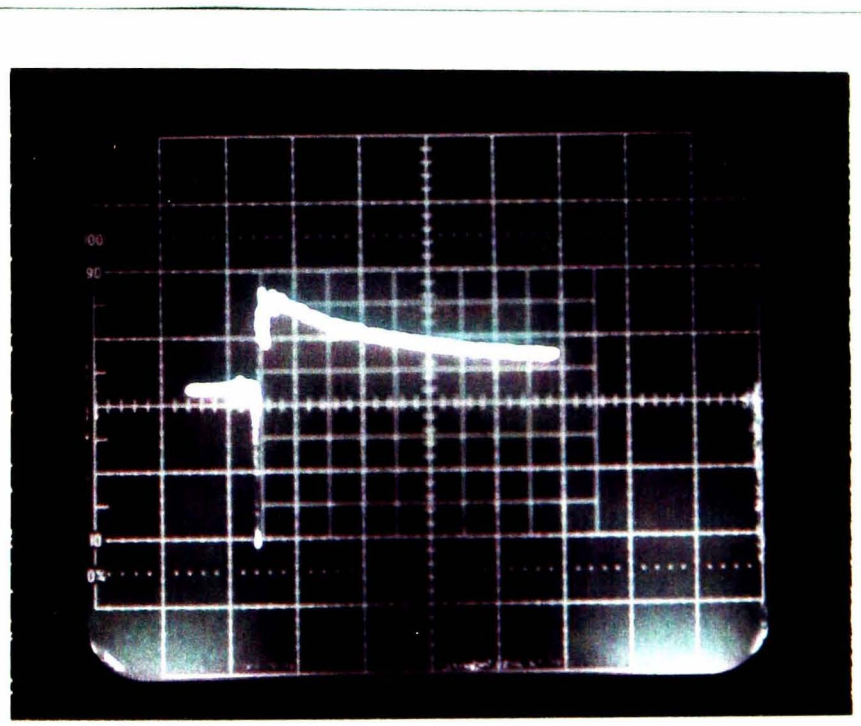

(C)

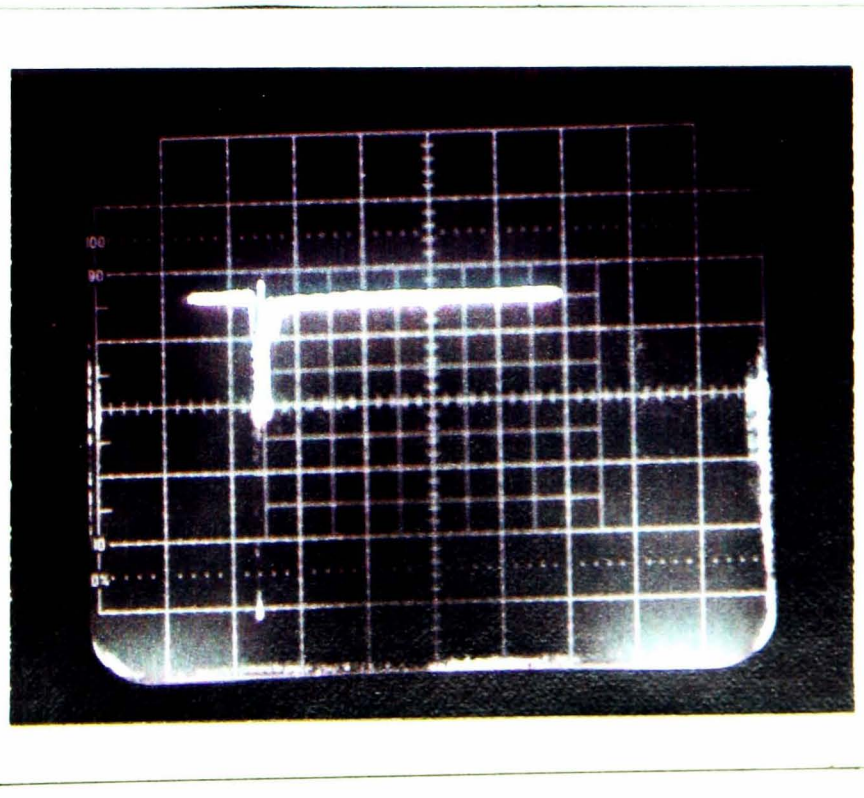

sense to the long tail, in the observed current transient which is present even in the absence of an applied bias (fig. 4.15a). The pulse width of this transient is of the order of nano seconds and is, in fact , comparable with the duration of the laser pulse. The intensity of this current spike increases when the bias applied to the top electrode is negative (fig. 4.15c) and decreases when the bias is positive (fig. 4.15b). Due to this behaviour and it's opposite sense to the main decay the effect is thought to be due to an induced charge effect caused by the high energy laser radiation [35].

The laser pulse has an energy of 3.3 eV which is larger than the band gap of ZnTe at 300K (2.26 eV). Therefore when the electron absorbs one photon not only is it excited across the forbidden band but may have sufficient energy to become a free charge on the surface of the semiconductor. This will produce a negative charge on the top surface which in turn results in an induced positive charge on the opposite face. These charges produce a change in the potential developed across the resistor, R, which is recorded by the scope, S. The origin of the nano second pulse is then probably due to a photovoltaic effect induced in the sample when irradiated and is not connected with the movement of carriers through the sample.

4.4 Conclusions

TSC data presented in this Chapter indicates that doping ZnTe with indium produces six indium related hole trapping levels in the material. The lowest activation energy trap was situated at E_V + 0.09 eV and found to be present in all the indium doped material. The other traps were all found to be hole traps and had activation energies of E_V + 0.1,0.16,0.21,0.3,and 0.38 eV. Only one trapping level was observed in aluminium doped material

and was found to possess an activation energy of E_V + 0.13 eV. This defect level, which has the same activation energy in indium and aluminium doped material, has a similar capture cross sections for holes in both materials ($\sim 10^{-19}$ cm^2) and therefore it is suggested that these defects arise from similar types of centre in both materials namely the $(V_{Zn}D_{Zn})'$ A-centre.

The origins of the deeper trapping levels in the indium doped material remain unknown. As the intensity of all TSC peaks observed in the material are seen to increase when additional indium is diffused into the samples and as the activation energy of the deeper trapping level varies from sample to sample then the deeper trapping levels observed in this study could result from indium having formed complexes with different impurities. This would explain the enhancement of the TSC peak after indium diffusion and also the observed variations in activation energy.

The concentrations of all the observed trapping levels were calculated to be above the maximum permissible for spectrometer operation given in Chapter One ($<10^{14}$ cm^{-3}). Time of flight measurements also indicate that trapping levels are present in both ZnTe:In and ZnTe:Al in high concentrations. Furthermore the time of flight measurements also show that as holes move through the doped materials they undergo many trapping and detrapping processes.

The main conclusion to be drawn from the work which has been presented in this Chapter is that trapping levels, which are found in high concentrations, greatly reduce the mobility of the charge carriers and therefore any devices fabricated from either the indium or the aluminium doped material are likely to act only as radiation detectors but not as radiation spectrometers.

CHAPTER FOUR REFERENCES

[1] Akutagawa W., Zanio K., J. Appl. Phys. 40 3838 (1969)

[2] Siffert P., Berger J., Scharager C., Cornet C., Stuck R., IEEE Trans. Nucl. Sci. 23 159 (1976)

[3] Spear W.E., J. Non Crys. Sol. 1 197 (1969)

[4] Canali C., Martini M., Ottoviani G., Phys. Rev. B 4 422 (1971)

[5] Zanio K.R., Akutagawa W., Mayer J.W., Appl. Phys. Lett. 11 5 (1967)

[6] Zanio K.R., Appl. Phys. Lett. 14 56 (1969)

[7] Canali C., Nava F., Ottaviani G., Zanio K.R., Sol. Stat. Comm. 13 1255 (1973)

[8] Malm H.L., Canali C., Mayer J.W., Nicolet M-A., Zanio K.R., Akutagawa W., Appl. Phys. Lett. 26 344 (1975)

[9] Kasherininov P.G., Matveev O.A., Matyukhin D.G., Sov. Phys. Semis. 13 756 (1979)

[10] Hoschl P., Moravec P., Prosser V., Sakalas A., Jasinskaite R., Phys. Stat. Solidi a 66 K41 (1981)

[11] Blashkiv V.S., Gomenyuk A.F., Sov. Phys. Semis. 10 166 (1976)

[12] Iida S., J. Phys. Soc. Jpn. 32 149 (1972)

[13] Kase K., Jap. Jrnl. Appl. Phys. 17 1805 (1978)

[14] Larsen T.L., Varotto C.F., Stevenson D.A., J. Appl. Phys. 43 172 (1972)

[15] Nahory R.E. and Fan H.Y., Phys. Rev. 156 825 (1967)

[16] Verity D., Bryant F.J., Scott C.G., Shaw D., Sol. Stat. Comm. 46 795 (1983)

[17] Pautrat J.L., Sol. Stat. Elec. 23 661 (1980)

[18] Magnea N., Bensahel D., Pautrat J.L., Pfister J.C., Phys. Stat. Solidi (b) 94 627 (1979)

[19] Luschik C.B., Dok. Akad. Nauk. SSSR 101 641 (1955)

[20] Halperin A., Braner A.A., Phys. Rev. 117 408 (1960)

[21] Chen R., Chem. Phys. L11 371 (1971)

[22] Hoogstraaten W., Philips Res. Repts. 13 515 (1958)

[23] Bube Photoconductivity of Solids Chap

[24] Haering R.R., Adams E.N., Phys. Rev. 117 408 (1960)

[25] Unger K., Phys. Stat. Sol. 2 1279 (1962)

[26] Boiko I.I., Rashba E.I., Trofimenko A.P., Sov. Phys. Sol. Stat. 2 99 (1960)

[27] Grossweiner L.I., J. Appl. Phys. 24 1306 (1953)

[28] Sandomiriskii V.B., Zhadan A.G., Sol. Stat. Elec. 13 69 (1978)

[29] Garlick G.F.J., Gibson A.F., Proc. Phys. Soc. 60 574 (1948)

[30] Rabie S.A., Phys. Rev. B 14 2569 (1976)

[31] Tanimizu S., Otomo Y., Phys. Lett. 25A 745 (1967)

[32] Tews H., Schneider M., Legros R., J. Appl. Phys. 54 677 (1983)

[33] Seitz F., Trans. Faraday Soc. 35 74 (1939)

[34] Huang K., Rhys A., Proc. Roy. Soc. (London) A204 406 (1951)

[35] Ready J.F., Effects of High Power Laser Radiation

CHAPTER FIVE

Electron Paramagnetic Resonance Studies

Introduction

The technique of Electron Paramagnetic Resonance (EPR) has been successfully employed to determine the nature and properties of defects in both II-VI (e.g. CdS [1]; ZnS [2]; CdTe [3]; ZnSe, ZnTe [4]) and III-V (e.g. GaAs [5]) compound semiconductors by many authors. Magnetic resonance measurements are able to provide information on both the crystalline environment and the charge state of any paramagnetic defect centre (either intrinsic or extrinsic in nature) within a semiconductor. Using this information it may then be possible to establish the likely role of the defect in the electrical and optical processes taking place within the host material.

EPR studies have been particularly successfully employed in the II-VI compounds. This is due, in part, to the low abundance of isotopes of the elements of the host material having non-zero nuclear magnetic moments (e.g. ^{67}Zn-4.12%, ^{123,125}Te-0.89%,7.03% $\left.\begin{matrix}\\ \\ \\ \end{matrix}\right\}$ vs. ^{69,71}Ga-60.2%,39.8%, ^{75}As-100%). This means that the resonance lines, produced by paramagnetic defects in II-VI compounds, will not be greatly broadened by strong superhyperfine interactions. In fact the lines are more likely to be accompanied by weak satellites due to the superhyperfine interaction which may provide additional information on the structure of the defect centre.

In undertaking EPR studies in ZnTe it is hoped that the nature and symmetry of defect centres present in the material may be identified, their possible roles in the electrical and optical properties of the material established and from this their effects on device performance inferred. The

aluminium doped material (CPB 7,8,9), the indium doped material (CPB 3,4,5) and the high resistivity lead doped material (CPB 11) were all studied using this technique but only signals due to Fe^{+} (Al and Pb doped) and Cr^{2+} (all materials) were observed. The Cr^{2+} signals were not investigated here as they have been previously studied by Title [4] and as the presence of chromium has previously been detected in amounts <1 p.p.m..

5.1 EPR and the Effective Spin Hamiltonian Description

This section presents a brief outline of the origins of the type of equation needed to interpret the data which will be presented in section 5.3. For a more detailed description of the Spin Hamiltonian approach the reader is referred to textbooks such as Orton [6], Pake and Estle [7], and Abragam and Bleaney [8].

In general a free paramagnetic ion will have a total angular momentum, $\underline{J}$, comprising a spin angular momentum, $\underline{S}$, and perhaps an orbital angular momentum, $\underline{L}$. Since both S and L are vector quantities J will be given by the vector sum of the two, thus:

$$\underline{J} = \underline{L}+\underline{S} \qquad (1)$$

The orbital motion of the electron may be thought of as a circulating charge. This constitutes a current. Associated with this current there is a magnetic dipole which will have a magnetic moment given by:

$$\mu = -g\beta\,\underline{J} \qquad (2)$$

where β is the Bohr magneton - a constant

and, in the Russell-Saunders coupling approximation, g is the Lande g-factor (or just g-value), which is given by:

$$g = \frac{3}{2} - \left[\frac{L(L+1) - S(S+1)}{2J(J+1)}\right] \qquad (3)$$

and represents the amount by which the orbital and spin angular momenta are coupled.

The magnetic dipole will precess about an applied static magnetic field, B. The energy of interaction is quantised so that the components of the total angular momentum along the field direction, M_J, take only specific values:

$$-J, -J+1, \ldots, J-1, J$$

i.e. 2J + 1 possible orientations of the dipole. The corresponding energy values are given by:

$$E_Z = g\beta B M_J \qquad (4)$$

where E_Z is the Zeeman energy.

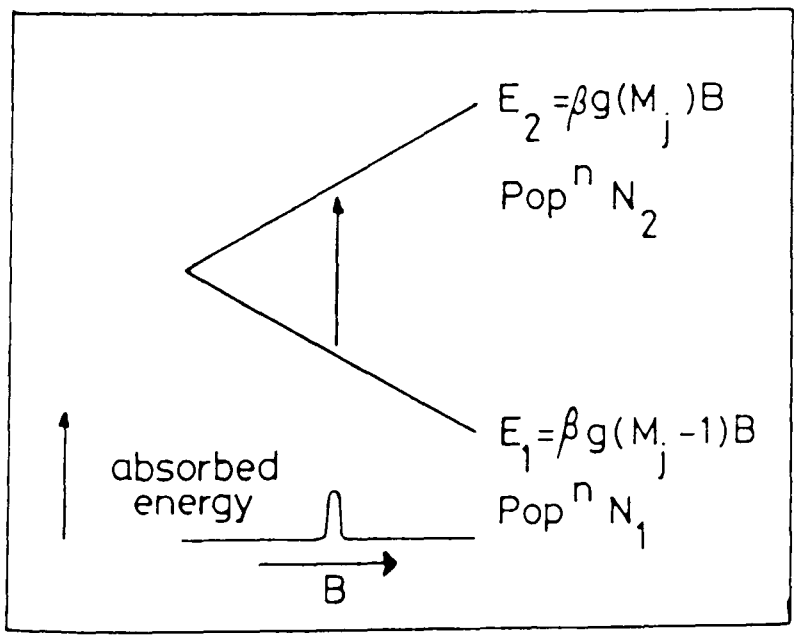

Figure 5.1 Zeeman split energy levels E_1 and E_2 illustrating a resonance transition at a microwave frequency

Transitions may only occur between adjacent Zeeman levels ($\Delta M_J = \pm 1$). Such a transition is represented in figure 5.1 and involves a gain or loss of a quantλ^{um} of electromagnetic radiation of frequency υ, such that the condition

$$h\upsilon = g\beta B \qquad (5)$$

holds.

There is an equal probability of both the absorption of the energy, $h\upsilon$, exciting the electron from the level E_1 to E_2 and of the emission of the same quantλ^{um} of energy as an electron falls from E_2 to E_1.

In order for a net absorption of radiation to occur, enabling an EPR signal to be detected, the population of level E_1 (N_1) must be greater than that of E_2 (N_2). This will be true for a system in equilibrium with it's surroundings. In this case, applying Maxwell-Boltzman statistics to the system, the relative distribution of population may be given by:

$$N_1/N_2 = \exp[\ h\upsilon\ /kT\ ] \qquad (6)$$

From equation (6) it can be seen that the use of as high an energy of radiation and as low a temperature as possible is preferable. Experimentally the maximum frequency of radiation used is governed by the maximum strength of the static magnetic field that can be applied to the sample (eqn. (5)).

The energy levels of an ion placed in a crystal may differ greatly from those of the free ion. This is due to coulombic interactions between the crystalline electric field and the electrons of the ion. The orbital motion of the electron is affected and the orbital degeneracy of the free ion may be removed, leaving a ground state in which L=0. The g-value should then be that of the free electron:

$$g_e = 2.0023$$

Deviations of the g-value from 2 usually occur because of interactions between the spin momentum of the ground state and the orbital momentum of a higher state which leads to the degeneracy not being fully removed.

Anisotropy is also often found in the measured g-value. This is due to the dependence of the energy levels of the system on:

1) The symmetry of the local electric field

2) Interactions with the ligand ions

The behaviour of the energy levels due to these various effects may be described by an "effective" spin Hamiltonian. The part of the spin Hamiltonian describing the Zeeman effect is analogous to that of the free ion and may be written as

$$\mathcal{H}_z = \beta \underline{B}.\tilde{g}.\underline{S} \qquad (A)$$

where S is now an effective spin, constructed so that the observed degeneracy of the ground state comprises a set of (2S + 1) levels.

Other terms must now be added to the spin Hamiltonian in order to describe the effects of other interactions.

If there is more than one unpaired electron on a paramagnetic ion then the energy of interaction between these must be considered. Since this interaction is coulombic in nature it will be modified by the electrostatic crystal field and as a result is highly dependent on the field symmetry. Energy level splittings may even occur in the absence of an externally applied magnetic field.These level splittings give rise to an experimentally observed fine structure which may be described by

$$\mathcal{H}_f = \underline{S}.\tilde{D}.\underline{S} \qquad (B)$$

If the nucleus of the paramagnetic centre possesses spin then the

resultant nuclear magnetic moment (I) will add to or subtract from the applied magnetic field.

This gives rise to the hyperfine interaction which may be described by

$$\mathcal{H}_{HF} = \underline{S}.\tilde{A}.\underline{I} \qquad (C)$$

Nuclear magnetic moments of the ligand ions may also affect the magnetic field experienced by the paramagnetic ion. This type of interaction giving rise to a superhyperfine splitting which may be described by

$$\mathcal{H}_{SHF} = \sum_{i}^{n} \underline{S}.\tilde{A}_n.\underline{I}_n \qquad (D)$$

where the quantity n describes the n^{th} ligand ion effect.

Other interactions exist (e.g. nuclear quadrupole interaction) adding terms to the spin Hamiltonian, however these do not make observable contributions to the EPR signals presented in this chapter and will not be discussed further. The general spin Hamiltonian used to interpret the EPR data presented here is given by

$$\mathcal{H} = \quad (A) \quad + \quad (B) \quad + \quad (C) \quad + \quad (D)$$

or

$$\mathcal{H} = \beta\, \underline{B}.\tilde{g}.\underline{S} + \underline{S}.\tilde{D}.\underline{S} + \underline{S}.\tilde{A}.\underline{I} + \sum_{i}^{n} \underline{S}.\tilde{A}_n.\underline{I}_n \qquad (E)$$

where $\tilde{g}$,$\tilde{D}$,$\tilde{A}$ and $\tilde{A}_n$ are, in general, 3x3 tensor matrices representing the magnitude of the various interactions.

5.2 Experimental Details

5.2.1 EPR System Arrangement

All of the EPR data presented in section 5.3 was obtained using a Q band (approx. 35 GHz) spectrometer system, the resonant cavity of which, was immersed in liquid helium. Figure 5.2 shows a block diagram of the system used.

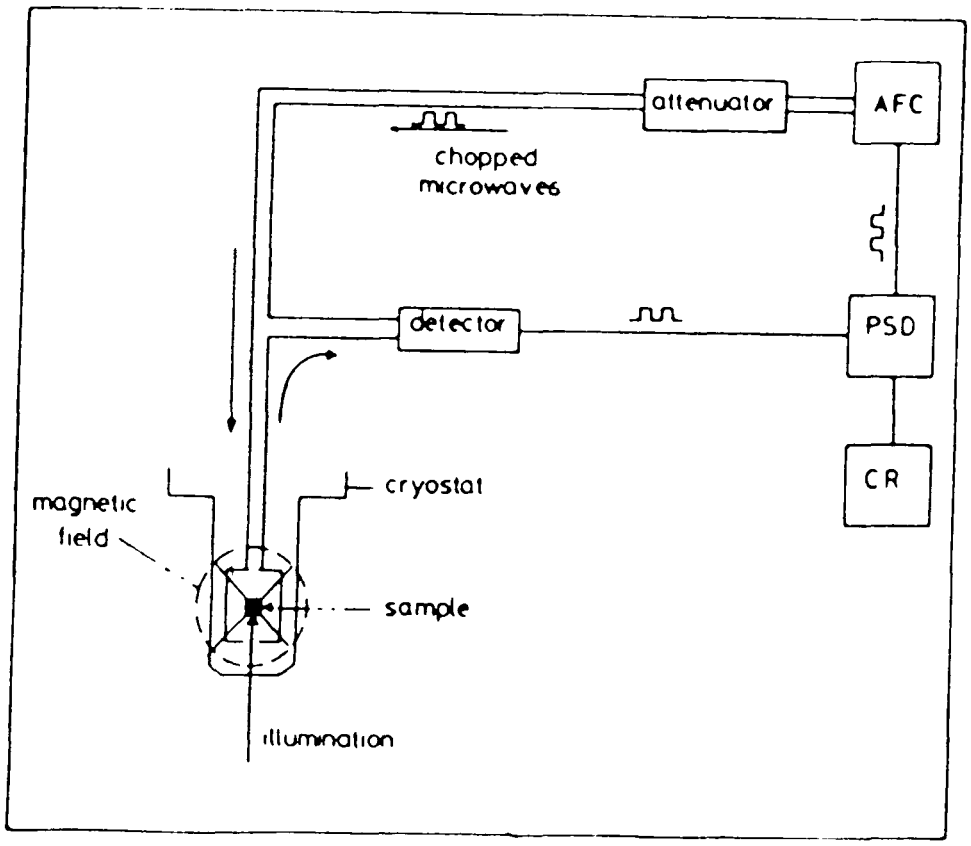

Figure 5.2 Schematic representation of experimental arrangement for the the detection of EPR

The microwaves were supplied by a Microspin W953 microwave generator fitted with an E.M.I. high voltage Klystron with automatic frequency control (AFC). The microwaves were guided by a rectangular waveguide into a resonant cavity where a standing wave was set up.

An external magnetic field of up to 1.5 Tesla was provided by a Newport copper wound, water cooled electromagnet. This could be rotated about a vertical axis, enabling the angular dependences of the EPR signals to be

studied. The precise determination of the magnetic fields at which resonances occurred was achieved by using a proton resonance head inserted between the pole pieces of the magnet.

In order to reduce detector noise the magnetic field was modulated at a frequency of 100 kHz. The signal was then phase sensitive detected (PSD) at this frequency and observed using either an oscilloscope or a Y-T chart recorder (CR).

The samples were mounted with a (110) cleavage plane against the top of a quartz light pipe and positioned in the cavity in the position of maximum magnetic field. Using this arrangement in situ illumination of the sample could be provided and the angular dependences were taken for the field rotated in the (110) crystal plane.

5.2.2 Optical Measurements

Monochromatic illumination of the sample was achieved by focussing light form a quartz-halogen lamp which had passed through a 35 cm focal length Mini-spex monochromator onto the base of the light pipe. The effect of the optical energy upon the decay of the photosensitive EPR signal was investigated as follows:

The sample was initially illuminated with radiation of energy close to 514 nm (2.41 eV) for five minutes in order to create the photosensitive signal. This illumination was then removed and the sample left in the dark for one minute, in order to establish a steady state condition. The EPR signal was then recorded to produce the time = 0 measurement shown in figure 5.9. Quenching radiation, at longer wavelengths, was then supplied to the sample and the EPR signal was recorded at time intervals after commencement of illumination. The EPR signal was then re-established using the 2.41 eV radiation and the experiment repeated using quenching radiation of a different energy. The decay of the EPR signal without quenching radiation

was found to be negligible over the period of each experiment (typically twelve minutes).

5.3 Results and Discussion

5.3.1 The Fe Signal in Lead Doped ZnTe

The spin Hamiltonian describing the Fe^{+} ($3d^{7}$ electron configuration) ion in a tetrahe dral symmetry has been shown by Woodbury et al [9] to be of the form

$$\mathcal{H} = \beta\, \tilde{g}\underline{B}.\underline{S} + u\,\beta\{(S_x{}^3B_x+S_y{}^3B_y+S_z{}^3B_z) - \underline{S}.\underline{B}(3S(S+1)-1)\} \quad (7)$$

The value of S is 3/2 and x,y,z denote the cubic axes of the crystal.

The first term describes the Zeeman interaction and the second was shown by Bleaney [10] to be allowed by symmetry. Neglecting terms of the order of $(u/g)^2$ the M=+1/2 to M=-1/2 transition was shown by Bleaney to occur at a value of the magnetic field, B, given by

$$B = \frac{h\upsilon}{\bar{g}\beta}\,(1 + (9u/5\bar{g})p) \quad (8)$$

$$\text{where } p = 1 - 5(l^2m^2+m^2n^2+n^2l^2) \quad (9)$$

l,m and n are the directional cosines of B with respect to the cubic axes x,y, and z.

Figure 5.3 shows the relationship between l,m and n and θ (the angle between B and the 110 direction)

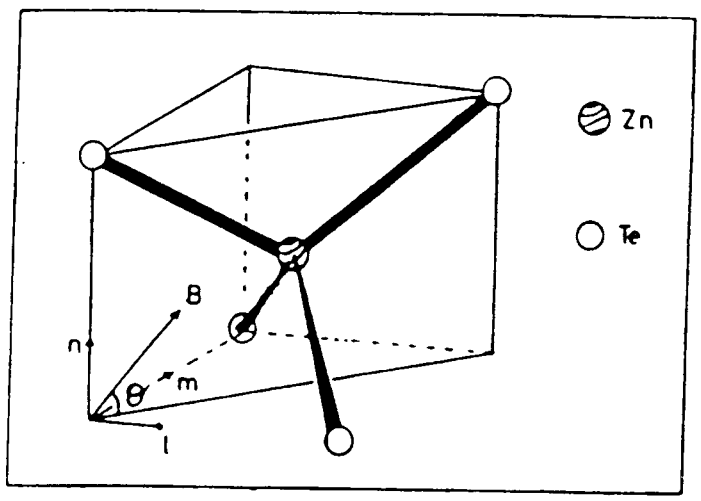

Figure 5.3

Relationships between l,m,n,B and θ

It can be seen from this diagram that the directional cosines may be expressed in terms of the experimentally measurable value θ as

$$l = \frac{1}{\sqrt{2}}\cos\theta : m = \frac{1}{\sqrt{2}}\cos\theta : n = \sin\theta \qquad (10)$$

and that by substituting these values into equation (9) p becomes

$$p = 1 - \frac{5}{4}\cos^2\theta(4-3\cos^2\theta) \qquad (11)$$

Equation (11) gives the theoretical angular variation of the magnetic field value of the Fe^+ EPR signal.

Figure 5.4 shows the anisotropic EPR signal that was observed in this material after the sample was illuminated with above band gap energy light at 2.41 eV. The angular dependence of the central ($M_s = \frac{1}{2} \longrightarrow M_s = -\frac{1}{2}$ transition) line is shown in figure 5.5. the solid line being the best fit of equations (8) and (11) to the experimentally determined values (*), using the value of

$$g = 2.280$$

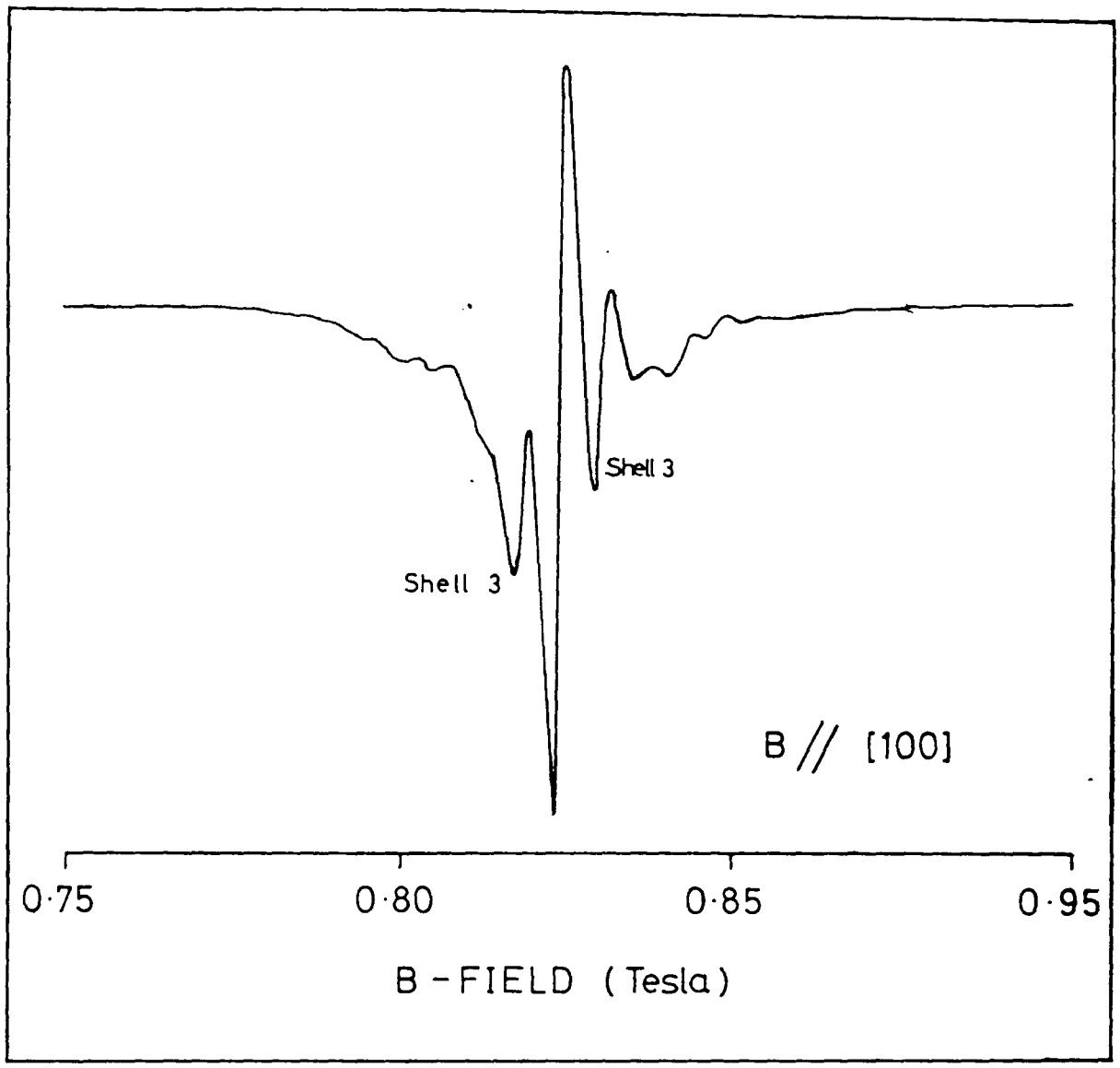

Figure 5.4 Fe^{+} EPR signal observed in ZnTe:Pb. Super hyperfine (Shf) structure due to the Te third shell interactions are also shown.

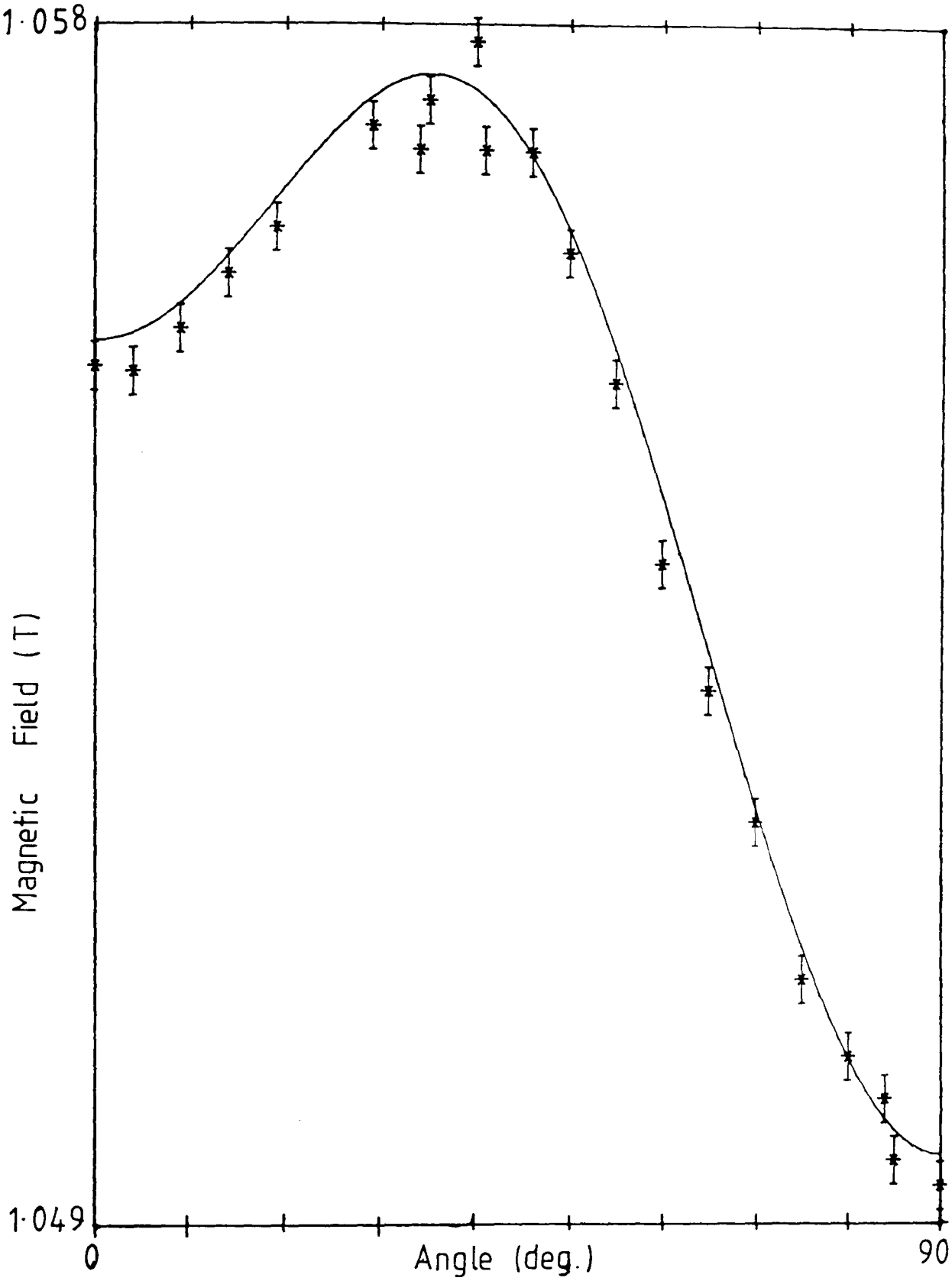

Figure 5.5 Angular dependence of the central M_s=1/2 to M_s=-1/2 transition of the Fe^+ signal. The solid line is calculated after equations (8) and (11).

The two closest satellite signals (marked as shell 3 in figure 5.4) are thought to be the SHF structure due to interactions between the Fe^+ centre and the ^{125}Te isotope of tellurium which has a non-zero nuclear spin (I=1/2 and a 7.03 % abundance). The field splitting between the central, zero isotope line, and either of the satellites is 1.2 ± 0.2 Gauss. This corresponds to an A term of $(1.12 \pm 0.20)x10^{-4}$ cm^{-1} in equation D and remains constant irrespective of the relative orientation of the sample in the external magnetic field.

Since, from the angular dependence of the central line, the defect centre is seen to possess an axial symmetry one would expect the SHF lines to show some angular variation if the interaction was with the first tellurium shell (see figure 5.6). However as the splitting is constant the interaction cannot be with the first shell but has been shown by Estle and Holton [11] to be due to interactions with the third shell of twelve tellurium ions.

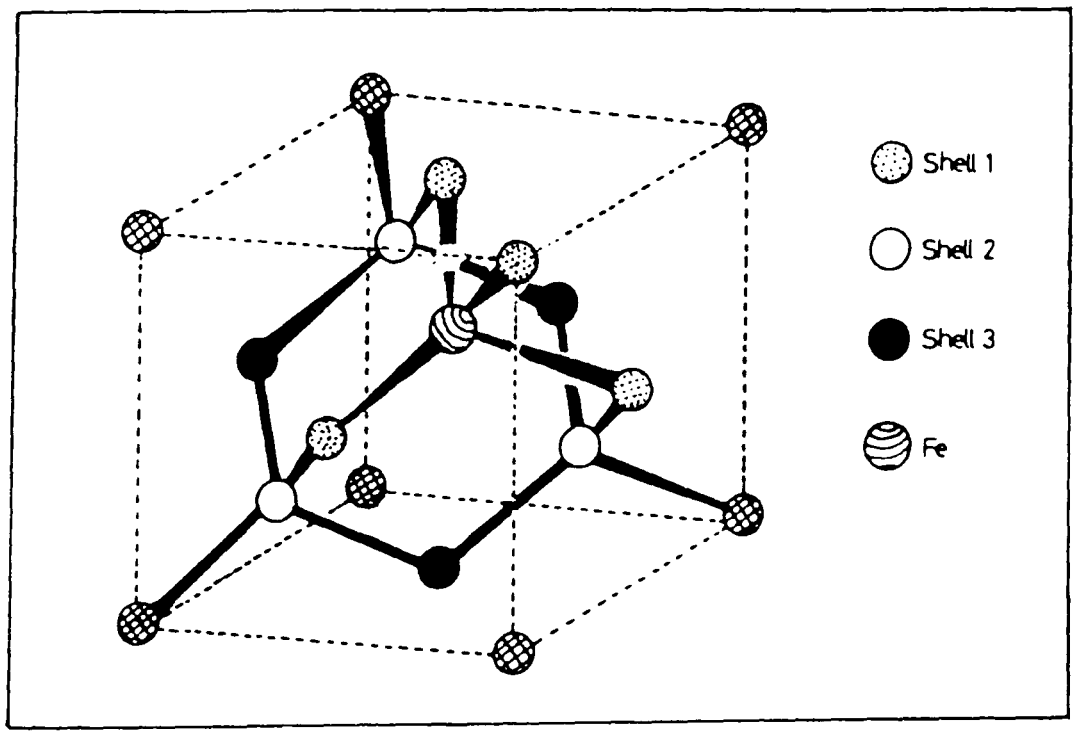

Figure 5.6 The ZnTe unit cell indicating the position of the Fe impurity and shells 1 (Te), 2 (Zn) and 3 (Te)

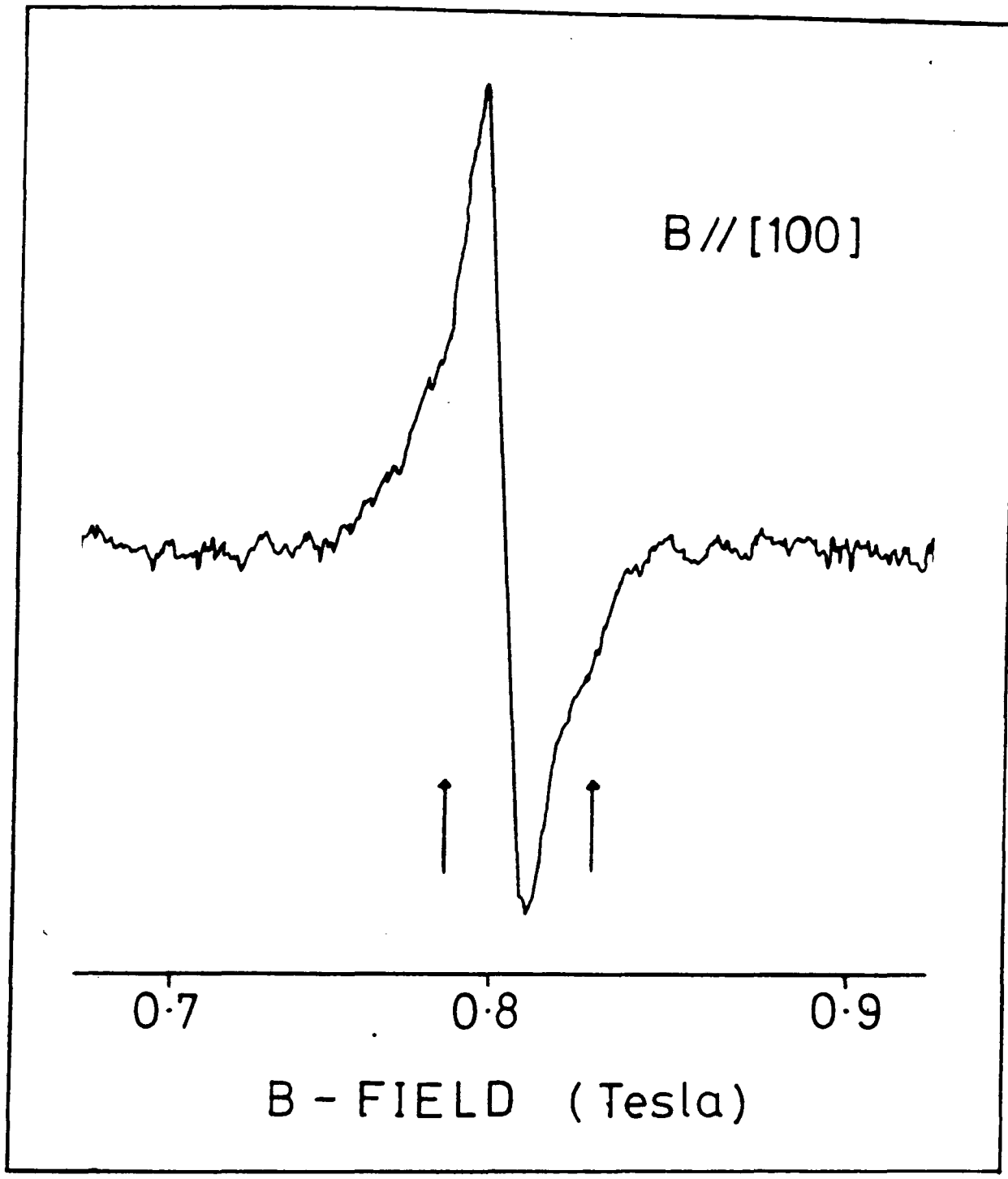

Figure 5.7 Fe^{+} EPR signal observed in ZnTe:Al.
The positions of thesuper hyperfine (Shf) structure
due to the Te third shell interactions are marked
by arrows.

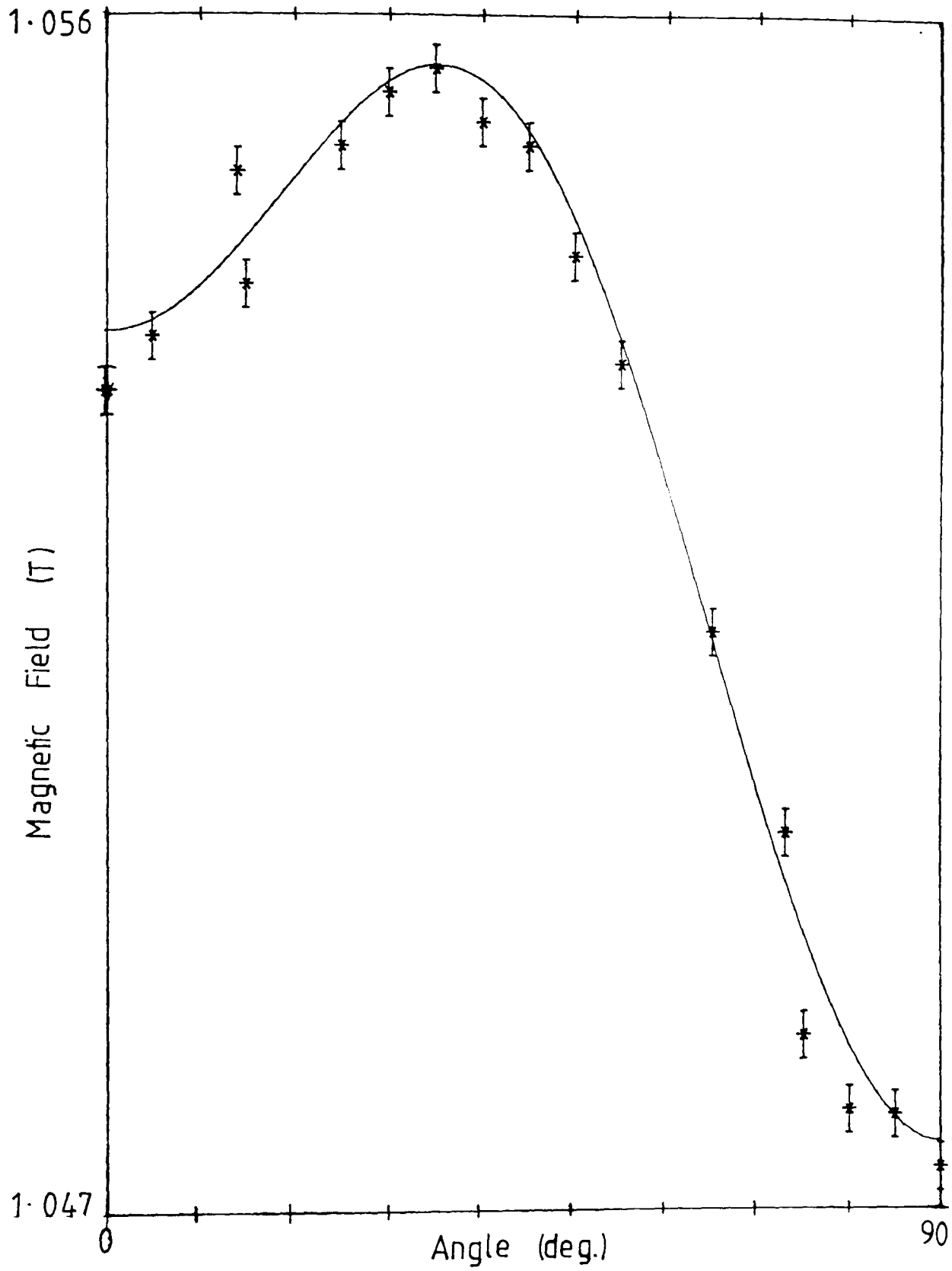

Figure 5.8 Angular dependence of the central M_S=1/2 to M_S=-1/2 transition of the Fe^+ signal in ZnTe:Al.
The solid line is calculated after equations (8) and (11).

Estle and Holton measured a SHF splitting of 1.4 Gauss (i.e. an A term of 1.31×10^{-4} cm^{-1} which, as it represents the third shell interaction, is an average value). The SHF interaction with the first shell was undetected, perhaps because of the low probability of any of the four ions posessing a nuclear spin which would make the EPR signal produced by such an interaction very weak. As both the SHF splitting, A, and the g value are the same, to within experimental accuracy, as those values ascribed to the Fe^+ signal in ZnTe by Estle and Holton the defect centre responsible for the EPR signal reported here is assigned to Fe^+.

5.3.2 The Fe^+ Signal in Aluminium Doped ZnTe

Figure 5.7 shows a typical EPR spectrum taken from samples doped with 60 and 100 ppm aluminium. The SHF structure is visible as humps on the wings of the central zero isotope line. This may be due to the broadening of the central EPR signal perhaps by strain or by chemical broadening by the Al dopant.

The best fit (solid line) to the experimentally observed angular dependence (*) was again achieved using a g value of 2.280 in equations (8) and (11) and is shown in figure 5.8 for the 40 ppm Al doped sample. The signal was photosensitive, being enhanced by 2.41 eV light and quenched by near infra-red light, and is therefore assigned to Fe^+, that is iron substituting for zinc in the ZnTe lattice.

5.3.3 Optical Quenching of the Fe^+ EPR Signal

In their EPR studies of the iron transition group elements in II-VI compounds Estle and Holton noted that the Fe^+ signal in ZnTe was photosensitive and was enhanced by irradiation of the sample with 2.25 eV light. This effect was also seen in the ZnTe:Pb and ZnTe:Al samples studied here, moreover the signal was only observed after the sample was illuminated

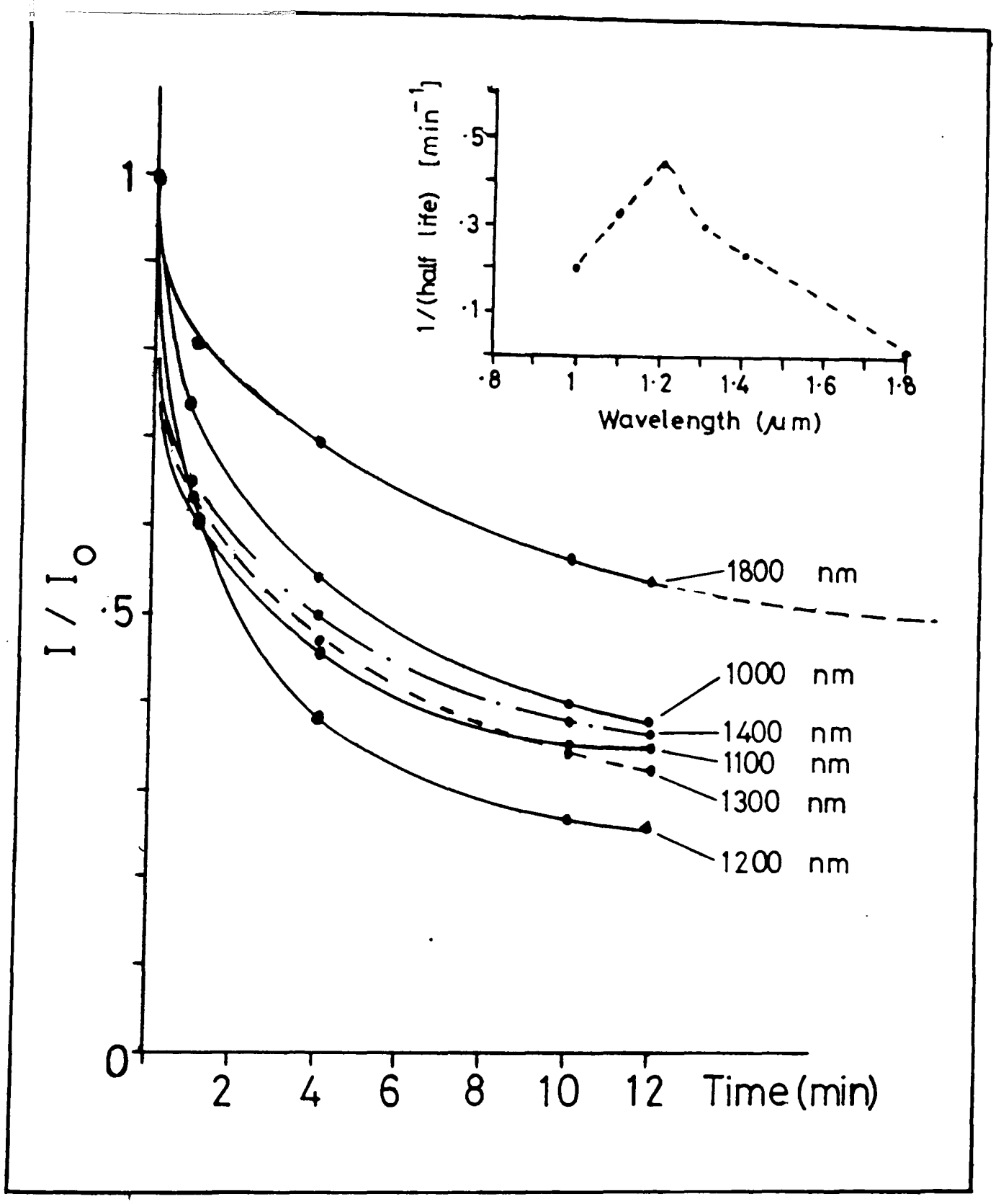

Figure 5.9 The variation in intensity (I/I_o) with time for various energies of incident radiation.

The insert shows how the rate of quenchng varies with energy.

with above band gap light.

In addition to this enhancement the work presented here also shows that the signal can be quenched by illumination with near infra-red radiation. Figure 5.9 shows how the rate of quenching varied with energy of incident radiation. As is illustrated in this figure the most efficient energy for quenching was found to be close to 1200 nm (1.03 eV).

In Chapter Three it was proposed that the most likely model that could explain the type I infra-red emission (zero phonon emission 1.13 eV), observed in the aluminium and the high resistivity lead doped ZnTe, involved the radiative recombination of an electron bound to the Fe^+ centre with a free hole in the valence band. The type II emission was proposed to result from the recombination of the Fe^+ electron with an acceptor hole. In compensated p-type material, doped with either aluminium or indium, both donor and acceptor levels are present but the electron bound to the Fe^+ centre will only be able to recombine with those acceptors which are very close to it (perhaps only one or two lattice spacings away). This is because Fe^+ behaves as a deep centre, situated approximately mid-gap, and therefore the electron will be tightly bound with the consequence that its wavefunction will only extend over one or two lattice sites. If in the case of Al and Pb doped material the concentration of acceptors in the material is such that the spatial separation between the Fe^+ centres and the acceptors is large, then recombination of electrons trapped at the Fe^+ centres with holes in the valence band will be more likely than recombination with neutral acceptors and the type I luminescence band will be observed. If on the other hand in the In doped material there is a large concentration of acceptors then the probability of finding an acceptor close to an Fe^+ centre will be greater and recombination between holes bound to the acceptors and Fe^+ electrons will occur, resulting in type II emission. The recombination process involving acceptors is more likely to occur than

Figure 5.10 Schematic representation of the model used to explain the the observed properties of the Fe^{+} signal.

(a) Before illumination the material contains ionised donors (D^{+}), ionised and unionised acceptors (A^{-} and A^{O}). The iron is in the Fe^{2+} state and no EPR signal is seen.

(b) When the sample is illuminated with above band gap energy light free electrons and holes are created. The holes become trapped by ionised acceptors and the electrons become trapped by Fe^{2+} ions. This converts them to Fe^{+} and an EPR signal is seen.

(c) After removal of the illumination the Fe^{+} EPR signal decays slowly as electrons trapped at the Fe^{+} ions recombine with holes trapped at ionised acceptors.

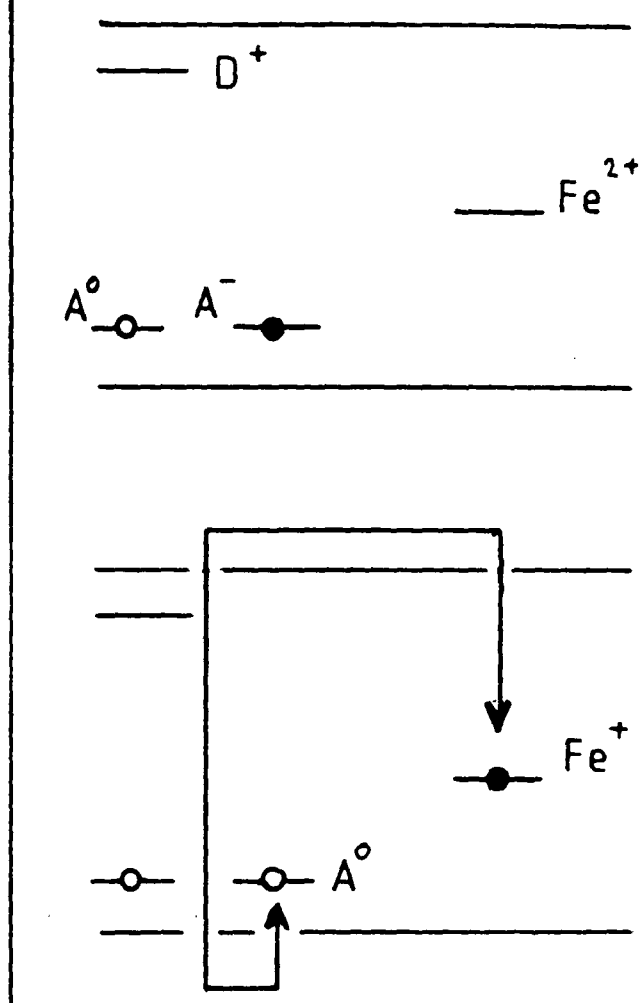

(a)

No illumination :-
no EPR signal

(b)

Illumination :-
EPR signal

(c)

Illumination off :-
slow decay of
EPR signal

Fig. 5.10

that involving free holes since there is no need to conserve translational energy in the former process and therefore less requirement for phonon involvement.

Based on this model, which described the near infra-red luminescence, it is possible to explain:

(i) The presence of the Fe^{+} EPR signal in the aluminium and lead doped material and the lack of EPR signal in the indium doped material;

(ii) The photo-creation of the Fe^{+} EPR signal followed by its slow decay when illumination ceases and

(iii) The photo-quenching of the signal.

This is shown schematically in the energy band diagrams of figure 5.10.

The luminescence studies carried out in Chapter Three showed that in ZnTe residual impurities, such as copper and lithium, form shallow acceptors which are assumed to cause the observed p-type conductivity. It was hoped that by doping with Al or In, for example, some of these acceptors would be compensated and high resistivity material produced. Furthermore the absence of an Fe^{+} EPR signal before illumination indicates that iron enters the lattice as Fe^{2+} (figure 5.10a). The Fe^{+} EPR signal is observed after above band gap illumination when the iron is converted to Fe^{+} by the capture of an electron which has been excited across the energy gap. Some of the photogenerated holes, which are also created in this process, are then trapped at ionised acceptors (figure 5.10b). If, after photo-creating the EPR signal, the illumination source is removed there are no free holes for the Fe^{+} electrons to recombine with and recombination can only occur between the Fe^{+} electrons and holes bound to neutral acceptors (figure 5.10c). As the electron is tightly bound to the Fe^{+} centre the recombination with acceptors becomes much more probable as the spatial separation between the Fe^{+} centre and the acceptor is reduced. However the concentration of

neutral acceptors in the Al and Pb doped material is small (which is why type I emission is observed) so the spatial separations between the acceptors and the Fe^+ centres are large and therefore, because of the small recombination probability, a slow decay of the EPR signal in the dark is observed (figure 5.10c).

It has been shown (figure 5.9) that the most efficient energy of quenching radiation is 1.03 eV. Since the zero phonon emission of the type I band occurs near 1.13 eV, which from the luminescence model places the Fe^+ centre approximately 1.27 eV below the conduction band ($E(Fe^+) = E_g - 1.13$), the quenching of the EPR signal cannot be due to the excitation of the Fe^+ electrons back into the conduction band. Instead the quenching process which is shown in figure 5.11 (process A) is thought occur. This involves the excitation of electrons from the valence band (VB) into deep acceptor levels situated approximately 1.03 eV above VB, leaving a free hole in the valence band which is then able to recombine with the Fe^+ electron and thus cause quenching of the associated EPR signal.

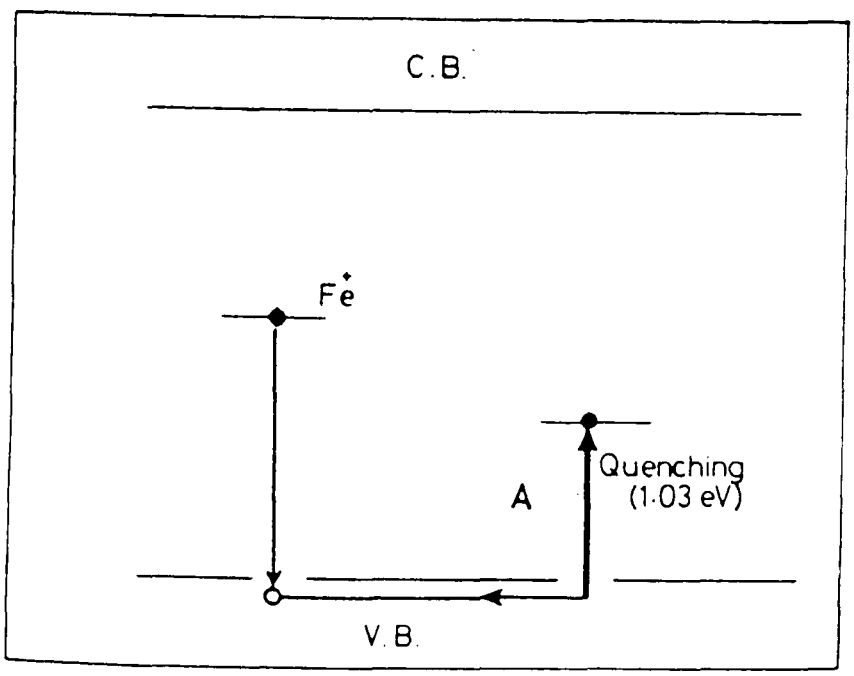

Figure 5.11 A possible model to explain the quenching of the Fe^+ EPR signal.

The tail in the quenching spectrum (figure 5.9) towards lower energies represents the energy spread in the depth of acceptor levels that are

present in the material. Thermal quenching of the EPR signal was also seen to occur if the sample was heated to above 20 K. This may be explained using the same mechanism as that of optical quenching if it is assumed that electrons are now thermally excited from the valence band into shallow acceptor levels.

In ZnTe:In samples the absence of an EPR signal may be explained if it is assumed that In doping produces many more acceptor centres in the material. This would reduce the spatial separation between the acceptors and the Fe^+ ions with the consequence that the recombination of Fe^+ ions with acceptor holes takes place much more readily (This results in type II luminescence) so that there are never sufficient Fe^+ centres present in the sample at any one time for the EPR signal to be observed.

5.4 Conclusions

EPR measurements have shown that both iron and chromium are common contaminants in the ZnTe grown for this study. The presence of these impurities in the Zn and Te starting materials has already been established using mass spectrograph techniques (Chapter Two) where it was found that chromium was present in amounts <1 p.p.m. and iron in amounts 3 p.p.m.

It has been observed in this study that the samples which show the Fe^+ EPR signals (CPB11, CPB 7,8,9) all show an identical infra-red luminescence band peaking close to 1.06 eV whereas those which show no Fe^+ EPR signal (the indium doped samples CPB 3,4,5) show a different infra-red luminescence band which peaks near 1.02 eV. These and the other properties of the Fe^+ EPR signal that have been described in this chapter such as the slow decay and photo- creation and quenching of the signal have all been explained using the infra-red luminescence model described in Chapter Three, so the results presented in this chapter tend to enforce the validity of that model.

CHAPTER FIVE REFERENCES

[1] Morigaki K. and Hoshina T., J. Phys. Soc. Jpn. 23 820 (1967)

[2] Holton W.C., Schneider J. and Estle T.L., Phys. Rev.133 A1638 (1964)

[3] Kaufmann U., Windschief J. and Bruthaler G., J. Phys. C 17 6169 (1984)

[4] Title R.S., Phys. Rev. 133 A1613 (1964)

[5] Goltzene A., Meyer B. and Schaub C., Semi Insul. III-VI Mat. Page 231 (Evian 1982)

[6] Orton J.W., Electron Paramagnetic Resonance CH 4 (edited Gordon and Breach)

[7] Pake G.E. and Estle T.L., Physical Principles of EPR CH 4 (W.A. Benjamin Inc. 1973)

[8] Abragam A. and Bleaney B., EPR of Transition Metal Ions CH 3 (Clarenden Press-Oxford 1970)

[9] Woodbury D., Ham F.S., Ludwig G.W. and Watkins G., Phys. Rev. Let. 5 468 (1960)

[10] Bleaney B., Proc. Roy. Soc. (London) A73 939 (1959)

[11] Estle T.L. and Holton W.L., Phys. Rev. 150 159 (1966)

CHAPTER SIX

Device Fabrication and Testing

Introduction

Samples were sawn from each boule that produced material of resistivity of greater than $10^5 \Omega$ cm and fabricated into surface barrier detectors, which were then investigated for their performance as nuclear radiation detectors.

It was found that only one sample from boule CPB8 was able to detect nuclear radiation and the results obtained for this are presented here.

6.1 Principles of Device Operation

6.1.1 The Surface - Barrier Detector

The construction of a surface-barrier radiation detector is shown in figure 6.1. The surface-barrier is formed by evaporation of a metal (in this study aluminium is used) onto the front surface of the p-type ZnTe to make a Schottky contact. An ohmic contact (electroless gold plate) is then made to the rear surface (infact during the preliminary studies both contacts were formed from evaporated aluminium. One was then forward biased whilst the other was reverse biased).

When a reverse bias is applied to the device the depletion region, which was created by the Schottky contact, will extend further into the bulk of the device. Any electron-hole pairs created in that region due to the interaction of radiation with the material will be swept towards their respective contacts under the influence of the external electric field. Thus the presence of radiation is detected by the device as a current pulse, the

intensity of which depends upon the number of electron-hole pairs generated within the device by the incident radiation.

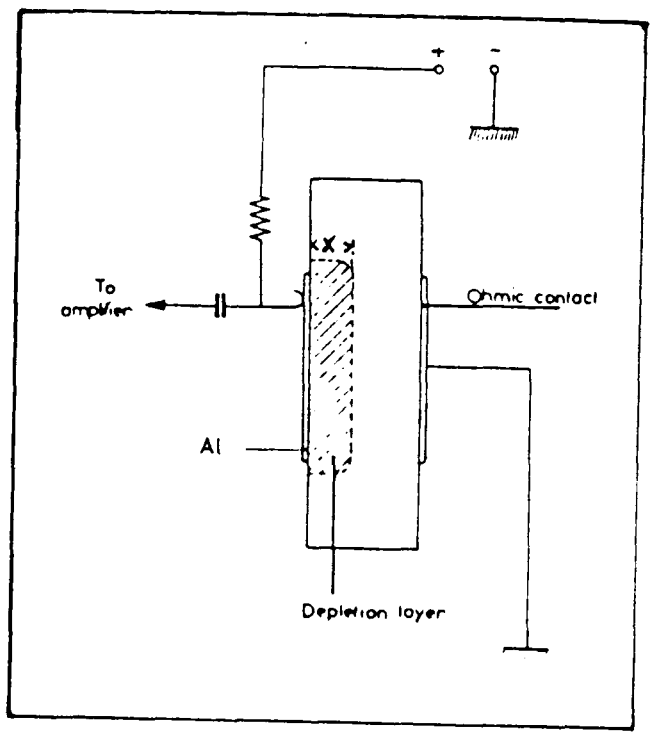

Figure 6.1 Schematic representation of a surface barrier detector

The width, X, of the depletion region critically affects device performance since the more penetrating the incident radiation the greater X must be to ensure a sufficiently large number of interactions for a current to be detected and in the case of gamma ray detectors it is desirable that X extends across the entire width of the device (typically 2mm). The depletion region width, under the influence of an external voltage, V, is given by [1]

$$X \approx \left[\frac{\varepsilon_s V}{2qN_T}\right]^{1/2} = (2\varepsilon_s \mu\rho V)^{1/2} \qquad (1)$$

where $N_T = |N_D - N_A|$; ε_s is the dielectric constant of the semiconductor; μ the mobility and ρ the resistivity of the material.

6.1.2 Schottky Contact Formation

The theory of rectifying barrier formation between metals and semiconductors was first published by Schottky [2] in 1939. An outline of this is presented below.

Consider the case, shown in figure 6.2a, of a metal with a work function ϕ_M and a p-type semiconductor with a work function ϕ_S and an electron affinity χ_S. The work functions of both the metal and semiconductor are defined as the energy required to raise an electron from the Fermi Level to the Vacuum Level without giving it kinetic energy. χ_S is defined as the energy difference between the Vacuum Level and the minimum of the Conduction Band.

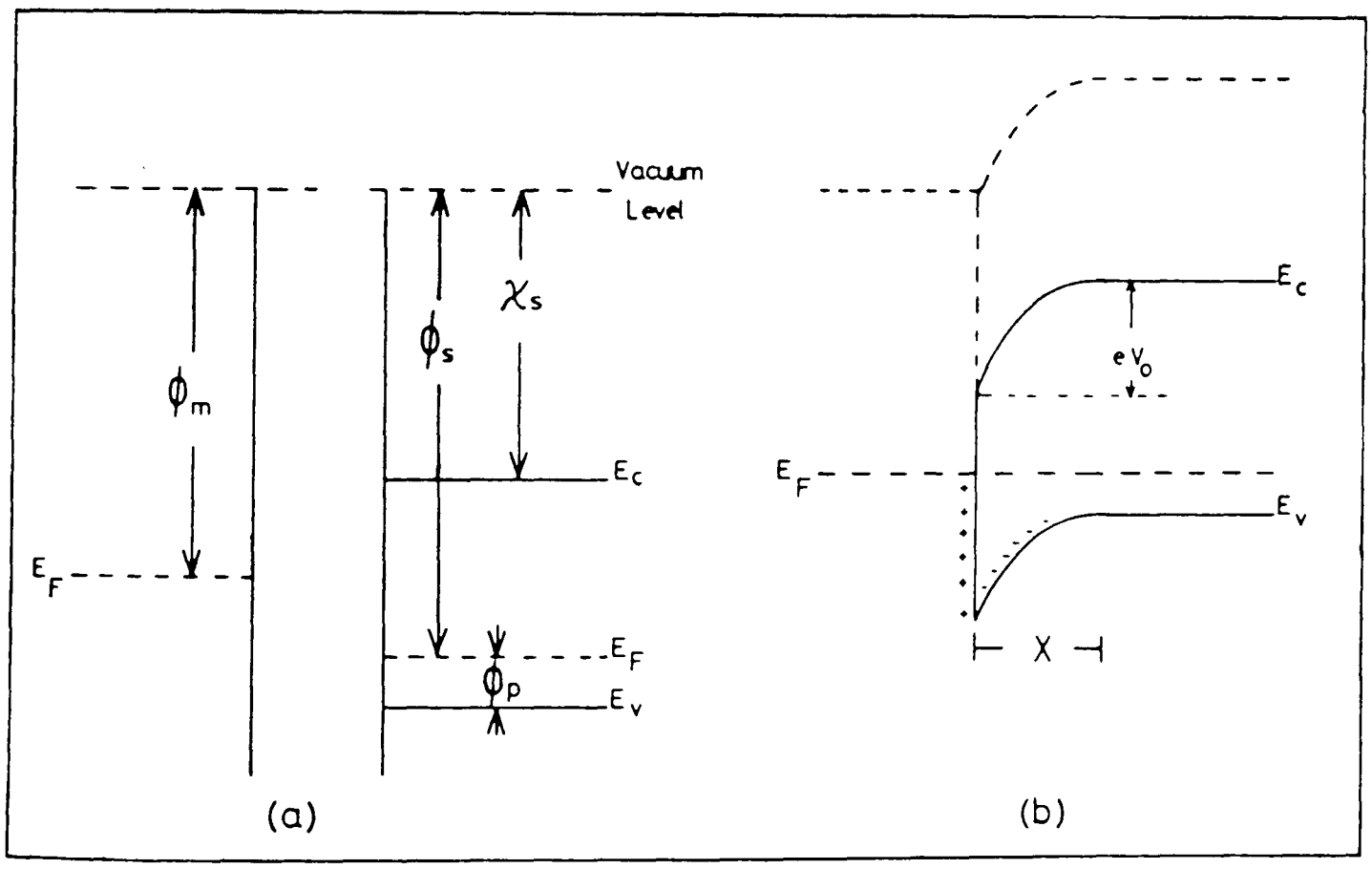

Figure 6.2 Electron energy band diagrams for metal - P-type semiconductor contact with work functions ϕ_m ϕ_s respectively. (a) neutral and separated materials. (b) thermal equilibrium situation after contact is made.

When the metal and semiconductor are brought into contact the two Fermi Levels must align (for a system in thermal equilibrium) by electrons flowing from the metal into the semiconductor. These electrons are minority carriers and recombine with acceptors in the material to form a space charge layer of ionised acceptors. The energy band diagram for this system is shown in figure 6.2b. Since χ_S is unaffected after contact formation and since the vacuum levels must be continuous across the barrier the degree of band bending depends only on the difference in work functions. This difference, V_0, is known as the contact potential and is

$$V_0 = (\phi_s - \phi_M)/q \qquad (2)$$

where q is the electronic charge

The barrier height, ϕ_B for holes is given by

$$\phi_B = \chi_S + E_g - \phi_M \qquad (3)$$

the quantity ϕ_p is given by

$$\phi_p = \chi_S + E_g - \phi_S \qquad (4)$$

thus

$$\phi_B = qV_0 + \phi_p \qquad (5)$$

As the metal semiconductor contact is reverse biased V_0 changes to V_0+V and, as is seen from equations (1) and (5), both X and ϕ_B increase and little current flows. ϕ_B increases more rapidly with respect to X with the result that the region close to the interface becomes narrower and eventually carriers are able to tunnel through the barrier. The contact is

then said to have broken down and a rapid increase in current flow occurs.

The behaviour of the real metal-semiconductor contact can deviate greatly from that of the simple Schottky approximation. These deviations are due, in the main, to the state of the surface of the semiconductor and can cause small depletion regions and large leakage currents in the device.

Bardeen [3] explained the effects of the surface on the contact properties in terms of the presence of localised surface states. These states were present because the lattice periodicity ended at the surface and therefore each surface atom possessed unpaired electrons that would have, in the bulk, been used in bonding. These bond electrons he termed "dangling bonds". The dangling bonds give rise to localised states within the band gap which were able to modify the charge in the depletion region and the barrier height. Bardeen showed that if the density of surface states was large enough then when the metal was brought into contact with the surface the flow of charge required to align the Fermi levels would take place entirely between the metal and the surface. The barrier height and depletion region width would therefore be less than expected. Rhoderick and Northrop [4] showed that the presence of an oxide layer at the interface of the contact could also adversely affect the contact properties. The effects were shown to depend on oxide layer thickness and that below about 20Å the layer became transparent to the electrons. As the layer thickness increased then more and more of the applied potential was dropped across this insulating oxide layer. This meant that less was dropped across the semiconductor which affected the depletion width.

6.2 The Polarisation Effect in ZnTe Detectors

The effect of polarisation is to cause a decrease in both the signal amplitude and counting rate of a detector. It occurs as a consequence of a high concentration of trapping centres in the material and therefore the time dependence of the effect should be affected by the capture cross-section and depth of the trap (or traps).

The polarisation effect in the early crystal counters was described by Hofstadter [5] as a progressive reduction of the electric field within a detector and explained as being due to the time dependent increase of the occupancy of deep levels located either in the bulk or close to the surface of the device. In this description it was assumed that the trapped charge carriers were initially generated by the incident radiation.

However, Siffert et al [6] have shown that the polarisation effect in chlorine doped cadmium telluride radiation detectors occurred even in the absence of a radioactive source and consequently proposed a different model to explain the polarisation effect. In this model carrier injection from the contacts is proposed as the mechanism for the supply of the carriers to be trapped. This model assumes that initially the device material is an insulator with an electron trapping level located just above the Fermi level in the bulk of the material.

In thermal equilibrium the free electron density may be given by

$$n = N_C \exp[(E_F - E_C)/kT] \qquad (6)$$

where N_C is the density of states in the Conduction Band

The density, n_T, of traps of depth E_T, that are occupied by electrons is given by

$$n_T = N_T \, [1 + \exp[\, (E_T - E_F)/kT \,]]^{-1} \qquad (7)$$

where N_T is the total density of traps

When an electric field is applied there will be a change in the free carrier density due to injection [7]. The balance between free and trapped electrons will alter with the free carrier density.

With each position, x, measured perpendicular to the surface, the free and trapped electrons will still be in thermal equilibrium but the Fermi level, $E_{F(x)}$, will alter with the free electron concentration, $n_{(x)}$, which varies with distance from the positive electrode. In this case the equations (6) and (7) may be re-written as

$$n_{(x)} = N_C \exp[\, (E_{F(x)} - E_C)/kT \,] \qquad (8)$$

$$n_{T(x)} = N_T \, [1 + \exp[\, (E_T - E_{F(x)})/kT \,]]^{-1} \qquad (9)$$

As the injection level increases the Fermi level will shift towards the Conduction Band and as the Fermi level moves through the trapping level the traps will become filled, producing a space charge within the device. This space charge will then modify the electric field causing a reduction in detector efficiency.

6.3 Experimental Details

The boules were sawn and lapped in alumina to provide single crystals of up to 1 cm in diameter and 2 mm thickness. These were then polished to gamma grade (0.5 μm diameter powder) before being etched for 10 seconds in a solution of 10 % bromine in methanol to remove the damage caused by the mechanical polishing.

Contacts were then formed on each face by evaporating approximately 100 Å of aluminium onto the crystal. Gold wires were attached to the contact using an indium cold welding procedure and the performance of the device as a detector was then assessed using the arrangement shown in figure 6.3.

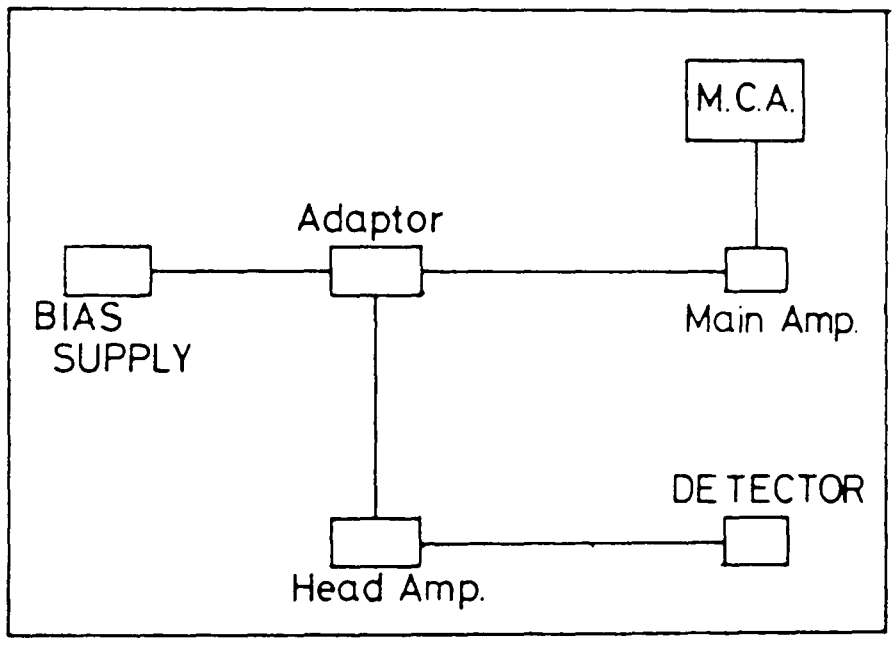

Figure 6.3 Representation of experimental arrangement for assessment of detectors.

The crystal was attached via an AERE head amplifier to a multi channel analyser (MCA). Using this arrangement bias voltages of between 10 to 300 volts were available with the radiation incident upon either contact.

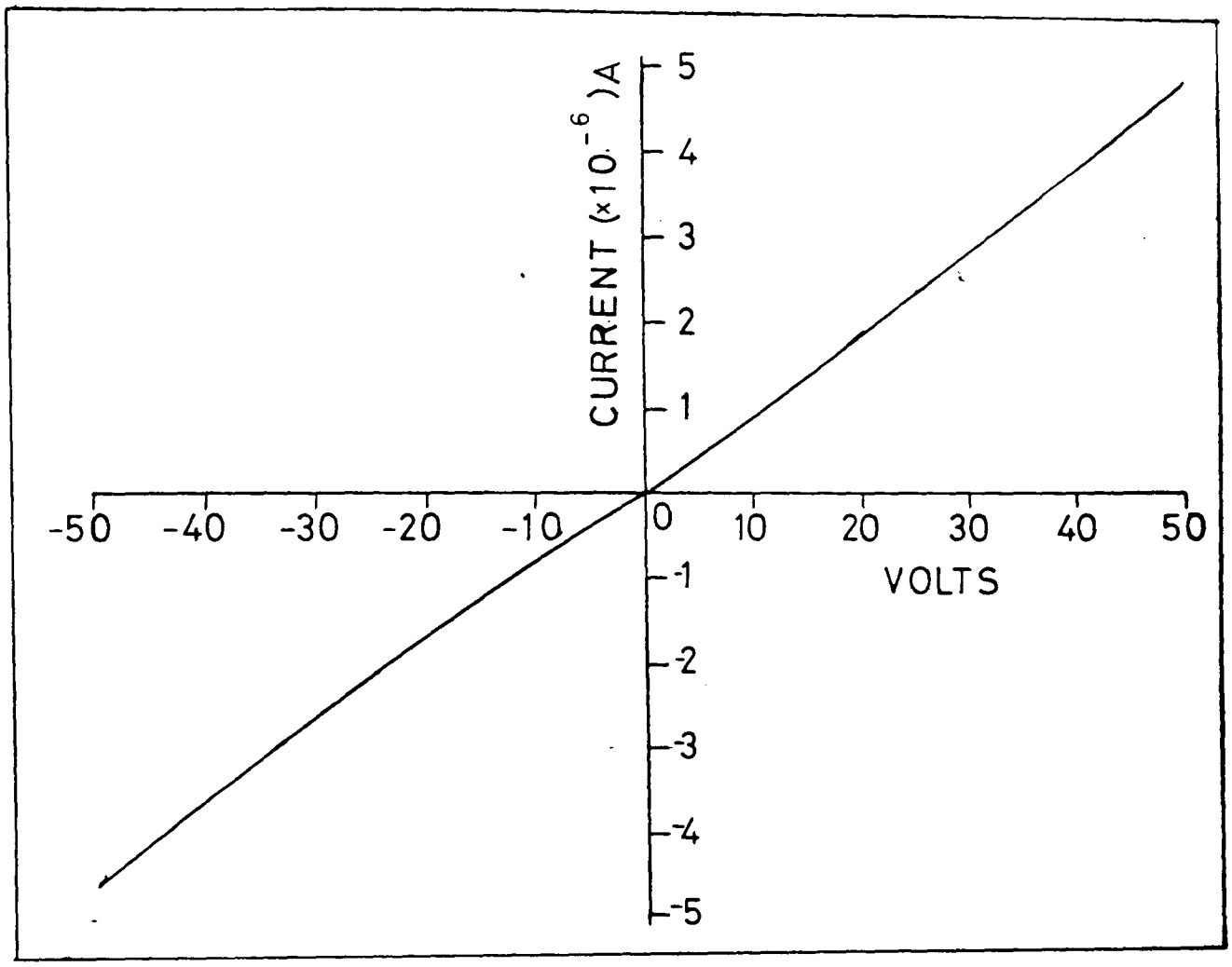

Figure 6.4 I - V characteristics of aluminium contacts on the material.

Figure 6.5 Alpha - particle spectra obtained using the aluminium doped material CPB8.

(a) The initial spectrum when the +20 V bias was applied.

(b) The spectrum obtained after three hours irradiation under a bias of +20 V.

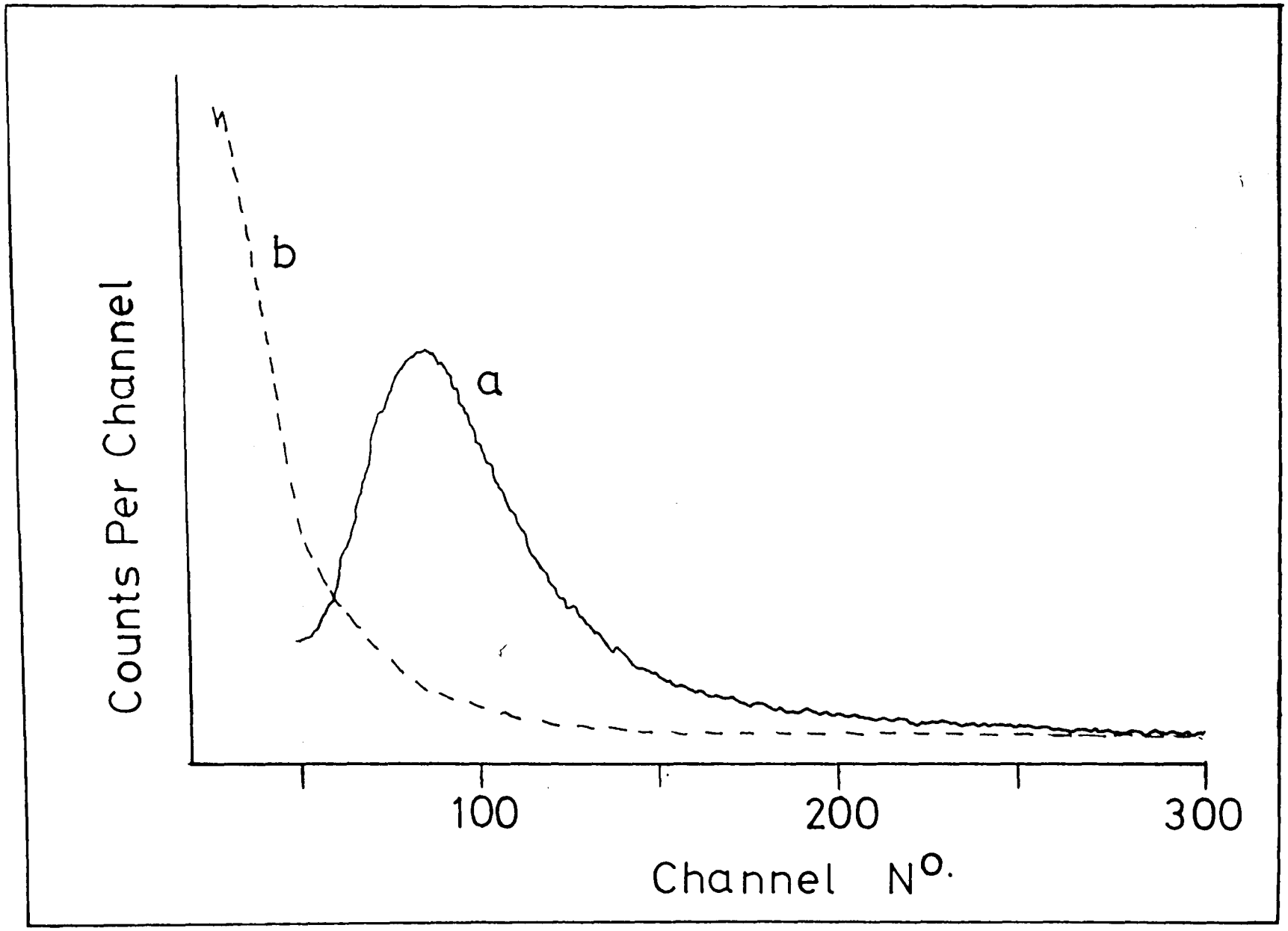

Fig. 6.5

6.4 Results and Discussion

High resistivity samples of ZnTe doped with indium, aluminium and lead were formed into a total of 12 devices which were evaluated as nuclear radiation detectors. It was found that only one sample from CPB8 was able to detect nuclear radiation, in the form of α-particles, but was unable to detect gamma-rays.

The I-V characteristics of the aluminium contact ,on both indium and aluminium doped material, is shown in figure 6.4 and, as can be seen, shows an almost ohmic behaviour.

Figures 6.5 show the spectra produced by the device under a bias of +20 V when the positive contact was irradiated by 5.48 MeV α-particles produced from a ^{241}Am source. Figure 6.5a shows the spectrum obtained when the bias was initially applied and 6.5b is that spectrum obtained after three hours irradiation under bias. This degradation of signal with time is known as the polarisation effect and figure 6.6a indicates how the count rate varied with time. When this data was plotted on a semi-log scale (fig 6.6b) it was seen that the decay of the count rate occurred with two different time constants.

Assuming Siffert's model of the polarisation effect in which injected carriers are trapped by a defect having a characteristic trapping time constant, τ, of the form

$$\tau = 1/nS_T V_e \qquad (10)$$

where S_T is the capture cross-section

V_e is the thermal velocity

n is the free electron density

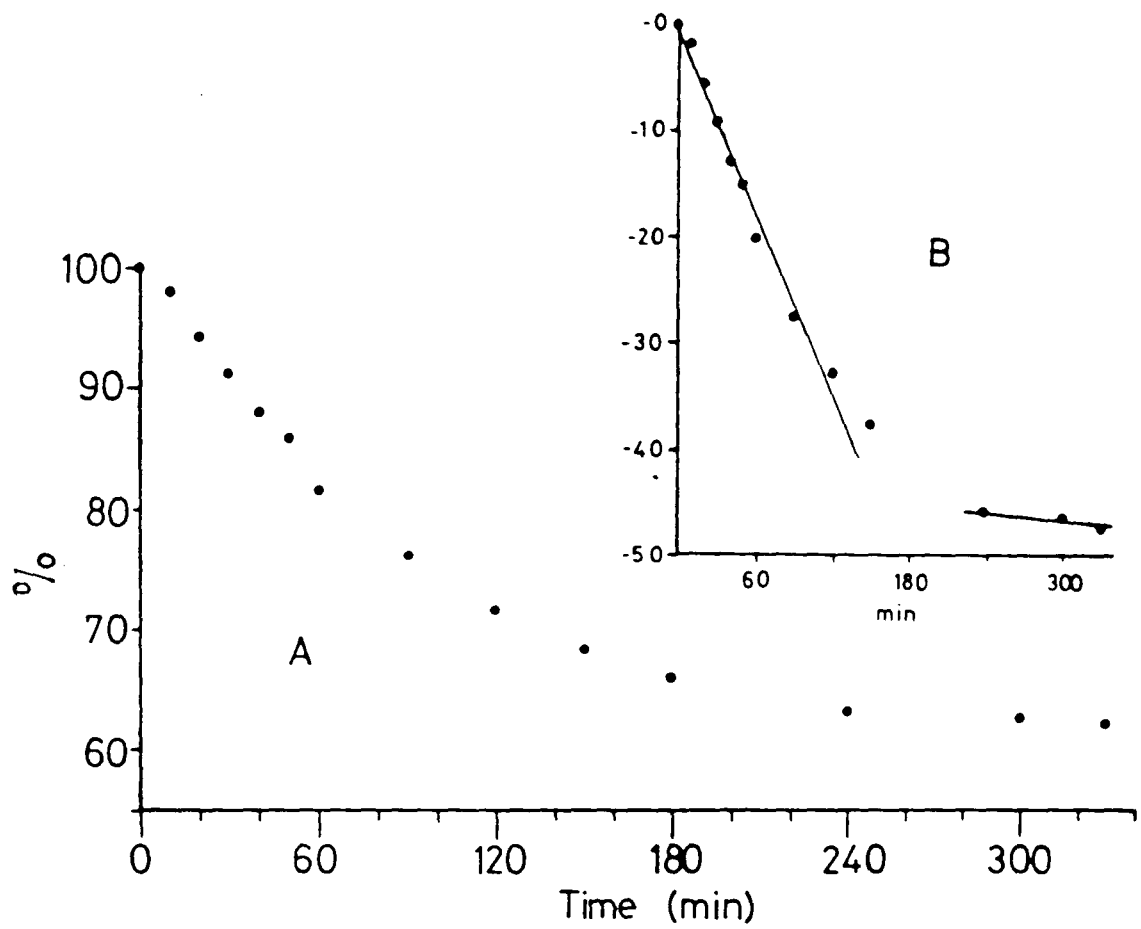

Figure 6.6 Variation of count rate with time.

(A) shows the percentage change with time.

(B) the same data plotted on a semi-log scale.

then there must be two different types of trapping centre in the material to account for the observed form of the count rate decay with time since the polarisation time constant must depend upon S_T.

This device was found to be incapable of detecting γ-rays. A possible expla nation for this is related to the fact that γ-rays penetrate the entire volume of the device causing carriers to be generated mainly within the bulk of the device. If the material contains many trapping centres the carriers generated by the gamma-rays may be trapped and detrapped many times before collection at the contacts. This would broaden the signal detected by the MCA and if the trapping was severe then the carriers may not produce a signal at all. The α-particles, on the other hand, have a penetration depth of only a few μm in ZnTe and therefore electron-hole pairs are generated close to the contact which is being irradiated. Because of this carriers generated by the α-particles will undergo less trapping and detrapping processes before they reach the contacts. It is possible, therefore, that a device containing many trapping centres may detect α-particles but not γ-rays.

Another cause of the lack of signal from gamma-ray interactions in a device which will detect α-particle generated carriers may be the presence of a small depletion region within the device. Again, because of the greater penetration of the gamma-rays, the majority of interactions would remain unobserved in such a case. Since the α-particles generate carriers only close to the incident face of the detector the presence of a small depletion region would still enable their detection to be made. This explanation as the cause of the lack of signal from gamma-ray interactions is supported by the observation that when the bias polarity was reversed no signal due to the α-particles was recorded. When the bias is reversed the depletion region will extend from the opposite contact to the one being irradiated. If the depletion region did not extend the entire width of the device the

α-particles would remain undetected since the penetration depth of the radiation is very small compared with the thickness of the device and all of the electron-pairs will be generated outside the depletion region.

It is expected, from equation (1), that the depletion width, X, should be $\sim$2 cm in a device operating under a 50 V applied bias, assuming ρ = 1 x 10^6 Ω cm ; μ = 100 $cm^2V^{-1}s^{-1}$. This means that in the devices fabricated for this study the depletion width should extend across the entire width of the detector. The effect of reversing the applied bias on the α-particle signal, described above, showed that this, infact, did not occur. The three physical parameters of the ZnTe detector that affect X are ρ , μ and V. The resistivity, ρ, of all the material that was fabricated into devices was measured using the Van der Pauw technique and found to be 10^5 - 10^6 Ωcm and is sufficiently large to give a depletion region across the entire width of the devices studied providing the entire voltage was dropped across the device. Therefore it is the carrier mobility and a small voltage drop across the device which adversely affect X. Both the voltage drop across the device and the observed poor quality Schottky contacts (see figure 6.4) may have been affected by the presence of surface states. The mobility of the carriers may have been reduced by the presence of the large number of trapping centres which were detected in the material through TSC and mobility measurements (Chapter Four) and which leads to the charge carriers undergoing many trapping and detrapping processes. It is therefore likely that the existence of a small depletion region within the device and a large number of trapping centres caused the gamma-ray interactions to remain undetected.

6.5 Conclusions

Both the presence of traps and a small depletion region may account for the poor device performance observed in the present studies. The presence of two deep trapping centres in the material is thought to contribute to the polarisation effect which has been shown to be present in this material and shallower traps, such as those observed in the TSC studies presented in Chapter Four, with trapping times less than the transit time of either carrier may be responsible for the observed lack of response to gamma-rays.

It is interesting, and disappointing, to note that only one out of the twelve devices investigated has been able to detect nuclear radiation. Even material from adjacent positions in the same boule has failed to produce a similar device even though this exhibited essentially the same optical and electrical properties as the sample from which the device was fabricated. As the samples were similar before device fabrication the differences are likely to have been introduced during the fabrication procedures i.e. the sample polishing and contacting stages. These procedures mainly affect the condition of the surface of the material and as was noted in Section 6.1.2 the condition of the surface plays an important role in contact formation. The condition of the surface could, in part, explain the poor quality Schottky contacts found on these devices.

CHAPTER SIX REFERENCES

[1] Sze S.M., Phys. Semicond. Dev. Chap 2 (Published J. Wiley and Sons, New York 1981)

[2] Schottky W., Z. Physik 113 367 (1939)

[3] Bardeen J., Phys. Rev. 71 717 (1947)

[4] Northrop D.C. and Rhoderick E.H., Variable Impedance Devices Chap 2 Ed. Howes and Morgan (Published J. Wiley and Sons, New York 1978)

[5] Hofstadter R., Nucleonics 2 29 (1949)

[6] Siffert P., Berger J., Scharger C., Cornet A. and Stuck R., IEEE Trans. Nuc. Sci. NS-23 159 (1976)

[7] Rose A., Phys. Rev. 2 97 (1955)

CHAPTER SEVEN

Conclusions and Suggestions for Future Work

7.1 Conclusions

The main aims of this study were the production and characterisation of high resistivity zinc telluride with the purpose of determining the feasibility of it's use as a material for the fabrication of nuclear radiation detectors. The results presented in the previous chapters serve to indicate that although high resistivity material could be grown by compensation using the Bridgman technique the majority of the material was not suitable even for radiation counter material.

As grown ZnTe exhibits a highly p-type conductivity. By comparing the results obtained from the photoluminescence studies with the results of similar studies by other authors it has been found that the conductivity is dominated by the presence of shallow acceptors due, not to native defects, but to impurity atoms such as lithium and copper. These produce the neutral acceptors Li_{Zn} and Cu_{Zn} which have activation energies of E_V + 0.06 eV and E_V + 0.146 eV respectively and which manifest themselves in the neutral bound exciton lines that have been observed in the luminescence studies.

In an attempt to produce high resistivity material elements from Groups III, IV and VII of the Periodic Table were introduced into the ZnTe during growth. It was expected that these elements would introduce shallow donors into the material which would compensate the shallow acceptors. Doping with either the Group IV (Pb and Sn) or the Group VII (F) elements has proven to be an unsuccessful method of producing the required high resistivity. This aim was achieved by doping with the Group III elements aluminium and indium. However acceptor levels associated with these elements were also produced.

The $(V_{Zn}\ Al_{Zn})'$ acceptor was observed in the photo luminescence studies on the aluminium doped material. It was seen from these studies that the visible luminescence was dominated by a broad DAP band between 2.16 and 2.18 eV. ODMR studies by Cox et al [1] showed that a similar band involved the recombination between the $(Al_{Zn})^{\bullet}$ and the above acceptor. Larsen et al [2] calculated the activation energy of this acceptor to be between 0.22 and 0.25 eV which concurs with the photoluminescence measurements made in this study.

TSC measurements carried out on aluminium doped material revealed the presence of only one type of trapping level, a hole trap with a thermal activation energy of 0.13 $\pm$ 0.03 eV. The identification of which was suggested to be the $(V_{Zn}Al_{Zn})'$ acceptor. Similar studies carried out on indium doped material suggested the presence of an isomorphic centre. The $(v_{Zn}In_{Zn})'$ possesed a thermal activation energy of 0.09 $\pm$ 0.03 eV and was observed in all indium doped material. Other, deeper, hole traps were also observed in the indium doped material which, from their observed behavior when additional indium was added, are thought to involve the dopant. All of the trapping levels observed in the TSC studies were found to be present in concentrations in excess of 10^{16} cm^{-3}.

None of the material that was grown for this study produced a device capable of detecting γ - rays, even at room temperature. The main conclusion to be drawn from this study must therefore be that although high resistivity material was grown by the Bridgman process, using the compensation technique, the material produced from this posessed high concentrations of dopant related hole trapping centres making it unsuitable for fabrication into nuclear radiation spectrometers.

7.2 Suggestions for Future Work

The process of compensation used in this study to achieve the high resistivity material has been shown to have one major limitation namely the production of deep hole traps associated with the dopant. As the dopant is introduced to compensate shallow acceptors present in the material which are due to impurities another method of producing the high resistivity is available that involves either the purification of the starting material (a source of the impurities) or the purification of the grown material by the multi-pass technique developed by Triboulet et al [3] and used with some success on CdTe.

The evaporation of metal on to the surface of ZnTe, used in this study as the method of contact formation onto the material, has been shown to be unreliable. A possible cause of this unreliability was indicated as being a damaged or contaminated surface and indeed several authors [4,5] have previously reported that such surface conditions for CdTe proved detrimental to contacts deposited on that surface. It was shown by Bilbe [6] that pulsed laser annealing of the surface of CdTe resulted in the removal of surface damage and, as a consequence, better contact characteristics. It is therefore recommended that future investigations into the use of this method of surface preparation before contacts are deposited be carried out. Pulsed laser annealing of metal contacts deposited onto the surface of CdTe [7] has been shown to result in reproducible contact formation. It is possible that this technique when applied to ZnTe will have similar results and therefore it should be investigated as a means of contact formation.

CHAPTER SEVEN REFERENCES

[1] Cox R.T., Bittebierre J., Phys. Rev. B 34 N°. 4 (1986)

[2] Larsen T.L., Varotto C.F., Stevenson D.A., J, Appl. Phys. 43 172 (1972)

[3] Triboulet R., Marfaing Y., J. Crystal Growth 51 89 (1981)

[4] Dabrowski A.J., Chaszewska J., Iwanczyk J., Triboulet R., Marfaing Y., Rev. Phys. appl. 12 297 (1977)

[5] Ponpon J.P., Appl. Phys A27 11 (1982)

[6] Bilbe R.M., PhD Thesis University of Hull (1983)

[7] An C., Tews H., Report to American Inst. Phys. (1982)

CHAPTER EIGHT

Determination of the Signs of the Electron g-Factors in II-VI Materials

Introduction

Band structure calculations have played a fundamental role in understanding the behaviour of semiconductors. Such calculations are undertaken using $\vec{k}.\vec{p}$ perturbation theory.

In this respect measurements of the Lande g-factor for electrons in semiconductors is of fundamental interest as this parameter is one of the few quantities that can easily be calculated from $\vec{k}.\vec{p}$ perturbation theory. It may therefore be used to test the validity of the assumptions used in the theoretical calculation of band parameters.

The g-factor can, and has been, measured accurately in several ways, notably by magnetic resonance, Zeeman spectroscopy and studies of magnetic circular polarisation. Although these techniques produce, in most cases, agreement in the magnitudes of the g-factor there is some dispute as to it's absolute value, i.e. as to whether the value is a positive or negative quantity. This dispute arises because the sign of the g-factor can only be deduced indirectly through the monitoring of optical transitions and therefore is reliant upon assumptions about the optical selection rules.

This uncertainty in the absolute value of the g-factor hinders the comparison between theory and experiment. In this Chapter a method of determining the signs of the g-factors of shallow donor electrons directly is described. The technique is then applied to the shallow donor systems in CdS, ZnS, ZnSe and ZnS_xSe_{1-x} (x=0.6). A tentative assignment to the sign of the electron g-factor in CdTe is also made from the results of ODMR studies in $CdS_{1-x}Te_x$ (x=0.02).

8.1 Previous Assignments to the Signs of the g-Factors

Theoretical calculations of the conduction electron g-factors in the II-VI compounds were carried out by Cardona [1] using both the three band k.p approach [2] and the two band Roth's formula [3]. The latter is given below:

$$g^*/g_o = 1 - (\Delta /(3E_g - 2\Delta) \times (m_o/m^* - 1)) \qquad (1)$$

where g_o and m_o are the g-factor and mass of the free electron; g^* and m^* are the effective values in the material; E_g the material's band gap and Δ is the Spin-Orbit splitting of the material's valence band.

In this way Cardona showed that in theory the signs of electron g-factors for ZnS, ZnSe, ZnTe, CdS and CdSe were positive and that for CdTe was negative.

From early Zeeman studies of bound excitons in CdS Hopfield [4] and Thomas and Hopfield [5] both determined the sign of the electron g-factor to be negative. However in later papers, concerning spin flip Raman scattering in CdS, Thomas and Hopfield [6] quoted the electron g-factor without a sign, but probably assumed it to be positive. A positive sign for the g-factor in CdS was also quoted by Henry et al [7] from Zeeman studies on the same material.

Free exciton magneto reflectance studies carried out in ZnSe by Venghaus [8] yielded a positive sign for the electron g-factor. A positive sign was also determined by Holsher et al [9] from two photon absorption studies on excitonic states in this material. Magnetic studies on circularly polarised emission from DAP transitions in ZnSe also led Cavenett and Hagston [10] to assign a positive value to the electron g-factor.

MATERIAL	SIGN	REFERENCE
CdS	+ ve	[1]
	- ve	[4]
	- ve	[5]
	+ ve	[6]
	+ ve	[7]
	+ ve	This work
CdSe	+ ve	[1]
CdTe	- ve	[1]
	- ve	[17]
	- ve	[18]
	- ve	[19]
	+ ve ?	This work
ZnS	+ ve	[1]
	- ve	[11]
	+ ve	[12]
	+ ve	This work
ZnSe	+ ve	[1]
	+ ve	[8]
	+ ve	[9]
	+ ve	[10]
	+ ve	This work
ZnTe	+ ve	[1]
	- ve	[13]
	- ve	[14]
	+ ve	[15]
	+ ve	[16]

TABLE 8.1 The signs of donor g-factors in II-VI compounds :-
A comparison between past and present work.

Wheeler and Miklosz [11] carried out Zeeman studies on the bound exciton states in ZnS from which they determined the sign to be negative. This was later am ended to a positive sign by the same authors [12].

Zeeman studies on neutral donor bound excitons in ZnTe have led to the deduction of a negative g-factor by Schmieder et al [13] and Romestain et al [14]. However magneto optical investigations using selective pair luminescence (SPL) on the lithium DAP band in ZnTe:Li [15] indicated the sign to be positive. Killoran et al. [16] also proposed a positive sign from ODMR studies in ZnTe:P

A negative value for the electron g-factor in CdTe has been deduced from magneto luminescence [17], from ODMR [18] and from NMR measurements on the Cd^{113} nucleus [19].

The literature cited here servesto indicate that different authors, studying the same system, can deduce conflicting signs of the electron g-factor. In the case of the CdS literature conflicting reports have been found for the same system studied by the same group.

The results of this Section, together with the results presented in this Chapter, are summarised in table 8.1.

8.2 Determination of the Signs of g-Factors Using Magneto Optical Methods

Determination of the sign from Zeeman and other magneto optical studies on the various semiconductor systems previously mentioned is made indirectly. This evaluation relies on assumptions about optical selection rules. Some confusions that may arise in this process will be illustrated in this Section.

Consider the case of an exciton (comprising a hole from the heavy hole band) bound to a neutral shallow donor, $D^{o}X$. In a magnetic field the energy

levels of the ground and excited states are split by the Zeeman interaction. The energies of the resultant levels are described by

$$E = \beta g B M_J \qquad (2)$$

For the D^oX centre the excited state comprises the energy states of the hole only, as the spins of the donor and the exciton electrons are anti-parallel and are said to be paired. The ground state of the system is that of the neutral donor. The energy levels of such a system are shown in figure 8.1.

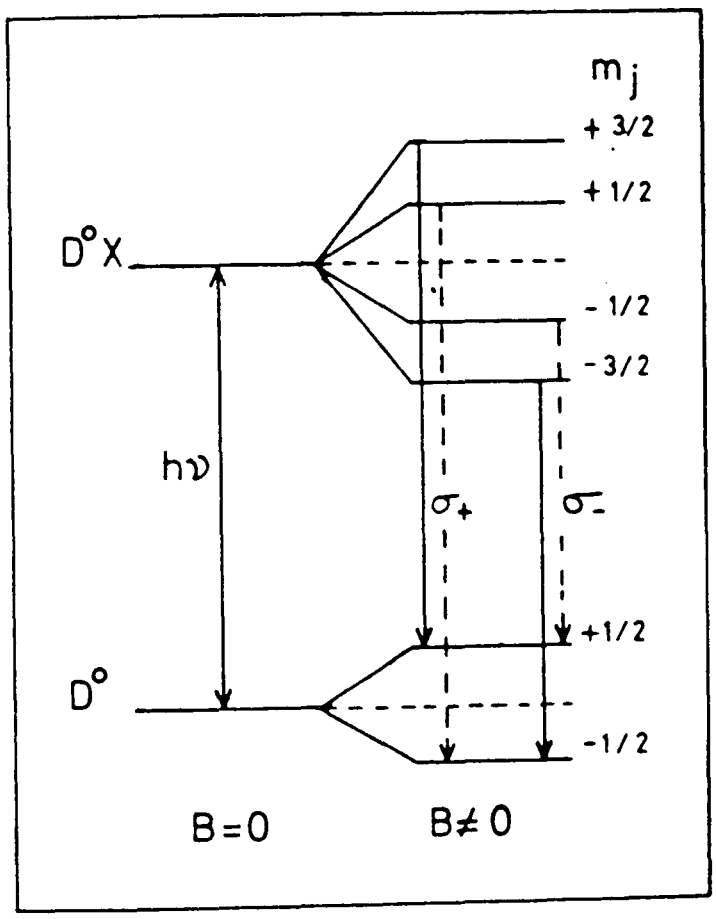

Figure 8.1 Energy levels of a neutral donor bound exciton in a magnetic field, B.

Here the energy levels are calculated using the convention of describing the spin of the hole as being the spin of the remaining unpaired electron in the Valence Band (the signs of the spin states of the hole would be reversed if the opposite convention of describing the hole spin as that of the removed electron was used) and the sense of polarisation of the emitted photon is described using a convention that the emitted photon is

right circularly polarised, σ_+, if it carries with it +1 unit of angular momentum and that the emitted photon will be left circularly polarised, σ_-, if it carries -1 unit of angular momentum (this latter convention is generally but not always [13] used).

By studying the energies of the σ_+ and σ_- components of the luminescence of such a system the g-factor may be deduced for the transitions shown by solid lines in figure 8.1 (a similar argument applies for those transitions described using the broken lines) as follows:

In the case of the electron g-factor being positive the σ_+ component of the emission will have the energy

$$E_+ = h\nu + \frac{3}{2} g_h \beta B - \frac{1}{2} g_e \beta B$$

If the sign of the electron g-factor is negative then the signs of the m_j levels of the ground state of figure 8.1 will be reversed (the highest energy state is now the - 1/2 state) and the energy of the σ_+ component will now be

$$E_- = h\nu + \frac{3}{2} g_h \beta B + \frac{1}{2} g_e \beta B$$

These energies of emission are clearly different and therefore by monitoring the energy positions of the σ_+ emissions the sign of the electron g-factor may be deduced. Using this method confusion as to the sign of the g-factors could arise if the sense of circular polarisation was not correctly interpreted, perhaps because of the implementation of a different convention for describing σ_+ and σ_-.

It is important to note that all of the methods described above are also model dependent and therefore if the model proposed to describe the emission process was incorrect then the signs of the g-factors could also be incorrect.

8.3 Theoretical Considerations of Experimental Method

From data presented in this Chapter the signs of the g-factors of the shallow donor electrons in CdS, ZnS, ZnSe and ZnS_xSe_{1-x} (x=0.6) have been directly determined, whilst that in CdTe has only been inferred from conventional ODMR measurements on the $CdS_{1-x}Te_x$ (x=0.02) system. These direct measurements have been achieved by using a variation of the standard technique of ODMR which employs a circularly polarised microwave magnetic field. As there are a number of excellent reviews concerning conventional ODMR [e.g. 20,21] this section only deals briefly with the concept of ODMR and illustrates how, by using a circularly polarised microwave magnetic field the signs of the g-factors are determined directly, without relying on measurements of the circularly polarised luminescent emission or on models that describe that emission.

Consider the case of the simple DAP recombination process illustrated in figure 8.2a where both the donor electron and acceptor hole have spins of S=1/2. Upon application of an external magnetic field, B, both the donor and acceptor energy levels are split due to the Zeeman interaction. Recombination now is spin dependent with the electrons and holes having anti-parallel spins more likely to recombine (Pauli exclusion principle).

Using the same convention as the previous Section and taking the spin of the hole as the spin of the remaining unpaired electron the energy level diagram of the spin system in a magnetic field will be that shown in figure 8.2b. The most probable, spin conserving, DAP luminescencent transitions are shown together with the microwave transitions that occur during ODMR experiments. Thus, providing that spin - lattice relaxation is slow compared with the recombination times, levels 2 and 3 rapidly become depleted and at resonance population is transferred to the emitting states increasing the luminescence. It is this increase that is monitored during ODMR.

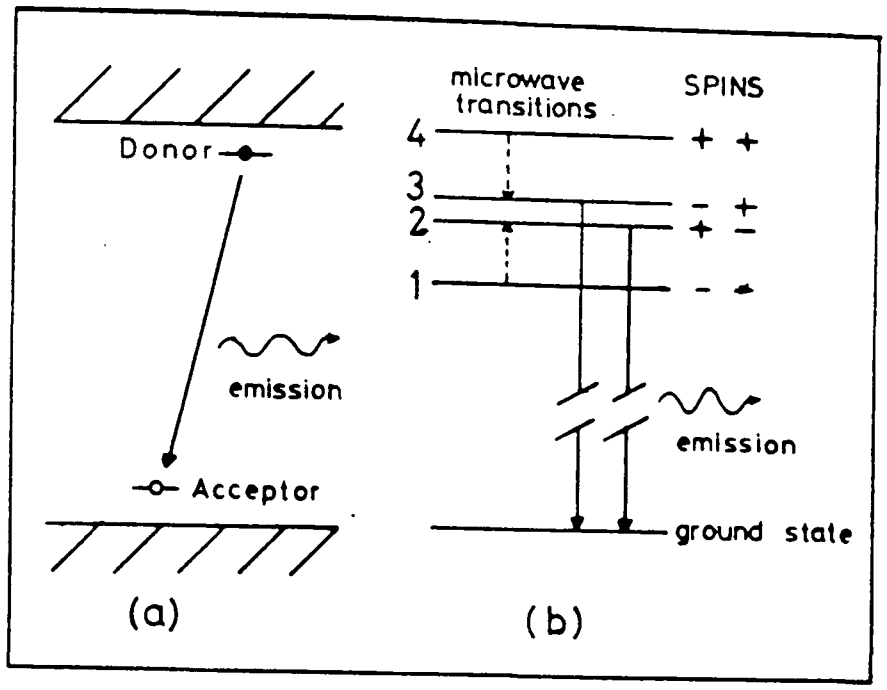

Figure 8.2 (a) Simple DAP recombination process.

(b) Energy level diagram of donor-acceptor spin states in a magnetic field. Allowed optical transitions are shown together with the donor magnetic resonance transitions.

In conventional ODMR the microwave magnetic field, B', is always linearly polarised. However, in an experiment to directly determine the sign of the g-factor, the microwave magnetic field has to be circularly polarised about an axis (taken to be the z axis) parallel to the direction of the external field, B.

For an isotropic centre with $S=\frac{1}{2}$ the Spin Hamiltonian may be written as

$$\mathcal{H} = \beta g\underline{B}.\underline{S} = \beta gBS_z \qquad (3)$$

The effect of B' is to produce a perturbation term to be added to this

Hamiltonian which takes the form

$$\mathcal{H}' = \beta g(B'_x S_x + B'_y S_y) \qquad (4)$$

For the case of a circularly polarised B' $B'_x = B' \cos wt$ and $B'_y = B' \sin wt$ where $w/2\pi$ is the microwave frequency, ν, so that

$$\mathcal{H}' = \beta gB\ (S_+ e^{-iwt} + S_- e^{iwt})/2 \qquad (5)$$

The effect of the operator $\mathcal{H}'$ is to induce transitions from $M_s = +1/2$ to $M_s = -1/2$ and vice versa. The probability of finding the system (originally in the state M_s) in a state $M_s \pm 1$ after a time, t, is given by [22]

$$(\beta gB')^2 \ < M_s \pm 1 | S_\mp | M_s >^2 \quad \frac{\sin^2[(\hbar w - \beta gB)t/2\hbar]}{(\hbar w - g\beta B)^2}$$

$$= (\beta gB')^2 \frac{\sin^2[(w - w_L)t/2]}{\hbar^2 (w - w_L)^2} \qquad (6)$$

where $w_L/2\pi$ is the Larmor frequency = $\beta gB/h$

Thus it can be seen that the transition probability is high only if $w = w_L$ and <u>not</u> if $w = -w_L$. This can be visualised in terms of a semi classical model, shown in figure 8.3, in which the electron (posessing a spin S and a magnetic moment $\mu = -\beta gS$) precesses about the external magnetic field.

If both the sense of rotation of B' and its angular frequency are the same as those of the Larmor precession of the magnetisation vector then microwaves will be absorbed. In the case shown in figure 8.3 this means that microwaves will be absorbed when $w = w_L$ i.e. only for a positive g-factor.

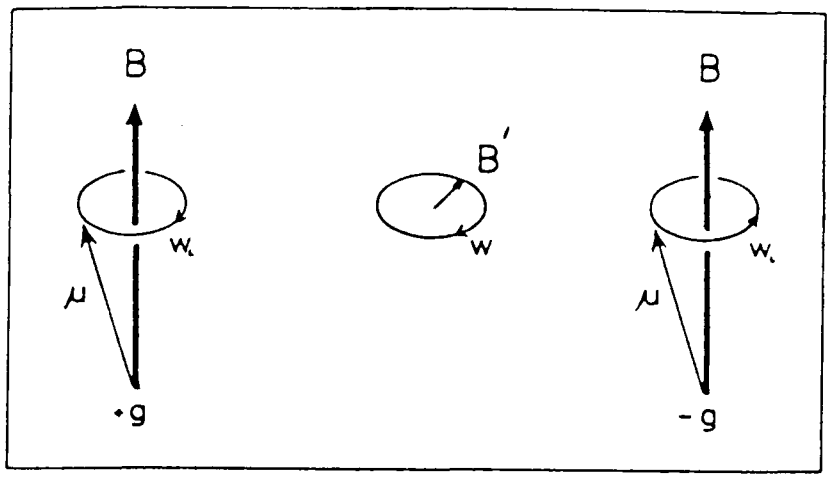

Figure 8.3 Larmor precession of μ with angular frequency w_L for a + ve g factor. A comparison with the sense of rotation of microwave magnetic field B' possessing an angular frequency w.

In the case of the DAP recombination shown in figure 8.2 both of the microwave transitions will be induced for $\hbar w = \beta gB$ but neither will be induced for $\hbar w = -\beta gB$ (assuming g to be positive). If the external field (B) is reversed then the sense of the Lamor precession of μ is reversed and now neither microwave transition show in figure 8.2 will be induced at resonance (assuming g to be positive).

So by monitoring the ODMR signal at resonance the sign of the g-factor can be determined directly from the change of the signal size that results from the reversal of the external magnetic field. This is done by comparing the intensity of the ODMR signals for the two senses of the external magnetic field. In one direction of the external field the the angular precesion of the electron spins should be in the opposite sense to that of the microwave magnetic field and therefore no ODMR signal should be

observed.

8.4 Experimental Method

The method of obtaining the circularly polarised microwave magnetic field is similar to that described by Pake and Estle [23]. The arrangement used for these studies is shown in figure 8.4.

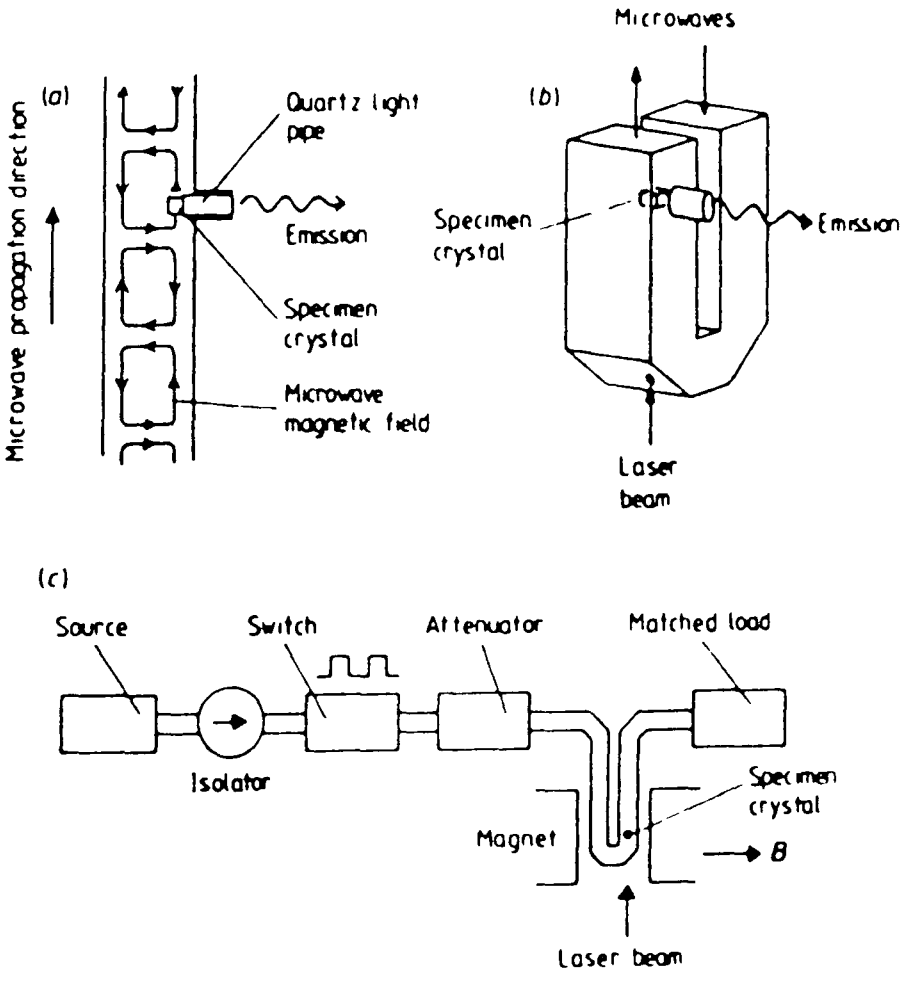

Figure 8.4 Experimental arrangement for detection of ODMR with circularly polarised microwave field.

The specimen is placed on one side of a standard rectangular X-band waveguide along which passes a travelling wave (fig. 8.4a). As the wave passes the specimen the microwave magnetic field, B', will rotate about an axis perpendicular to the broad side of the wall of the guide. The external

field, B, is also orientated parallel to this axis and it is only for the correct sense of rotation of B' relative to B that resonance occurs. For resonance to occur for a specimen with a g-factor of opposite sign, placed in the same position in the guide, the direction of B' has to be reversed. Resonance would also occur if that specimen was placed in the opposite side of the guide (maintaining the original direction for B). Thus by monitoring the intensity of the ODMR signal for both directions of the external field the sign of the g-factor can be determined.

The correct functioning of the apparatus was verified by monitoring the microwave absorption at resonance caused by a specimen of DPPH placed first at one side of the guide then the other. A change in the microwave absorption was also produced when the direction of the static magnetic field was reversed. The absolute direction of the field at which the absorption was a maximum was then determined by monitoring the deflection of a current carrying wire placed in the magnetic field. The sense of deflection was consistent with the sign of the free electron g-factor being positive, as one would expect.

Small circular apertures were cut to allow the specimen to be illuminated and the ODMR signal to be monitored perpendicular to the external field (fig. 8.4b). The sample was placed in direct contact with liquid helium at 2K. The incident microwaves were chopped by a PIN modulator (fig. 8.4c) and changes in the emission intensity occuring at the chopping frequency were detected using a photomultiplier and lock-in system.

Although the microwave system has no resonant cavity the loss in sensitivity is not as great as would be expected for conventional EPR. This is because the detection is by optical means and also because the available microwave power of close to 1W (from a Plessey ATVO 161 Impatt device which operates at 9.5 GHz) is sufficient to approach saturation of the magnetic resonance transitions.

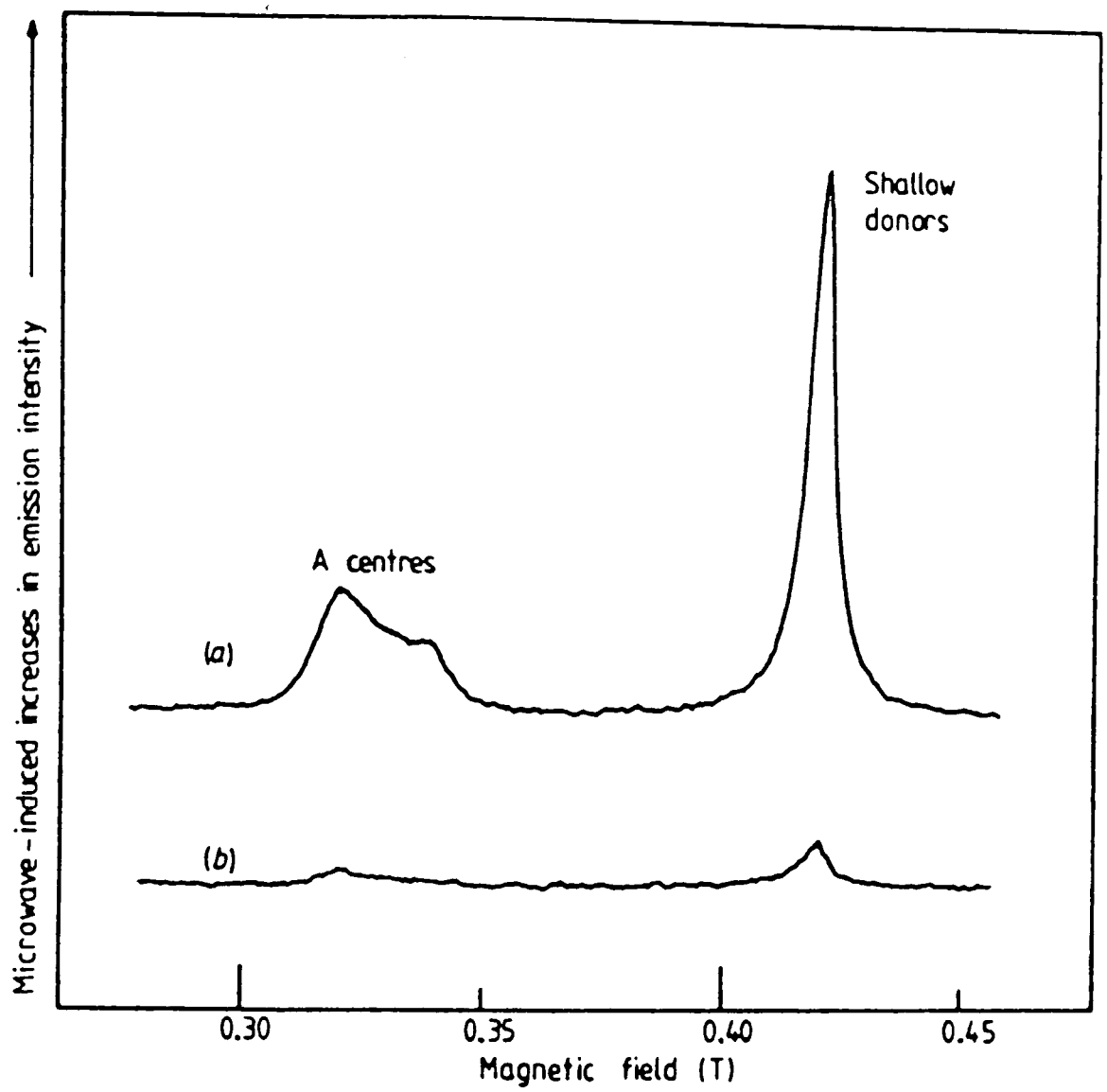

Figure 8.5 (a) The ODMR spectrum observed from a sample of $ZnS_{0.6}Se_{0.4}$ at 2K.

(b) The spectrum recorded under the same conditions as used in (a) except that the direction of the magnetic field was reversed.

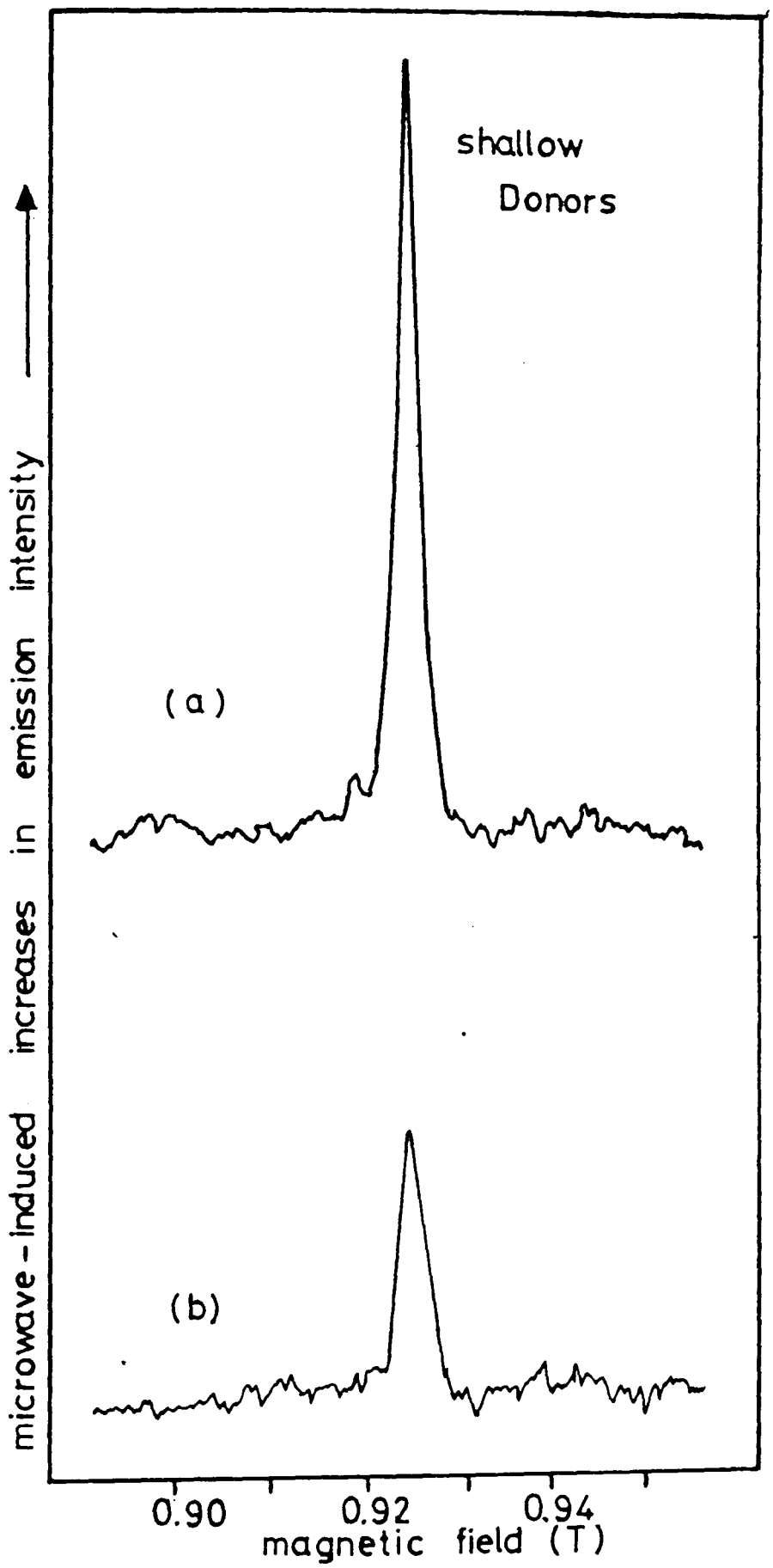

Figure 8.6 (a) The ODMR spectrum observed from a sample of CdS at 2K.

(b) The spectrum recorded under the same conditions as used in (a) except that the direction of the magnetic field was reversed.

A large deviation frequency modulation at 100 KHz is also imposed on the incident microwaves which provides the enhancement effect produced in conventional ODMR by 100 KHz field modulation [24](see Section 8.6.1).

8.5 Results and Discussion

The ZnS and Zn_xSe_{1-x} crystals used in this study were supplied by Mr. B. Lunn and Mr. G.L. Bucknell and the ZnSSe alloy was supplied by Dr. R. Mach of Zentralinstitut fur Electronenphysik der Akademie der Wissenschaften der DDR, Berlin. The CdS samples were of unknown origin but were probably Eagle Picher.

Two examples of the ODMR signals that were obtained using this system are shown in figures 8.5 and 8.6 for $ZnS_{0.6}Se_{0.4}$ and CdS respectively for the two senses of external field. As can be seen the discrimination between the spectra shown in a and b of figures 8.5 and 8.6 is not total which is probably because of reflections in the microwave circuit which would tend to produce a microwave magnetic field that is elliptically (rather than circularly) polarised. Despite this it is clear that in one sense of the external field the ODMR signals are much stronger and therefore by knowing the direction of this field the sign of the g-factor is readily determined.

The DAP recombinations that have been studied here are:

(i) the shallow donor to shallow acceptor recombination that produces the green edge emission in CdS

(ii) the shallow donor to deep acceptor (A-centre) recombination that gives rise to the blue self activated emission in ZnS

(iii) the corresponding recombination that gives rise to the red self activated emission in ZnSe

(iv) the corresponding recombination that produces the yellow self activated emission in the $ZnS_{0.6}Se_{0.4}$ alloy

All of these crystals have been the subject of previous, conventional ODMR investigations [25,26,27,28] where all were found to produce strong donor electron signals. In the investigations presented here on the self activated emissions the A-centre resonances were also observed. The shallow acceptor resonances in CdS were, however, unobserved. This is because these transitions are forbidden and only become allowed due to the mixing of the states by the magnetic field. Thus they are more readily observed at 23 GHz [25], where the field at which resonance occurs is higher.

The effect of reversing the direction of the external magnetic field was such as to show unequivocally that the sign of the g-factors for the donor electrons in <u>all</u> the systems studied were <u>positive</u> and that the values for the A-centres in ZnS, in ZnSe and in the ZnSSe alloy were also found to be <u>positive</u>.

8.6 Sign of the g-factor in CdTe Using Conventional ODMR

The sign of the donor electron g-factor in CdTe has been ascertained indirectly through conventional ODMR measurements on the $CdS_{0.98}Te_{0.02}$ alloy system. The sign cannot be measured for CdTe using the previously described system as the intensity of the ODMR resonance due to the donor electron is too weak to be observed. The g-factor was therefore measured for this system and then, since the sign in CdS has been shown to be <u>positive</u>, the sign of the donor g-factor in CdTe was deduced to be <u>positive</u> by assuming that the g-factor varied linearly and continuously across the entire alloy composition range from CdS to CdTe.

8.6.1 Experimental Arrangement

The experimental arrangement for the detection of conventional ODMR is shown in figure 8.7 and is similar to that used for ODMR using a travelling wave except that now the sample is placed in a resonant microwave cavity.

The sample was placed with it's C-axis horizontal and on top of a quartz light pipe which protruded vertically into a TE_{011} microwave cavity. The light pipe and crystal arrangement could be rotated about a vertical axis. This allows the field position of the ODMR signal to be investigated as the angle between the external magnetic field and the C-axis is varied.

Emission was excited by passing 514 nm radiation from a Spectra Physics Argon Ion laser along the light pipe and onto the sample and was subsequently detected, through slots in the cavity wall, perpendicular to the static magnetic field. Wratten W16 and W29 filters (or a 30 cm focal length Spex spectrometer) were used to isolate the emission responsible for the ODMR signal before the light was incident on a S20 photomultiplier tube.

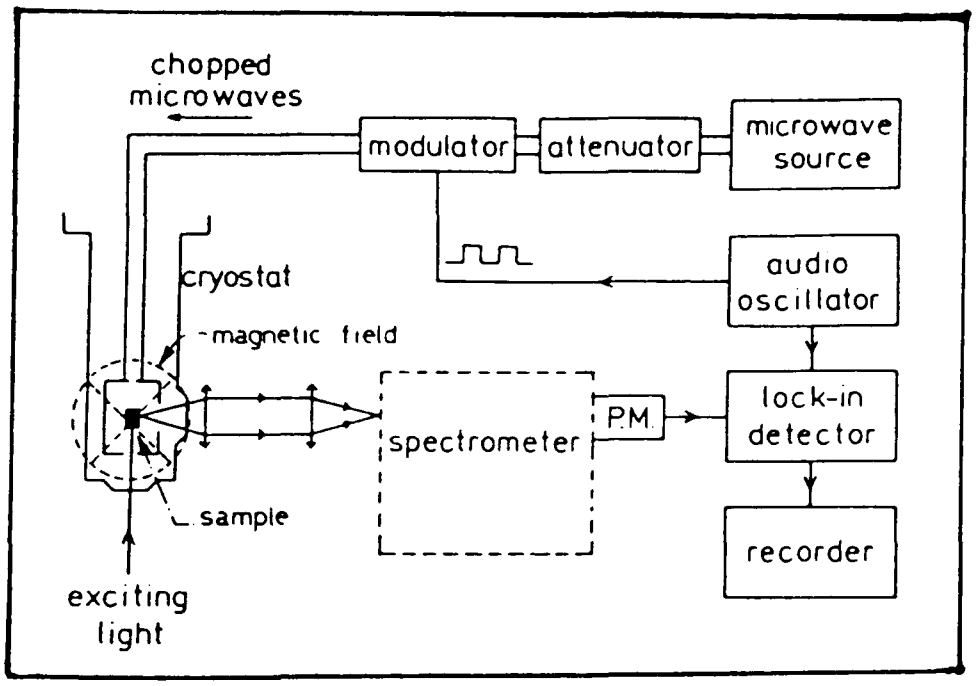

Figure 8.7 Arrangement used to detect the conventional ODMR

The incident microwaves (of a frequency of 23 GHz: K-band) were chopped at 1.2 kHz and synchronous changes in the emission intensity, that constitute an ODMR signal, were detected using a lock-in system.

In addition to the static magnetic field a 100 kHz modulated field (of a few mT intensity) was also applied by passing a 100 kHz current through a wire loop which was placed around the sample. This was done to create enhancement of the ODMR signal [24]. This enhancement is achieved because the paramagnetic centre is not isolated but is surrounded by other paramagnetic centres spatially separated from it. Therefore, in most cases, the observed ODMR signal comprises a number of homogeneously broadened lines. This is because the magnetic field of each centre adds to or subtracts from the external magnetic field and causes the value of the external field at which resonance of each centre occurs to differ for each centre. The consequence of this is to produce the inhomogeneously broadened ODMR signal shown in figure 8.8. which is made up of a number of homogeneously broadened resonance lines.

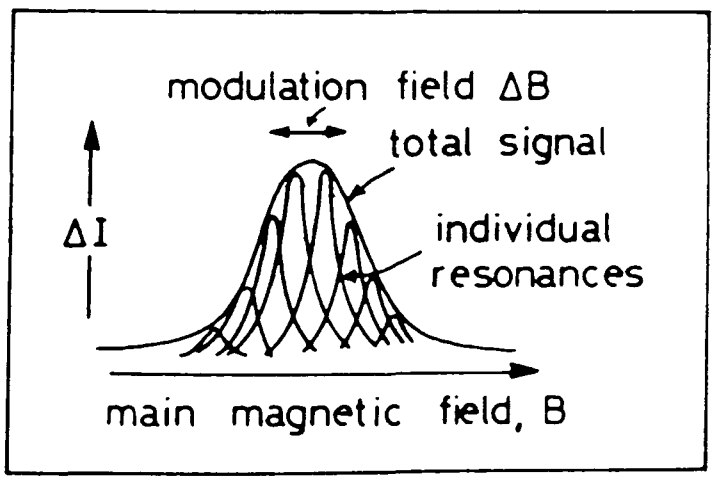

Figure 8.8 Construction of inhomogeneously broadened signal due to the magnetic field of other centres.

If an additional oscillating field is then applied more centres will be brought into the resonance condition at each value of the static field producing an enhancement of the ODMR signal. This is provided that the amplitude of the oscillations is greater than the width of an individual spin packet and that the frequency of oscillation is such that the periodic

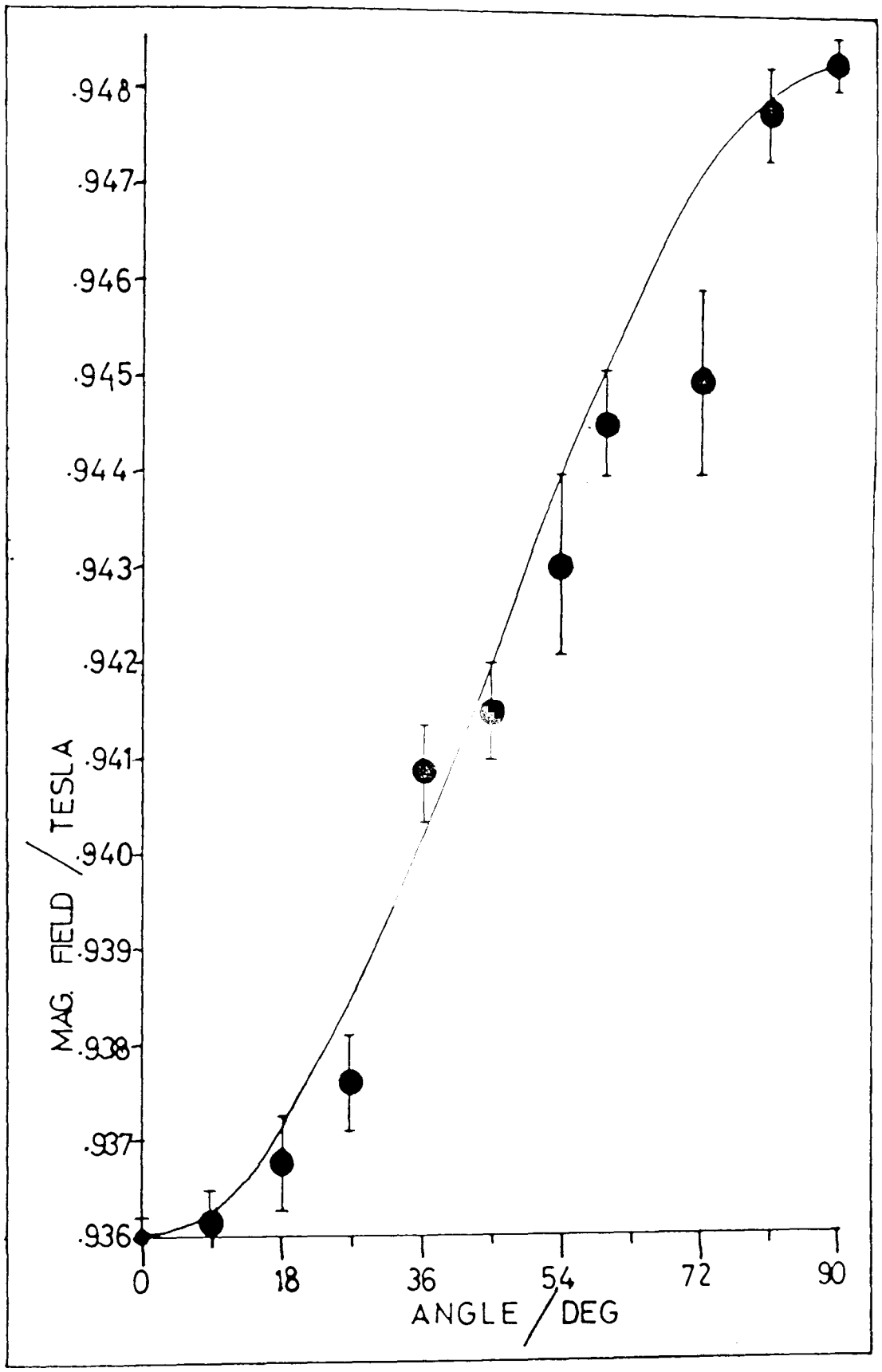

Figure 8.9 Angular dependence of donor resonance observed in samples of $CdS_{0.98}Te_{0.02}$. The solid line is calculated after equation (7).

time is less than the spin-lattice relaxation time.

8.6.2 Results and Discussion

The alloy used in this study was supplied by Dr. O. Goede of the Sektion Physik der Humbolt-Universitat zu Berlin, DDR.

The angular dependence of the donor ($S=\frac{1}{2}$) ODMR signal detected in $CdS_{0.98}Te_{0.02}$ is given in figure 8.9. The solid curve is the best fit to the experimental data (•) and is described by an effective spin Hamiltonian of the form

$$\mathcal{H} = \beta g_{\parallel} S_z B_z + \beta g_{\perp} (S_x B_x + S_y B_y) \qquad (7)$$

where the z axis is parallel to the C axis of the crystal.

and with the values of:

$$|g_{\parallel}| = 1.781 \pm 0.002 \text{ and}$$

$$|g_{\perp}| = 1.758 \pm 0.004$$

The donor g-factors in CdS were measured by Patel et al [25] to be:

$$|g_{\parallel}| = 1.7877 \pm 0.00005$$

$$|g_{\perp}| = 1.7720 \pm 0.00007$$

and that of CdTe was measured by Nakamura et al [18] to be:

$$g_D = 1.59 \pm 0.02$$

Assuming that the magnitude of the donor g-factor varies linearly and continuously across the composition range and knowing, from our previous work, that the donor g-factor in CdS is positive then for an alloy containing 2% Te the g-factors would be either:

$$|g_{\parallel}| = 1.7837 \pm 0.0004$$

$$|g_{\perp}| = 1.7684 \pm 0.0005$$

if the sign of the donor g-factor in CdTe was positive or:

$$|g_{\parallel}| = 1.7196 \pm 0.0004$$

$$|g_{\perp}| = 1.7048 \pm 0.0005$$

if the sign were negative.

From these calculations it is clear that with the assumptions that the g-factor varies linearly with composition across the alloy range the experimental data is best described by a positive sign for the donor electron g-factor in CdTe.

The assumption that the g-factor varies linearly across the composition range has been shown by Schneider et al [29] to be only approximate in other alloys, such as ZnS_xSe_{1-x}, and is probably not valid for the CdS_xTe_{1-x} alloy system. The actual variation of the electron g-factor has been shown in equation (1) to depend upon the variation of the band gap energy; the electron effective mass and the valence band splitting with concentration. These are unknown in this alloy system and therefore a definite assignment of the sign of the donor g-factor in CdTe can only be made if either the value of the donor g-factor can be measured across the entire compositional range or if a travelling wave ODMR measurement can be made on CdTe.

8.7 Conclusion

Experimental methods reported in this Chapter have, for the first time, been able to measure directly the signs of the electron g-factors in II-VI materials through novel ODMR measurements on shallow donors. The results of these experiments have demonstrated that the signs of the g-factors in CdS

in ZnS in ZnSe and in the mixed crystal $ZnS_{0.6}Se_{0.4}$ are all positive; confirming the theoretical calculations of Cardona [1].

Measurements on the mixed crystal $CdS_{0.98}Te_{.02}$ using conventional ODMR techniques have lead to a tentative assignment of a positive value for the sign of the g-factor of the conduction electron in CdTe. This is in disagreement with the theoretical calculations of Cardona. However Cox [30] did suggest that the narrowness of the donor resonance he measured in CdTe [31] implied that the sign of the donor g-factor is positive. It was reasoned that the only way a negative sign could be produced was if there was a significant orbital contribution to the total momentum of the electron (see Chapter Five equation (3)). As the orbit of the electron would be sensitive to strain in the lattice the donor ODMR signal would be broadened and this was not observed. Until further measurements are made the problem of the sign of the donor electron g-factor will remain unresolved.

CHAPTER EIGHT REFERENCES

[1] Cardona M., J. Phys. Chem. Sol. 24 1543 (1963)

[2] Kane E.O., J. Phys. Chem. Sol. 1 82 (1956)

[3] Roth L.M., Lax B., Zwerdling S., Phys. Rev. 114 90 (1959)

[4] Hopfield J.J., J. Appl. Phys. S32 2277 (1961)

[5] Thomas D.G., Hopfield J.J., Phys. Rev. 128 2135 (1962)

[6] Thomas D.G., Hopfield J.J., Phys. Rev. 175 1021 (1968)

[7] Henry C.H., Faulkner R.A., Nassau K., Phys. Rev. 183 798 (1969)

[8] Venghaus H., Phys. Rev. B 19 3071 (1979)

[9] Holsher H.W., Nothe A., Uihlein Ch., Phys. Rev. B 31 2379 (1985)

[10] Cavenett B.C., Hagston W.E., Sol. Stat. Comm. 16 1235 (1975)

[11] Wheeler R.G., Miklosz J.C. Proc. 7th Int. Conf. Semis. (Paris) pg. 873 (1964)

[12] Phys. Chem. II-VI Comp. Chapter 7 private comm. (Aven and Pren er 1967)

[13] Schmieder G., Maier W., Liu Pu-Lin, Klingston C., J. Lumin. 28 357 (1983)

[14] Romestain R., Le Si Dang, Nahmani A., J. Physique 45 1175 (1984)

[15] Tews H., Sol. Stat. Comm. 18 1283 (1976)

[16] Killoran N., Cavenett B.C., Dean P.J., Sol. Stat. Comm. 38 739 (1981)

[17] Simmonds P.E., Venghaus H., Souryakumar R., Dean P.J., Sol. Stat. Comm. 43 311 (1982)

[18] Nakamura S., Paget D., Hermann C., Weisbuch C., Lampel G., Cavenett B.C., Sol. Stat. Comm. 30 411 (1979)

[19] Look D.C., Moore D.L., Phys. Rev. B 5 3406 (1972)

[20] Cavenett B.C., Advances In Physics 30 475 (1981)

[21] Davies J.J., Contemp. Phys. 17 275 (1976)

[22] Abragam A., Bleaney B., EPR of Transition Metal Ions Chapter 2 (London OUP 1970)

[23] Pake G.E., Estle T.L., Physical Principles of EPR Chapter 2 (1973)

[24] Davies J.J., J. Phys. C 11 1907 (1978)

[25] Patel J.L., Nicholls J.E., Davies J.J., J. Phys. C 14 1339 (1981)

[26] Nicholls J.E., Davies J.J., Cavenett B.C., James J.R., Dunstan D.J., J. Phys. C 12 361 (1979)

[27] Dunstan D.J., Nicholls J.E., Cavenett B.C., Davies J.J., J. Phys. C 13 6409 (1980)

[28] Nicholls J.E., Davies J.J., Poolton N.R.J., Mach R., Muller G.O., J. Phys. C. 18 455 (1985)

[29] Schneider J., Dischler B., Rauber A., J. Phys. Chem. Sol. 29 431 (1968)

[30] Cox R.T., Private communication

[31] Cox R.T., Brunthaler G., Jantsch W., Kaufmann K., Schneider J., Proc. Int. Conf. Semicond. Coronado (1984)

CHAPTER NINE

ODMR Investigations of the Tellurium Cluster Bound Exciton Emission in $CdS_{1-x}Te_x$

Introduction

At low concentrations Te substitutional impurities act as isoelectronic traps in CdS [1,2] which are able to bind excitons. The mechanism for this is given by the Thomas-Hopfield-Lynch model [3]. Initially a hole is bound to the defect via a short range potential, developed due to a large difference in electronegativities of the Te and S, and then an electron is bound by Coulombic attraction to the hole. This forms the bound exciton, the annihilation of which leads to the emission that will be discussed in Section 9.1.2.

At concentrations for which $x > 0.01$ Te pairs, Te_2, occur (i.e. Te atoms occupying nearest neighbour anion positions) [4,5,6]. These too are able to bind excitons in the same manner as the isolated Te, Te_1. The binding of the exciton to the pair is greater than that to the single Te and therefore the Te_2 bound exciton emission is shifted towards higher wavelengths with respect to that of the Te_1 bound exciton emission. Luminescence studies on samples from a wide range of $CdS_{1-x}Te_x$ mixed crystals by Goede et al [5,6] demonstrated that excitons could be bound at Te_n clusters with n up to 5. Cluster bound exciton emission is also observed in this study and is discussed in Section 9.1.2.

The binding of excitons to isoelectronic impurities has also been found to occur in $ZnS_{1-x}Te_x$ [6] but not in $CdS_{1-x}Se_x$ where only a continuous shift of the emission energy of the single free exciton as a function of x was observed [7,8]. Onodera and Toyozawa [9] proposed a theoretical model which

predicted that there were two types of mixed crystal, showing different luminescent properties. The first type was the amalgamation type (e.g. $CdS_{1-x}Se_x$) which showed only a single free exciton due to the mixed crystal and the second type was the persistence type (e.g. $CdS_{1-x}Te_x$) in which bound excitons corresponding to those found in each of the constituent substances (i.e. CdS and CdTe) were observed to persist across the composition range. The theory showed that the type of mixed crystal behaviour could be determined from a consideration of Δ, the difference between the free exciton energies at x=0 and x=1, and of T, the width of the energy band; if the ratio $\Delta/T > 0.5$ then the mixed crystal would be a persistence type. Measurements on $CdS_{1-x}Te_x$ by Goede et al [5] showed that this ratio was 0.51 and therefore isoelectronic impurity bound excitons were to be expected and were indeed observed.

The purpose of this present chapter is to report the observation of ODMR signals due to the Te cluster bound exciton. These observations are the first reports of ODMR signals from such excitons and confirm that the 1.78eV emission involves the recombination of a cluster bound exciton, an assignment which was given by Goede et al [5,6].

9.1 Photoluminescence (PL) Studies

Crystals of $CdS_{1-x}Te_x$ with x=0.006,0.02,0.029 and 0.6 have been kindly provided by Dr. O. Goede of the Humboldt University, Berlin,DDR and were all studied using the PL technique.

9.1.1 Experimental Details

The experimental arrangement used in the PL studies is described in more detail in Section 4 of Chapter 3. The samples were immersed in overpumped liquid helium at 2K and luminescence excited with 100 mW of 514

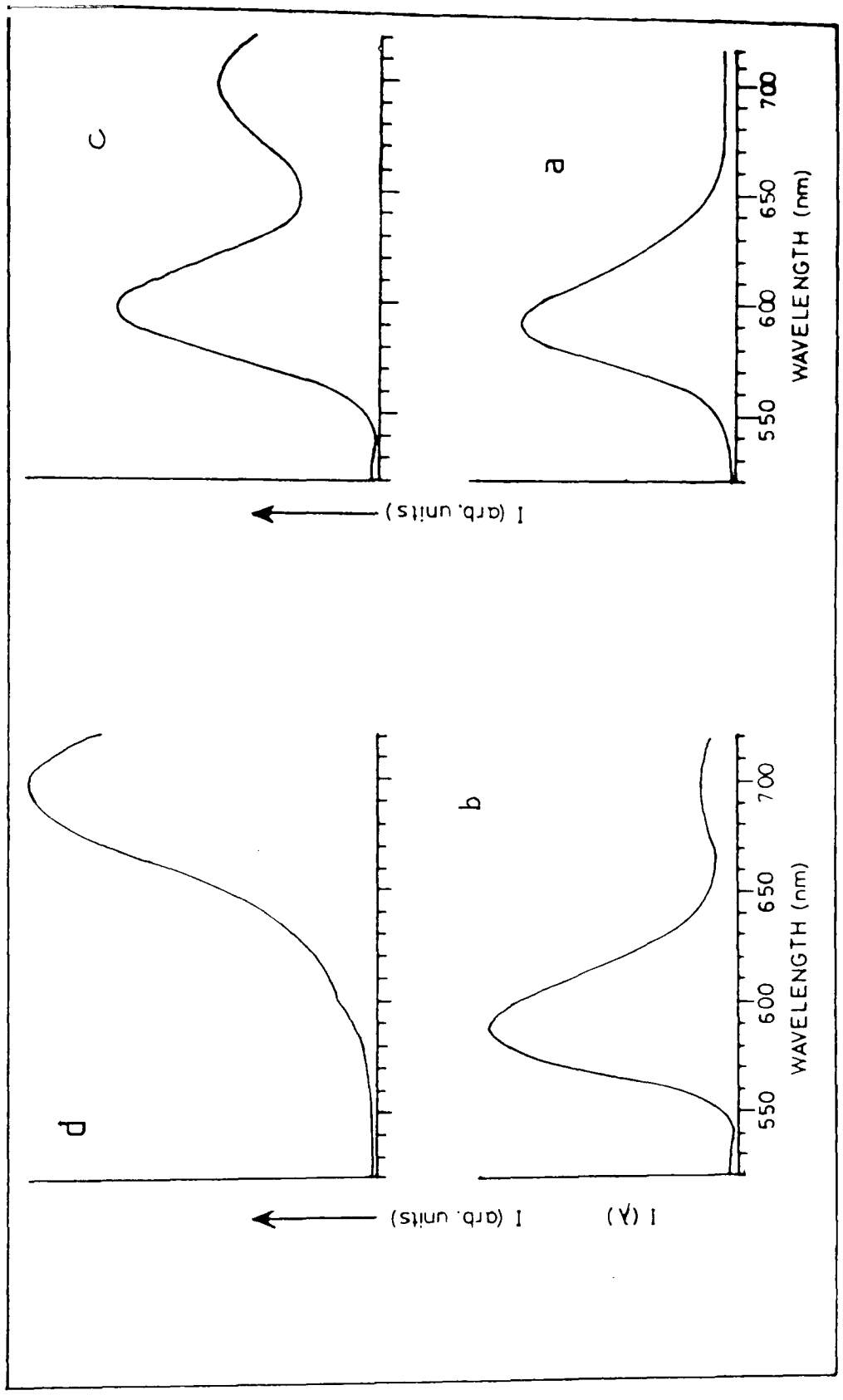

Figures 9.1 Photoluminescence spectra obtained from samples of $CdS_{1-x}Te_x$ with x equal to :

(a) 0.0006

(b) 0.02

(c) 0.029 and

(d) 0.06

A gradual transition is observed from the regime in which the Te_1 bound exciton (595 nm) dominates to one in which the Te cluster bound exciton (695 nm) dominates.

nm (2.41 eV) radiation from an Argon Ion laser. The emission was monitored using a Spex 1m focal length monochromator and a multialkali photomultiplier.

9.1.2 PL Results and Discussion

The PL spectra obtained for the samples of $CdS_{1-x}Te_x$ are shown in figure 9.1 a,b,c,d for x=0.006,0.02.0.029,0.06 respectively. As can be seen from these results a transition from the regime in which the emission band near 595 nm (2.08 eV) dominates to one in which the PL spectrum is dominated by the emission near 695 nm (1.78 eV) is observed as the concentration (x) of the tellurium impurity increases.

Bands with peak energies similar to those observed in these studies have previously been reported by Thomas et al [1], Fukushima et al [2] and Goede et al [4,5,6]. In all studies it was reported that the 2.08 eV was due to the recombination excitons bound to Te_1 isoelectronic traps while the emission near 1.78 eV involved the recombination of excitons bound a clusters of Te impurities. The higher energy emission observed in these studies is therefore assigned to the recombination of the Te_1 bound exciton whilst the lower energy emission is assigned to the recombination of the Te cluster bound exciton.

The probability ($W_n(x)$) of there existing a cluster (Te_n), containing n Te atoms, at a concentration (x) is given by [5]

$$W_n(x) = x\binom{12}{n-1}x^{n-1}\ (1-x)^{12-(n-1)} \qquad (1)$$

and is represented graphically in figure 9.2 for n=1 to 5 and x up to 1.

Using equation (1) it can be calculated that in the x region of interest for the samples under study here there exists the largest probabilities of finding only Te_1 and Te_2 clusters. It is therefore

concluded that the cluster emission near 1.78 eV principally involves the Te_2 cluster. This agrees with the conclusions reached on a similar emission band by Goede et al [5].

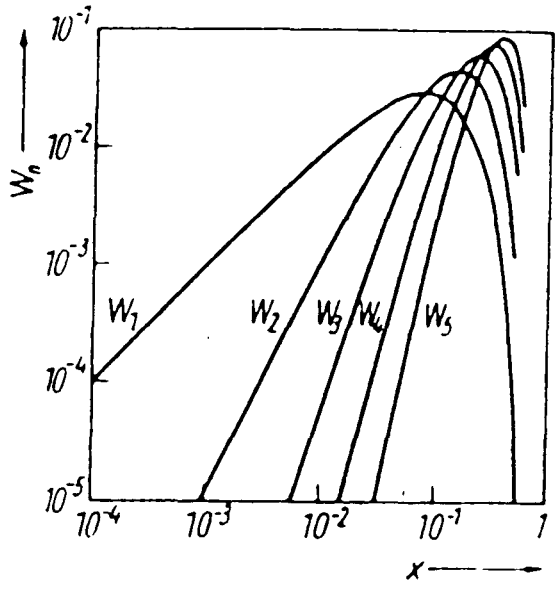

Figure 9.2 Statistical probability, W_n, for n atomic cluster (n=1 to 5) to exist in $CdS_{1-x}Te_x$ as a function of concentration, x.

Following the arguments of Hopfield et al [1] which lead to the conclusion that the binding energy of the Te_2 bound exciton was approximately that of the hole (the binding energy of the hole was found by Goede [5] to be 500 meV) and assuming the model of the hole being trapped in a square potential well (a model demonstrated to be valid by Goede [5]) then the amplitude (U(r)) of the hole wavefunction at a distance, r, outside the well is given by [10] to be

$$U(r) \propto \exp\left[-(2m^* W)^{1/2} \frac{r}{\hbar}\right] \qquad (2)$$

where m^* is the effective mass of the hole = 5 m_e // c-axis

and W is the hole binding energy = 0.5 eV

The probability per unit volume of finding the hole outside the well is $U(r)^2$ and therefore the distance, l, at which the probability of finding the hole outside the well is e^{-1} is

$$l = 3.9 \text{ Å}$$

The nearest neighbour sulphur separation in CdS is 4.1 Å and so the hole is

likely to interact only with another tellurium if it is on a nearest neighbour site.

The model that will be developed in the next section to explain the observed ODMR signals will be based upon an exciton bound to two nearest neighbour Te isoelectronic impurities.

9.2 Optically Detected Magnetic Resonance (ODMR) Studies

All of the crystals studied using PL were also subjected to ODMR investigations. However ODMR signals have only been observed in the $CdS_{0.98}Te_{0.02}$ samples.

9.2.1 Experimental Arrangement

The basic experimental arrangement for ODMR was described in Section 8.4 of Chapter 8 and is shown in figure 9.3.

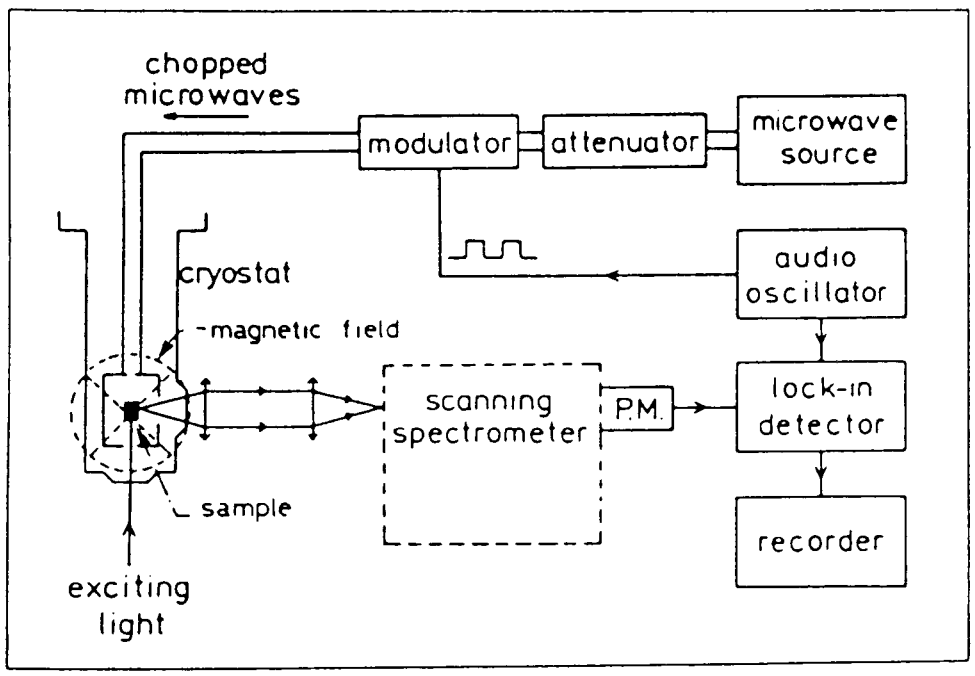

Figure 9.3 Arrangement used to detect ODMR. (The monochromator is used in spectral dependence measurements)

In addition to the 23 GHz (K-band) apparatus described there, experiments in this Chapter have also been carried out using a microwave frequency of 9.5 GHz (X-band). The principles of the detection of the signal, however, remain unaltered.

In all of the ODMR experiments the luminescence was excited using 100 mW of 514 nm radiation from an Argon Ion laser. The luminescence band due to the Te_2 bound exciton recombination was isolated using Wratten W29 and W16 filters. The emission at right angles to the magnetic field was passed through a linear polaroid and monitored using an S20 photomultiplier. The incident microwaves were chopped at 1 KHz and synchronous changes in emission intensity, that constitute the ODMR signal, were detected using the lock in detector system. The crystal could to be rotated in a plane parallel to the magnetic field which allowed the change in the value of the magnetic field at which resonance occurred to be found as a function of angle (known as the angular dependence of the signal).

In order to determine which emission involved the donor a 35 cm focal length monochromator is placed between the emission and the S20 detector. This so called 'spectral (or wavelength) dependence' of the donor is recorded by firstly setting the magnetic field to the resonance condition and scanning through the luminescence, recording the emission change, ΔI as a function of wavelength. This measurement is complicated by the presence of a non-resonant background signal. Such background signals are often observed in ODMR experiments in semiconductors but their origins still remain unknown. As the size of this signal is usually found to be independent of the magnetic field value the spectral dependence of the ODMR signal may be found by monitoring the spectral dependence with the magnetic field set both on and off resonance. The difference between these two spectra is then the true spectral dependence of the resonance.

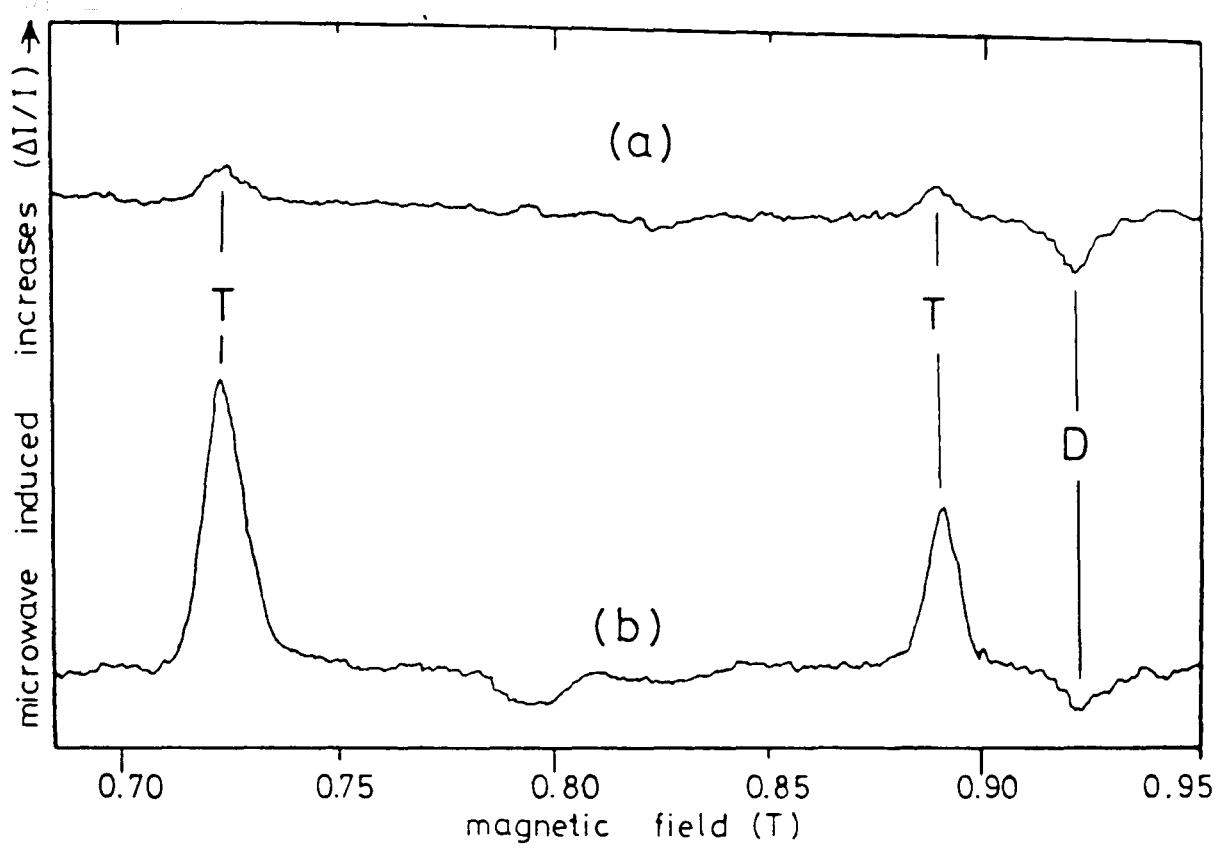

Figures 9.4 The ODMR spectra obtained from a sample of $CdS_{.98}Te_{.02}$ for the c-axis 13^{o} to the magnetic field.

(a) Monitoring all light.

(b) Monitoring the light linearly polarised in a plane parallel to the magnetic field direction.

9.2.2 ODMR Results and Discusion

Figure 9.4a shows the ODMR spectrum obtained from a sample of $CdS_{.98}Te_{.02}$ for the c-axis 13^{o} to the magnetic field and represents the fractional change in emission intensity ($\Delta I/I$) at resonance. It was recorded at K-band (23 GHz) by monitoring the unpolarised luminescence from the 1.78 eV (Te_2) emission band.

The resonance signal near 0.92 T (labelled D in the figure) is due to a shallow donor in the material (see Section 9.2.2.1). It was found to be slightly anisotropic and corresponded to a decrease in emission intensity when the microwaves were applied. The two resonance signals (labelled T) were found to be very anisotropic and corresponded to an increase in emission intensity when microwaves were applied. These signals are interpreted as being due to the triplet system of the Te_2 bound exciton (see Section 9.2.2.2).

The effects on the ODMR spectrum when only the Te_2 bound exciton luminescence linearly polarised in a plane parallel to the magnetic field was monitored is shown in figure 9.4b. It was found that the ODMR intensity of the exciton signal (T) increased by a factor of 4 but the donor resonance signal (D) remained unaffected. When the linear polaroid was rotated through 90^{o} the ODMR signal due to the triplet resonances increased by about a factor of 4 but the sense of the signal was in the opposite direction, showing a decrease in the emission intensity at resonance. The donor resonance was again unaffected. These effects will be discussed in Section 9.3.

9.2.2.1 The Donor Resonance

As in CdS [11] the shallow donor electron in $CdS_{1-x}Te_x$ will have a spin $S^D = 1/2$. The corresponding ODMR spectrum may be described by an effective spin Hamiltonian of the form

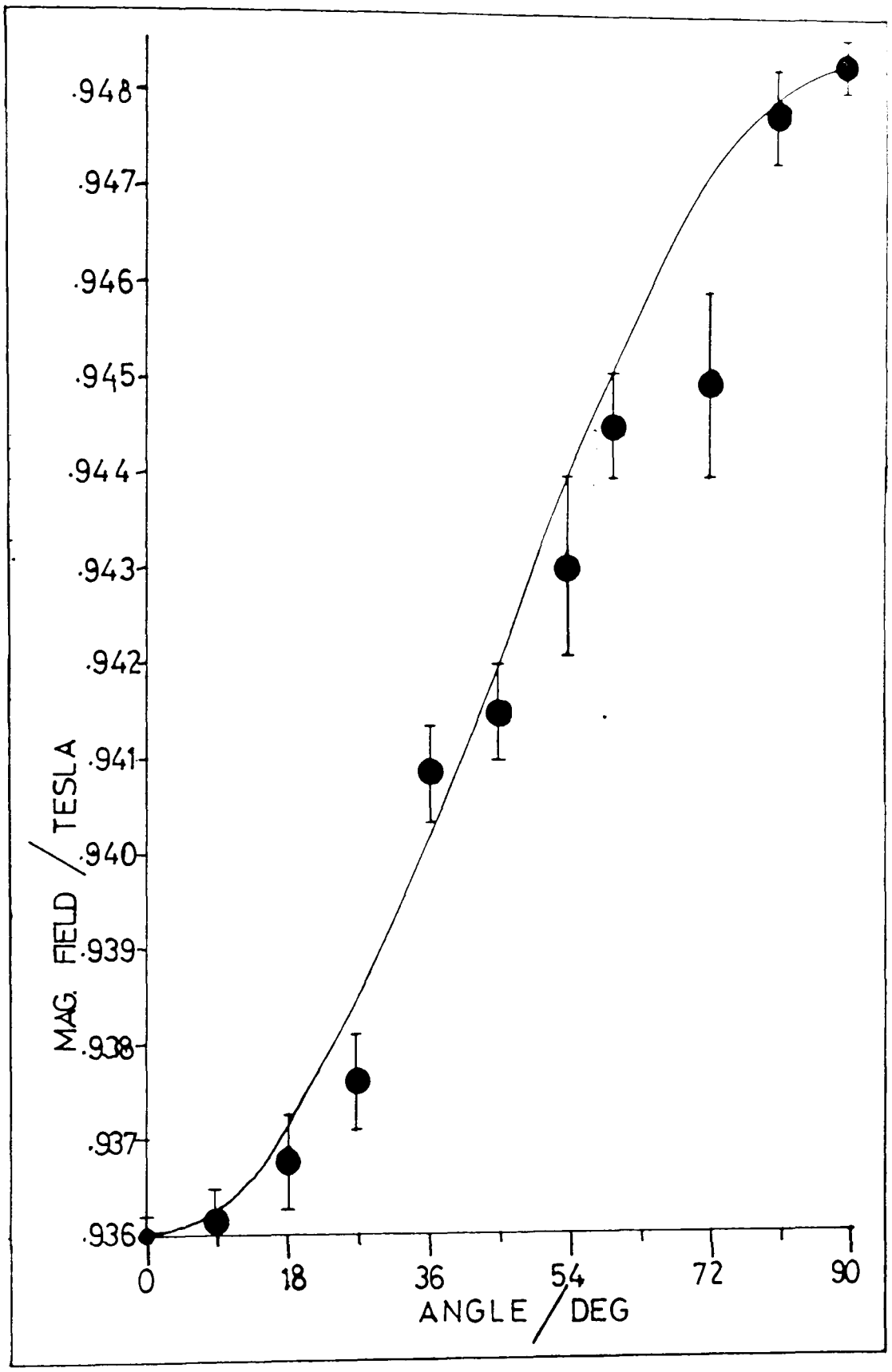

Figure 9.5 The angular dependence of the donor resonance (•). The theoretical curve is calculated using equation (3).

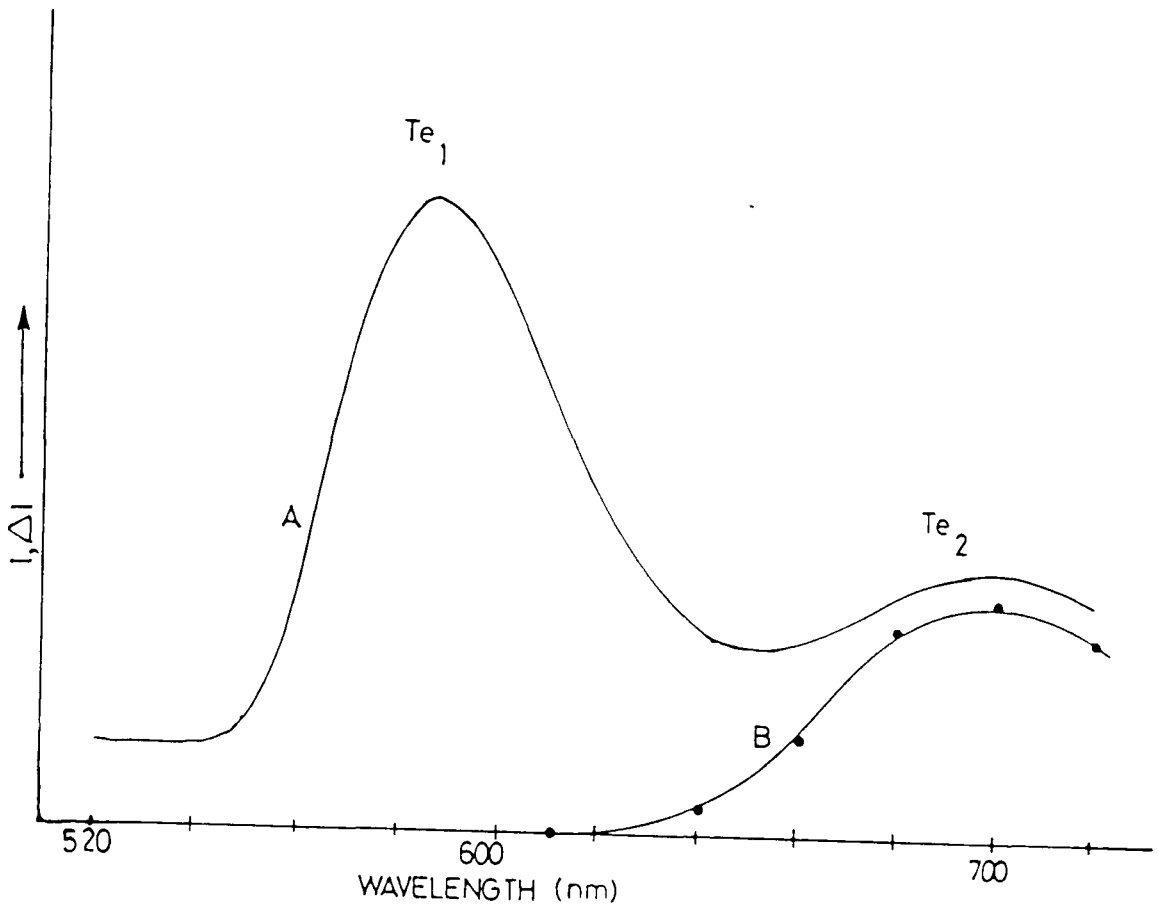

Figures 9.6 (A) Luminescence observed in the $CdS_{.98}Te_{.02}$ sample recorded in situ in the ODMR cryostat. Te_1 and Te_2 bound exciton emission is observed.

(B) Wavelength dependence of the donor ODMR signal.

$$\mathcal{H}_D = \beta\, g_{\parallel}^{D} S_z B_z + \beta\, g_{\perp}^{D} (S_x B_x + S_y B_y)) \qquad (3)$$

where z is taken to be along the c-axis of the crystal

The angular dependence of the donor signal is shown in figure 9.5. The best fit to the experimental points (•) was found from equation (3) with the values

$$|g_{\parallel}^{D}| = 1.781 \pm 0.002$$
$$|g_{\perp}^{D}| = 1.758 \pm 0.004$$

(see Chapter 8: Section 8.6). The wavelength dependence of the donor signal is shown in figure 9.6 together with the emission spectrum observed in the sample. A comparison of the two spectra shows that the donor is also involved in the Te_2 bound exciton emission that is observed near 695 nm.

The involvement of the donor in the 695 nm emission will be discussed further in Section 9.3.

9.2.2.2 The Exciton Triplet Resonance

The mechanism by which an exciton becomes bound to a Te_2 cluster is identical to that by which an exciton is bound to the Te_1 isoelectronic trap. Thus a hole, from the heavy hole band (J=3/2), is bound to the tellurium cluster through a short range potential that is developed due to the difference in electronegativities of the Te and S atoms. An electron (S=1/2) is then bound electrostatically to the hole; forming the bound exciton. The energy states of the exciton are then formed into the J=1 and J=2 levels through J-J coupling of the spins. If the coupling is strong (as is expected for an exciton bound to a deep Te_2 trap) the J=1 and J=2 energy levels split as is shown in figure 9.7a.

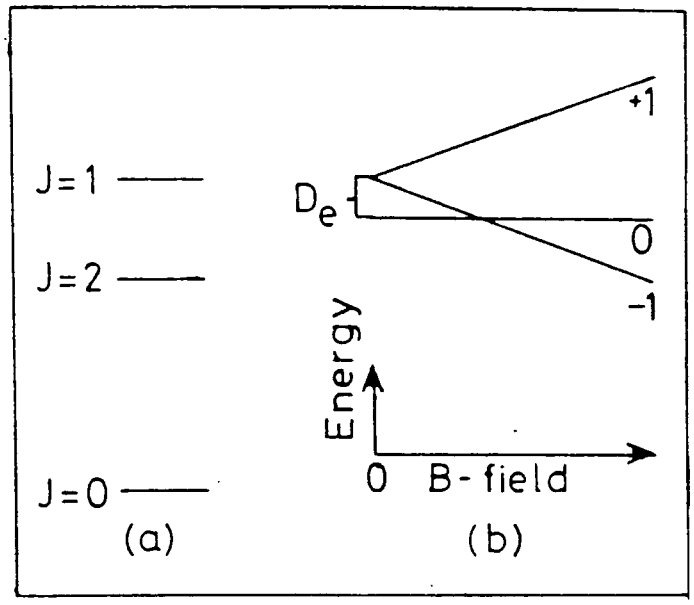

Figures 9.7

(a) The energy levels of the exciton system.

(b) The Zeeman split J=1 level showing a zero field splitting, D_e.

As the optical transitions $\Delta J=\pm 2$ are only weakly allowed it is assumed that the emission observed at 695 nm is due largely to transitions from the triplet (J=1) state to the ground (J=0) state. The triplet energy levels of the system in the presence of an external magnetic field are shown in greater detail in figure 9.7b. The energy levels of this system may be split, by an amount D_e, even in the absence of an external magnetic field. This so called 'zero field splitting' of the triplet system can be thought of as resulting from magnetic dipole-dipole interactions and anisotropic exchange interactions between the electron and hole [12].

The effective spin Hamiltonian that describes the triplet system in an external magnetic field, B, can be written as

$$\mathcal{H}_T = \beta\, \underline{B}.\tilde{g}.\underline{S} + \underline{S}.\tilde{D}.\underline{S} \qquad (4)$$

where $\tilde{D}$ is $D_e/2$ and $\tilde{g}= (g_{//}^2\cos^2\theta + g_{\perp}^2\sin^2\theta)^{1/2}$

(// and $\perp$ are with respect to the c-axis)

This can be shown [13] to produce the theoretical values of the applied field at which resonance occurs when

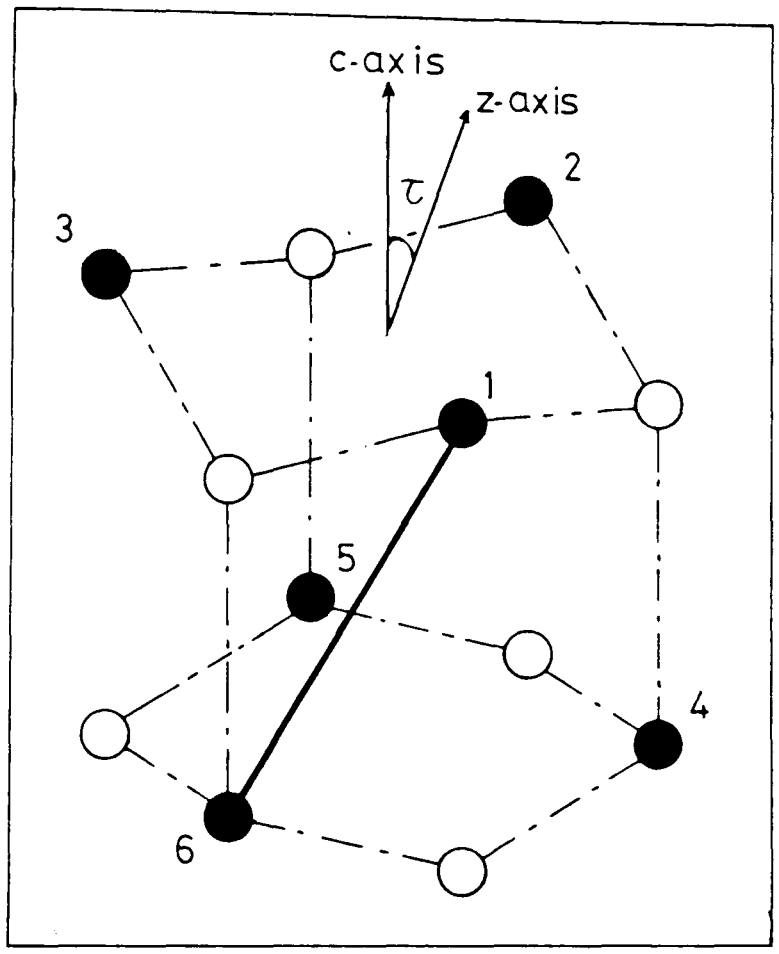

Figure 9.8 Schematic representation of two adjacent planes in an hexagonal crystal lattice. The anions are depicted as ● and the cations as ○. Tellurium may substitute for sulphur at any of the six anion sites shown. The tellurium pairs which were considered in the theoretical calculations are 1,6; 1,4; 2,4; 2,5; 3,5; 3,6. The magnetic z-axis of one such pair (1,6) is shown in the diagram tilted through an angle τ with respect to the crystal c-axis.

$$B = \frac{h\nu}{g\beta} - \frac{D}{2g\beta}\,\frac{3g^2\cos^2\theta - g^2}{g^2}\,(2M_s - 1) \qquad (5)$$

ODMR signals were not observed for the excitons in which the hole was captured by pairs of Te in a plane at right angles to the c-axis. Figure 9.8 shows the six different combinations of nearest neighbour Te pairs which were considered when calculating the theoretical values of B using equation (5). Figure 9.8 also shows the tilt angle, τ, of the z-axis of the magnetic centre with respect to the crystal c-axis. This was found experimentally to be 14^{o}.

The 'best fit' of equation (5) (solid curves) to the experimentally determined values of the B-field at which resonance occurred (•) using the X-band system is shown in figure 9.9. This fit was achieved by substituting the values of

$|g_{\parallel}| = 2.08$

$|g_{\perp}| = 1.92$

$|D| = 8.18 \times 10^{-2}\ cm^{-1}$

into equation (5). The data collected at X-band shows that the triplet spectrum is repeated when the external magnetic field, B, is about 60^{o} to the original c-axis. This may be explained if there is another c-axis at 60^{o} to the original i.e. the crystal is twinned. The resulting theoretical angular dependence of the ODMR signal is shown by the broken curves in figure 9.9. Infact the backscattered Laué X-ray pattern, taken with the beam incident along the c-axis, showed that the crystal comprised many small crystallites the majority of which had a preferred direction of the c-axis. Since the crystal was obviously of such poor quality it is possible that another preferred c-axis direction lay at 60^{o} to the first although it was not observed in the aforementioned Laué picture.

The best fit at K-band is shown in figure 9.10 and was achieved by

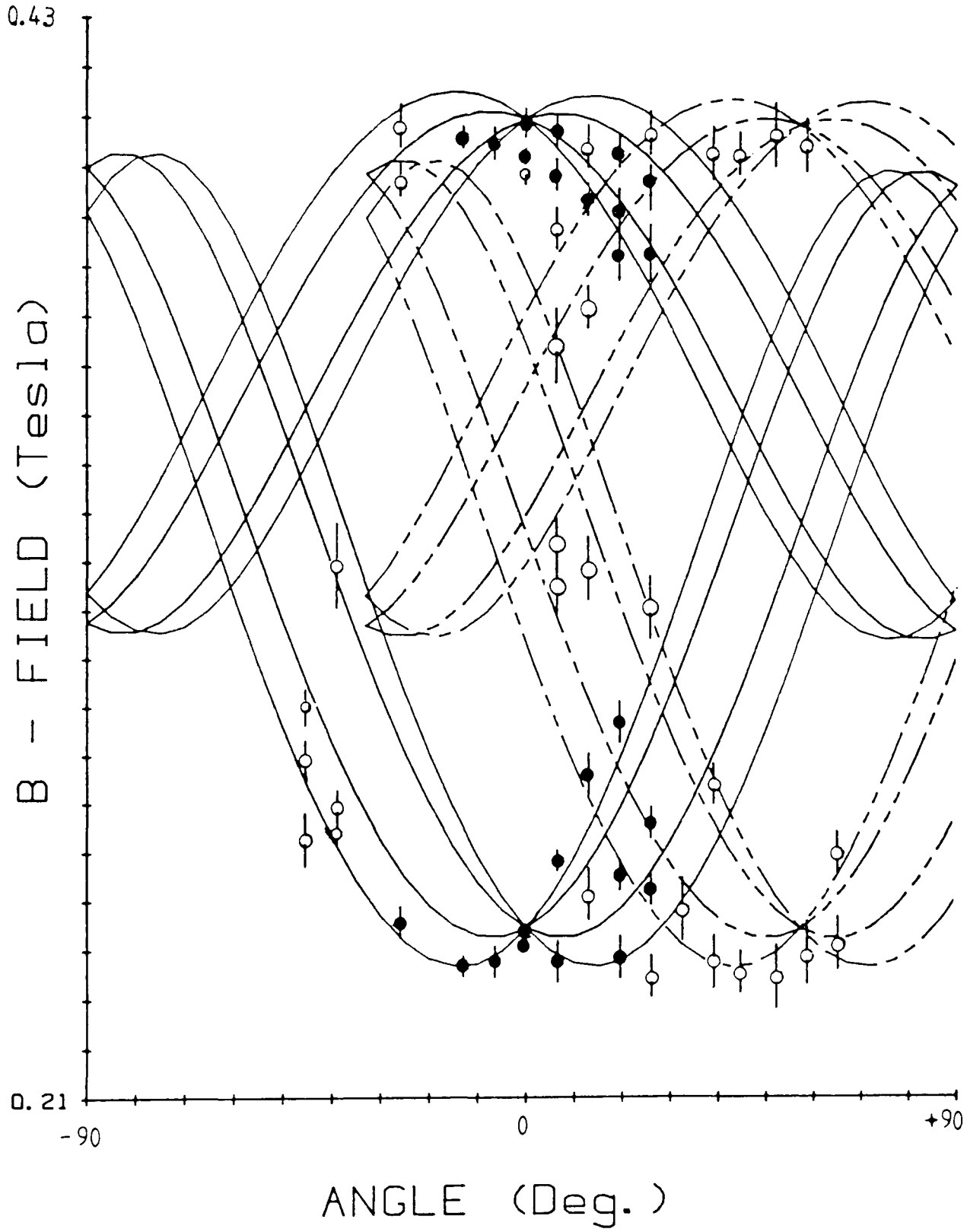

Figure 9.9 Angular dependence of the triplet resonance recorded at X-band. The stronger signals are shown as (•) and the others as (o). The theoretical curves are calculated using equation (5). The broken curve shows the angular dependence produced by a twin with its c-axis at 60^{o} to the first (solid curve).

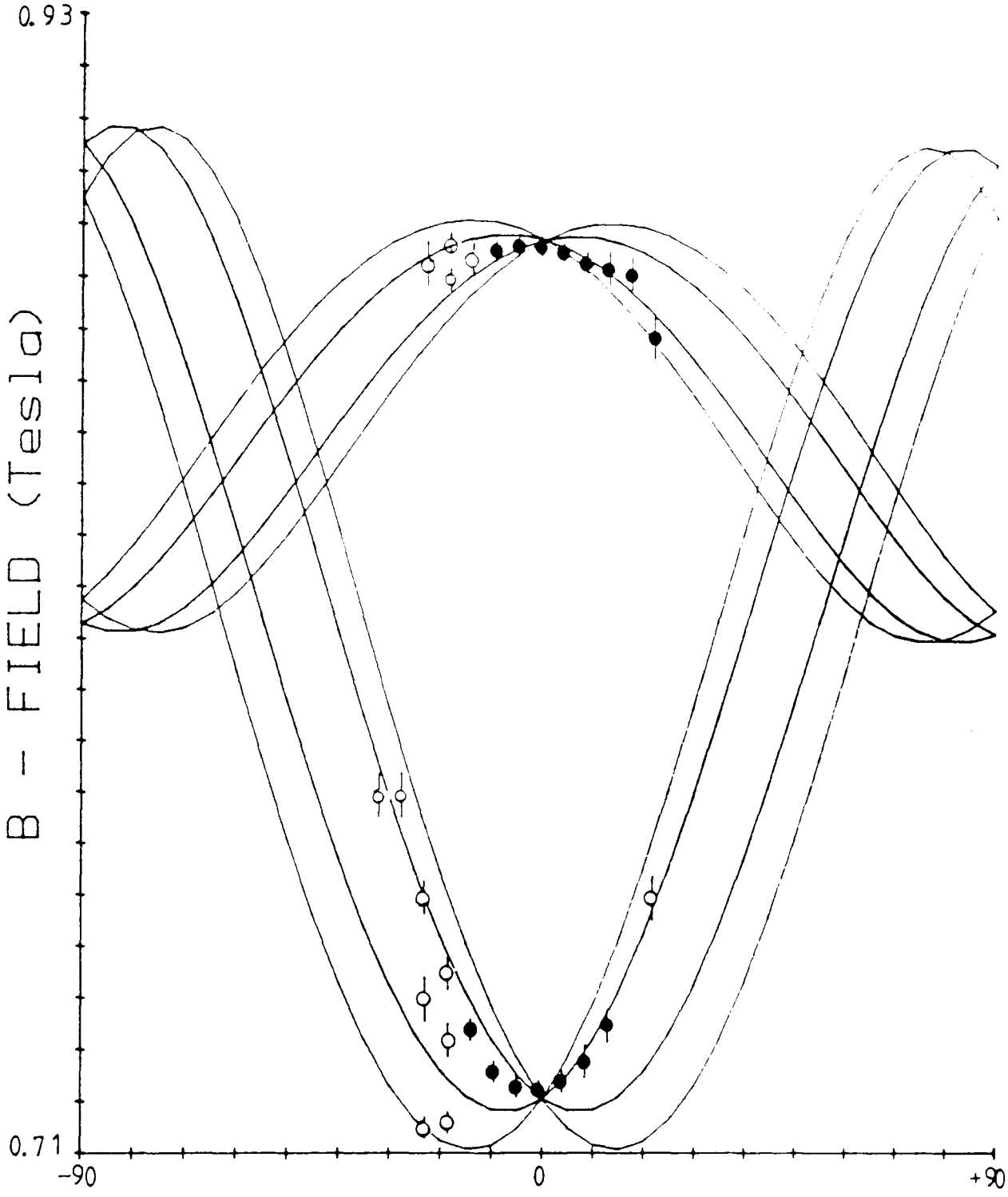

Figure 9.10 Angular dependence of the triplet resonance recorded at K-band. The stronger signals are shown as (•) and the others as (o). The theoretical curves are calculated using equation (5).

substituting the values of

$$|g_{\parallel}| = 2.06$$

$$|g_{\perp}| = 1.92$$

$$|D| = 8.18 \times 10^{-2}\ cm^{-1}$$

into equation (5).

Although no experimental points were observed when the magnetic field was at right angles to the c-axis anisotropy in the g-values used at X and K bands was needed to give the correct curvature of the theoretical curves near to the c-axis. The disparate values of $g_{\parallel}$ at the two microwave frequencies suggests that the theory given above may be an oversimplification and other terms in equations (4,5) may be necessary to account for this. The most probable cause of the failure of the isolated triplet model in completely describing the observed angular dependence is the effects of any interactions between the J=1 and J=2 exciton energy levels. The effects of these interactions are likely to produce a greater discrepancy between the theoretical curves generated using equation (5) and the experimental values of the resonances at K-band than at X-band. This is because the values of the B-field at which the resonant absorption of microwaves occur are higher at K-band than X-band and therefore the magnitude of the Zeeman splitting of both the J=1 and J=2 levels is greater with the result that the Zeeman levels of the J=1 state and the J=2 state are closer at K-band and therefore mixing of the two states will be more pronounced at K-band.

The involvement of the bound exciton with the Te_2 cluster emission and not the Te_1 emission was inferred from the observed absence of any ODMR signal when the 595 nm emission band was isolated and monitored.

9.3 The Exciton Model and the ODMR Spectrum

When the emission polarised in a plane parallel to the direction of the B field was monitored, by placing a linear polaroid in front of the photomultiplier, it was found that both triplet ODMR signals were enhanced by a factor of 4 with both ODMR signals showing an increase in the emission intensity at resonance (figure 9.4b). If the polaroid was rotated through 90^{o} then the enhancement of the signals still occurred but both ODMR signals showed a decrease in the emission intensity at resonance. These polarisation effects can be explained using a model based on the assumption that the recombination process principally involves the triplet state of the Te_2 bound exciton.

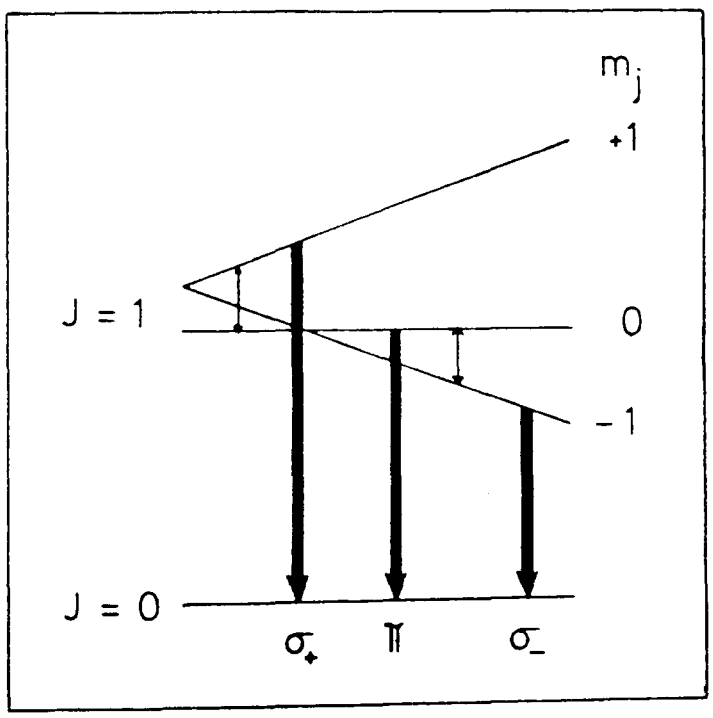

Figure 9.11 Emission from and microwave induced transitions between the Zeeman levels of the exciton triplet state.

Emission from the Zeeman split triplet system can be right circularly polarised $\sigma_+(\Delta m_j=1)$, left circularly polarised $\sigma_-(\Delta m_j=-1)$, and linearly polarised π $(\Delta m_j=0)$, depending on which state the exciton was in when it recombined. These emissions are shown in figure 9.11 together with the possible microwave transitions between the Zeeman split triplet states which

occur at resonance.

Let the populations of the levels $m_j = +1,0,-1$ be n_1, n_0, n_{-1} respectively. If the system were thermalised then the populations of the three levels would be such that $n_1 < n_0 < n_{-1}$ and therefore at resonance the microwaves would induce changes from the level $m_j = -1$ to the level $m_j = 0$, <u>increasing</u> the emission intensity, and from the level $m_j = 0$ to the level $m_j = +1$, <u>decreasing</u> the emission intensity. Therefore if the triplet system were thermalised the two triplet ODMR signals would be of opposite sense. If the radiative decay of the $m_j = 0$ level was much faster than that of the $m_j = {}^{+}1$ levels and if it was also faster than the spin lattice relaxation rate then the system would be unthermalised such that $n_{-1} = n_{+1} > n_0$. At resonance population would be transferred from the level $m_j = -1$ to the level $m_j = 0$, <u>decreasing</u> the σ_- emission intensity, and from the level $m_j = +1$ to the level $m_j = 0$, <u>decreasing</u> the σ_+ emission intensity, and so the observed triplet ODMR signals would both be in the same sense. As the triplet ODMR signals observed in this study were both in the same sense this indicates that the Te_2 bound exciton system is probably unthermalised.

In this study the emission is monitored at right angles to the applied field and therefore both senses of circularly polarised light are observed as linearly polarised light with the plane of the electric component of that light at 90° to the plane parallel to the direction of the B-field. It has been shown above that for the unthermalised system where $n_{+1} = n_{-1} > n_0$ both the σ_- and the σ_+ components of the emission will show a decrease in intensity at resonance. Therefore when the linearly polarised emission is observed in a plane at 90° to the plane parallel to the direction of the B-field a <u>decrease</u> in emission intensity at resonance should be observed. This agrees with the experimental data. When the polaroid is rotated through 90°, so that linearly polarised emission is observed in a plane parallel to the direction of the B-field an <u>increase</u> in

the emission intensity at resonance should be observed since population is being transferred to the $m_j = 0$ level (the level responsible for the emission). This again agrees with the experimental data. Thus the polarisation effects that have been observed in this study may be explained using a model in which the triplet system is unthermalised.

It has also been observed (figures 9.4) that a donor resonance is also observed when monitoring the Te_2 bound exciton emission and is observed as a <u>decrease</u> in emission intensity at resonance. Any model that is developed to explain how shallow donor electrons are invoved in the Te_2 bound exciton formation must, then, explain

a) why a decrease in emission occurs at resonance and

b) why no donor resonance was observed when monitoring the Te_1 bound exciton emission.

The optical band gap, $E_g(x)$, of the $CdS_{1-x}Te_x$ alloy system has been shown by Tai et al [14] to follow the expression

$$E_g(x) = (xE_g(CdTe) + (1-x)E_g(CdS)) - x(1-x)b \qquad (6)$$

where $E_g(CdTe)=1.59$ eV and $E_g(CdS)=2.58$ eV and are the band gap energies of CdTe and CdS respectively and where b was calculated to be 1.7 eV [14].

The expression (6) yields a value of 2.53 eV for the band gap energy of the $CdS_{0.98}Te_{0.02}$ alloy system. In the studies presented in this chapter all luminescence was excited using 2.41 eV (514 nm) radiation and therefore neither the Te_1 bound excitons nor the Te_2 bound excitons could have been formed by the capture of electrons that have been excited from the valence band directly into the conduction band. However results from excitation spectroscopy experiments carried out by Goede et al [5] showed that Te_2 bound excitons were created very efficiently by absorption at 2.41 eV whereas absorption at this energy only inefficiently creates Te_1 bound

excitons. As both types of bound exciton are created through the absorption of energy at 2.41 eV this mechanism may account for why both Te_1 and Te_2 bound exciton luminescence can be observed at the same time. It does not explain the observed shallow donor electron involvement in the creation of Te_2 bound excitons. However other processes, may occur when the 2.41 eV radiation is absorbed by the sample and one such process, which may account for the involvement of the donor electrons, is shown in figure 9.12.

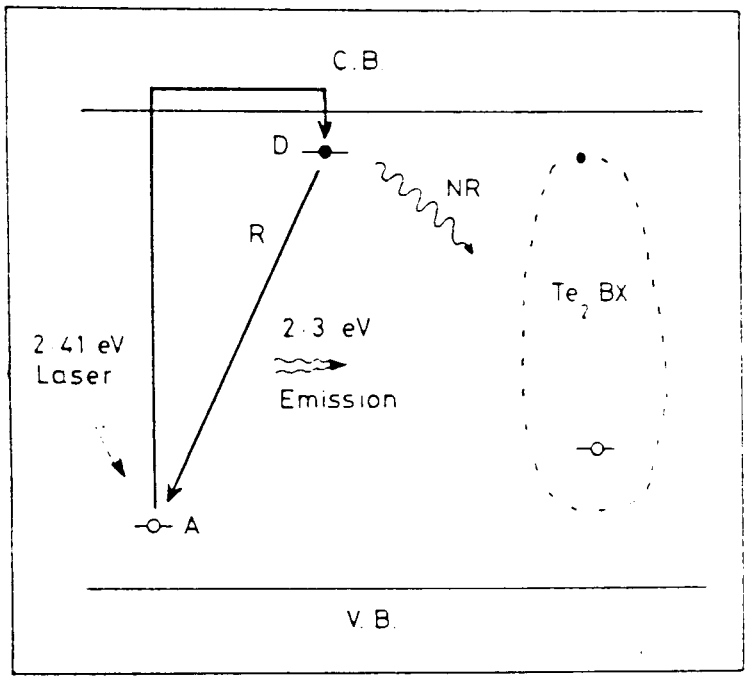

Figure 9.12 A possible model to explain the donor involvement in the Te_2 bound exciton (Te_2 BX) formation.

In this case electrons are excited from acceptor levels, A, into the conduction band, CB, when the sample is illuminated with 2.41 eV radiation and are subsequently captured in shallow donor levels, D. These donor electrons may now recombine radiatively (R) with holes trapped at the shallow acceptor levels or create Te_2 bound excitons via a non radiative (NR) process. The radiative DAP transitions involving shallow donors and acceptors in CdS were shown to release photons of energy near 2.3 eV [15]. As this energy is close to that which most efficiently directly creates the Te_2 bound exciton one may suppose that the energy released in the radiative

transition may be reabsorbed to create the exciton. However for the reasons that will be given below this process will not produce the observed decrease in emission intensity at donor resonance.

The recombination between an electron from a shallow donor and a hole from a shallow acceptor can be represented by the energy level diagram of figure 9.13.

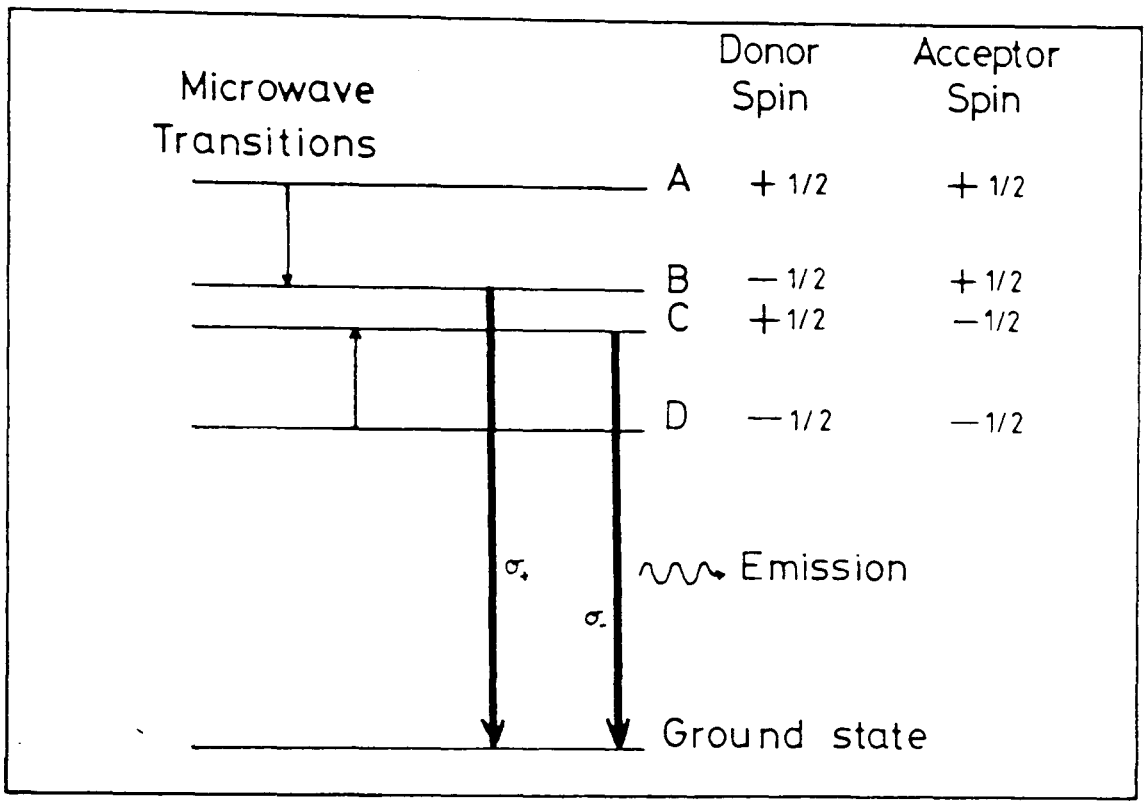

Figure 9.13 Energy levels of a shallow donor acceptor pair orientated along the c axis of the crystal. The effective spin states of the donors and acceptors which make each level are also shown together with the allowed donor microwave transitions and the levels from which non radiative transitions of the donor electrons occur.

The selection rules for radiative recombination [16] will depend upon the angle between the magnetic field and the c axis. When this angle is 0 only radiative transitions from the levels B and C are allowed. In the case shown in figure 9.13 the rate of radiative recombination may be increased by changing the spin distribution in the donor states by resonantly absorbing microwaves (the allowed donor electron microwave transitions are also shown

in figure 9.13). If the re-absorption of this emission was a mechanism responsible for the creation of the Te_2 bound exciton then when microwaves were resonantly absorbed by the donor electrons an <u>increase</u> in emission intensity of the bound exciton luminescence would have been observed. The donor ODMR signal that was observed in this study was infact due to a <u>Decrease</u> in that emission intensity. It is therefore proposed that non radiative transitions involving donor electrons in the energy states A and D could be responsible for the formation of the Te_2 bound exciton. The microwave transitions would <u>decrease</u> the population of donor electrons in these states and therefore a <u>decrease</u> in the emission intensity of the exciton band would be observed. This is in agreement with the experimental data.

9.4 <u>Conclusions</u>

Although $g_\perp$ for the system could not be measured accurately because of the lack of experimental points when B was at 90^o to the c-axis of the crystal the results presented in this chapter show that the experimental data (i.e. the angular dependence and the sign of $\Delta I/I$ of the ODMR signal) is best described using an exciton triplet state model in which the magnetic axis (z-axis) of the system lies almost parallel to the crystal c-axis. This study has also shown that the triplet ODMR originates from the 695 nm emission band that was observed in this material and which has been shown by Goede et al to be due to the radiative recombination of an exciton bound to a pair of Te atoms (Te_2). Therefore the results presented in this chapter represent the first reports of ODMR signals involving Te_2 bound excitons and serve to confirm Goede's assignment of the 695 nm luminescence band as involving Te_2 bound excitons.

CHAPTER NINE REFERENCES

[1] Cuthbert J.D., Thomas D.G., J. Appl. Phys. 39 1573 (1968)

[2] Fukushima T., Shionoya S., Jap. Jrnl. Appl. Phys. 15 813 (1976)

[3] Hopfield J.J., Thomas D.G., Lynch R.T., Phys. Rev. Lett. 17 312 (1966)

[4] Goede O., Hennig D., John L., Phys. Stat. Sol. b 96 671 (1979)

[5] Goede O., Heimbrodt W., Muller R., Phys. Stat. Sol. b 105 543 (1981)

[6] Heimbrodt W., Goede O., Phys. Stat. Sol. b 135 795 (1986)

[7] Lai S., Klein M.V., Phys. Rev. Lett. 44 1087 (1980)

[8] Permogorov S., Reznitsky A., Verbin S., Muller G.O., Flogel P., Nikiforova M., Phys. Stat. Sol. b 113 589 (1982)

[9] Onodera Y., Toyozawa Y., J. Phys. Soc. Jpn. 24 341 (1968)

[10] e.g. Park D.A., Introduction to the Quantum Theory pg.188

[11] Patel J.L., Nicholls J.E., Davies J.J., J. Phys. C 14 1349 (1981)

[12] Owen J., Harris E.A., Electron Paramagnetic Resonance Chap. 6 (ed. Geschwind 1972)

[13] Pake G.E., Estle T.L., Physical Principles of Electron Paramagnetic Resonance Chap. 5 (ed. Benjamin 1973)

[14] Tai H., Nakashima S., Hiri S., Phys. Stat. Sol. (a) 30 K115 (1975)

[15] Henry C.H., Nassau K., Shiever J.W., Phys. Rev. B 4 2453 (1971)

[16] Thomas D.G., Hopfield J.J., Augustynaik W.M., Phys. Rev. 140 A202 (1965)

APPENDIX A

Values of the ZnTe Physical Constants Used in This Study

SYMBOL	DESCRIPTION	VALUE	REFERENCE
E_g	Energy gap	2.28 eV (at 300 K)	[1]
		2.391 eV (at 4 K)	[2]
ε_s	Static dielectric constant	10.1 ε_o	[3]
ε_∞	Optical dielectric constant	7.28 ε_o	[4]
	L.O. phonon energy	0.026 eV	[5]
m_e^*	Effective mass of conduction band electrons	0.128 m_e	[6]
m_h^*	Effective mass of valence band holes	0.6 m_e	[7]

[1] Larach S., Shrader R.E. and Stocker C.F., Phys. Rev. 108 587 (1957)
[2] Segall B., Phys. Chem. II-VI Comps. N. Holland Publishing Company (1967)
[3] Berlincourt D., Jaffe H. and Shiozawa L.R., Phys. Rev. 129 1009 (1963)
[4] Marple D.T.F., J. Appl. Phys. 35 539 (1964)
[5] Dean P.J., Venghaus H., Pfister J.C., Schaub B. and Marine J., J. Lumin. 16 363 (1978)
[6] Clerjaud B., Galineau A., Galland D. and Samindayer K., Phys. Rev. B 19 2056 (1979)
[7] Aven M. and Segall B., Phys. Rev. 130 81 (1963)

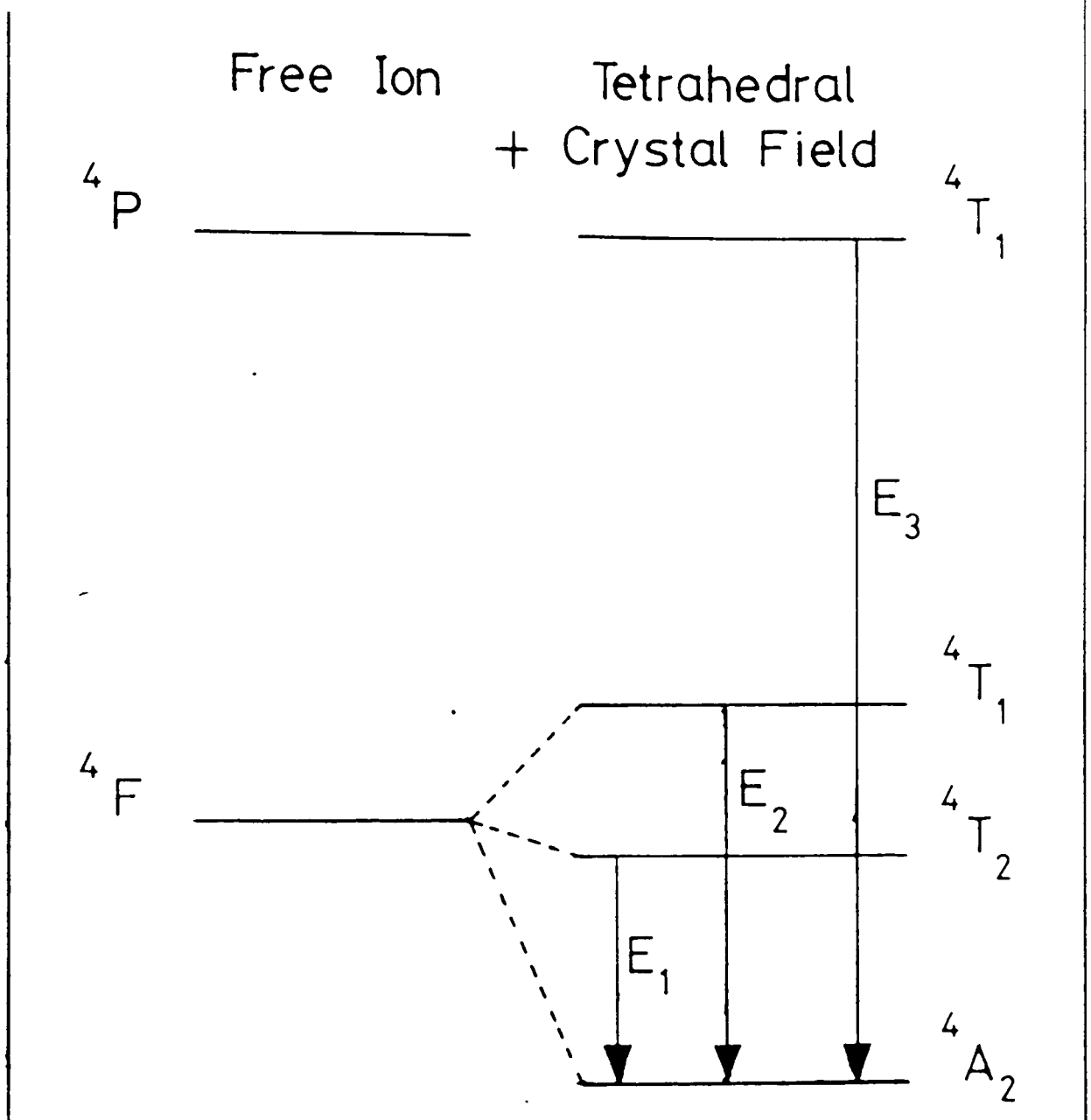

Figure B.1 The splitting of the ^4F ground state of the Fe^+ ion in a tetrahedral crystal field. The ^4P excited state is also shown.

APPENDIX B

The Ground State of the Fe^+ Ion in a Tetrahedral Field

In Chapter three it was propsed that an electron transition within the energy levels of Fe^+ may be a possible model to explain the luminescence band at 1.06 eV. In this appendix the energy level splittings of the ground state of a d^7 ion situated in a tetrahedral field are given. Using these the theoretical expressions for the energies of internal transitions may be calculated and thus the "real" value of the Racah B parameter [1] is deduced from the energy of the luminescence transition.

Figure B.1 shows the splitting of the ^4F ground state of the d^7 Fe^+ free ion when placed in a tetrahedral crystal field (ZnTe) together with the possible electron transitions which may result in infra-red luminescence.

The expressions for the energies of the transitions E_1, E_2 and E_3 were shown by Gördövsky et al [2] to be

$$E_1 = 10\ Dq \tag{B1}$$

$$E_2 = 1.5(10\ Dq) + 7.5B - 0.5b \tag{B2}$$

$$E_3 = 1.5(10\ Dq) + 7.5B + 0.5b \tag{B3}$$

where b is given by

$$b = [(10\ Dq - 9B^2) + 144B^2]^{1/2} \tag{B4}$$

which may be approximated by

$$b = 12\ B \qquad (B5)$$

Using a value of 317 cm^{-1} for Dq and assuming that the infra-red transition at 1.13 eV ($\sim$ 9114 cm^{-1}) is most probably due to the electron transition from the ^4P excited state into the lowest ground state ($^4A_2$) then from equations (B3,B4) B must have a value of

$$B \approx 323\ cm^{-1}$$

This value of B must be compared with that calculated for the free ion which is

$$B = 810\ cm^{-1}$$

Screening of the d^7 electrons by the bonding electrons and any distortions in the crystal field would both serve to reduce the B parameter in the crystal, possibly to the value calculated here. A discrepancy between the free ion value of B and that in ZnTe has been observed in Co^{2+} (d^7) by Baranowski et al [3]. Their experimentally determined value was 460 cm^{-1}, compared with the theoretical value of 1115 cm^{-1} for the free ion, the difference being explained by possible screening effects.

The experimentally deduced value of B for Fe^+ in ZnTe calculated here may be correct even though it is much less than that of the free ion. However, as no other experimental evidence has been found to corroborate this the use of an internal transition model to explain the luminescence band can remain only tentative.

[1] Racah, Shadmi, Bull. Soc. Coun. Israel 8F 15 (1959)

[2] Gardavsky J., Werner A., Hochheimer H.D., Phys. Rev. B 24 4972 (1981)

[3] Baranowski J.M., Allen J.W., Peason G.L., Phys. Rev. 16 627 (1967)